Abstract of “An Absolute Calibration of Sub-1 keV Nuclear Recoils in Liquid Xenon Using D-D Neutron Scattering Kinematics in the LUX Detector” by James Richard Verbus, Ph.D., Brown University, May 2016.

We propose a new technique for the calibration of nuclear recoils in large noble element dual-phase time projection chambers (TPCs) used to search for WIMP dark matter in the local galactic halo. This technique provides a measurement of the low-energy nuclear recoil response of the target media using the measured scattering angle between multiple neutron interactions within the detector volume. Several strategies for improving this calibration technique are discussed, including the creation of a new type of quasi-monoenergetic 272 keV neutron source. We report results from a time-of-flight-based measurement of the neutron energy spectrum produced by an Adelphi Technology, Inc. DD108 neutron generator, confirming its suitability for the proposed calibration.

The Large Underground Xenon (LUX) experiment is a dual-phase liquid xenon TPC operating at the Sanford Underground Research Facility in Lead, South Dakota. Our proposed calibration technique for nuclear recoils in liquid xenon was performed *in situ* in the LUX detector using a collimated beam of mono-energetic 2.45 MeV neutrons produced by the DD108 fusion source. The nuclear recoil energy from the first neutron scatter in the TPC was reconstructed using the measured scattering angle defined by two-site neutron events within the active xenon volume. We measured the absolute charge (Q_y) and light (L_y) yields at an average electric field of 180 V/cm for nuclear recoil energies spanning 0.7 to 74 keV and 1.1 to 74 keV, respectively. This calibration of the nuclear recoil signal yields will permit the further refinement of liquid xenon nuclear recoil signal models and clearly demonstrates measurable ionization and scintillation signals in this medium at recoil energies down to $\mathcal{O}(1\text{ keV})$. The low-energy reach and reduced systematics of this calibration have particular significance for the low-mass WIMP sensitivity of several leading dark matter experiments.

An Absolute Calibration of Sub-1 keV Nuclear Recoils in Liquid Xenon Using D-D Neutron Scattering Kinematics in the LUX Detector

by

James Richard Verbus

Submitted in partial fulfillment of the requirements
for the Degree of Doctor of Philosophy in the
Department of Physics at Brown University

Providence, Rhode Island

May 2016

This dissertation by James Richard Verbus is accepted in its present form by the Department of Physics as satisfying the dissertation requirement for the degree of Doctor of Philosophy.

Date ______________ ______________________________
Professor Richard J. Gaitskell, Director

Recommended to the Graduate Council

Date ______________ ______________________________
Professor Ian Dell'Antonio, Reader

Date ______________ ______________________________
Professor Meenakshi Narain, Reader

Approved by the Graduate Council

Date ______________ ______________________________
Professor Peter Weber
Dean of the Graduate School

Vita

James Richard Verbus was born in a suburb of Cleveland, OH on February 12, 1987. James began working on the LUX experiment in 2007 as an undergraduate student. He obtained his Bachelor of Science in Physics from Case Western Reserve University in May 2009. He began working on LUX as a graduate student at Brown University in September 2009. He earned his Master of Science in Physics in May 2010.

Acknowledgments

I am extremely grateful for the incredible support and guidance I have received over the years from my advisor Richard Gaitskell. Rick's enthusiasm and insight is something to behold, and I feel very lucky to have had the opportunity to share in such a great endeavor. His consistently high expectations combined with frequent, immediate, and clear feedback have been invaluable to my development as a physicist.

I thank the members of the LUX collaboration and those at the Sanford Underground Research Facility for their collaboration over the years, without which this work would not have been possible—especially Tom Shutt who gave me my first opportunity to get involved in the LUX effort during my undergraduate years at Case Western Reserve University. I am grateful to my committee members, Ian Dell'Antonio and Meenakshi Narain, for their careful review of this document. I thank those at Adelphi Technology, Inc. for their operational support and data on the DD108 neutron generator.

I thank Samuel Chan, Jeremy Chapman, Alastair Currie, Attila Dobi, Carlos Faham, Simon Fiorucci, Dongqing Huang, David Malling, Monica Pangilinan, Casey Rhyne, and Will Taylor for their friendship and collaboration during our shared time at Brown. I thank Peter Sorensen and Luiz de Viveiros for showing that it can be done, and for providing invaluable advice over the past seven years. I thank Max Genecov, Soumya Ghosh, and Alexander Moskowitz for their work on the neutron time-of-flight measurement during the summer of 2013.

I thank Carmen Carmona, Samuel Chan, Jeremy Chapman, Richard Gaitskell, Dongqing Huang, Brian Lenardo, David Malling, Evan Pease, Casey Rhyne, Mathew Szydagis, and Luiz de Viveiros for their significant contributions to the D-D calibration work. I thank Dan McKinsey, Harry Nelson, and Mike Witherell for their valuable input and discussion during the D-D calibration and analysis process. I am indebted to the many members of the LUX collaboration that provided extensive feedback on the manuscripts in preparation that parts of this thesis are based upon—with special thanks to Henrique Araújo, Alastair Currie, Simon Fiorucci, Richard Gaitskell, Kareem Kazkaz, Brian Lenardo, Isabel Lopez, Aaron Manalaysay, Dongming Mei, Harry Nelson, Evan Pease, Peter Sorensen, and Mathew Szydagis.

I thank Valerie Marchenko for her love and support, and for tolerating many late night proof-reading sessions. I thank my parents Richard and Marilyn Verbus, and my sister Emily Verbus, for their unwavering support and encouragement in all things.

Contents

⋆ Parts of this thesis are based directly upon manuscripts in preparation for journal submission [1, 2]. I am the corresponding author of both articles.

List of Tables

List of Figures

Chapter 1

An In Situ Absolute Nuclear Recoil Calibration Using Neutron Scattering Kinematics

1.1 Introduction

Dark matter experiments using liquid noble detector media have placed the most stringent limits on the spin-independent WIMP-nucleon cross-section over the majority of the WIMP mass range spanning 1–1000 GeV/c^2. The most sensitive of these liquid noble detectors over this WIMP mass range is currently the LUX Dark Matter Experiment [5]. Calibration of the nuclear recoil signal response of the target media over the recoil energy range used for the WIMP search is required to understand detector efficiency for the observation of potential dark matter events. The sensitivity of these experiments to low-mass WIMPs of mass <10 GeV/c^2 is strongly dependent upon the nuclear recoil response for low-energy nuclear recoils. The low-mass WIMP signal interpretations of several recent dark matter experiments [6–8] are in tension with recent exclusion limits placed by liquid xenon dark matter experiments [5, 9]. This tension reinforces the need for new low-energy, high-precision calibration of the nuclear recoil signal response in liquid noble detectors.

Dual-phase liquid noble time projection chambers (TPCs) detect both the scintillation and ionization resulting from an energy deposition in the target media. The most common type of TPC used in the dark matter field uses photomultiplier tubes (PMTs) to record both the scintillation and ionization signals. The scintillation signal (S1) is promptly detected by PMTs lining the top and bottom of the detector's active region. The ionization signal is produced by electrons that drift to the liquid surface under the influence of an applied electric field E_d. The electrons are extracted into the gas phase via an electric field E_e, where they produce secondary scintillation light (S2) via electroluminescence.

We define the single quanta gain values relating the number of scintillation photons and ionization electrons to the corresponding observed number of detected quanta as g_1 and g_2. The variables g_1 and g_2 have units of detected-photons-per-scintillation-photon and extracted-electrons-per-ionization-electron, respectively. Due to the difficulty of calibrating the detector-specific g_1 value, the scintillation yield is traditionally reported in terms of $\mathcal{L}_{\mathrm{eff}}$, the measured scintillation yield relative to a monoenergetic electron recoil standard candle often provided by ^{57}Co or $^{83\mathrm{m}}$Kr. Recent large liquid noble detectors have precisely measured both g_1 and g_2 simultaneously using the anti-correlation of S1 and S2 signals [5]. This allows the *in situ* calibration of both the light (L_y) and charge (Q_y) yields for nuclear recoils in the absolute units of photons/keV$_{\mathrm{nr}}$ and electrons/keV$_{\mathrm{nr}}$, respectively. In this thesis, we use the units keV$_{\mathrm{nr}}$ (keV$_{\mathrm{ee}}$) to indicate energy deposited in the form of nuclear (electronic) recoils.

Dark matter experiments have traditionally used a continuum neutron source placed adjacent to the detector's active region to obtain an *in situ* nuclear nuclear recoil calibration. Frequently used calibration sources include ^{252}Cf and ^{241}Am/Be, which are examples of spontaneous fission and (α, n) sources, respectively. These sources emit a continuous spectrum of neutrons with energies extending up to $\sim$10 MeV, and produce a relatively featureless recoil spectrum in the energy region of interest for WIMP searches. The large, high-energy gamma ray to neutron ratio of these sources creates unwanted electromagnetic contamination during TPC calibrations. The emitted gamma ray to neutron ratio is ∼2 and 0.6 for ^{252}Cf and ^{241}Am/Be, respectively [10, 11]. The energy of these gamma rays is typically in the range 1–10 MeV [12, 13]. In the case of ^{241}Am/Be, the ratio here is calculated for the 4.4 MeV gamma rays that are produced by the excited ^{12}C state remaining after the $^{9}\mathrm{Be}(\alpha, \mathrm{n})^{12}\mathrm{C}$ reaction.[1] Extraction of nuclear recoil signal yields using these sources requires precise modeling of the source neutron spectrum and scattering inside passive detector materials to create a best-fit Monte Carlo comparison to the observed recoil spectrum [14–16]. The energy scale in these methods is often left as a free parameter in the overall fit to the observed signal spectra.

Existing calibrations using a fixed scattering angle to set an absolute energy scale have focused on *ex situ* calibrations in liquid noble test cells [17–20]. In these experiments monoenergetic neutrons with a known direction interact in a small liquid noble detector. Coincident pulses in a far secondary detector are used to tag valid events. The neutron source and detector geometry is arranged to enforce a known fixed scattering angle in the liquid noble target media. The recoil energy $E_{\mathrm{nr},A}$ is determined by Eq. 1.1, where m_A is atomic mass of the target element, E_n is the incident energy of the neutron, m_n is the mass of the neutron, and θ_{CM} is the scattering angle in the center-of-mass frame:

$$E_{\mathrm{nr},A} = \zeta E_n \,, \tag{1.1}$$

where

$$\zeta = \frac{4 m_n m_A}{(m_n + m_A)^2} \frac{(1 - \cos\theta_{\mathrm{CM}})}{2} \,. \tag{1.2}$$

The relationship between θ_{CM} and the scattering angle in the laboratory frame, θ_{lab}, is given by:

[1] The rate of 60 keV gamma rays is much higher relative to the ^{241}Am/Be neutron output: for 10^6 primary alpha particles from the ^{241}Am decays, only 70 neutrons are emitted [10]. The dominant gamma ray emission from ^{241}Am alpha decays is this coincident 60 keV gamma ray; these can be more easily screened out in practice due to their low energy.

$$\tan\theta_{\mathrm{lab}} = \frac{\sin\theta_{\mathrm{CM}}}{m_n/m_A + \cos\theta_{\mathrm{CM}}}\,. \tag{1.3}$$

For target elements with large atomic mass, the approximation $\theta_{\mathrm{CM}} \approx \theta_{\mathrm{lab}}$ is often made, and Eq. 1.1 can be used directly. The maximum error on the calculated recoil energies using this approximation for neon, argon, and xenon target nuclei is 10%, 5%, and 1.5%, respectively. This error is determined by comparing the recoil energy in Eq. 1.1 when using the exact value of θ_{CM} to that calculated using the approximation $\theta_{\mathrm{CM}} \approx \theta_{\mathrm{lab}}$.

These *ex situ* calibrations can suffer from several undesirable background contributions. First, neutrons can scatter in passive materials either before or after interacting in the liquid noble test cell, and then subsequently complete the journey to the far detector. These neutrons lose an undetermined amount of energy during their scatters in passive material and have a poorly defined scattering angle in the liquid noble test chamber. These effects make inference of the deposited nuclear recoil energy in the target medium difficult. Neutrons that scatter in passive materials during their journey between the liquid xenon cell and the far detector provide a similar source of background events. Second, it is difficult to differentiate events consisting of multiple elastic scatters in the liquid noble target during single-phase operation as is typically used for *ex situ* L_y studies. These multiple elastic scatter events will have a systematically high observed scintillation signal and a measured scattering angle that is no longer directly related to the path taken through the liquid noble target. Finally, due to the physical size of the detectors, there is a systematic uncertainty associated with the range of allowed scattering angles. It is possible to attempt to accommodate these effects on average and estimate the associated systematic uncertainties using a neutron transport Monte Carlo simulation with a model of the experimental setup, but a more direct calibration technique can eliminate these systematic uncertainties entirely.

Recently, photoneutron sources such as ^{88}Y/Be have been used for low-energy nuclear recoil calibrations in various dark matter search technologies using the feature presented by the recoil spectrum endpoint [21]. The ratio of gamma rays to neutrons produced by a typical ^{88}Y/Be source is $\sim 4\times 10^5$ to 1 [10]. High-Z shielding of thickness $\gtrsim$10 cm surrounding such a source is required to reduce the gamma ray rate to manageable levels for a nuclear recoil calibration. Extracting the signal yields using such a source requires a Monte Carlo simulation, which includes a model of the initial neutron energy spectrum produced by the source and calculation of neutron energy loss in passive shielding and detector materials.

We present a new scattering-angle-based technique for an *in situ*, absolute nuclear recoil calibration in modern, large, liquid noble based TPCs used for rare event searches [22–25]. In this technique, neutrons of known energy and direction are fired into a large liquid noble TPC. The detector's position reconstruction capabilities provide the (x, y, z) coordinates of each vertex in multiple scatter events. The calculated scattering angle provides a direct measurement of the recoil energy at each scattering vertex according to Eq. 1.1.

An ideal neutron source for this type of measurement should have the following characteristics:

- The neutron source should be compact and portable to allow deployment in deep underground laboratory space.

- In order to precisely define E_n, the neutron source must produce a monoenergetic energy spectrum, ideally with a width (σ/μ) subdominant to other systematic effects contributing to spectrum broadening described in Sec. 1.2.

- To calibrate noble gas detectors in the nuclear recoil energy region of interest, the techniques described in this chapter require an incident neutron beam with a mean energy between 100 keV and several MeV.

- The total flux into 4π solid angle of the neutron source should be greater than $\sim 10^7$ n/s to achieve useful calibration rates using the technique described in Sec. 1.2. A flux of $\sim 10^9$ n/s or greater is advantageous for the creation of a 272 keV neutron backscatter source as described in Sec. 1.3.2.

- The ability to pulse the neutron beam provides several advantages. First, controlling the duty cycle provides a precise tuning mechanism for the neutron yield. Second, the known "beam on" time during low duty cycle operation can provide a powerful reduction in calibration backgrounds. Third, if neutron bunch widths of $\lesssim$10 μs are achievable, then more sensitive measurement techniques described in Sec. 1.3 become feasible.

Several candidate monoenergetic neutron sources are available that provide required energy, flux, and pulsing characteristics. The endothermic $^7\mathrm{Li(p,n)}^7\mathrm{Be}$ reaction has a Q value of -1.644 MeV [26]. This reaction can provide a source of monoenergetic neutrons of tunable mean energy by accelerating the incident protons to a fixed energy above the reaction threshold. A dedicated proton accelerator facility is required to generate the $\sim$2 MeV protons used for this reaction. A number of recent *ex situ* nuclear recoil calibrations have made use of such facilities [20, 27, 28]. These proton-beam-based neutron sources can have unwanted broadening of the neutron energy spectrum due to proton energy losses in the target material. The exothermic $^2\mathrm{H(d,n)}^3\mathrm{He}$ (deuterium-deuterium or D-D) and $^3\mathrm{H(d,n)}^4\mathrm{He}$ (deuterium-tritium or D-T) reactions have a Q value of 3.269 MeV and 17.590 MeV, respectively [26]. The modest 100 kV potential typically used to accelerate deuterium ions used for these reactions can be easily generated via compact, commercially available high-voltage supplies. It is typically possible to achieve higher neutron yields using D-T, due to the larger reaction cross-section for 100 keV deuterium ions; however, the 14 MeV neutrons produced by the D-T reaction are higher in energy than desired for low-energy nuclear recoil calibrations. The D-D reaction provides neutrons with an average energy of 2.45 MeV, which is more appropriate for generating low-energy nuclear recoils with a measurable scattering angle in liquid noble targets.

The content of the following sections is arranged as follows: in Sec. 1.2 we propose a new neutron scattering angle based nuclear recoil calibration technique for large liquid noble TPCs; several potential enhancements to the newly proposed technique are described in Sec. 1.3, including the creation of a monoenergetic 272 keV neutron source in Sec 1.3.2. the neutron energy spectrum of a commercially available Adelphi Technology, Inc. DD108 neutron generator is measured in Ch. 3

to demonstrate its suitability for the proposed nuclear recoil calibration techniques.

1.2 Proposed nuclear recoil calibration using neutron scattering kinematics in a large liquid noble TPC

The current generation of liquid noble TPCs are commonly located at the center of large ($\mathcal{O}$(10 m) diameter) water tanks used to shield the TPC from unwanted external radioactive backgrounds during rare event searches [5, 25, 29]. A collimated beam of neutrons with known direction can be created by positioning a gas-filled (or evacuated) conduit inside the water tank spanning the space from the TPC cryostat to the wall of the water tank. A monoenergetic neutron source, such as a commercially available D-D neutron generator, placed outside the water tank in line with the conduit can be used to fix the incident neutron energy and direction into the TPC. Using a 4m-long, 5 cm diameter neutron conduit with a neutron generator producing 10^8 n/s into 4π, we expect $\sim 10^3$ n/s incident upon the detector. This incident neutron rate can be finely tuned by adjusting the duty cycle using available D-D generator pulsing capability.

This technique allows one to exploit the self-shielding properties of large TPCs to avoid contamination due to neutron scatters in passive materials that contribute to background events in more traditional *ex situ* scattering angle based measurements. Monte Carlo studies of neutron transport in a realistic experimental setup indicate that the application of simple fiducial analysis volume cuts in line with the neutron beam projection inside the TPC can ensure that 95% of accepted events are produced by neutrons with energies within 6% of the initial energy at the source [30]. The collimated D-D neutron beam can also function as a very effective calibration source for the distribution of S2 vs. S1 for recoils. The ratio of S2 to S1 is frequently used as a discriminant between nuclear and electronic recoils in liquid noble TPCs. The neutron conduit can be aligned near the liquid xenon surface to provide a well-collimated beam of neutrons far from the reverse field region below the detector cathode—a common source of multiple scintillation, single ionization type event contamination in nuclear recoil band calibrations [31, 32].

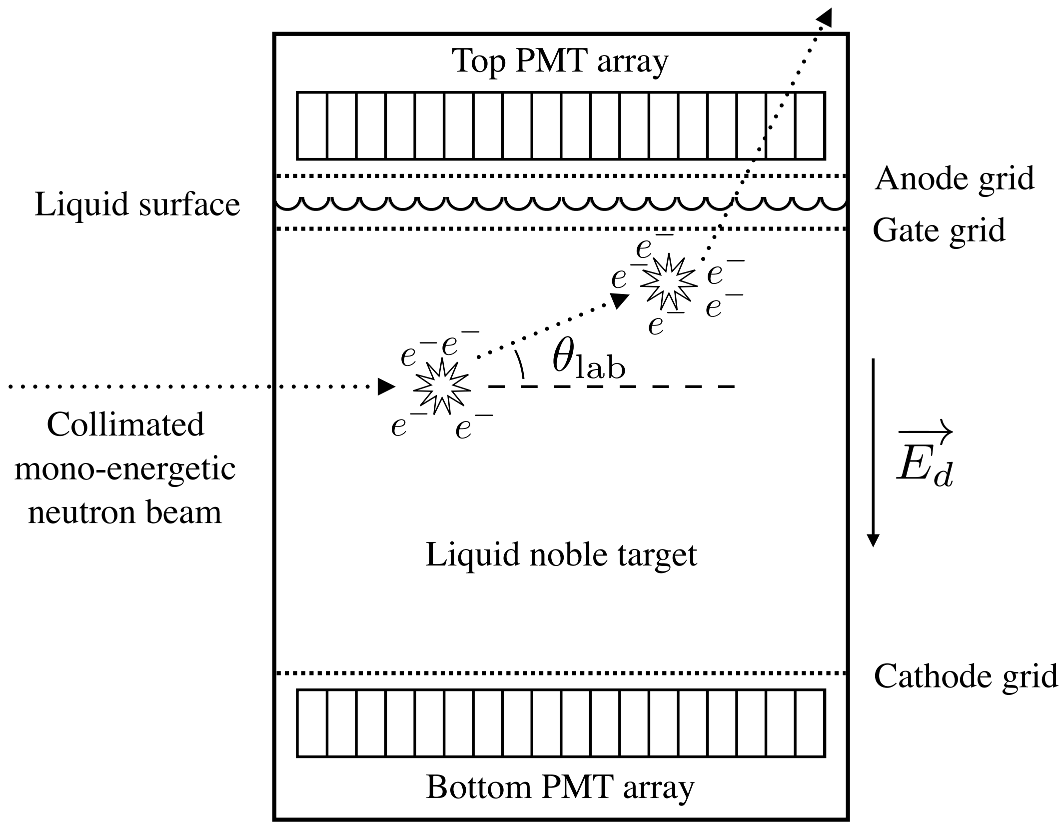

Figure 1.1: Diagram of a monoenergetic neutron scattering twice in a large TPC. The (x, y, z) position of both interactions can be reconstructed to provide a measurement of the scattering angle at the first vertex, θ_{lab}. The prompt scintillation signals from each vertex typically overlap in the event record, but may be separately resolvable in some target media. The ionization signal from each vertex can be individually resolved in the event record for vertices separated in z by a few mm. The signal generation and reconstruction parameters for liquid argon and xenon are listed in Table 1.1. The nuclear recoil energy at the first scattering vertex can be reconstructed using the measured θ_{lab}. The observed signals and measured energy at the first vertex provide a direct measurement of the signal yields.

The direct extraction of the signal yields depends upon the time structure of the S1 and S2 signals from each scattering vertex in the event record. For scattering vertices separated by several mm in z, the S2 signal from each scattering vertex can be individually resolved in noble targets given the typically-achieved electron drift velocities of 1–2 mm/μs reported in Table 1.1. The ionization yield, Q_y, of the target medium can be directly probed with an absolute measurement of nuclear recoil energy by fully reconstructing the scattering angle for multiple-vertex events and using the

Table 1.1: Relevant dual-phase liquid noble TPC parameters for Ar and Xe.

Noble Target Characteristic	Ar [a]	Xe [b]
2.45 MeV total mean free path [cm]	15	13
2.45 MeV elastic mean free path [cm]	19	20
272 keV total mean free path [cm]	17	14
272 keV elastic mean free path [cm]	18	15
singlet lifetime [ns]	6 [c]	3.1 [d]
triplet lifetime [ns]	1.6×10^3 [c]	24 [d]
e^- drift velocity in large TPCs [mm/μs]	0.93 ± 0.01 (200 V/cm) [e]	1.51 ± 0.01 (180 V/cm) [f]

[a] Mean free paths calculated for ^{40}Ar (99.6% relative abundance) using Ref. [33].
[b] Mean free paths calculated for natural Xe using Ref. [33]. [c] [34] [d] [35] [e] [29] [f] [24]

corresponding $S2$ information from each individual vertex. Recent large TPCs using argon and xenon as the target media have achieved (x, y) position reconstruction uncertainties of $\mathcal{O}(1\text{ cm})$ [36, 37] using the position reconstruction algorithm described in Ref. [38].

The short timescale of the prompt S1 light makes direct extraction of the scintillation yield, L_y, more involved for some target media. The 2.45 MeV neutrons produced by the D-D reaction have a velocity of 2.2 cm/ns. In the case of liquid xenon, the similar singlet and triplet lifetimes in Table 1.1 combine to produce an S1 pulse envelope with a decay time of 20–30 ns. The 45 ns time constant for electron-ion recombination in xenon is suppressed due to the drift field [39]. Even the longest path lengths available in the current generation of liquid noble TPCs of ∼1 m provide a time separation between interactions that competes with the characteristic time constant of the S1 pulses themselves, leading to S1 pulse overlap in the event record. Due to the large time difference between the singlet (6 ns) and triplet (1.6 μs) lifetimes for Ar, the time structure of the prompt S1 light is dominated by photons produced by the singlet state; it may be possible to separate the singlet S1 contribution from each vertex in multiple-scatter events in that target media.

A direct, absolute calibration of L_y in multiple scatter data using the observed neutron scattering angles can be achieved via a comparison of the S1 photon arrival times to the expected S1 pulse time structure given the location of the multiple neutron scattering vertices. The measured S1 photon contribution from each vertex of known energy can be extracted via a maximum likelihood based comparison. This pulse envelope time structure analysis promises to be more powerful when combined with the techniques described in Sec. 1.3. Alternatively, the scintillation yield can be extracted from the sample of single neutron scatters in line with the neutron beam projection in the TPC. The absolutely calibrated S2 yield from the multiple scatter D-D technique can be used to set the energy scale for observed single-scatter (1x S1, 1x S2) events, which allows for a precise extraction of the light yield via comparison with a Monte Carlo simulation.

1.3 Extension of the technique providing lower measured recoil energies and reduced calibration uncertainties

1.3.1 Reduction of neutron bunch time structure

The neutron output of many commercially available D-D neutron generators can be pulsed. The duration and frequency of the neutron pulses can be controlled using an external pulse generator. The neutron generator model used in Ch. 3 supports a nominal minimum pulse width of 100 μs.

Alternative pulsing solutions exist to provide neutron pulses with a duration as short as 1 ns to 1 μs [26]. Reducing the neutron bunch width time structure provides two powerful improvements over the technique described in Sec. 1.2. First, narrowing the time envelope of the neutron pulse improves background rejection proportionally to the duty cycle. Only events with prompt signals consistent with the generator pulse time and neutron propagation time to the detector are valid nuclear recoil candidates. This allows rejection of backgrounds due to accidental coincidences and other spurious signals, which become increasingly prevalent when working close to threshold during analysis of small nuclear recoil signals. This delivers a lower-energy threshold and reduced systematics for the calibration signal event set. Second, when the neutron pulse width becomes sufficiently narrow, it can be used to establish the t_0 for the electron drift of a scattering event. This t_0 information is traditionally provided by the S1 in dual-phase TPCs. Establishing the t_0 independently of the observation of an S1 signal permits the investigation of the S2 associated with neutron scatter events that are so low in recoil energy that the associated S1 signal is typically undetected. In liquid xenon, we would expect this to extend the S2 signal yield studies down to $\mathcal{O}(100\ \mathrm{eV_{nr}})$. This ultra-low-energy charge yield calibration technique is significant for determining the sensitivity of TPC experiments to low-mass WIMPs using S2-only searches.

The z position of a particle interaction in these detectors is typically determined by measuring the electron drift time using the pulse timing information provided by the S1 and S2 signals. The known electron drift velocity (Table 1.1) for a given electric drift field $\vec{E_d}$ applied across the target media allows the reconstruction of the z position with a precision of $\sim$1 mm. A reduction in the neutron bunch width time structure to 10 μs will provide position reconstruction of S2-only events in the z dimension with a resolution of roughly 2 cm, similar to the (x, y) reconstruction precision provided by PMT top array hit-pattern analysis of S2 signals. The ability to reconstruct S2-only events to high precision in three dimensions allows for the identification of candidate S2-only events that are consistent with a neutron interaction in the detector given the expected drift time for events in line with the beam pipe. It is then possible to determine the number of single-scatter events with zero detected photons for a given observed S2 pulse size. This allows for an additional L_y calibration technique providing stronger statistical constraints on the S1 yield for a given S2 size.

Further narrowing the neutron bunch to a width of $\mathcal{O}(100\ \mathrm{ns})$ may be possible. This improved time definition of the neutron pulse would permit the use of time-of-flight (ToF) energy tagging for neutrons generated by the D-D source. The neutrons of interest for this type of calibration scatter in a deliberately positioned hydrogenous moderator outside of the water tank near the neutron generator, yielding a sample of neutrons with a broad spectrum of kinetic energies traveling down the beam pipe to the TPC. The measured ToF would then provide the neutron kinetic energy on a per-event basis. The calculated ToF for neutrons from 1–2450 keV is shown in Table 1.2. Assuming a 4 m beam path from the hydrogenous moderator to the TPC active region, moderated neutrons ranging from 1–2450 keV would have an expected ToF between 200 ns and 10 μs.

Table 1.2: The time-of-flight (ToF) dependence upon neutron energy. The corresponding nuclear recoil spectrum endpoint energy in argon and xenon is given in columns three and four, respectively.

E_n [keV]	ToF [ns/m]	Maximum Recoil [keV$_{\mathrm{nr}}$]	
		Ar	Xe
1	2286	0.1	0.03
10	723	1	0.3
100	229	10	3
272	139	26	8
1000	72	96	30
2450	46	235	74

1.3.2 Reduction in neutron energy using a deuterium-loaded reflector

The technique described in this section can provide an inexpensive and portable quasi-monoenergetic source 272 keV neutrons that can be used to extend the kinematic calibration, described in Sec. 1.2, nearly an order of magnitude lower in energy. This lower-energy source is well matched to the nuclear recoil energy region for low-mass WIMP searches and the expected coherent elastic neutrino neutrino-nucleus scattering (CENNS) signal in upcoming large liquid noble dark matter detectors [40, 41].

1.3.2.1 A monoenergetic 272 keV neutron source

A beam of quasi-monoenergetic 272 keV neutrons can be obtained by positioning a deuterium-loaded material (the "reflector") behind the D-D neutron generator, directly in line with the neutron collimation conduit leading to the TPC (see Fig. 1.2).[2] The limited solid angle presented by the neutron conduit is used to collect neutrons that scatter in the deuterium-loaded reflector with a scattering angle of $\sim$180°. Deuterium is an optimal reflector material; its low atomic mass provides the most significant reduction in neutron energy possible for $\sim$180° elastic scatters [42]—larger energy reductions from neutron scatters on ^{1}H are discussed addressed below. These backscattered neutrons have a minimum kinetic energy of 272 keV. In addition, a double-scatter (both scatters

[2]This section is part of a paper in preparation for publication [1]. I am the corresponding author of this paper. The simulations and analysis in this section were primarily performed by Casey Rhyne at Brown University. The text was written in collaboration with Casey Rhyne.

must be neutron-deuteron) elastic scattering event with a summed scattering angle of 180° within the deuterium-loaded reflector also provides an outgoing 272 keV neutron. Although neutron-hydrogen scattering can result in neutron energies below 272 keV, all neutron scatters are in the forward direction with a scattering angle of 0–90° in the lab frame. With a hydrogen reflector, small variations in the neutron scattering angle produce large fluctuations in reflected neutron energy. In contrast, using direct backscatters provided by deuterium's significant differential scattering cross-section at 180° suppresses the effects of variations in scattering angle, and provides a better defined quasi-monoenergetic neutron beam. Deuterium has the strongest preference for direct 180° scatters of all potential reflector materials.

The $\times 9$ reduction in the neutron beam energy provided by the deuterium reflector has several advantages for low-energy nuclear recoil calibration. The use of 272 keV neutrons provides a reduction in the uncertainty associated with kinematic energy reconstruction for low-energy events. A 1 $\mathrm{keV_{nr}}$ nuclear recoil produced by a 2.45 MeV neutron in liquid xenon corresponds to a neutron scattering angle of 13°, which is a 4.6 cm deflection over a length of 20 cm. By comparison, a 1 $\mathrm{keV_{nr}}$ nuclear recoil produced by a 272 keV neutron in liquid xenon has a scattering angle of 41°, which is a 14 cm deflection over the same vertex separation. In large liquid xenon TPCs, the typical uncertainty associated with (x, y) position reconstruction of each vertex in events of this nuclear recoil is 1–3 cm as shown in Sec. 6.1.2. We estimate that in the 1–4 $\mathrm{keV_{nr}}$ range, the (σ/μ) resolution for angle-based recoil energy reconstruction may be improved by a factor of $\times 2$ due to this increase in the average scattering angle for a given recoil energy. The increased scattering angle for nuclear recoils of a given energy improves the efficiency of the detection of calibration events below 1 $\mathrm{keV_{nr}}$. This improved efficiency allows the technique to directly measure recoil energies of $\mathcal{O}(100\ \mathrm{eV_{nr}})$ in liquid xenon, where the expectation is 1–2 ionization electrons at 180 V/cm.

This backscatter technique reduces the neutron flux incident on the TPC by $\times 1/450$ compared to the calibration described in Sec. 1.2 when using similar neutron generator operating parameters. The reduction of the relative event rate in the TPC can be more than compensated for by the use of the following techniques:

i. Increase the D-D source neutron flux from 10^7 n/s to 10^9 n/s.

ii. Expand the neutron conduit diameter from 5 cm to 15 cm. This provides $\times 60$ increase in the neutron flux entering the TPC given the dimensions in Fig. 1.2. For a typical experimental configuration, this larger neutron conduit diameter increases the angular acceptance from $\pm 0.4°$ to $\pm 1°$ and provides $\times 9$ greater neutron flux.

iii. The larger differential scattering cross-section in xenon for 272 keV neutrons compared to 2.45 MeV neutrons provides a $\times 2.5$ increase in the low-energy recent rate.

1.3.2.2 Simulation of the deuterium-loaded neutron reflector

In order to optimize the technique and select the best type of deuterium-based reflector, a series of Geant4-based [43] simulations using the geometry shown in Fig. 1.2 were performed [44]. To eliminate contamination at the TPC from 2.45 MeV neutrons, the D-D neutron generator must have a non-zero offset from the center of the calibration conduit leading to the TPC. Given the dimensions in Fig. 1.2 and a generator head offset of 5 cm from the beam line, reflected neutrons collected by the solid angle accepted by the neutron conduit have a mean energy of 290 keV. The neutron generator offset, reflector length, reflector size, and reflector type were varied to study the effects on the resultant neutron energy spectrum at the TPC. Each simulated reflector configuration was evaluated based on both the number of reflected neutrons reaching the TPC within a usable energy band and the beam contamination from neutrons of other energies. The figure of merit for the energy contamination study was the ratio of the number of neutrons entering the TPC with energies within $\pm 10\%$ of the backscatter peak to the number with energies <1 MeV. Nuclear recoils from neutrons entering the TPC with energies >1 MeV can be rejected in analysis based upon the size of the ionization signal relative to the measured scattering angle.

Three potential reflector types were considered in this study: gaseous D_2, liquid D_2, and heavy

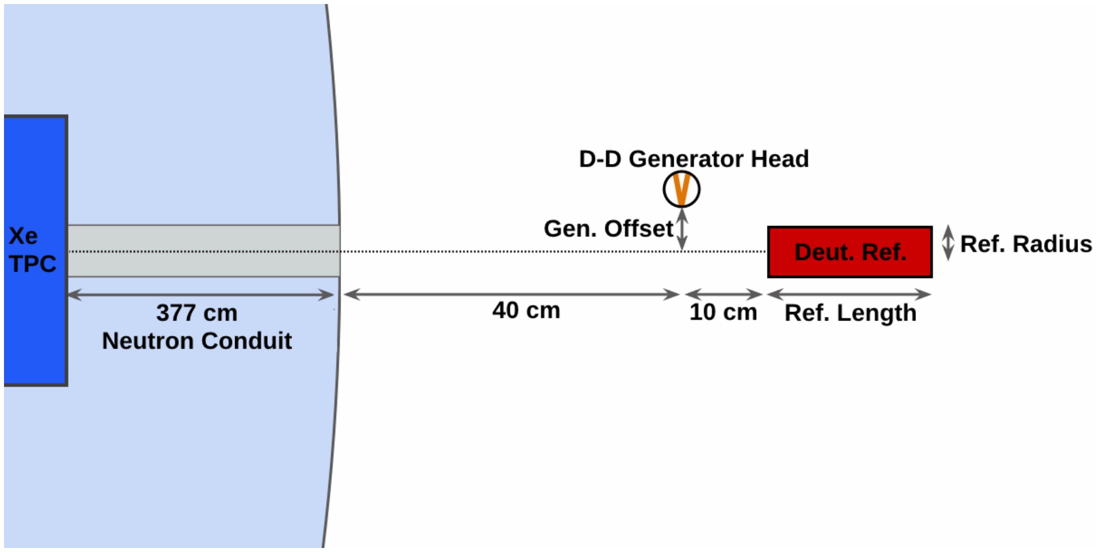

Figure 1.2: Simulation geometry setup for neutron reflector studies. Neutrons produced by the D-D source elastically scatter through an angle ∼180° in the deuterium reflector and are selected by the solid angle of the neutron conduit. The reflector material type, length, and radius as well as the generator head offset were individually varied to determine the optimal configuration. The neutron generator must be placed out of line with the neutron conduit to eliminate line-of-sight 2.45 MeV neutrons from the D-D source entering the TPC. This figure was produced by Casey Rhyne.

water (D_2O). The gaseous D_2 reflector was simulated with a gas pressure achievable in existing cylinders (340 bar, density of 0.047 g/cm^3) and with the surrounding container materials for an available commercial product (the Luxfer T45J, a type III carbon-fiber-based cylinder). The impact of varying container thicknesses for a gaseous D_2 reflector was studied. The liquid D_2 reflector (density of 0.16 g/cm^3) was simulated without containment to demonstrate the highest achievable performance with respect to energy purity and neutron flux. Simulations of pure (gaseous or liquid) D_2 reflectors were used to independently vary aspects of the geometry (such as reflector radius, length, orientation, end cap shape, density, generator offset and conduit radius) to determine the impact of each parameter on the resulting neutron spectrum at the TPC. The heavy water reflector (D_2O) was simulated without containment; its container can be negligibly thin-walled in practice. The effects due to the oxygen atoms in the D_2O were studied.

Representative simulation results comparing gaseous D_2 and D_2O reflector media are shown in Fig. 1.3. The low-energy neutron peak produced by both types of reflector media is visible at

~300 keV. The peak observed at higher energy in the gaseous D_2 and D_2O simulations is produced by neutrons that interact with passive container materials and neutron-oxygen scatters in reflector, respectively. The energy purity figure of merit is nearly identical for gaseous D_2 and D_2O (57% purity in D_2 compared to 60% in D_2O); however, the use of the D_2O results in a $\times 2.3$ increase in the reflected neutron flux within ±10% after collimation. D_2O is a more favorable reflector material based upon the defined energy purity and neutron flux criteria when compared to a gaseous D_2 reflector at the pressures achievable using thin-walled commercially available containment (Luxfer's T45J cylinder).

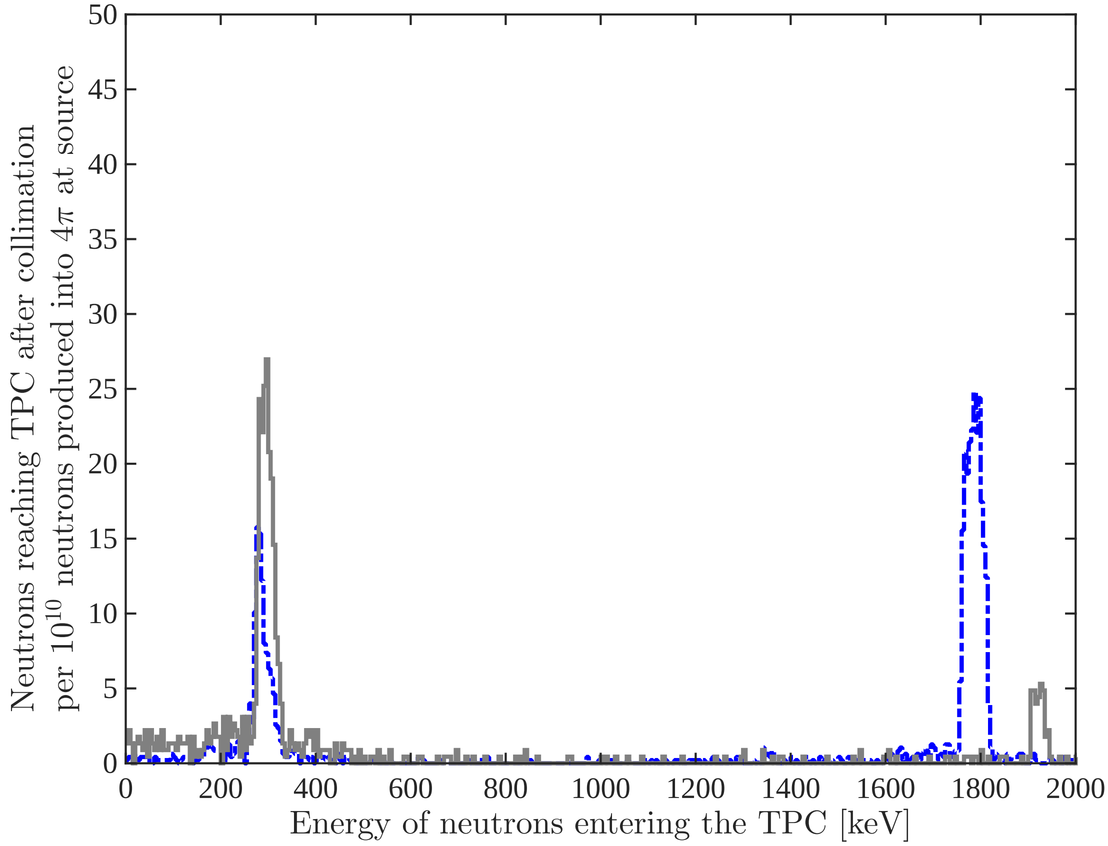

Figure 1.3: Gaseous D_2 cylinder vs. D_2O reflected neutron spectrum comparison. The simulated energy spectra of neutrons incident upon the TPC are shown after scattering in either the gaseous D_2 (blue dashed-dotted) or D_2O (gray solid) reflectors. The gaseous D_2 reflector used a container geometry based upon the Luxfer T45J carbon fiber cylinder. This figure was produced by Casey Rhyne.

Representative simulation results comparing the D_2O and liquid D_2 reflector media are shown in

Fig. 1.4. The liquid D_2 reflector outperformed both the gaseous D_2 and D_2O reflectors in terms of energy purity (67%). The liquid D_2 also provided the largest low-energy neutron flux incident upon the TPC. These results indicate that a high-pressure gas or a liquid D_2 reflector could exceed the performance of a D_2O reflector.

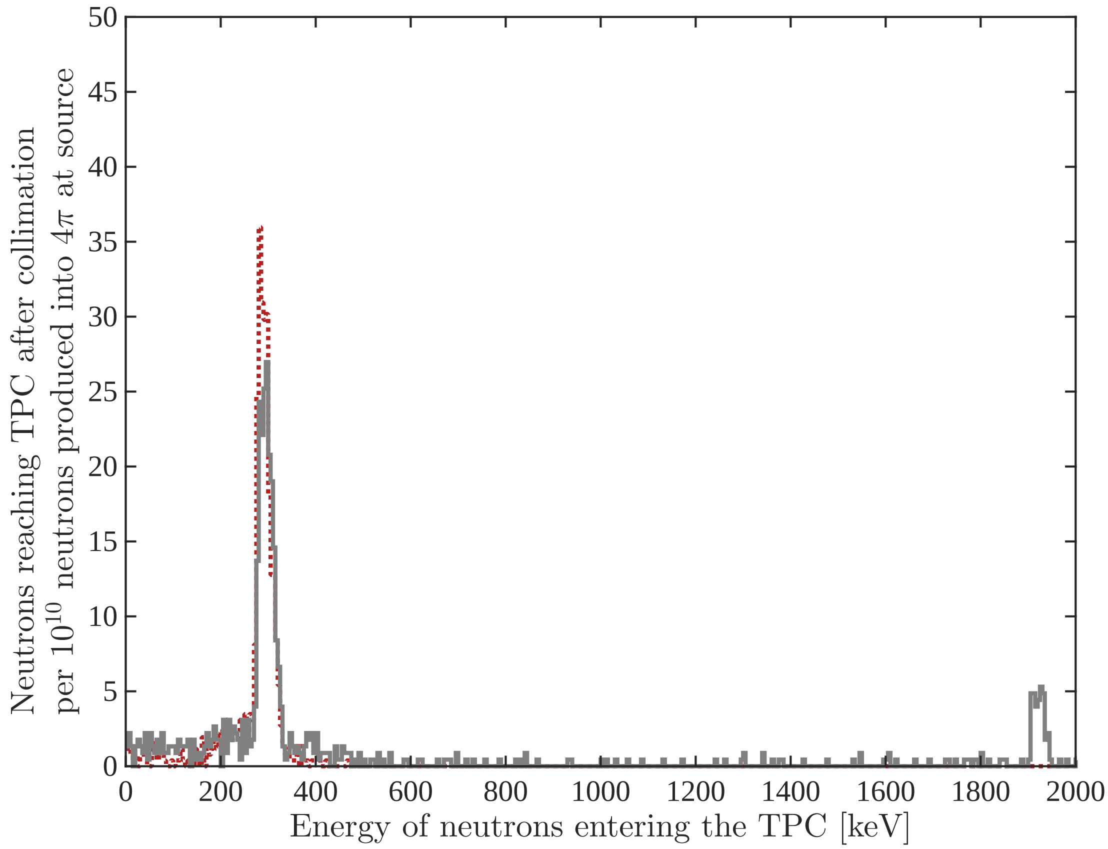

Figure 1.4: Liquid D_2 vs. D_2O reflected neutron spectrum comparison. The simulated energy spectra of neutrons incident upon the TPC are shown after scattering in either the liquid D_2 (red dotted) or D_2O (gray solid) reflectors. This figure was produced by Casey Rhyne.

1.3.2.3 TPC calibration backgrounds when using the deuterium reflector

Neutrons scattering off materials other than deuterium in the reflector setup provide a source of high-energy neutron contamination in the neutron energy spectrum at the TPC. Secondary oxygen recoils in the D_2O reflector create a high-energy neutron background that scales with the reflector mass. A size restriction on effective D_2O based reflector is set by the mean free path between oxygen recoils in the reflector media. Increasing both the D_2O reflector diameter and the neutron conduit diameter from 5 cm to 15 cm results in a $\times60$ increase in flux. This increase in flux comes at the cost of energy purity; there is more than a $\times2$ drop in the beam purity due to oxygen recoils in the reflector. In comparison, a liquid D_2 reflector enlarged in the same way results in a similar flux increase, but only a $\times1.6$ reduction in beam purity. It was found that the performance of the gaseous D_2 reflector can also be improved by increasing the D_2 density and by reducing the containment wall thicknesses. While a D_2O reflector is currently the most effective and easily deployable option, the scaling properties and lack of oxygen in the reflector media make pure D_2 reflectors a compelling topic for further study.

A simulation of the water shielding surrounding the neutron conduit was used to estimate the relative magnitude of contaminating background effects due to neutrons scattering in the water. For a D-D source with a 5 cm offset from the neutron conduit, 20% of the neutrons entering the TPC have lost energy in the water shield. The simulation indicates that 85% of the neutrons entering the TPC after losing energy in the water are either substantially above (>1600 keV) or substantially below (<1 keV) the energy region of interest for backscattered neutrons and would not interfere with TPC calibration. The end result is that 97% of events in the energy region of interest are direct neutrons from the deuterium reflector with energy $\sim$272 keV.

The large drop in the ^{56}Fe neutron scattering cross-section at 274 keV can be used to improve the energy distribution of reflected neutrons [44, 45]. A similar technique was used in Ref. [27]. By placing a 2.5 cm radius iron cylinder in line between the generator and the neutron conduit, all neutrons except those at the desired low-energy peak can be eliminated from the beam. This effect can be used to reduce contamination from off-energy neutrons and improve the width of the energy distribution of neutrons entering the TPC.

1.3.3 Direct scintillation yield measurement using the S1 photon arrival time structure

Analysis of the S1 pulse envelope time structure can provide a direct L_y calibration using the measured scattering angle between neutron interactions. For double-scatter events in the TPC with a given vertex separation, the time separation between the S1 signals from each scatter in the event record is $\propto 1/\sqrt{E_n}$ based upon the neutron travel time between interactions in the target media. The ToF for a variety of neutron energies is shown in Table 1.2. For the direct 2.45 MeV neutrons from the D-D source, a double-scatter event with 50 cm of separation between neutron interactions in the TPC has a 23 ns difference between the time of the first and second scatters. After scattering once, the probability of a 2.45 MeV neutron traveling $\geq$ 50 cm before scattering again in the target media is 2% for xenon and 4% for argon, based upon the total mean free path values in Table 1.1. Given the time constants for S1 signal generation in Table 1.1, it is possible to perform a likelihood-based analysis on the pulse shape envelope of the scintillation signal to determine the photon contribution from the first scatter.

A more clear identification of the S1 contributions from the first and second scattering vertices is made possible when using 272 keV neutrons produced by backscatter source described in Sec. 1.3.2. The corresponding time difference over the same 50 cm path length between scatters when using 272 keV neutrons is 70 ns. This $\times 3$ reduction in neutron velocity compared to the direct 2.45 MeV neutrons from the D-D source provides sufficient time separation to clearly identify the S1 photons from each individual interaction in a liquid xenon TPC. After scattering once, the probability of a 272 keV neutron traveling $\geq$ 50 cm before scattering again in the target media is 3% for xenon and 5% for argon, based upon the total mean free path values in Table 1.1. The scattering-angle-based measurement of the recoil energy at the first scattering vertex can be compared to the observed number of S1 photons to provide a direct measurement of the L_y similar to the Q_y measurement described in Sec. 1.2.

Chapter 2

The Large Underground Xenon Dark Matter Experiment

2.1 Searching for dark matter

The existence of non-baryonic, cold dark matter is supported by overwhelming observational evidence [46–52]. The fractional energy density of baryonic matter, cold dark matter, and dark energy in the universe is represented by Ω_b, Ω_{cdm}, and Ω_Λ, respectively [52]:[1]

$$\begin{aligned}
\Omega_b &= 0.0482 \pm 0.0008\,, \\
\Omega_{\mathrm{cdm}} &= 0.275 \pm 0.005\,, \\
\Omega_\Lambda &= 0.692 \pm 0.010\,.
\end{aligned} \tag{2.1}$$

These numbers indicate that 85% of the mass of the universe is in the form of dark matter which has yet to be detected. The local cold dark matter density at the location of our solar system in the Milky Way is expected to be ~0.3 $\mathrm{GeV\,c^{-2}\,cm^{-3}}$ [53]. This local density varies by roughly a

[1] These values were calculated using a dimensionless Hubble parameter of $h = 0.6780 \pm 0.0077$, also from Ref. [52].

factor of two depending upon the model of dark matter distribution in the galaxy [53]. Weakly interacting massive particles (WIMPs) of mass ~10 GeV/c^2 to 1 TeV/c^2 are a favored cold dark matter candidate particle as their expected thermal relic density is consistent with the observed density of non-baryonic matter in the universe today [54].

2.1.1 Direct dark matter detection

The expected ~0.3 GeV c^{-2} cm^{-3} density of WIMP dark matter at our local position in the galaxy has motivated a number of experiments intent on directly detecting WIMP interactions using baryonic matter targets. These direct detection experiments typically involve the measurement of ionization, scintillation, or phonons produced via particle interactions in the detector's target media. A canonical review of the expected event rates due to dark matter particles in direct detection experiments is provided by Lewin and Smith [55], which is closely followed here. For the most basic case of a stationary (with respect to the galaxy) direct detection experiment, the differential energy spectrum of nuclear recoils is given by

$$\frac{dR}{dE_{\mathrm{nr}}} = \frac{R_0}{E_0 r} e^{-E_{\mathrm{nr}}/(E_0 r)} \,, \tag{2.2}$$

where E_{nr} is the recoil energy of a nucleus in the target material, E_0 is the most probable energy of an incident WIMP particle with mass m_χ, the mass of the target nucleus is given by m_A, and the total event rate per unit target mass is represented by the variable R. The variable r represents a dimensionless reduced mass term:

$$r = \frac{4 m_\chi m_A}{(m_\chi + m_A)^2} \,. \tag{2.3}$$

The total WIMP event rate R_0 for a stationary detector in a galaxy with an infinite escape velocity, v_{esc}, is given by

$$R_0 = \frac{2}{\sqrt{\pi}} \frac{N_0}{A} \frac{\rho_\chi}{m_\chi} \sigma_0 v_0 \,, \tag{2.4}$$

where N_0 is Avogadro's number (6.022×10^{26}/kg), the local density of dark matter is given by ρ_χ, σ_0 is the zero momentum transfer cross-section[2], and v_0 is the most probable WIMP velocity. Using the values for the earth's location in the Milky Way of $v_0 = 230$ km/s and $v_{\rm esc} = 600$ km/s, a more sophisticated estimate of the total WIMP event rate in a detector can be obtained:

$$R_0 = \frac{405}{Am_\chi} \left(\frac{\sigma_0}{1\,\mathrm{pb}}\right) \left(\frac{\rho_\chi}{0.3\mathrm{GeV}\,c^{-2}\,\mathrm{cm}^{-3}}\right) \left(\frac{v_0}{230\,\mathrm{km\,s}^{-1}}\right) \mathrm{kg}^{-1}\,\mathrm{day}^{-1} \,. \tag{2.5}$$

This form does not account for the $\pm 6\%$ yearly variation in the average WIMP velocity due to the motion of the earth around the sun; detector specific efficiency, resolution, or threshold effects; or nuclear physics effects such as spin-dependence/independence and the form factor of the nucleus. A detailed discussion of these effects is available in Ref. [55]. A plot of the expected WIMP induced nuclear recoil energy spectrum including effects from the spin-independent rate enhancement ($\propto A^2$) and the Helm nuclear form factor [56] is shown in Fig. 2.1.

We would expect a dark matter halo composed of 100 GeV/c^2 WIMPS with a spin-independent cross-section of 9×10^{-46} cm^2 (currently the most sensitive limit set by a direct detection experiment) to produce six nuclear recoils in a liquid xenon target mass of 100 kg over a period of 100 days. This is the underlying recoil rate in the target before accounting for detection efficiencies. There are four detector characteristics that are critical for a competitive modern dark matter experiment given the low recoil energy and very infrequent interaction rate. The detector must have a large target mass and a low energy threshold, while simultaneously being radioactively quiet. Additionally, the use of signal-based discrimination capabilities to differentiate between electron recoils (background) and nuclear recoils (potential WIMP signals) is advantageous.

Liquid xenon has many favorable properties that make it a strong candidate target material for WIMP direct detection experiments, and in particular for dual-phase liquid xenon time projection

[2]For zero momentum transfer, the nuclear form factor is normalized ($F(q = 0) = 1$).

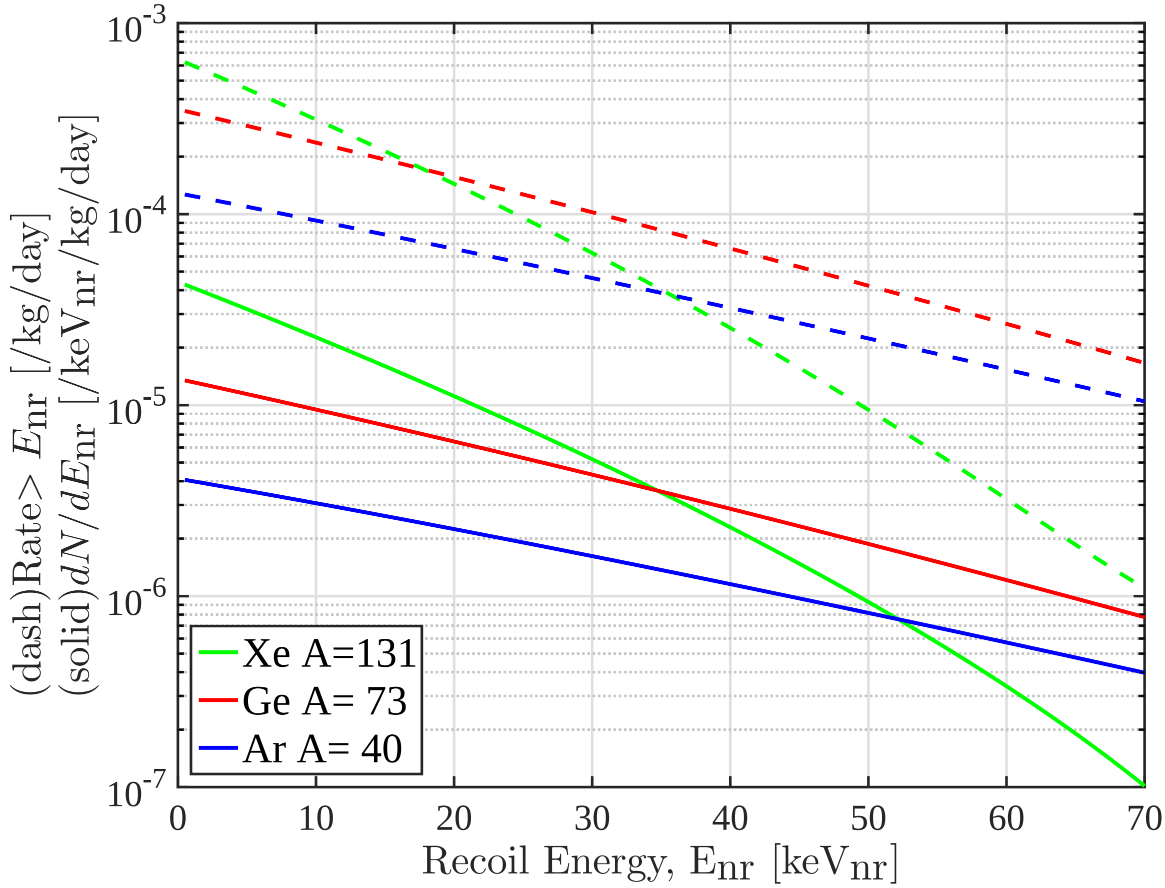

Figure 2.1: The integrated (dashed) and differential (solid) nuclear recoil spectra in argon (blue), germanium (red), and xenon (green) for a 100 GeV/c^2 WIMP with a WIMP-nucleon spin-independent cross-section of 9×10^{-46} cm^2.

chambers (TPCs). The comparatively high liquid xenon density of 2.9 g/cm^3 provides a large target mass within a scalable monolithic detector volume. The scalar WIMP-nucleon interaction rate is $\propto A^2$, which gives an additional enhancement over alternative (argon, germanium) lower atomic mass target nuclei. Additionally, liquid xenon contains $\sim$50 % odd nuclei, which provide a significant target mass with spin-dependent coupling. These and other desirable properties of liquid xenon are discussed in more detail in Sec. 2.3. The most stringent spin-independent limits over the majority of the WIMP mass range have been achieved by dual-phase liquid xenon TPCs. Currently, the most sensitive of these xenon detectors is the Large Underground Xenon (LUX) experiment [5]. In addition, the LUX detector has also set the most stringent spin-dependent WIMP-neutron direct detection limits [57].

2.2 A new nuclear recoil calibration in the LUX detector

We used the technique described in Ch. 1 to perform an *in situ* nuclear recoil calibration in the LUX detector. This new nuclear recoil calibration refines the LUX nuclear recoil signal detection efficiency estimates and also proves the kinematic accessibility of more WIMP-mass parameter space, given the local galactic escape and Earth-halo velocities. Due to the absence of any nuclear recoil calibrations in the literature for kinematically defined nuclear recoil energies <3 $\mathrm{keV_{nr}}$, the first LUX spin-independent WIMP search sensitivity result was conservatively limited by assuming no signal yield <3 $\mathrm{keV_{nr}}$, where detector efficiency was nevertheless expected to be significant (and, in retrospect, was) [24]. This new LUX calibration result provides an improvement in the instrument's sensitivity at low WIMP masses using the existing 2013 WIMP search dataset by demonstrating signal yield in both channels for nuclear recoil energies as low as 1.1 $\mathrm{keV_{nr}}$ [5].

We describe the LUX detector in the following sections of this chapter. The experimental setup for the nuclear recoil calibration in the LUX detector using the D-D source is described in Ch. 4. I led the development of the LUX D-D nuclear recoil program. This includes the design and deployment of the calibration hardware, as well as the data taking, operations, and analysis work for the first D-D campaign during LUX Run03 in September-November of 2013. The D-D calibration results presented in this thesis are from this Run03 calibration unless otherwise specified. Due to the success of the D-D source calibration program at the end of Run03, it became the standard nuclear recoil calibration technique for the ongoing 300 live day LUX Run04 WIMP search.

2.3 The LUX detector

LUX is a dual-phase liquid/gas xenon TPC operating in the Davis Cavern at the 4850 ft level of the Sanford Underground Research Facility in Lead, South Dakota. The LUX detector is sensitive to the scintillation and ionization produced by particle interactions in its 370 kg (250 kg active) liquid xenon volume. A diagram of the components of the LUX TPC within the outer vacuum cryostat is shown in Fig. 2.2.

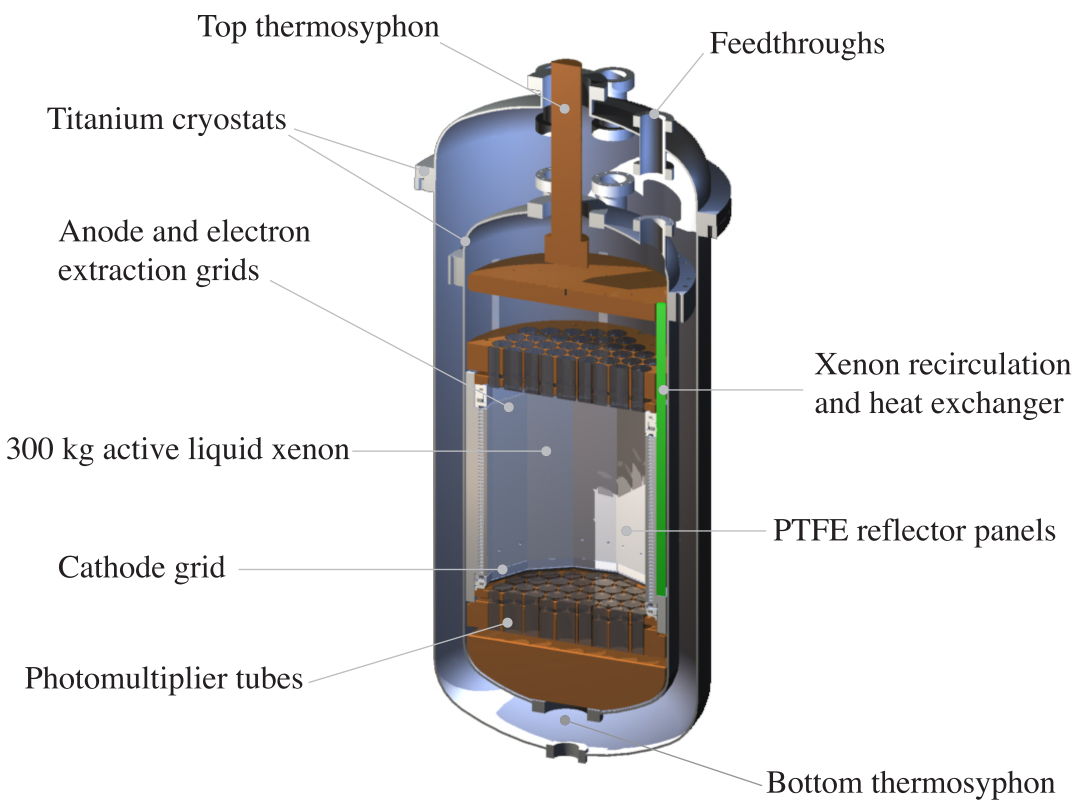

Figure 2.2: The principal components of the LUX detector within the outer vacuum cryostat. This figure is reproduced from Ref. [58].

A general overview of liquid xenon TPC operation is presented in Sec. 2.3.1. Additional detail on major LUX detector hardware subsystem components is provided in Sec. 2.3.2. We describe the strategies used to escape radioactive backgrounds in Sec. 2.3.3. The data processing software infrastructure is described in Sec. 2.3.5. A general overview of the techniques used to calibrate the LUX detector response to both electron recoils and nuclear recoils is provided in Sec. 2.3.6.

I began working on LUX as a graduate student at Brown in September of 2009. Before leading the development of the LUX D-D calibration program starting in late 2012, I contributed to the development and assembly of critical LUX infrastructure spending a total of 309 days on site in Lead, SD for commissioning and operations work. I had a lead role developing the data acquisition control interface, the data quality monitoring database, and software tools used for LUX data analysis and visualization. Carlos Faham and I led the design of the LUX data processing framework; I was the primary developer Python-based framework described in Sec. 2.3.5 and led the deployment of the production data processing pipeline using this framework. I had a lead role defining the LUX data mirror strategy and associated software, and was the first administrator of the LUX primary data repository. In the interest of time, this thesis focuses upon my more recent D-D calibration work.

2.3.1 LUX TPC operation and observed signals

Energy depositions in the liquid xenon target produce both scintillation photons and ionization electrons. The prompt scintillation photon signal (S1) is directly detected by the PMTs. The ionization electrons drift to the liquid surface under an average applied electric field of 180 V/cm, where they are extracted into the gas region and produce a signal (S2) in the PMTs via photon emission due to electroluminescence. The pulse areas associated with the S1 and S2 signals are position-corrected as described in Ref. [5, 59] and are referred to using the variables $S1$ and $S2$ (note the italics when referring to the measured quantity). In the several instances where uncorrected S1 and S2 signal sizes are used, the variables will be labeled as "raw" $S1$ and $S2$. The raw and corrected variables $S1$ and $S2$ are given in units of detected photons (phd). These units differ from the traditional unit of photoelectrons (phe) by accounting for the probability of double photoelectron emission from a single absorbed vacuum ultra-violet (VUV) photon [60], which was measured for each LUX PMT. This VUV correction is used when determining the observed signal size via incorporation into the per-channel PMT gain values (the average signal size at the output of each PMT produced by a single detected photon at the input) used for the analysis.

The nuclear recoil band analysis described in Sec. 4.5 uses an alternative technique to characterize the S1 signal size. When using this technique, the S1 signal size, represented by the variable $S1_{\mathrm{spike}}$, is measured by counting the number of single photon "spikes" in the per-channel waveforms. This is the same S1 signal size variable used in the recent LUX WIMP search results [5, 57].

The single quanta gain values for scintillation photons (g_1) and ionization electrons (g_2) escaping the interaction site were calibrated directly in LUX and have units of phd per scintillation photon and phd per ionization electron, respectively [5, 59]. This D-D analysis uses a g_1 of 0.115 ± 0.004 and a g_2 of 11.5 ± 0.9. These gain values were optimized for the D-D calibration time period as described in Sec. 2.3.6. These precisely measured g_1 and g_2 values allow us to directly report the nuclear recoil signal yields in liquid xenon in terms of the absolute number of quanta produced. This is particularly notable in the case of the light yield result in Ch. 7, which is the first direct measurement of nuclear recoil scintillation reported in absolute units. Previous measurements have reported the nuclear recoil light yield relative to a standard candle electron recoil source due to the difficulty of measuring the detector specific g_1 value.

A diagram of an example single-scatter event in the LUX detector is shown in Fig. 2.3. Here, a particle enters the liquid xenon volume and interacts at a single localized site before escaping the active region of the detector. It is possible that the particle deposited all of its energy at the single interaction site—commonly the case for electron recoil interactions.

2.3.1.1 Signal production in liquid xenon

Particle interactions depositing energy in liquid xenon generate both scintillation photons and ionization electrons at the ionization site. We use the notation Xe^* and Xe^+ to indicate excited ionized xenon atoms, respectively. The creation of scintillation photons and ionization electrons as signal carriers occurs according to the process herein described, following the presentation in Refs. [61, 62]. Scintillation photons from the initial population of excited xenon atoms are produced via

$$\begin{aligned}
&\mathrm{Xe}^* + \mathrm{Xe} \rightarrow \mathrm{Xe}_2^* \,, \\
&\mathrm{Xe}_2^* \rightarrow 2\mathrm{Xe}^* + h\nu \,,
\end{aligned} \tag{2.6}$$

where two excited xenon atoms (excitons) combine to form a excited dimer Xe_2^* that de-excites via

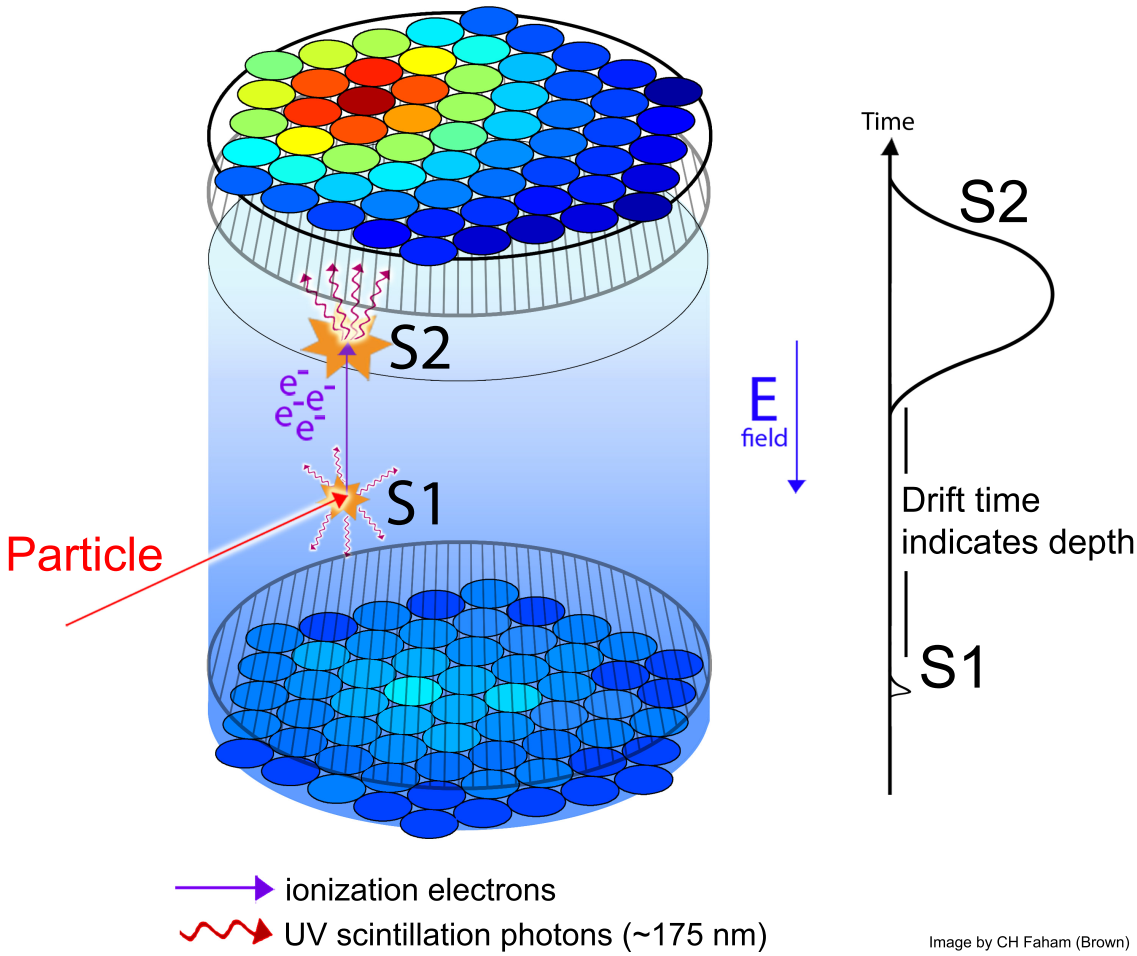

Figure 2.3: A diagram of the active region of the LUX detector showing a single-scatter event. The particle interaction in the liquid xenon bulk is shown on the left. The corresponding digitized event record summed across all 122 channels is shown on the right. The maximum observed drift time from the cathode to the liquid surface is 324 μs. The z coordinate of the particle interaction is determined to a precision of $\sim$1 mm using the measured drift time between the S1 and S2. The (x, y) coordinates are reconstructed using the S2 hit pattern in the top PMT array with a precision of $\sim$1 cm. Figure produced by C. H. Faham.

the emission of a 7 eV photon (178 nm wavelength). Scintillation photons are emitted by the excited dimer with two characteristic time constants, which depend upon the spin state of the dimer. For xenon, the singlet and triplet dimer states have characteristic relaxation times of 3.1 ns and 24 ns, respectively [35]. As a result of scintillation production via dimer de-excitation, xenon is transparent to its own scintillation photons.

A fraction of the available xenon ions recombine with free electrons at the interaction site. Recombination of xenon ions with ionization electrons at the interaction site provides an additional source of scintillation photons:

$$\begin{aligned} &\mathrm{Xe}^+ + \mathrm{Xe} \rightarrow \mathrm{Xe}_2^+ \,, \\ &\mathrm{Xe}_2^+ + e^- \rightarrow \mathrm{Xe}^{**} + \mathrm{Xe} \,, \\ &\mathrm{Xe}^{**} \rightarrow \mathrm{Xe}^* + \mathrm{heat} \,. \end{aligned} \tag{2.7}$$

This recombination process is suppressed when an electric field is applied across the liquid xenon target. The exponential time constant associated with the recombination process is 45 ns [39]. In the absence of an electric field, recombination dominates the observed S1 pulse shape. Of the electrons liberated during the initial ionization of xenon atoms, only those that escape the recombination process in Eq. 2.7 contribute to the observed ionization signal. There is an anti-correlation between the observed distribution of scintillation and ionization signals due to the fluctuations in recombination.

It is possible for two excitons in the particle track to interact and partially de-excite via the emission of an ionization electron [63]:

$$\mathrm{Xe}^* + \mathrm{Xe}^* \rightarrow \mathrm{Xe} + \mathrm{Xe}^+ + e^- \,. \tag{2.8}$$

The resulting electron can either escape the interaction site under the influence of the applied drift electric field and contribute to the observed ionization signal, or recombine via Eq. 2.7 and produce a single scintillation photon. In either case, this represents a reduction in the observed scintillation signal as two excitons produce one or zero scintillation photons. This process is called biexcitonic quenching.

2.3.1.2 The S1 signal

The photons produced by the processes described in Sec. 2.3.1.1 are detected by the PMTs in the top and bottom arrays. These photons have a wavelength of 178 nm. Due to total internal reflection at the liquid surface, the majority of the S1 signal is detected in the bottom PMT array. An example waveform corresponding to a S1 signal is shown in the event record in Fig. 2.4 after summing across all 122 channels. This particular event was produced by a neutron scattering twice in the active xenon volume. Scintillation photons from both interaction sites overlap in the event record producing a combined S1 signal. A WIMP signal would only have a single-scatter (1$\times$ S1, 1$\times$ S2) contributing to the observed waveforms.

2.3.1.3 The S2 signal

Electrons escaping the interaction site drift to the liquid surface under the average applied field of 180 V/cm. The maximum observed drift time is 324 μs and the averaged measured electron drift speed is 1.51$\pm$0.01 mm/μs [24]. Upon reaching the liquid surface, the electrons are extracted with an efficiency of 0.49$\pm$0.03 and 0.48$\pm$0.04 during the Run03 WIMP search and D-D calibration periods, respectively. The extracted electrons produce secondary scintillation photons via electroluminescence as they traverse the gas gap. The number of photons produced per extracted electron is given by

$$\frac{n_{\mathrm{ph,SE}}}{d} = \left(0.140\frac{E_{\mathrm{gas}}}{N \times 10^{-17}} - 0.474\right) N \times 10^{-17}\,, \tag{2.9}$$

where $n_{\mathrm{ph,SE}}$ is the mean number of photons produced by a single extracted electron, d is the length of the gas gap in units of cm, E_{gas} is the electric field in the xenon gas, and N is the number density of xenon atoms in the gas in units of atoms/cm^3 [35, 64]. The single electron size was measured to be 24.66 ± 0.02 phd in the top array and 10.47 ± 0.01 phd in the bottom array during the Run03 WIMP search period. The single electron size was measured to be 23.77 ± 0.01 phd during the D-D calibration period following the Run03 WIMP search.

2.3.1.4 An example D-D neutron double-scatter event in LUX

The event record from a double-scatter neutron event in the D-D dataset used for the low-energy Q_y analysis is shown in Fig. 2.4.[3] The scattering angle at the first vertex was measured to be $13° \pm 4°$ based upon the estimated (x, y, z) position reconstruction uncertainties for each interaction. This corresponds to a measured nuclear recoil energy of 1.0 ± 0.5 keV$_{\text{nr}}$ at the first scattering vertex. The reconstructed (x, y, z) position of each scattering vertex in this event is shown in Fig. 2.5. This event was chosen based upon the high-precision reconstruction of the low-energy first scattering vertex. The long path length between first and second scatter in the figure combined with the large signal size of the second scatter provides this high-precision recoil energy measurement for this particular ultra-low energy event. The uncertainty in the reconstructed x and y coordinates for the first scattering vertex was estimated to be 0.9 cm. The uncertainty in the reconstructed x and y coordinates for the larger second scattering was estimated to be 0.4 cm.

The first scatter in this event has $S2 = 181$ phd. This corresponds to 15.7 electrons escaping the interaction site, while the mean expectation is ∼9 electrons based upon the ionization yield measurement results in Ch. 5. It is expected that the observed S2 signal in this event would be larger than the mean expectation due to the selection criteria requiring used to select a precisely measured recoil energy. An above average $S2$ corresponds to reduced position reconstruction uncertainty at the first vertex and, correspondingly, a more precisely measured recoil energy. These effects are taken into account when calculating the mean measured recoil energy correction factor (see Ch. 6) used for the low-energy Q_y analysis.

[3] The code used to generate this event is located in the Brown Particle Astrophysics Group's GitHub organization [65] with the relative path "jverbus_lux_scratch/20141021_plot_DD_events/".

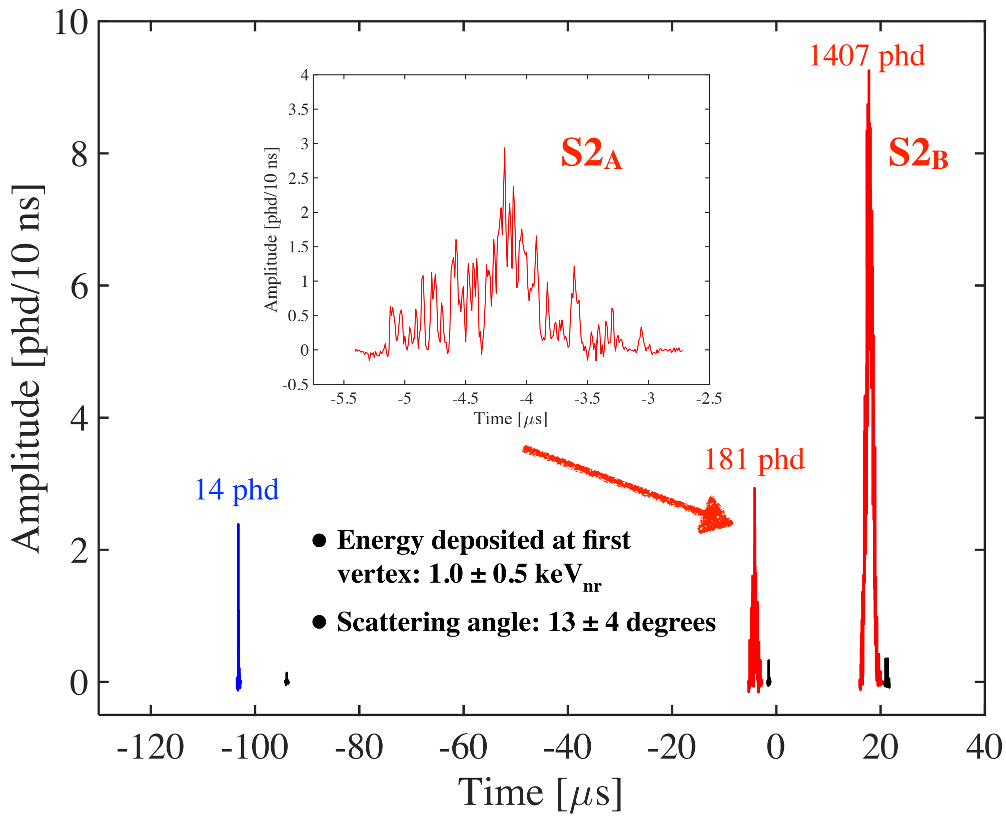

Figure 2.4: The event record summed across all channels for the double-scatter neutron event lux10_20131118T0300_e000235868 acquired during the Run03 D-D calibration. The combined S1 signal from both scatters is shown in blue. The individual S2 signals from both scatters are resolved and shown in red. Stray single photoelectrons in individual PMT channels are shown in black.

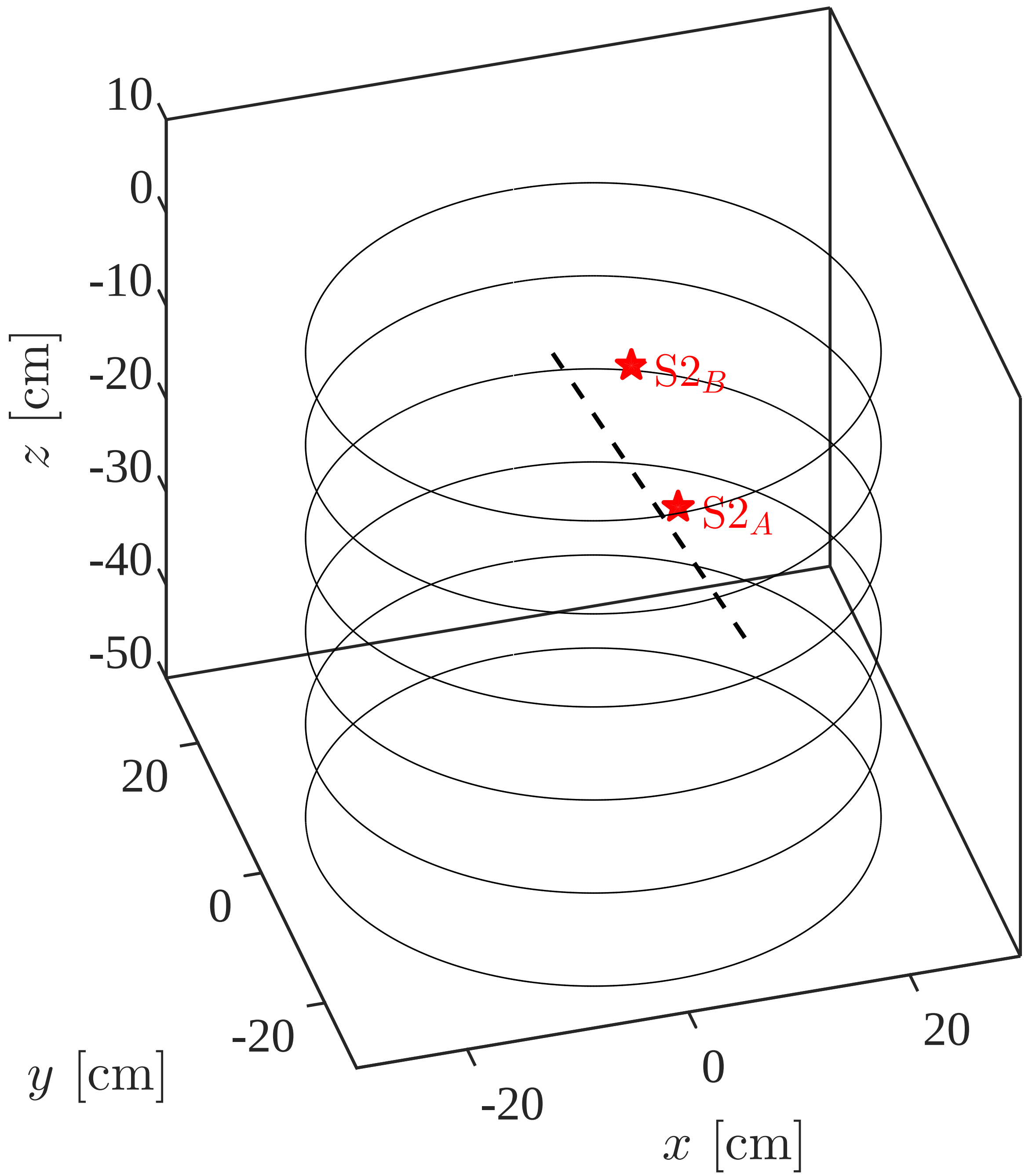

Figure 2.5: The reconstructed (x, y, z) position of both scattering vertices in the double-scatter neutron event lux10_20131118T0300_e000235868 acquired during the Run03 D-D calibration. The first scattering vertex is labeled S2$_A$ and the second is labeled S2$_B$. The boundaries of the TPC active region are represented by the black circles each separated by 10 cm along z for scale. The neutron beam enters from the south-east in the plot along the black dashed line.

2.3.1.5 Position reconstruction of particle interactions

The electroluminescence region is roughly 4.8 cm below the top PMT array when the detector is cold, ensuring a localized hit pattern in the top array from S2 signals. The localized hit pattern from the S2 signal in the top array provides information regarding the (x, y) position of the event. In LUX the (x, y) position of each particle interaction vertex in the active region of the detector is reconstructed using the Mercury algorithm [38, 59]. The position reconstruction uncertainty is typically $\mathcal{O}(1\text{ cm})$ in each of the reconstructed x and y coordinates. The z coordinate is reconstructed using the measured drift time between the S1 and S2 signals, as depicted in Fig. 2.3. The uncertainty associated with the z coordinate reconstruction is 1 mm [37]. A detailed Monte Carlo simulation study of the effect of these position reconstruction uncertainties on the LUX D-D nuclear recoil calibration is reported in Ch. 6. This simulation-based study is of particular importance for the Q_y measurement in Ch. 5, which uses the reconstructed (x, y, z) positions of double-scatter neutron events to calculate the neutron scattering angle within the TPC.

2.3.1.6 Electronic and nuclear recoil energy scales

The average energy required to produce either a scintillation photon or ionization electron in xenon is given by $W = 13.7 \pm 0.2$ eV [66]. For electron recoils, the sum of the observed number of scintillation photons and ionization electrons is linearly related to the energy deposited at the interaction site as

$$E_{\mathrm{ee}} = W \left(\frac{S1}{g_1} + \frac{S2}{g_2} \right) , \tag{2.10}$$

where $n_p = S1/g_1$ and $n_e = S2/g_2$ are the observed number of scintillation photons and ionization electrons, respectively [67]. The linear relationship between the deposited energy and observed $S1$ and $S2$ in Eq. 2.10 can be used to provide an estimate of the deposited energy for electron recoil events. This "combined energy scale" simultaneously uses the information provided by both the S1 and S2 signals in an electron recoil event, which accommodates the strong anti-correlation of

S1 and S2 due to the recombination fluctuations described in Sec. 2.3.1.1. Use of this energy scale minimizes the resolution of the reconstructed energy distribution for line sources and provides the best estimate of the reconstructed energy for a given electron recoil event.

For nuclear recoils, a significant fraction (>80% in the WIMP search energy regime) of the deposited energy is lost to heat (atomic motion), so Eq. 2.10 must be modified. The fraction of the deposited energy given to measurable electronic channels (ions and excitons) is typically modeled by the energy dependent Lindhard factor, $\mathcal{L}(E_{\mathrm{nr}})$ [68, 69].

$$E_{\mathrm{nr}} = \frac{W}{\mathcal{L}(E_{\mathrm{nr}})} \left(\frac{S1}{g_1} + \frac{S2}{g_2} \right) . \tag{2.11}$$

The reduced size of the observed signals due to this energy loss to heat is referred to as nuclear recoil signal quenching. We report upon a new measurement of the liquid xenon ionization yield (electrons/keV$_{\mathrm{nr}}$) in Ch. 5 and Ch. 8. We report upon new measurements of the liquid xenon scintillation yield (photons/keV$_{\mathrm{nr}}$) in Ch. 7 and Ch. 8. A detailed definition of the variables used for nuclear recoil energy reconstruction is described in the next sections.

2.3.1.6.1 Discussion of historical notation for nuclear recoil signal yields In general for liquid xenon TPCs, the $S1$ is traditionally related to the reconstructed nuclear recoil energy deposited at the interaction site, E_{nr} via

$$S1 = E_{\mathrm{nr}}\ \mathcal{L}_{\mathrm{eff}}(E_{\mathrm{nr}})\ L_{y,\,^{57}\mathrm{Co}}(\mathcal{E})\ \frac{S_{\mathrm{nr}}(\mathcal{E})}{S_{\mathrm{ee}}(\mathcal{E})} , \tag{2.12}$$

where $\mathcal{L}_{\mathrm{eff}}(E_{\mathrm{nr}})$ is the scintillation yield for nuclear recoils relative to the scintillation signal produced by the 122 keV ^{57}Co gamma ray at 0 V/cm. When operating at non-zero drift electric field $\mathcal{E}$, the scintillation signal from both nuclear and electron recoil interactions is quenched to a fraction of the 0 V/cm value. The quenching fractions for nuclear and electron recoil signals are represented by $S_{\mathrm{nr}(\mathcal{E})}$ and $S_{\mathrm{ee}(\mathcal{E})}$, respectively. The measured light yield for electron recoils from the ^{57}Co gamma at the TPC operating drift field is represented by $L_{y,\,^{57}\mathrm{Co}}(\mathcal{E})$. The 122 keV ^{57}Co gamma ray has an attenuation length of 2 mm in liquid xenon, which is not well suited for calibration in large TPCs such as LUX (0.5 m linear dimension).

The $S2$ is traditionally related to the recoil energy deposited at the interaction site by

$$S2 = E_{\rm nr}\; Q_y(E_{\rm nr}, \mathcal{E})\; g_2\,, \tag{2.13}$$

where $Q_y(E_{\rm nr}, \mathcal{E})$ is the ionization yield for nuclear recoils at the applied electric field given in units of electrons/keV$_{\rm nr}$.

Numerous measurements of both $\mathcal{L}_{\rm eff}$ and Q_y at low energies exist in the literature, primarily motivated by the need to understand the liquid xenon signal response for WIMP dark matter searches. Various experimental strategies are used to measure these quantities:

i. Nuclear recoil calibrations performed *in situ* in the dark matter detector itself via simulation-based best-fit models optimized to match the observed signal spectrum from neutron sources with a continuous energy spectrum [15, 16, 70].

ii. Mono-energetic neutron *ex situ* calibrations in a small liquid xenon test cell using the neutron scattering angle to kinematically define the recoil energy [17–19].

iii. Recoil spectrum endpoint-based calibrations [28].

To unambiguously identify the source of energy depositions in the liquid xenon, we use the units keV$_{\rm ee}$ and keV$_{\rm nr}$ for electron and nuclear recoils, respectively. The advantages and disadvantages of the various techniques are discussed in Ch. 1. Prior to the results in Ch. 7 and Ch. 5, the lowest-energy light and charge yield results determined using a kinematically-defined nuclear recoil energy scale were reported at 3 keV$_{\rm nr}$ [19] and 4 keV$_{\rm nr}$ [18], respectively.

2.3.1.6.2 Discussion of modern notation for nuclear recoil signal yields The LUX measurement of the nuclear recoil signal yields reported in this thesis provides the absolute energy scale of a kinematics-based calibration, while avoiding potential systematic uncertainties intrinsic in the translation of *ex situ* measurements by determining the yields *in situ* in the dark matter instrument itself. Additionally, the accurate measurement of g_1 to high precision in LUX [59] allows the light yield result to be reported directly in units of photons/keV$_{\rm nr}$. This form is symmetric with Q_y as defined in Eq. 2.13:

$$S1 = E_{\rm nr}\ L_y(E_{\rm nr}, \mathcal{E})\ g_1\ . \tag{2.14}$$

The variable $L_y(E_{\rm nr}, \mathcal{E})$ is the nuclear recoil light yield at field $\mathcal{E}$ in units of photons/keV$_{\rm nr}$. Reporting the light yield in absolute terms at the operating electric field as described in Eq. 2.14 also has the advantage of avoiding any assumptions about the field quenching factors ($S_{\rm nr}$ and $S_{\rm ee}$).

2.3.1.7 Distinguishing signal from background

There are several techniques using the observed signals that are used to suppress unwanted radioactive backgrounds in liquid xenon TPCs.

2.3.1.7.1 Self-shielding The high density and large size of modern liquid xenon TPCs provides a nearly background free fiducial analysis volume. The ability to resolve the (x, y, z) position of particle interaction vertices within the large liquid xenon active region provides a reduction in radioactive backgrounds. A related technique enabled by the large target volume and position reconstruction is the rejection of multiple scatter events. Given the exceptionally infrequent interaction rate (perhaps a few WIMP events per year), it is safe to say that a WIMP will never scatter twice in a terrestrial detector. For comparison, the total mean free path of a 2.45 MeV fast neutron is 12.6 cm. The mean free path of a 203 keV gamma ray is 0.9 cm and the mean free path of a 1 MeV gamma ray is 6.0 cm [71]. The rejection of multiple site events is a powerful tool to significantly reduce backgrounds due to residual radioactivity in detector construction materials. The LUX fiducial region has a background rate of $\sim 10^3$ counts keV$_{\rm ee}$ kg^{-1} day^{-1} for energies of $\mathcal{O}(1\ \text{keV}_{\rm ee})$ [30].

2.3.1.7.2 Ratio of ionization to scintillation The ratio of the ionization to scintillation signal provides a powerful discriminant between nuclear and electron recoils. The higher stopping power for recoiling xenon nuclei produces a denser ionization track structure than the lower stopping power associated with electron recoils [66]. The high density of electron-ion pairs in nuclear recoil tracks increases the fraction of ions that recombine with ionization electrons. The increased recombination along nuclear recoil tracks increases the size of the S1 signal and decreases the size of the S2 signal (relative to electron recoils) via the mechanism outlined in Sec. 2.3.1.1. Perhaps more significantly, the initial ion-exciton ratio is different for electron and nuclear recoils; this may play a larger role than the stopping power and ionization density in determining the observed discrimination power [66]. The ratio $\log_{10} S2/S1$ for electron recoil and nuclear recoil LUX data is shown in Fig. 2.6, where the clear separation between electron recoils and nuclear recoils is visible. The discrimination power, as defined by the rejection of electron recoil events below the nuclear recoil band centroid, is $99.8\% \pm 0.02\%(\text{stat}) \pm 0.1\%(\text{sys})$ for $1 < S1_{\text{spike}} < 50$ phd [72]. The details of the nuclear recoil band measurement using LUX D-D data are presented in Sec. 4.5.

2.3.2 LUX detector components

2.3.2.1 Photomultiplier tubes in the TPC

The LUX detector uses 122 Hamamatsu R8778 PMTs to detect the light produced by the scintillation and ionization signals. These PMTs have a 2 inch (5.08 cm) photocathode. The top PMT array in the xenon gas above the liquid surface and houses 61 PMTs in a triangular packing configuration. The bottom PMT array of 61 PMTs is in the liquid xenon below the bottom grid and uses a similar packing structure. The PMT high-voltage and signal cables are routed to the LUX breakout cart on the upper Davis level through 6 m-long flexible conduits.

The PMTs are individually biased to achieve an average gain of 5.08×10^6. The average bias voltage required to achieve this gain value is -1216 V. The quantum efficiency—the probability of

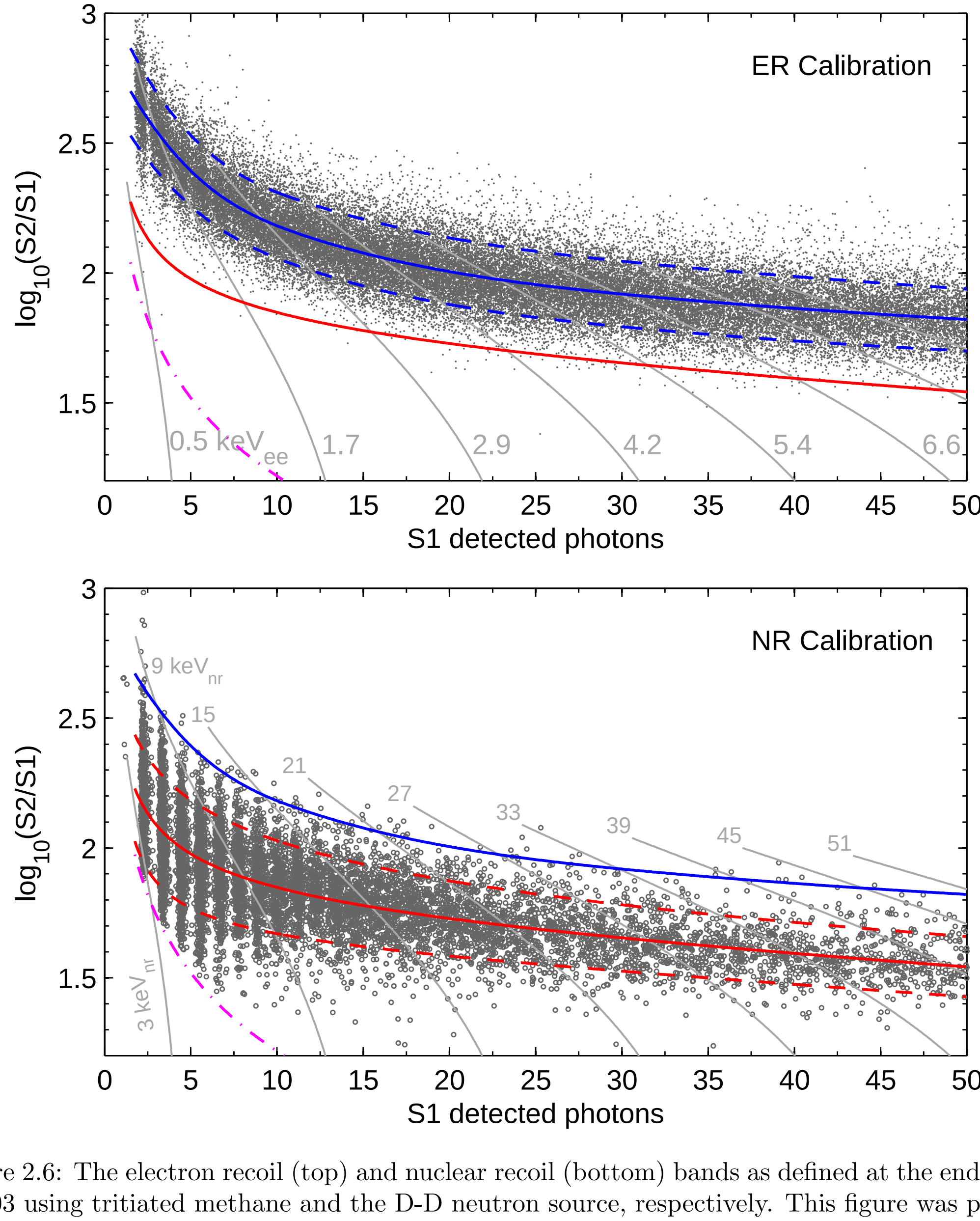

Figure 2.6: The electron recoil (top) and nuclear recoil (bottom) bands as defined at the end of LUX Run03 using tritiated methane and the D-D neutron source, respectively. This figure was produced by Claudio Silva (LUX collaboration).

the photocathode emitting an electron after absorbing an incident photon—of the LUX PMTs is typically 33% for 178 nm photons produced by xenon scintillation. The probability of the collection of an electron emitted by the photocathode on the first dynode is 90%. A detailed review of the LUX PMT program is available in Ref. [37].

The TPC walls are lined with polytetrafluoroethylene (PTFE), commercially known as Teflon, to reflect xenon scintillation light and improve light collection. The reflectivity of PTFE in liquid xenon to 178 nm scintillation light was measured to be consistent with 100% in LUX [73].

2.3.2.2 Electrode grids

The LUX TPC is instrumented with five grid electrodes spanning the active region volume. A diagram of the grids is shown in Fig. 2.7 where there are three grids labeled "top grids" and two grids labeled "bottom grids". We refer to the five grids as (starting from the top of the TPC): top grid, anode grid, gate grid, cathode grid, and bottom grid. During the Run03 D-D calibration campaign, the grids were nominally biased to -1 kV, +3.5kV, -1.5kV, -10 kV, and -2 kV, respectively. When cold the distance separating these grids is 3.8 cm, 1 cm, 47.1 cm, 4 cm, respectively. The distance from the top (bottom) grid to the top (bottom) PMT array is 1 cm. A detailed discussion of the LUX grid configuration is available in Ref. [37].

The electric field used to drift ionization electrons from particle interactions is applied between the cathode and the gate grid. A total of 47 field shaping rings are vertically arranged inside the PTFE walls of the active region between the cathode and the gate grid to provide a uniform drift field in the liquid xenon target. The field shaping rings are each spaced 1 cm apart. The electric drift field ranges from 150 V/cm at the bottom of the active region to 190 V/cm at the liquid xenon surface. The average electric drift field is 180 V/cm; this is also the measured field at the height of the D-D calibration conduit discussed in Ch. 4. A larger electron extraction field is applied across the gap between the gate and anode grids. The dielectric constant of liquid xenon is 1.95 [62]. The extraction electric field in the liquid is 3.1 kV/cm, while it is 6 kV/cm in the gas [24]. The top and

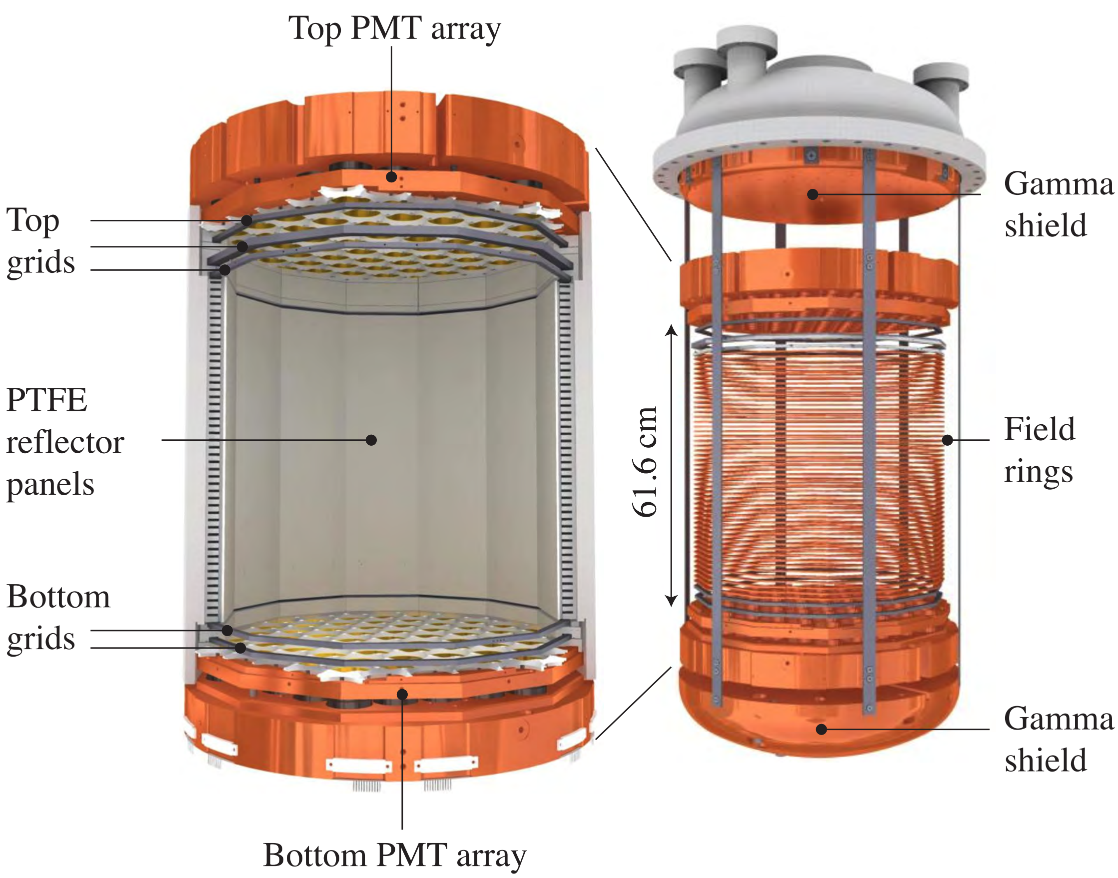

Figure 2.7: A diagram of the copper components and electrode grids inside the LUX TPC. This figure is reproduced from Ref. [58].

bottom grids are typically biased to 1 kV and 2 kV, respectively, to protect the PMTs arrays from the high electric fields applied by the cathode and the anode. The liquid level between the gate and anode grid is measured using capacitive sensors.

2.3.2.3 Liquid xenon circulation and purification

Trace impurities in the liquid xenon degrade the collection of both scintillation photons and ionization electrons. The liquid xenon used in the LUX detector is constantly circulated through a heated zirconium getter at a rate of 27 slpm to remove non-noble impurities contributing to the loss of signal carriers in the liquid xenon. This circulation rate represents a turnover of the full 400 kg xenon mass in roughly 40 hours. Multiple heat exchangers were used in the xenon circulation path to achieve a 90% reduction in the heat load compared to operation at 27 slpm with no heat exchangers [74].

The scintillation light produced by particle interactions can be absorbed by trace impurities in the liquid xenon. This process reduces the observed $S1$ for a given energy deposition. The most significant impurity contributing to the characteristic absorption length for scintillation light is water vapor. Water vapor can outgas out of detector construction materials, and the absorption spectra significantly overlaps with the 178 nm VUV photons produced by xenon scintillation [62]. The photon attenuation length was measured to be 11^{+2}_{-1} m during the LUX surface engineering runs, where the electron lifetime was measured to be 204 ± 6 μs [73]. This electron lifetime value is lower than the $\mathcal{O}(1\text{ ms})$ typically achieved during underground operation due to a unintended opening in the circulation path during surface running, which reduced the effectiveness of liquid xenon purification.

Electronegative impurities may capture free electrons in the liquid before they are extracted into the gas phase to produce the S2 signal. The characteristic time constant for electron capture by electronegative impurities is referred to as the electron lifetime, which is inversely proportional to the concentration of the impurity in question. As a result, the raw $S2$ for a given particle interaction is a function of the z position of the interaction below the liquid xenon surface. The exponential electron lifetime time constant can be measured by observing the decrease in the observed raw $S2$ as a function of the drift time between the observed S1 and S2 signals. The raw $S2$ dependence on the z position of the interaction due to this effect is corrected using the internal ^{83m}Kr source described in Sec. 2.3.6. The average electron lifetime over the course of the D-D calibration data-taking campaign used for the reported nuclear recoil results was measured to be 650 μs. All Run03 D-D calibration data was acquired when the measured electron lifetime was >500 μs.

Photoionization of trace impurities in the liquid xenon can produce free electrons in the drift region. The potential backgrounds for the low-energy signal yield analyses due to spurious single electron signals from this source (and others) are quantified in Ch. 5 and Ch. 7.

2.3.2.4 Cryogenics

The cooling power required to maintain the 180 K liquid xenon temperature in the inner cryostat was provided using a closed-circuit liquid nitrogen thermosyphon system. There are a total of five closed loops of stainless steel tubing running from the LUX cryostat to a liquid nitrogen bath mounted on the upper Davis level.[4] The individual closed thermosyphon loops are pressurized with nitrogen gas to start the cooling process. The nitrogen gas condenses in the liquid nitrogen dewar at the top of the loop, runs down the tubing under the influence of gravity, and evaporates on a cold head attached inside the LUX cryostat. The thermosyphons can be individually turned on (off) by pressurizing (evacuating) the appropriate closed loop.

The closed stainless steel thermosyphon loops are enclosed in several lengths of rigid stainless steel conduit connected by flexible bellows. The distance from the top copper shield in the TPC assembly to the liquid nitrogen bath for the thermosyphons is roughly 6 m. The exterior of the full thermosyphon assembly can be seen in Fig. 2.8. The bellows allow kinks in the rigid conduit around the thermosyphon lines ensuring there are no direct air gaps through the water shield to the

[4] The Davis Cavern is split into two floors as seen in Fig. 2.8; we refer to these as the upper and lower Davis.

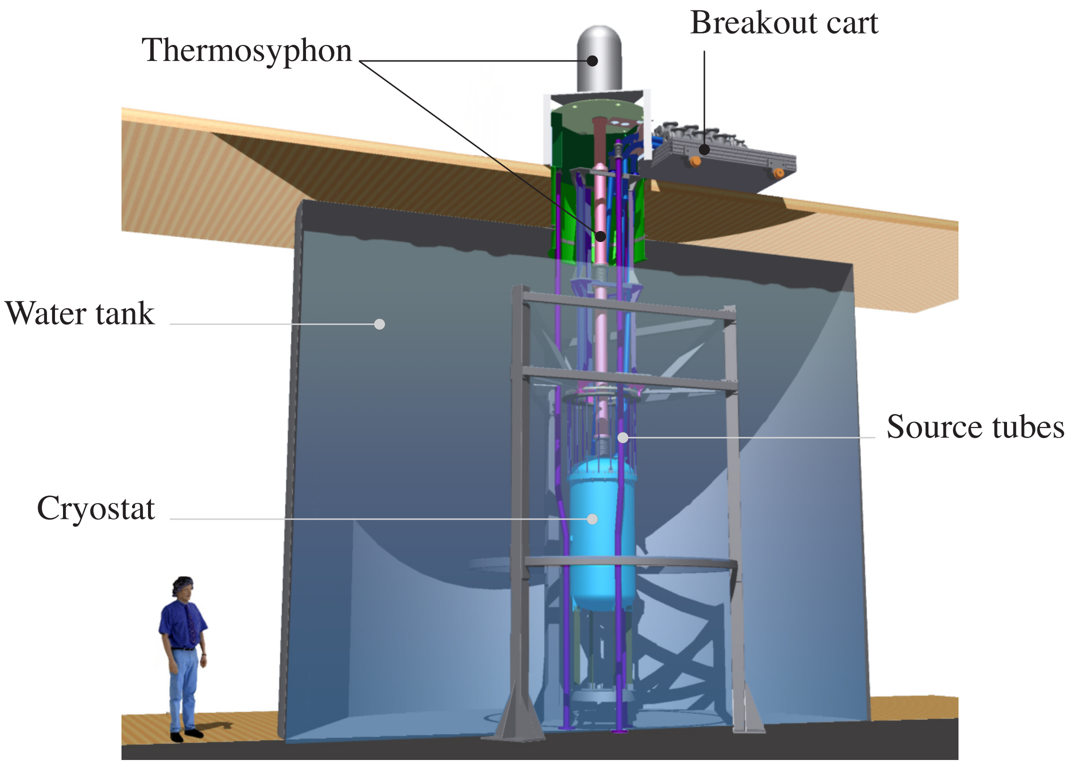

Figure 2.8: A solid model of the LUX installation in the Davis Cavern at SURF. A cutout off the water tank shows the cryostat, detector stand, source tubes, rigid conduit housing the thermosyphon lines, and flexible electrical conduits. The breakout cart and thermosyphon liquid nitrogen dewar are visible on the upper Davis level above the water tank. This figure is reproduced from Ref. [58].

cryostat. Fig. 2.9 shows the installation of the closed nitrogen gas loops during the assembly of one segment of the thermosyphon conduit structure.

Figure 2.9: Photograph of the assembly of a thermosyphon tower segment in the LUX surface lab at SURF prior to an engineering run. The author is pictured on the left guiding the thermosyphon liquid nitrogen supply lines into position.

The thermosyphon system has four cold heads attached to the copper TPC structure within the inner cryostat. Two of the cold heads are attached at the top and bottom of the detector—one attached to the top copper radiation shield above the top PMT array and one attached to the bottom of the copper gamma shield below the bottom PMT array.[5] There are two additional cold heads located halfway up along the vertical dimension of the inner cryostat. These two additional cold heads are mounted on a thin copper sheet wrapped around the outside of the inner cryostat to provide temperature control to the xenon near the cryostat walls. There is a fifth thermosyphon left unattached to the TPC structure for use with a charcoal trap in the vacuum space between the

[5]The bottom gamma shield was often referred to as the "filler-chiller-shield". The liquid xenon return line was directed through the large copper shield mass attached to the bottom thermosyphon head to equilibrate the xenon temperature before reintroduction into the active region.

inner and outer cryostat [75]. Each thermosyphon is capable of delivering 200–400 W of cooling power. All cold heads have thermometers and 50 W resistor-based heaters installed. The cold heads attached at the top and bottom of the detector each have an additional 750 W heater. The heaters and thermometers are included in a proportional-integral-derivative (PID) loop to ensure a stable temperature. These details are from Ref. [58], where more information on the cryogenic system can be found.

2.3.3 Suppression of radioactive backgrounds

In addition to the signal-based background suppression techniques described in Sec. 2.3.1, a number of design decisions were made to reduce the detector background to an acceptable level. These programs include shielding the detector nearly a mile underground, installing the TPC in an 8 m diameter water tank, and screening all detector construction materials in a gamma counter before commissioning the LUX detector.

2.3.3.1 LUX installation at the 4850 ft level of the Sanford Underground Research Facility

The LUX detector was installed at the 4850 ft (4300 mwe) level of the Sanford Underground Research Facility to escape background radiation from cosmic rays. On the surface, the measured muon flux of 0.019 ± 0.003 (measured in Appendix. B) produced an event rate in the liquid xenon filled LUX detector of 108.8 ± 0.3 Hz [73]. The cosmic ray muon flux at the 4850 ft level is $(0.044 \pm 0.001) \times 10^{-7}$ cm^{-2} s^{-1}—reduced by a of a factor of 2×10^{-7} compared to the surface [76].

A 8 m diameter, 6 m tall tank of ultra-pure water is used to screen the LUX TPC from background radiation in the cavern. The LUX TPC inside the shield before it was filled with 77,000 gallons of water is shown in Fig. 2.10. An active cosmic ray Cherenkov veto consisting of 20 Hamamatsu R7081 10 inch PMTs line the walls and floor of the water tank. The walls and floors of the water tank are covered in Tyvek to increase photon detection efficiency for the cosmic ray veto. The effectiveness of

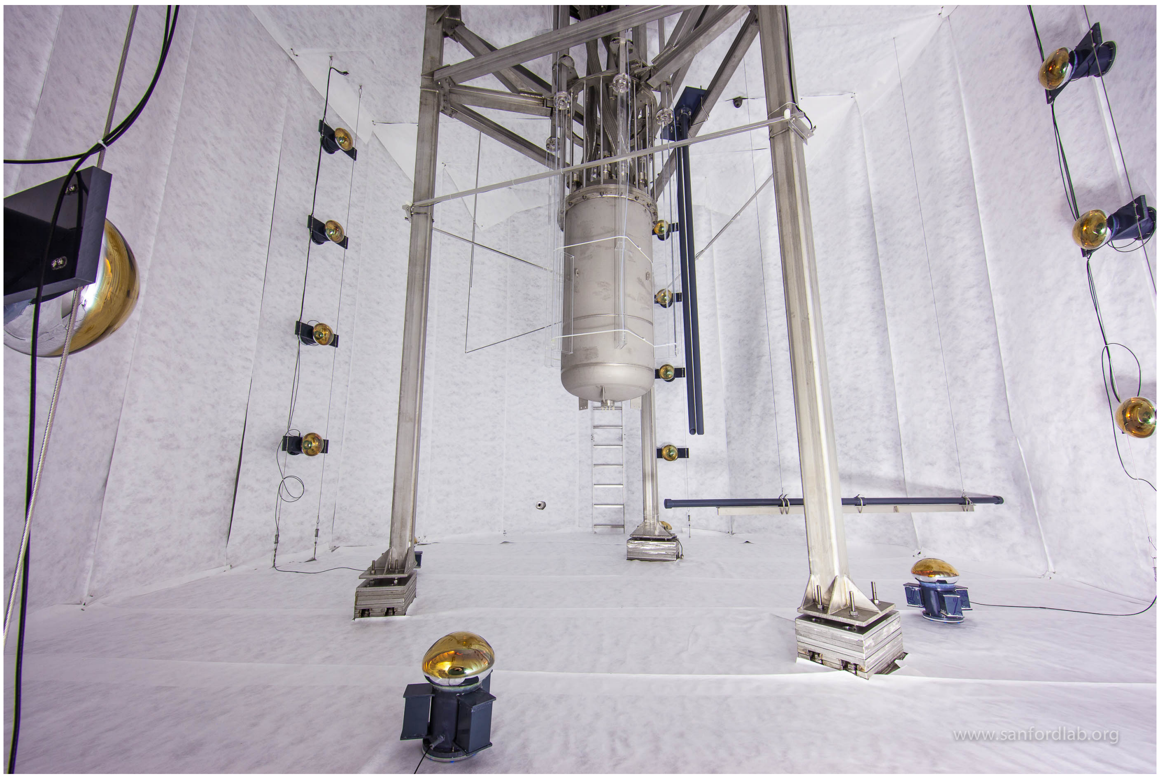

Figure 2.10: Photograph of the LUX detector inside the 8 m diameter water tank before it was filled with 77,000 gallons of ultra-pure H_2O in late 2012. The LUX titanium outer vessel cryostat can been seen suspended in the center of the image. The six clear, acrylic external calibration source tubes can been seen surrounding the outer cryostat. The D-D neutron calibration conduit is constructed from dark gray schedule 80 PVC and can be seen on the lower right region of the photo suspended from the top of the water tank. In this photo, it is out of line with the LUX detector in preparation for WIMP search running. Figure courtesy of SURF.

the water shield at attenuating ambient neutron and gamma ray backgrounds is shown in Fig. 2.11.

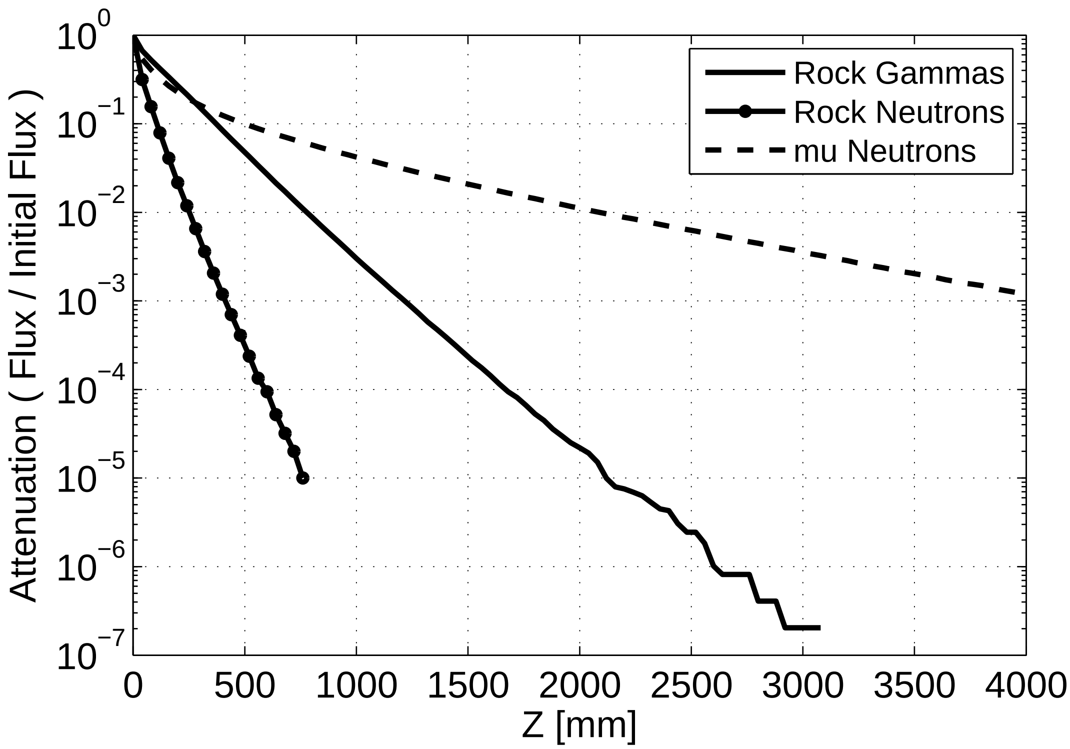

Figure 2.11: The simulated attenuation of ambient neutron and gamma ray radioactive backgrounds by a semi-infinite volume of water representing the LUX water tank. The "rock" neutrons and gammas are primarily due to the uranium, thorium, and potassium in the Davis cavern rock walls. The "mu" neutrons are induced by cosmic ray muons that penetrate the earth overburden. This figure is reproduced from Ref. [58].

A comprehensive detector component screening program was developed to count all TPC construction materials [30]. A Geant4-based LUXSim Monte Carlo incorporated the results of this counting program and was used to create PDFs of the expected electron recoil background for use in the profile likelihood ratio analysis used to set the Run03 WIMP search limit [5]. A detailed review of the LUX counting program and background model is available in Ref. [30].

2.3.3.2 Removal of trace noble gas radioisotope contaminants

A detailed account of the chromatographic separation program is available in Refs. [77, 78]. This section is based upon these references. The liquid xenon circulation and purification system described in Sec. 2.3.2.3 does not remove noble element impurities from the xenon. Even high-purity, research grade xenon contains an unacceptable level of contamination of the radioisotope ^{85}Kr and possibly ^{39}Ar. Both isotopes are beta emitters with half lives of 10.8 years and 269 years, respectively [79]. The beta particle endpoint energy for ^{85}Kr (^{39}Ar) is 687 keV (585 keV). The concentration of ^{85}Kr and ^{39}Ar must be reduced below 20 ppt and $\sim$1 ppb, respectively, to achieve a WIMP search background contribution subdominant to the PMTs [78].[6] As a consequence, a program was developed to remove trace quantities of the radioactive noble isotopes ^{85}Kr and ^{39}Ar from the xenon before it was transported to SURF for use in LUX. A custom-built, activated-charcoal-based chromatographic separation system was used to separate xenon from trace krypton and argon contaminants. A total xenon mass of 400 kg was purified using this system, which reduced the average ^{85}Kr concentration from 130 ppb to 3.5 ppt and the average ^{39}Ar concentration to $\sim$1 ppb [78].

2.3.4 Data acquisition system

The LUX data acquisition system (DAQ) begins with the cables attached to the PMT bases and ends with the .dat files containing the raw digitized waveforms written to disk on the acquisition computer. A detailed description of the LUX DAQ system is available in Refs. [80, 81]. A detailed review of the LUX trigger system is available in Ref. [82]. The details of this section are based upon these references. In this section, we describe the hardware configuration and settings used for the LUX Run03 WIMP search data taking. The LUX Run03 D-D calibration used identical data acquisition settings. A photograph of the underground commissioning of the DAQ system is shown in Fig. 2.12.

[6] The notation ppb and ppt is used to indicate parts-per-billion and parts-per-trillion (g/g).

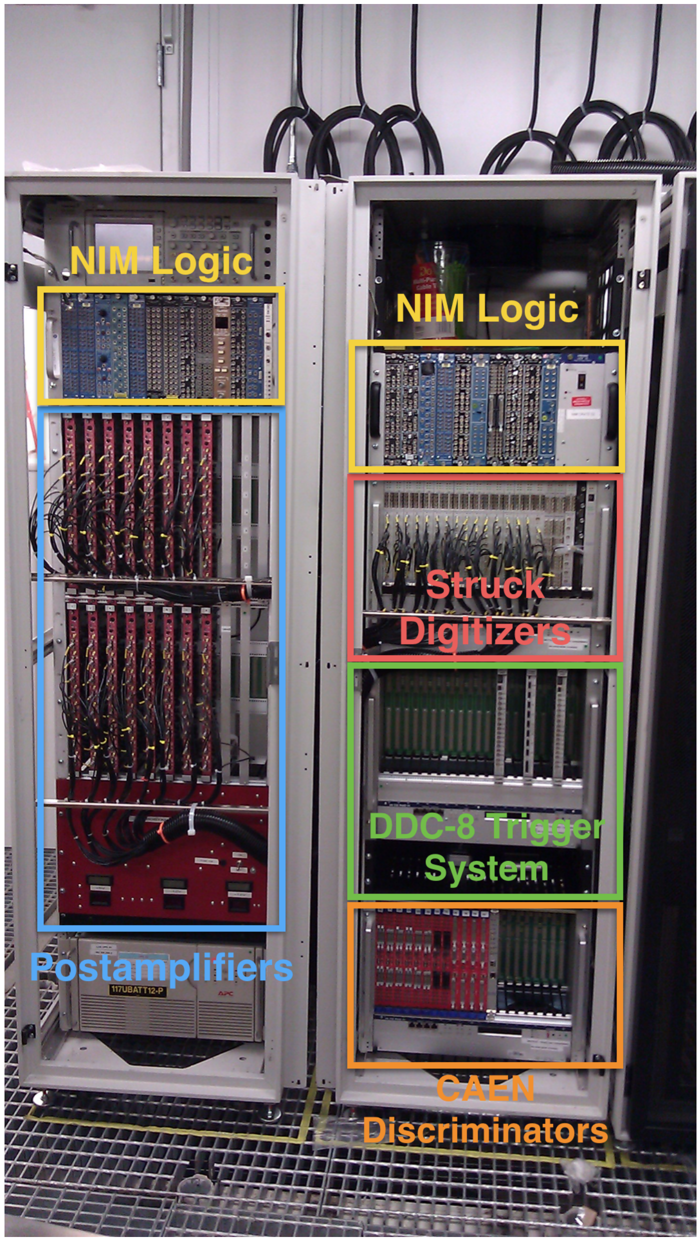

Figure 2.12: A photograph showing the two LUX DAQ system racks that contain the postamplifiers, Struck digitizers, DDC-8DSP trigger system, NIM logic, and CAEN discriminators. This photograph was taken in July 2012 during underground DAQ commissioning performed by James Verbus and Mongkol Moongweluwan (University of Rochester).

2.3.4.1 Analog amplifiers

The analog signals produced by the PMTs propagate along 10 m-long coaxial cables from within the LUX cryostat to preamplifiers mounted directly on the breakout cart. The custom made preamplifiers provide a $\times 5$ gain. The preamplified signals from each channel are routed to the postamplifier in the LUX DAQ racks via 10 m-long coaxial cables. The custom made postamplifiers provide three output signals for each input channel. The first output provides a $\times 1.5$ gain for the Struck SIS3301 digitizers. The second output provides a $\times 2.8$ gain for the DDC108 trigger system. The third output provides a $\times 18$ gain intended for CAEN discriminators, which are not used for the results presented in this thesis. In practice, this third output was often used to pick off the signals from individual channels for observation without disrupting the DAQ cabling configuration.

2.3.4.2 Struck SIS3301 digitizers

The LUX DAQ uses 17 eight-channel Struck SIS3301 digitizers. This corresponds to a total of 136 digitizer channels. One Struck channel is used to digitize each of the 122 PMT channels. The 20 water tank PMT channels are ganged into digitizer channels 129–136, but were not used during Run03 data taking. Each channel has 14 bits of resolution and is digitized using a 100 MHz sampling frequency. The Struck channels use an analog bandwidth filter with a 30 MHz cutoff frequency before digitization. The Struck boards are housed in a single VME crate. The VME bus is connected to the DAQ computer using a fiber optic connection. The maximum data transfer rate from the VME crate to the DAQ computer via the 2eVME protocol is 80 MB/s. As deployed, the data acquisition rate is limited to $\sim$30 MB/s due to the I/O on the single hard disk in the data computer. This is sufficient for the data rates required for LUX calibration, but future experiments based upon this DAQ setup could achieve a higher data rate using a striped RAID or solid state disk in the DAQ computer.

A custom, on-line, baseline suppression algorithm was implemented in the digitizer firmware. This functionality was developed by the vendor with support from LUX. The input waveforms for each pair of channels is digitized when the signal amplitude in one or both channels of the pair rises above a predefined pulse detection threshold. The pulse detection threshold is typically set to 1.5 mV, and the pulse end threshold is typically set to 0.5 mV. The pulse detection threshold is set at the level required to be 95% efficient for single photoelectron detection in each channel. This threshold level of 1.5 mV is $>5\sigma$ above the measured fluctuations in the baseline noise. The digitization of both channels continues until the signal amplitude in each channel of the pair falls below a pulse end threshold. Pretrigger and posttrigger regions are digitized outside of the time window defined by the pulse detection and pulse end threshold crossings. The pretrigger and posttrigger regions are typically defined to be 24 and 31 samples, respectively. A pulse overshoot threshold exists to continue digitization if the waveform exhibits bipolar ringing. The high data quality (low instance of bipolar pulses) rendered this option unnecessary, and it was disabled for the datasets used for our analysis. The amplitude value used for threshold decisions is defined relative to a rolling baseline average calculated using a 32 sample wide window. The value of this rolling average is frozen once the waveform crosses the pulse detect threshold to avoid bias effects due to the above threshold signal. The calculation of the rolling average is resumed after the end of the posttrigger region.

2.3.4.3 DDC-8 trigger system

The on-line hardware trigger system used for LUX is based upon the DDC-8DSP.[7] The LUX DAQ system uses two eight-channel DDC-8 boards. Each trigger channel has an analog bandwidth filter with a 24 MHz cutoff frequency. The sum of eight LUX PMT channels is used as an input to each DDC-8 channel to save on cost. The channel sum is performed by LeCroy 628 fan-in NIM modules. The PMT channels selected for each gang-of-eight were determined by the PMT position in the top and bottom PMT arrays. The pattern of PMTs in each summed trigger channel was chosen to maximize the dynamic range, while preserving precise (x, y) reconstruction and identification of events near the physical detector PTFE walls. The study to determine this pattern is discussed in

[7] This hardware was designed by LUX collaborators at SkuTek Instrumentation and the University of Rochester.

Ref. [82].

A limited set of the DDC-8's wide range of functionality was used for the analyses described in this thesis. This set of functionality was chosen based upon the requirements of the LUX WIMP search. The trigger was operated in S2 identification mode. In this mode, a digital finite impulse response filter is used to identify S2 pulses in the data stream in real time. The threshold of the filtered signal for each gang-of-eight trigger group was set to 8 phe. An S2 trigger signal was issued when there is a coincidence of $\geq$2 trigger groups within a 2 μs window. A hold-off period of 1–4 ms after each trigger was observed to prevent spurious triggers in the aftermath of large S2 signals. This trigger configuration is 99% efficient for S2 signals of 100 phe [82].

For each identified event trigger, the trigger system outputs a NIM pulse into a predefined Struck digitizer channel. This trigger signal is used by the event builder to organize the raw waveform data saved in the .dat file output from the DAQ computer into .evt files as described in Sec. 2.3.5. These .evt files only contain the digitized waveforms within a predefined time interval around the DDC-8 trigger signal.

2.3.5 LUX data processing

The LUX data processing pipeline begins as the .dat files containing the raw waveforms are transferred from the DAQ computer. The .dat files are immediately transferred from the DAQ computer to the primary data mirror at Brown University. As the .dat files arrive on the primary data mirror, they are used to produce .evt files, which contain only the raw waveform data within a predefined trigger window around the DDC-8 trigger pulse in the data stream. The trigger window is defined to be $\pm$500 μs around the DDC-8 trigger pulse. The $\pm$500 μs event window was chosen to be wide enough to capture the deepest events in the liquid xenon volume. These events at at the bottom of the detector have a measured electron drift time from the cathode to the liquid surface of 324 μs. The symmetric event window ensures that the S1 and all S2 pulses are captured in the event record regardless of which pulse induced the DDC-8 trigger signal.

The parent .dat files are compressed using gzip and stored on the primary data mirror for distribution to collaborating institutions. The .evt files are directly transfered to the Oscar cluster at the Center for Computation and Visualization at Brown University, where jobs are submitted for processing by the LUX data processing framework. After a full dataset of .evt files is transfered to Oscar, the .evt files on the primary mirror are compressed, stored, and served similarly to the .dat files. The LUX data processing framework parameterizes the waveforms in the .evt files and saves the resulting parameterization in compressed .rq.gz files. The .rq.gz files are transferred from Oscar to the primary data mirror. The majority of LUX analysis results are produced directly using the .rq.gz files. These files are duplicated in the .root and .mat file formats for easy loading on common software platforms.

2.3.5.1 Data processing framework

The LUX data processing framework was developed as an in-house solution to the collaboration's data processing needs. The framework runs a predefined series of analysis algorithm modules on each .evt.gz file in a given input dataset and produces a corresponding .rq.gz file. The data processing framework operates upon individual LUX datasets corresponding to a single acquisition.

The framework itself is agnostic of the language of the algorithm module as well as the details of the algorithm's implementation. Each algorithm module is called in the framework using a wrapper function that identifies the language of the module and initializes the algorithm subprocess accordingly. The inputs to each algorithm module are identical regardless of language to allow the framework to call each module using the same signature. Currently, the data processing framework uses >20 modules written in a mix of Matlab, ROOT/C++, and Python. The easy deployment of algorithms in a variety of languages provides a low barrier to entry for algorithm developers by ensuring they can contribute in their programming language of choice.

A comprehensive versioning system is integrated into the data processing framework to ensure the complete processing history of every dataset is uniquely defined in a central MySQL-based database. This versioning record in the database for each processed dataset includes the software revision, event builder settings, data processing settings, and the version number of all calibrations and corrections applied in the pipeline. A detailed description of the LUX data processing framework and the implementation of each algorithm is contained in Refs. [37, 81].

2.3.5.1.1 Cluster deployment The LUX data processing framework was designed to manage the parallel processing of individual datasets on high-performance computing clusters. The data processing framework was successfully deployed and used on the Oscar cluster at Brown University, PDSF at NERSC, and the LUX on-site cluster at SURF. All production data processing using the "stable release" code base is performed on the Oscar cluster. During periods of batch reprocessing (embarrassingly parallel), the data processing framework successfully scales to a demonstrated peak usage of >2000 cores. An average .evt processing rate of >100 GB/hour was achieved over a period of months of continuous reprocessing. This scaling was achieved by implementing dynamic RAM disk usage in the data processing framework. When a RAM disk is available, all inter-module communication is performed in RAM on the Oscar cluster nodes. This significantly reduces disk I/O, which would otherwise prohibit scaling beyond $\mathcal{O}$(100 cores).

2.3.5.2 Data storage and distribution

All .dat.gz, .evt.gz, and .rq.gz files are stored on the primary data mirror at Brown University for distribution to LUX collaborators. The primary mirror is connected to Internet2 using a 10 Gbit/s fiber optic link to Brown's Science DMZ. As of April 2016, a total of 400 TB of compressed data (1.2 PB uncompressed) is hosted on the primary data mirror. A full backup of the primary data mirror is implemented at NERSC for geographic redundancy.

Particular attention was paid to the limitations of the TPC protocol over long-distance, high-bandwidth networks. When sending data via the TPC protocol, each sequence of data is limited in size by the TCP window settings of the local and remote machines. Most modern machines in use as LUX servers use 65536 bytes as the TCP window size. The theoretical maximum transfer rate across long-distance, high-bandwidth networks when using the TPC protocol is a function of the round trip time (RTT) and the TCP window:

$$\text{maximum transfer rate [bytes/ms]} = \text{TCP window [bytes]} \,/\, \text{RTT [ms]} \,. \tag{2.15}$$

As an example, the RTT from Brown to the University of California at Davis was measured to be 93 ms. Using Eq. 2.15, this corresponds to a maximum transfer rate of 688 kiB/s—a very small fraction of the 10 Gbit/s Internet2 connection.

For Run03, a custom data transfer software package was created to facilitate high data rate transfers over long-distance, high-bandwidth networks. This utility spawns and monitors an arbitrary number of independent TCP streams when transferring a LUX dataset. In most LUX applications, the data transfer rate scales linearly with the number of TCP streams. The data transfer rate from SURF to the Brown primary data mirror increased by $\times 30$ using this technique. This custom LUX solution was replaced by the commercial solution Globus for Run04 [83].

2.3.6 Calibrations

The LUX experiment has pioneered the use of new calibration techniques to measure the electron recoil and nuclear response of large liquid noble detectors. These techniques are summarized in the following sections.

2.3.6.1 Electron recoil calibrations

The metastable ^{83m}Kr isotope is injected into the liquid xenon circulation to provide an internal, homogeneous standard candle source for detector response calibrations. A ^{83}Rb (86.2 day half-life) source is used to generate the ^{83m}Kr used for the TPC calibration [84]. ^{83m}Kr decays via the emission of a 32.1 keV$_{ee}$ conversion electron followed by a 9.4 keV$_{ee}$ conversion electron with a characteristic time separation of 154 ns [85]. These calibrations are typically performed weekly during periods of stable detector operation. The maximum event rate in the LUX detector following a ^{83m}Kr injection is typically ∼100 Hz. The half-life of ^{83m}Kr is 1.83 hours allowing the detector event rate to return to background within a fraction of a day. The standard candle provided by ^{83m}Kr is used to correct for any (x, y, z) variation in the detector response. This includes position-based variations in light collection and field-dependent signal production effects for both S1 and S2. The size of the observed raw $S2$ produced by ^{83m}Kr events as a function of the z position in the detector is used to measure the electron lifetime. The measured electron lifetime is used to correct for the z dependence of the S2 signal.

The electron recoil response of the LUX detector was defined using a novel technique involving the injection of tritiated methane directly into the liquid xenon. Tritium is a beta emitter with an endpoint energy of 18.6 keV$_{ee}$, providing an electron recoil energy spectrum that fully spans the WIMP search energy region. The 12.6 year half-life of tritium requires active removal of the tritiated methane from the detector media. Detailed *ex situ* tests were performed to ensure the necessary removal of the tritiated methane from detector media was possible. Over 170,000 tritium events were acquired and used to define the electron recoil band as shown in the top frame of Fig. 2.6. The high-statistics of the tritium calibration provides an unprecedentedly high-precision, low-energy electron recoil calibration. In addition to the electron recoil band definition, the tritium data was used to measure the charge yield, light yield, and recombination fluctuations for electron recoils between 1.3–17.0 keV$_{ee}$. These quantities were measured at the Run03 operating field of 180 V/cm and an alternative lower field of 105 V/cm during a separate run. The tritium data also provides an independent measurement of g_1, g_2, and the electron extraction efficiency by fitting a model of the tritium beta spectrum to the observed spectrum in data. Using this method, the best fit values are $g_1 = 0.115 \pm 0.005$ phd/photon and $g_2 = 12.1 \pm 0.9$ phd/electron. The best fit extraction efficiency was measured to be 0.51 ± 0.04 using the tritium data. This value is in agreement with the official extraction efficiency reported later in this section. These results are presented in greater detail in Ref. [72].

A number of gamma ray, x-ray, and internal conversion sources are used to define the electron recoil response at known energies. These sources include internal homogeneous sources that were deliberately injected ($^{83\mathrm{m}}$Kr) as well as naturally present from cosmogenic activation (activated Xe isotopes). A ^{137}Cs source was temporarily positioned outside of the LUX cryostat to obtain calibration data. ^{214}Bi is a naturally occurring radioisotope in the U chain. The integrated exposure to these gamma rays during the 95 live days of Run03 WIMP search data provided sufficient statistics for use as a line source in this analysis. The measured $S1$ and $S2$ in single-site events containing the full energy deposition of these monoenergetic line sources can be used to obtain a simultaneous, high-precision measurement of g_1 and g_2. When E_{ee}, $S1$, and $S2$ are known, only g_1 and g_2 remain as unknowns in Eq. 2.10. By fitting a line in $S1/E_{\mathrm{ee}}$ vs. $S2/E_{\mathrm{ee}}$ space to the mean $S1$ and $S2$ observed from these monoenergetic line sources, the values of g_1 and g_2 can be determined. Fig. 2.13 shows the constraints placed on g_1 and g_2 by these monoenergetic electron recoil sources.

The measured values of g_1 and g_2 are 0.117 ± 0.003 and 12.1 ± 0.8, respectively. This corresponds to an extraction efficiency during the Run03 WIMP search of 0.49 ± 0.03. These results are in good agreement with the measured values based upon the best fit tritium spectrum. The g_1, g_2, and extraction efficiency reported here are the official values for the LUX Run03 WIMP search period. The values were translated to the D-D calibration period by observing time variation in the $S1$ and $S2$ peak positions produced by the monoenergetic $^{83\mathrm{m}}$Kr source. The magnitude of this correction is discussed in Sec. 4.2.1.

2.3.6.2 Nuclear recoil calibrations

It is straightforward to measure the electron recoil signal yields in units of quanta per unit energy using line sources that fully deposit their known energy in the liquid xenon in a single interaction [59, 85]. Absolute calibration of the detector's response to nuclear recoils induced via neutron scattering are more challenging for several reasons: unlike electron recoil calibrations, there are no convenient sealed or injectable sources providing mono-energetic neutrons; due to the variable energy transfer

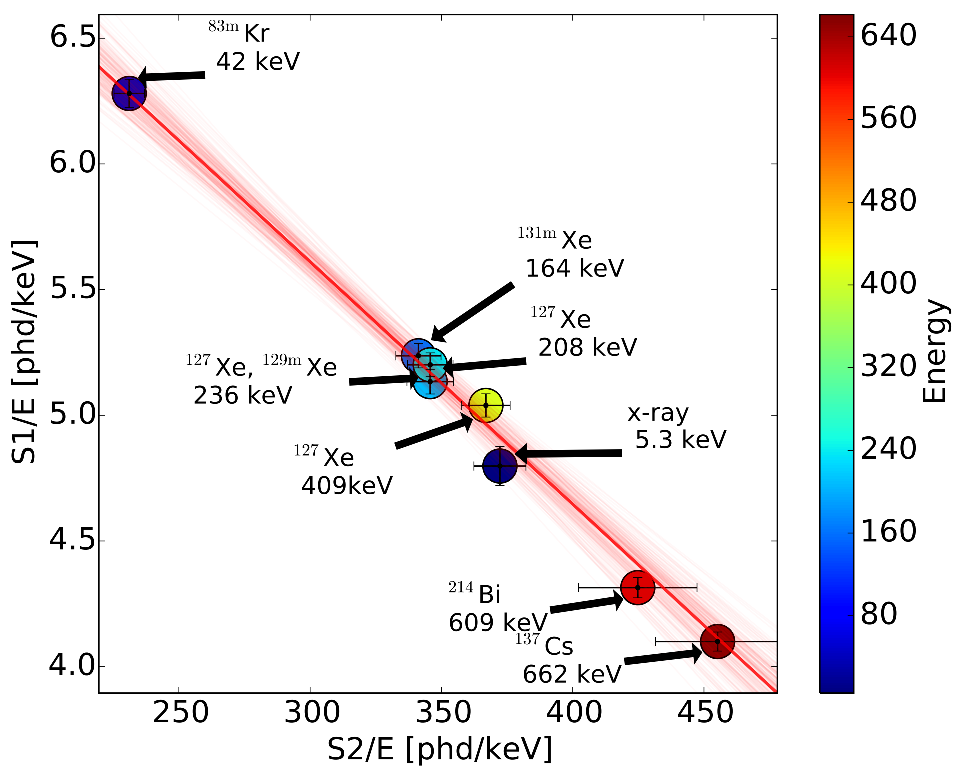

Figure 2.13: Constraints on g_1 and g_2 using the anti-correlation of $S1$ and $S2$ from electron recoil events produced by line sources. The 5.3 keV$_{ee}$ x-ray labeled in the plot is produced by ^{127}Xe. All data shown in this figure were acquired during the Run03 WIMP search run. This figure was produced by Attila Dobi and Richard Knoche (LUX Collaboration).

to the nucleus depending upon the neutron scattering angle, even mono-energetic neutrons produce a range of recoil energies; only a small fraction of the incident neutron energy is deposited at each interaction, and the neutron mean free path of $\mathcal{O}(10\text{ cm})$ typically results in multiple-site interactions in the detector medium and energy-loss in passive detector materials.

The nuclear recoil calibration using a D-D source described in Ch. 1 was used as the main calibration technique for the LUX nuclear recoil response. For the nuclear recoil yield result reported in this thesis, we use event-by-event kinematic reconstruction of neutron double-scatters to obtain an absolute measurement of the nuclear recoil energy, E_{nr}, and combine this with the LUX absolute e^- calibration (using g_2) to obtain a direct calibration of Q_y. This Q_y measurement provides a precise calibration of $S2$ as a function of recoil energy, which can be used to extract L_y from the single-scatter event population using the LUX g_1 to determine the absolute number of S1 photons collected. Because the calibrations of the signal yields are performed *in situ*, the uncertainty in g_2 drops out and does not contribute to the uncertainty in the L_y energy scale. Additionally, we use the known nuclear recoil energy spectrum endpoint for neutrons produced by our D-D source, again combined with the LUX g_1 and g_2, to absolutely measure the Q_y and L_y at 74 keV$_{\mathrm{nr}}$. In addition to the signal yield measurements, the nuclear recoil band was measured in LUX using the D-D source as first shown in Fig. 2.6. More detail on the nuclear recoil band measurement, including a comparison with simulation, is provided in Sec. 4.5.

The LUX D-D source calibration results in this thesis are organized as follows. The experimental setup for the LUX neutron calibration is described in Ch. 4. A low-energy (0.7–24.2 keV$_{\mathrm{nr}}$) measurement of Q_y using the measured scattering angle between double-scatter event vertices in LUX is reported in Ch. 5. A low-energy (1.1–12.8 keV$_{\mathrm{nr}}$) measurement of L_y using single-scatter events is reported in Ch. 7. The Q_y and L_y at the 74 keV$_{\mathrm{nr}}$ recoil energy spectrum endpoint is reported in Ch. 8. The LUX nuclear recoil band measurement was reported in detail in Sec. 4.5. A different set of event selection cuts was appropriate for each of these analyses. The specific cuts used for each analysis are outlined at the beginning of each section. Two new NEST [86] nuclear recoil models (one based on the Lindhard model [68], one based on the Bezrukov parameterization [87]) were created via a simultaneous fit to the reported Q_y, L_y, and nuclear recoil band results. These new NEST models are described in Sec. 9.2. The D-D calibration results presented in this thesis used several simulation frameworks to produce targeted results as appropriate for each section. The Monte Carlo setup and the software used for each section is described in the text of that specific analysis.

2.3.6.3 Extraction efficiency from radon alpha decays

We present an alternative measurement of the electron extraction efficiency during the Run03 WIMP search period using the measured ionization signals produced by alpha particles in LUX to existing *ex situ* xenon ionization yield data for alpha particles in the literature.[8] [9]

2.3.6.3.1 LUX Run03 radon alpha data A portion of the Run03 WIMP search dataset is used for this analysis. The LUX data used for this analysis consists of 5.49 MeV ^{222}Rn alpha particle events from a fiducial target defined by $r < 18$ cm and $38 <$ drift time < 305 μs. This is the same z cut used to define the fiducial volume for the LUX Run03 WIMP search. The LUX electric field was measured to be 180 ± 20 V/cm averaged over this region [5]. The sample of ^{222}Rn decays is shown in Fig. 2.14. We use the bottom PMT array only for this analysis to avoid potential PMT saturation effects.

The selection of ^{222}Rn decay events shown in Fig. 2.15 was used to determine the average $S2$ in the bottom array produced by a 5.49 MeV alpha particle. A histogram of the $S2$ (bottom array) values is shown in Fig. 2.15. The population mean was measured to be 24450 ± 60 phd using a skew Gaussian fit. The uncertainty is quoted as statistical uncertainty on the mean from the fit. The single electron calibration was obtained from the average single electron size value as measured in

[8] This section is based upon an internal LUX analysis performed in collaboration with Peter Sorensen and Dongqing Huang.

[9] The code used for this analysis is located in the Brown Particle Astrophysics Group's GitHub organization [65] with the relative path "jverbus_lux_scratch/ee/".

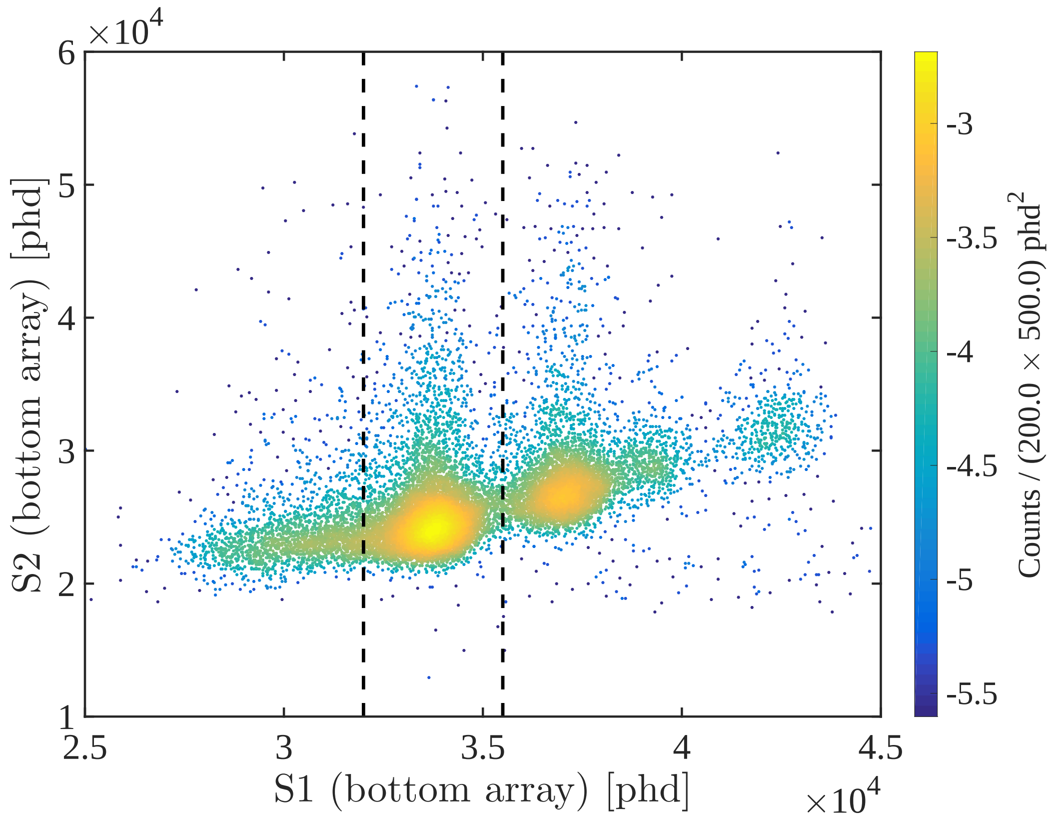

Figure 2.14: ^{222}Rn alpha decays in the LUX Run03 WIMP search data. The ^{222}Rn alpha decay population is selected between the two black dashed lines. The other populations correspond to subsequent alpha decays in the Rn chain.

Kr data during the WS campaign of 10.47 ± 0.01. These considerations result in an average observed signal of 2335 ± 6 electrons for 5.49 MeV alpha particles in LUX. Uncertainty is statistical on the mean only.

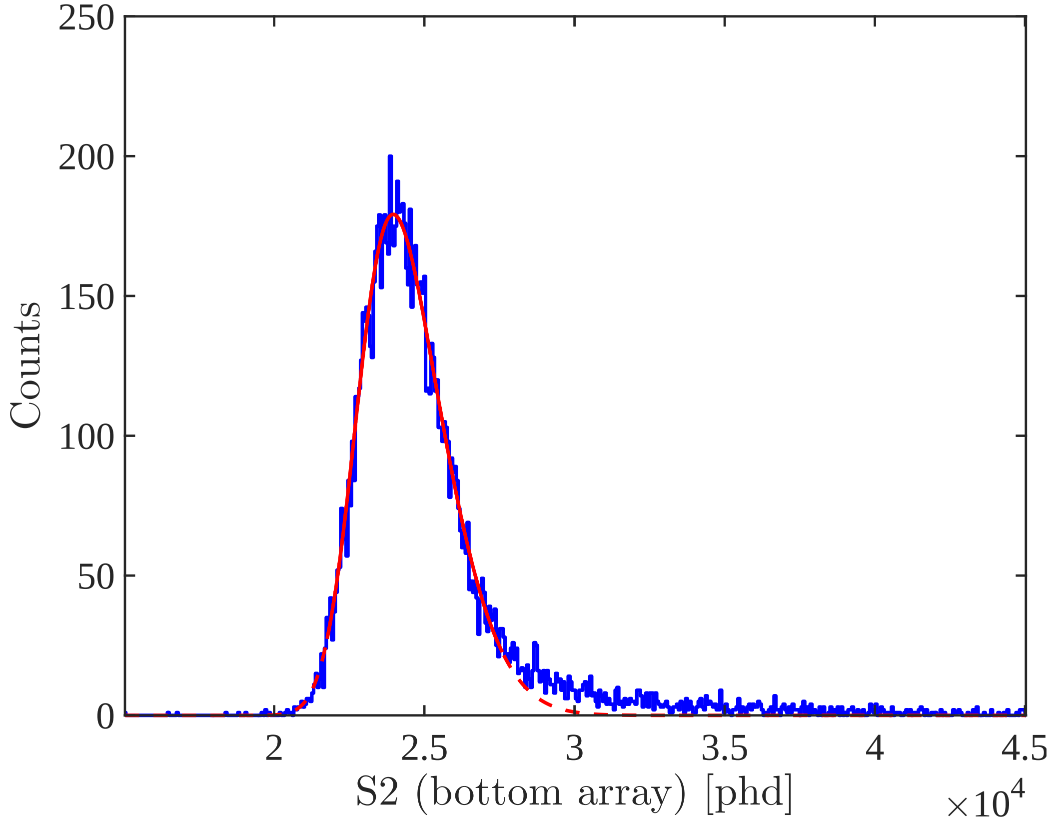

Figure 2.15: A $S2$ (bottom array) histogram of the ^{222}Rn alpha decay selection shown in Fig. 2.14 is shown in blue. A skew Gaussian was fit to the peak to extract the mean. The region used for the fit is shown by the solid red line. The fit has a χ^2/dof of 81.2/88, which gives a p-value of 0.68.

2.3.6.3.2 Ex situ reference data The ionization yield data in Ref. [3] were measured using a calibrated charge sensitive preamplifier in the liquid phase. The lowest electric field for which an ionization yield is reported is 210 V/cm. The data from Ref. [3] are shown in Fig. 2.16. Stated uncertainties are smaller than the size of the data points, which is not surprising considering the number of events populating the full energy peaks. The average LUX field of 180 V/cm is indicated by the dashed vertical line. A series of simple second order polynomial fits to the ^{241}Am data (conveniently also 5.49 MeV) were performed, using only the four, five, and six smallest (in electric field) data points. An example of fitting the lowest six data points is shown in the figure. From this exercise, the range of likely ionization yields at the LUX electric field value was inferred to be between 5209 e^- and 5349 e^-. This variation represents 1.5% systematic uncertainty on a mean value of 5270 ± 80 electrons. We repeat this procedure at 160 V/cm and 200 V/cm to estimate the systematic uncertainty due to the average LUX field of 180 ± 20 V/cm. This process indicates an additional $\pm 4\%$ systematic uncertainty due to the uncertainty in the average LUX electric field. The final value for the expected charge yield from 5.49 MeV alpha particles in liquid xenon at the LUX electric field is 5270 ± 225 electrons.

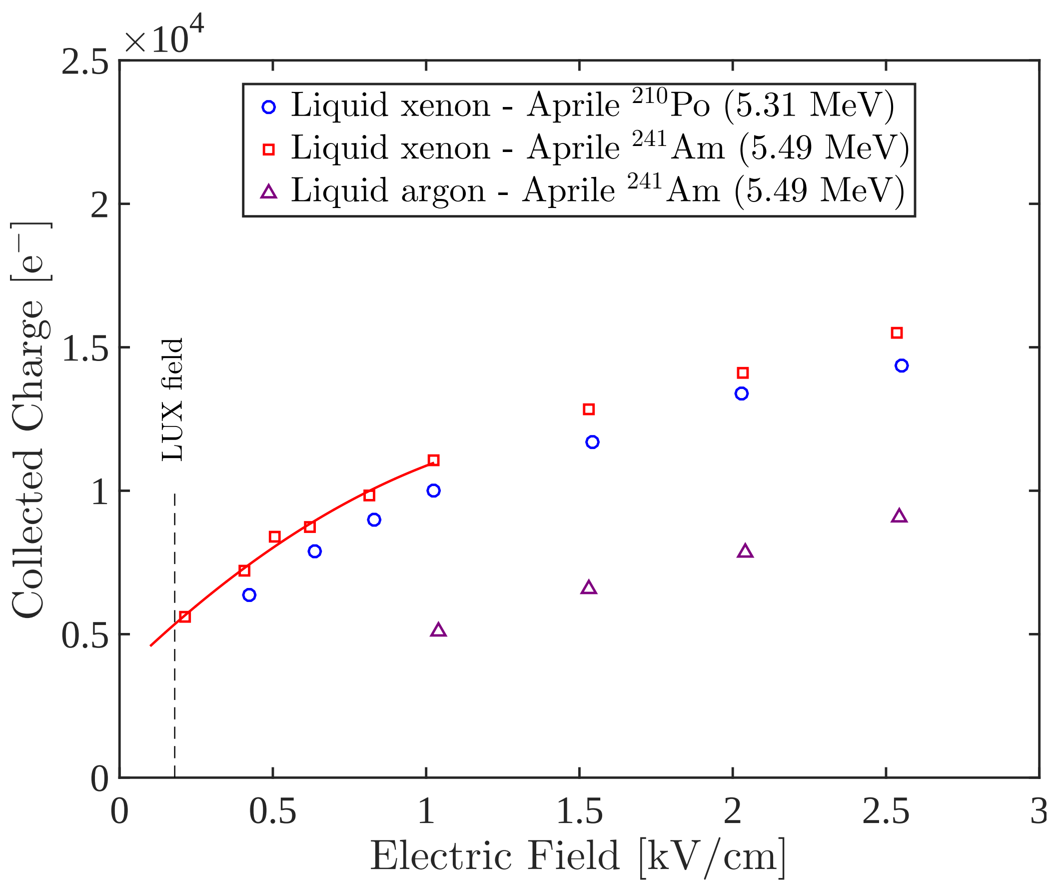

Figure 2.16: Collected charge for alpha decays at various drift fields as measured in Ref. [3]. The LUX field is represented by the vertical dashed line at 180 V/cm. A series of second order polynomial fits were performed to the lowest four, five, and six ^{241}Am data points in order of electric field magnitude to extrapolate from lowest measured field point to 180 V/cm with an associated estimated systematic error.

One potential systematic in the *ex situ* data not mentioned in Ref. [3] is the tolerance of the capacitor value used for the absolute charge calibration of the preamplifier. If the true capacitance value was measured in Ref. [3] then any systematic error contribution is negligible. The true value of the capacitor is not reported to greater precision than 1 pF, so we must assume that this is the nominal value of the capacitor as specified by the vendor.

There are many more alpha ionization measurements in the literature using liquid argon than using liquid xenon. One potential way to get a handle on the potential error due to the allowed variation in the calibration capacitor is to compare the measured collected charge values for ^{241}Am in liquid argon using the same apparatus in Ref. [3] to other liquid argon ionization measurements in the literature. The collected charge vs. drift field from Ref. [3] and Ref. [4] shown in Fig. 2.17 are in agreement below 4 kV/cm drift field and have a maximum deviation of $\sim$5% at 9 kV/cm. This agreement indicates there is not a significant systematic in the absolute calibration of the data in Ref. [3] due to a systematic uncertainty in the capacitance of the calibration capacitor, unless the measurement reported in Ref. [4] suffered the same systematic.

2.3.6.3.3 Measurement of the LUX extraction efficiency We take 5270 ± 300 electrons to be the best estimate for 5.49 MeV alpha particles in liquid xenon after combining all systematic errors discussed in the previous sections. Comparing this with the LUX ionization signal value of 2335 ± 6 results in an extraction efficiency of 0.44 ± 0.03 (statistical and systematic uncertainties have been combined in quadrature). If we disregard the comparison to Ref. [4] and assume a worst case uncertainty of 20% on the calibration capacitor based upon typical specification sheets for similar items, this yields a value of 0.44 ± 0.09 for the extraction efficiency during the WIMP search period. This value is in agreement with the more precisely measured extraction efficiency using electron recoil line sources in Sec. 2.3.6.1. This value is also in agreement with the extraction efficiency as measured using the tritium data.

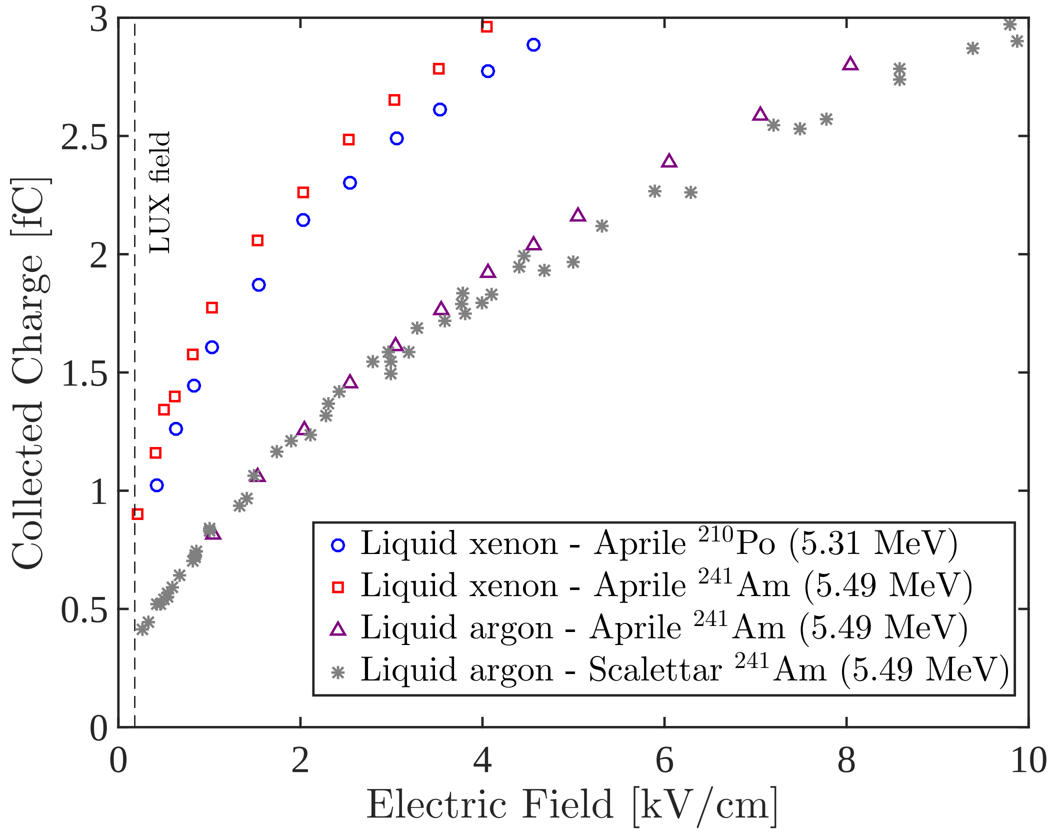

Figure 2.17: An overlap of the measured collected charge data for alpha particles in liquid argon from Ref. [3] with a similar measurement from Ref. [4]. Directly comparable data for liquid xenon wasn't found in the literature, so a comparison to ^{241}Am alpha particles in liquid argon was made to quantify any systematic from the calibration capacitor used in Ref. [3]. The agreement is better than 4% for all values shared between the two measurements.

Chapter 3

Measurement of the Adelphi Technology, Inc. DD108 Neutron Spectrum at Brown University

A monoenergetic source of neutrons is required to perform the absolute calibrations described in Sec. 1.2 and Sec. 1.3. Commercially available D-D neutron generators meet all of the criteria outlined in Sec. 1.1. In this section, we characterize the neutron energy spectrum produced by an Adelphi Technology, Inc. DD108 neutron generator using neutron ToF over a known distance to determine its suitability as a neutron source for the proposed kinematics-based TPC calibrations [88, 89].

3.1 Adelphi Technology, Inc. DD108 neutron generator

The DD108 is a beam-on-target D-D neutron generator with a maximum neutron output of $\sim 10^8$ n/s. Inside the DD108, deuterium ions are accelerated across a $\sim$100 kV potential difference into a titanium-coated copper target as shown in Fig. 3.1. The incident deuterium ions chemically bond with the titanium coating. Subsequent incident deuterium ions fuse with the captured deuterium in the target and produce neutrons into 4π solid angle via the $^2\mathrm{H(d,n)He}^3$ reaction. The mean outgoing neutron energy and flux are functions of the incident deuterium ion energy. The neutron energy and flux are also dependent upon the angle between the deuterium ion beam and the outgoing neutron direction [26]. The neutron flux varies by about a factor of $\times 2$ as a function of polar angle relative to the D-D generator beam target. The neutron energy as a function of angle relative to the deuterium ion beam is shown in Fig. 3.2 for a range of acceleration potentials.

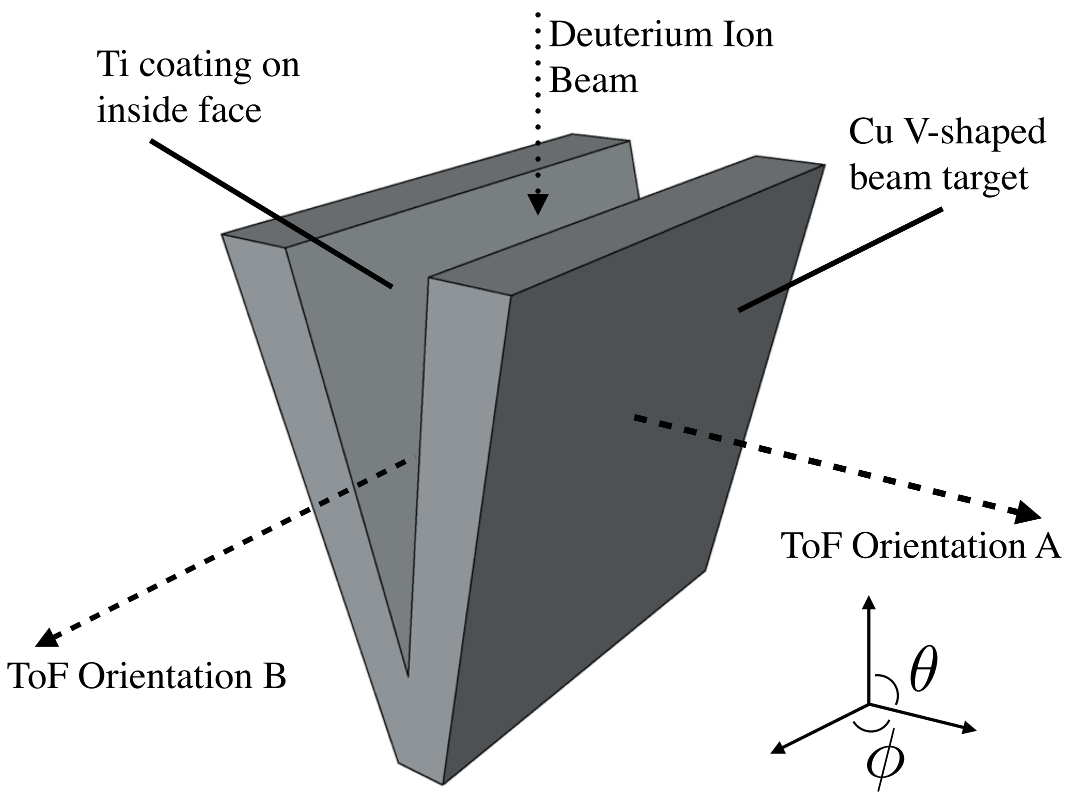

Figure 3.1: The copper V-shaped beam target of the Adelphi Technology, Inc. DD108 neutron generator. The deuterium ion beam is incident upon the target from the top of the figure. The ToF energy spectrum measurements were made at $\theta = \pi/2$. The ToF measurement at Orientation A was off-axis with the target V, and Orientation B was on-axis with the target V. This $\pi/2$ variation in ϕ between the off-axis and on-axis measurements was used to quantify any variation in the neutron spectrum due to the asymmetry of the neutron production surface.

The physical size and shape of the deuterium ion beam target can have an effect on the mean energy and width (σ/μ) of the neutron spectrum produced due to deuterium ion straggling in the

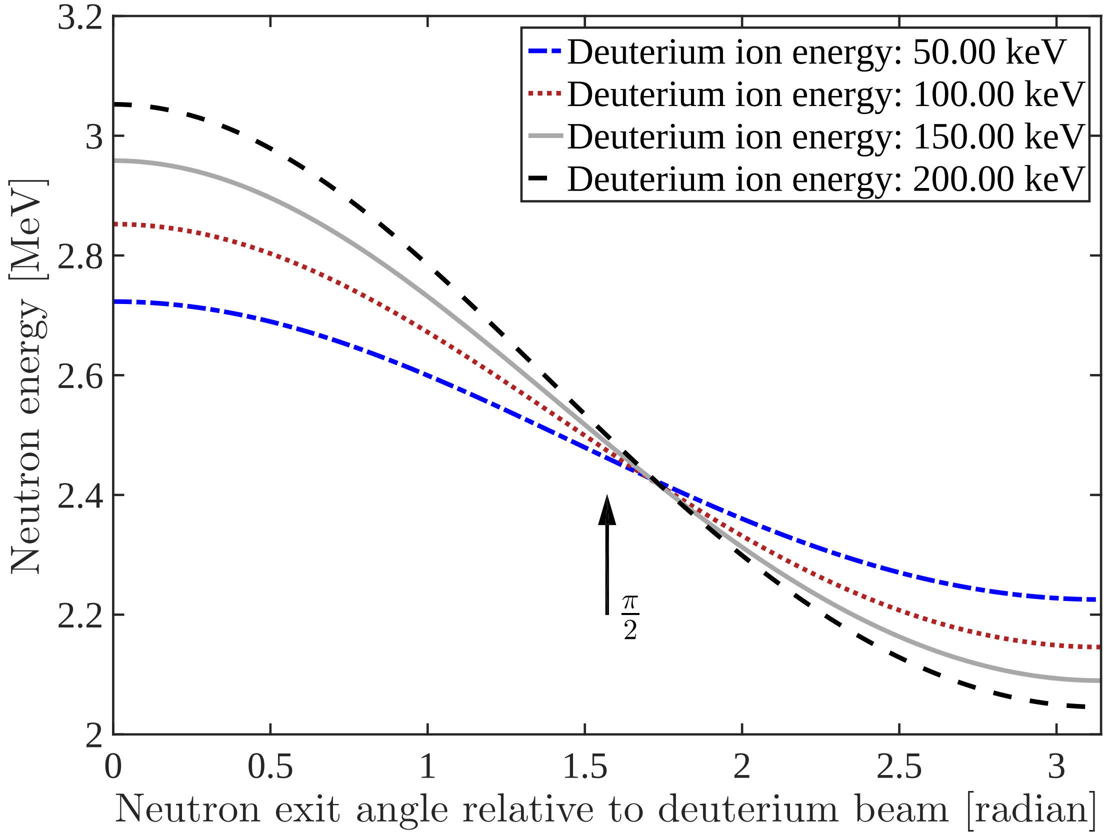

Figure 3.2: The neutron energy produced by the $^2\mathrm{H(d,n)^3He}$ fusion reaction as a function of angle. We show this function for several incident deuterium ion energies. The dependence of the neutron energy on the acceleration potential can be minimized by using neutrons produced at $\pi/2$ relative to the deuterium ion beam. Figure produced using information from Ref. [26].

target material before neutron production. The DD108 target is V-shaped, as shown in Fig. 3.1, to present an increased surface area to the incident deuterium ion beam for heat dissipation purposes. The dependence of the observed neutron spectrum upon the kinetic energy of the accelerated deuterium ion can be reduced by using outgoing neutrons at $\theta = \pi/2$ relative to the generator ion beam for nuclear recoil calibration purposes.

The neutron spectrum was measured using two separate DD108 target orientations to quantify any effects due to target asymmetry, and determine if there is an optimal configuration for the nuclear recoil calibrations described in Sec. 1.2 and Sec. 1.3. Orientation A ($\theta = \pi/2$, $\phi = 0$) measured the ToF spectrum of neutrons escaping perpendicular to the axis of the V-target, and orientation B ($\theta = \pi/2$, $\phi = -\pi/2$) did the same for neutrons escaping parallel to the axis of the

V-target.

The only gamma rays produced in the generator are via the ^{2}H(d, γ)^{4}He reaction with an energy of 23.84 MeV, which is suppressed by a factor of $\sim 10^{-7}$ relative to the neutron production rate [90]. This corresponds to roughly 10 γ/s when operating at the nominal maximum DD108 neutron yield of 10^8 n/s. The reactions Ti(d, γ) and ^{2}H(p, γ)^{3}He (5.5 MeV) on materials in the neutron generator are further suppressed [26, 91]. Electrons liberated by ion impacts on the target can back-stream across the 125 kV potential in the neutron generator and produce bremsstrahlung x-rays upon interaction with structural materials [92]. The V-shaped beam target is surrounded by a shroud electrode biased to a slightly higher voltage in order to prevent x-ray production by collecting the back-streaming electrons.

The neutron output of the Brown DD108 source was measured over a wide range of operating parameters by the vendor. The measured neutron yield as a function of acceleration voltage is shown in Fig. 3.3 for three different levels of power delivered to the deuterium plasma by the magnetron. An order of magnitude of dynamic range in neutron yield can be obtained by adjusting the acceleration high voltage. The increase in neutron flux is due to the increasing cross-section of the D-D reaction with deuterium ion energy. The acceleration current, a measure of the number of deuterium ions on target, remains constant as the acceleration voltage is increased.

Pulsing of the neutron output is achieved by deuterium ion source control. Magnetron operation is pulsed for fine adjustment of neutron bunch width using a TTL control signal. The pulse width and frequency can be arbitrarily varied to achieve the desired yield and time profile subject to the nominal minimum pulse width of 100 μs. The measured neutron yield and acceleration current is shown in Fig. 3.4 as a function of duty cycle for three distinct pulse width modes. In contrast to Fig. 3.3, the acceleration current scales linearly with increasing duty cycle tracking the measured neutron flux.

The neutron flux and acceleration current are shown as a function of deuterium plasma pressure in Fig. 3.5. The maximum neutron yield is achieved at a plasma pressure of $\sim$5 mTorr. There

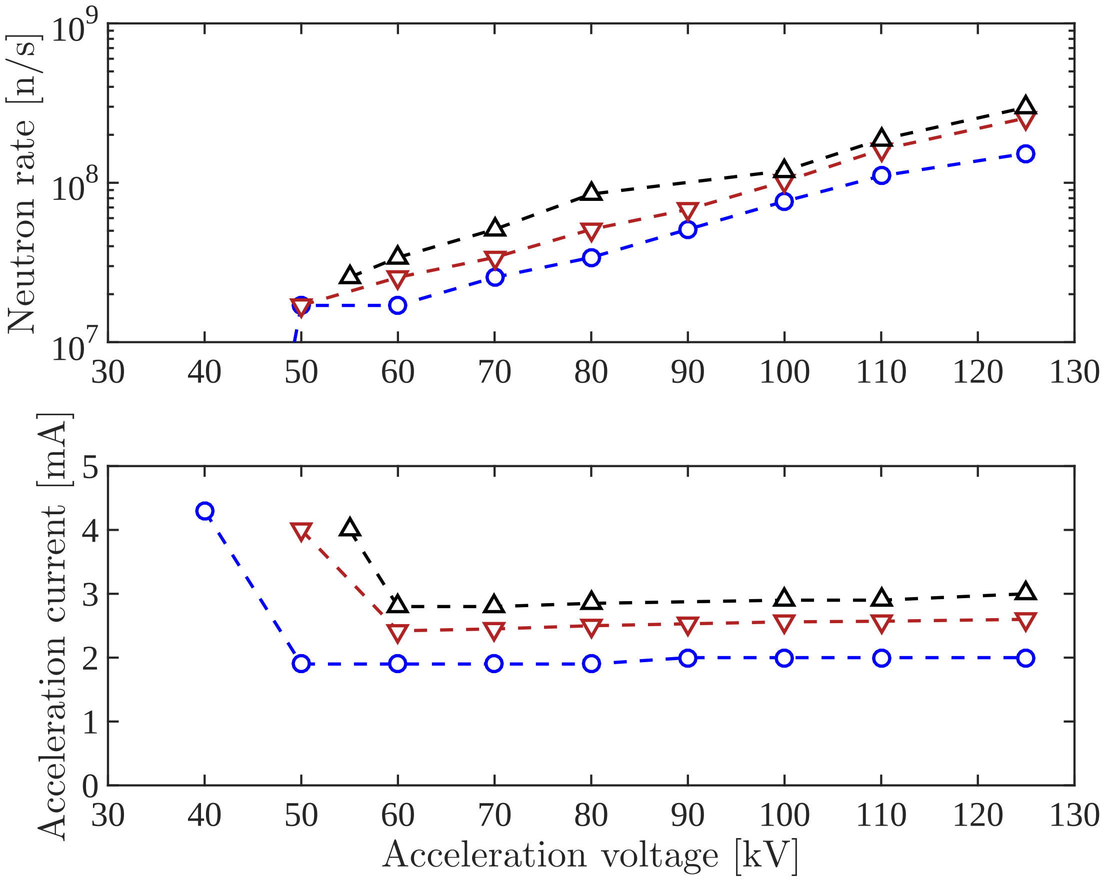

Figure 3.3: The measured neutron yield vs. acceleration voltage for the Brown DD108 neutron generator. The blue (◯), red (▽), and black (△) curves represent data collected with the magnetron delivering 273.6 W, 376 W, and 496 W, respectively, to the deuterium plasma. The neutron rate shown in blue drops off scale at 40 kV in the top frame to 0 n/s. Data provided by Adelphi Technology, Inc. and produced here with permission [93]. We estimate a factor of ~2 uncertainty on the total neutron rate.

are fewer available deuterium ions at lower plasma pressures, which reduces the neutron flux. At higher plasma pressures, the fraction of singly ionized molecular deuterium molecules (primarily $^2D^+$ and $^3D^+$) increases. The energy provided by the acceleration potential is split between the atoms in molecular deuterium projectiles incident upon the target. On average, the reduced energy per deuterium atom provides a lower cross-section for the nuclear D-D reaction and results in a lower neutron flux.

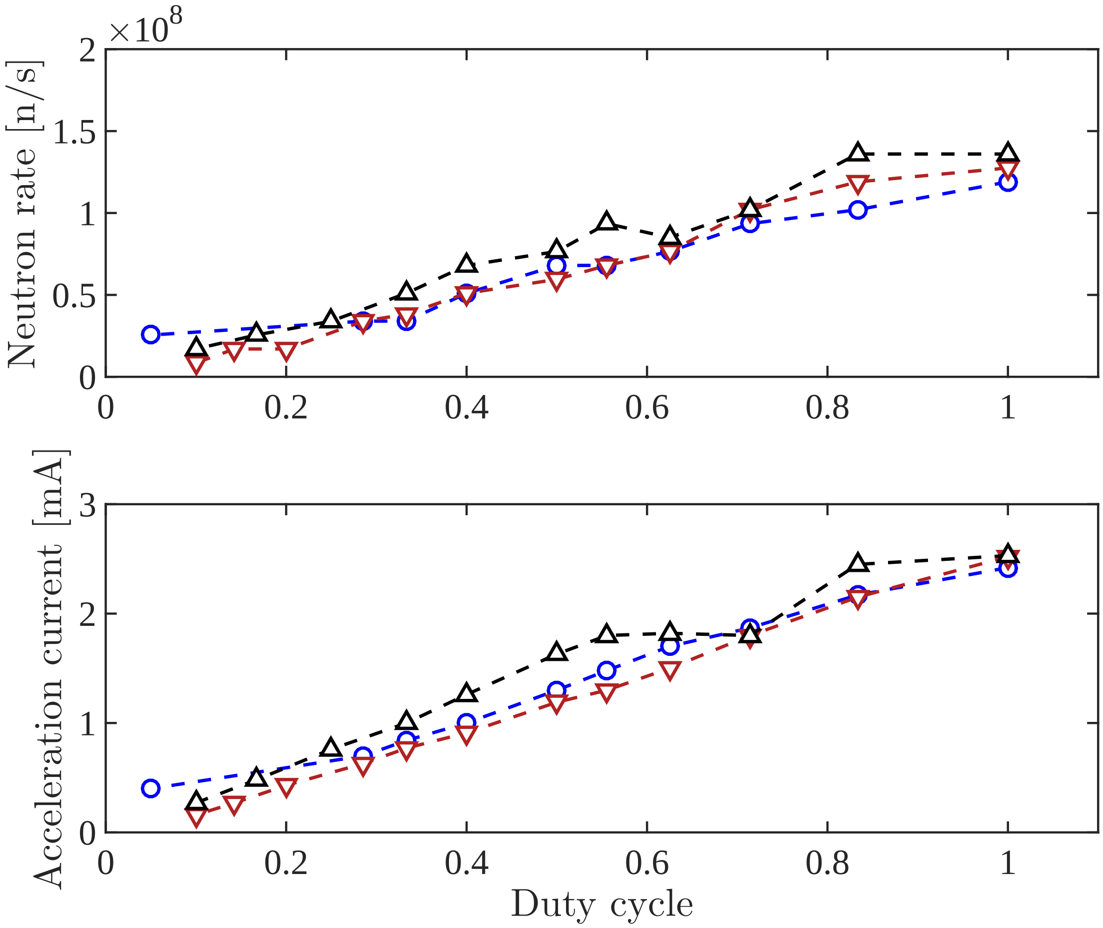

Figure 3.4: The measured neutron yield vs. duty cycle during pulsed operation for the Brown DD108 neutron generator. The blue (◯), red (▽), and black (△) curves represent magnetron pulse widths of 5 ms, 1 ms, and 100 us, respectively. The other operating parameters were held approximately constant: $V_{\mathrm{HV}} = 100$ kV, $I_m = 70$ mA. Data provided by Adelphi Technology, Inc. and produced here with permission [93]. We estimate a factor of ∼2 uncertainty on the total neutron rate.

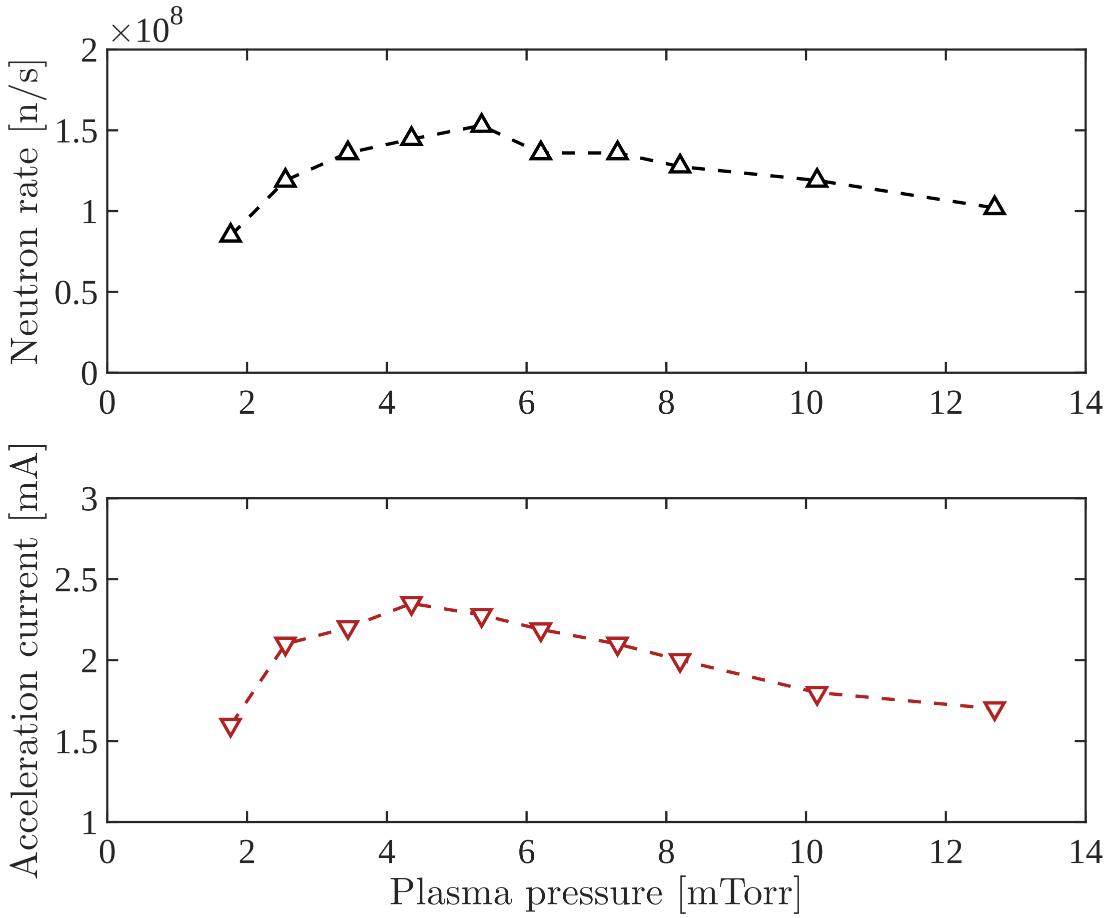

Figure 3.5: The measured neutron yield vs. plasma pressure for the Brown DD108 neutron generator. The black ($\triangle$) curve in the top frame shows the measured neutron flux as a function of plasma pressure. The red ($\bigtriangledown$) curve in the bottom frame shows the corresponding acceleration current. Data provided by Adelphi Technology, Inc. and produced here with permission [93]. We estimate a factor of $\sim$2 uncertainty on the total neutron rate.

3.2 Time-of-flight experimental setup

The ToF experimental setup shown in Fig. 3.6 was used to assay the energy spectrum of neutrons produced by the DD108 neutron generator.[1] A similar experimental configuration has been used by others for studies of the NaI(Tl) nuclear recoil quenching factor [94, 95].

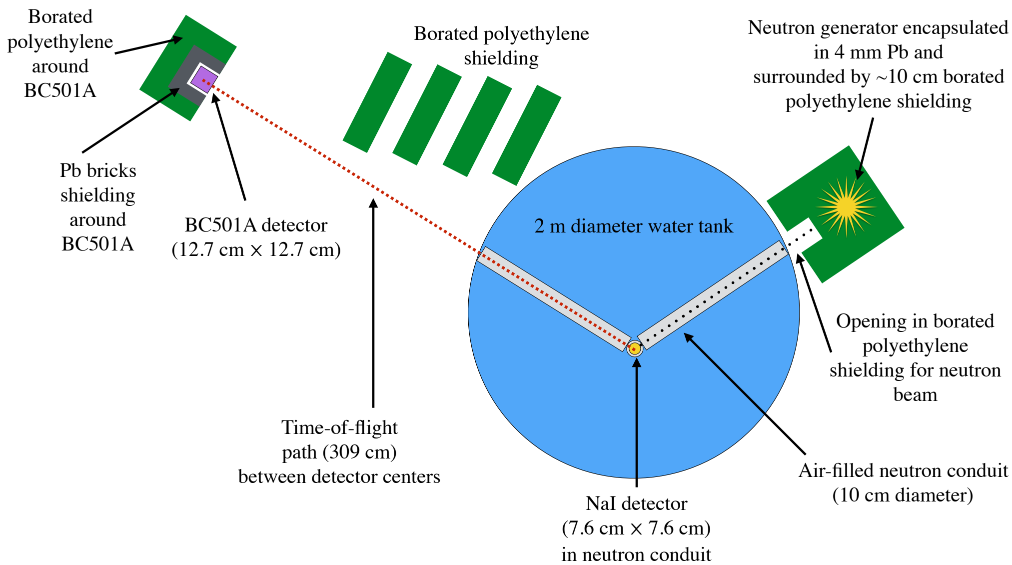

Figure 3.6: The experimental setup for the neutron time-of-flight (ToF) measurement performed at Brown University. The DD108 is shown at right encapsulated in borated polyethylene (green). The angled neutron collimation tube is depicted in gray inside the 2 m diameter water tank, with the 7.6 cm NaI(Tl) detector at the vertex. The far BC501A detector is shown in purple with surrounding Pb and borated polyethylene shielding. The incident neutrons from the generator accepted by the collimation path are represented by the black dotted line, and the 3 m ToF measurement path is shown by the red dashed line.

The neutron generator was encapsulated in $\sim$10 cm of borated polyethylene shielding with an opening to provide a beam of unmoderated neutrons. A 4 mm-thick Pb sheet was used to suppress bremsstrahlung x-rays produced by the device. A 10 cm diameter air-filled conduit was submerged in a 2 m diameter water tank and provided a kinked collimation path subtending an angle of 114°. This angled air-filled conduit enforced a scattering angle of $66 \pm 4°$ for neutrons following the collimation path through the water tank. A 7.6 cm diameter, 7.6 cm tall NaI(Tl) detector (Ludlum 44-20) was

[1]The experimental setup was constructed in part by Max Genecov, Soumya Ghosh, and Alexander Moskowitz during the summer of 2013. The opportunity for these undergraduates to participate in this research was made possible by the UTRA program at Brown University.

installed inside the vertex of the air-filled conduit to provide a t_0 for the ToF measurement. The water tank also functioned to reduce accidental coincidence backgrounds by shielding the NaI(Tl) detector from ambient gamma rays. A Bicron 501A (BC501A) liquid scintillator (12.7 cm diameter, 12.7 cm height) detector was placed in line with the second leg of the collimation path.

The average ToF path was measured to be 309 ± 4 cm from the center of the NaI(Tl) detector to the center of the BC501A. Coincident events in the NaI(Tl) and BC501A detectors were used to characterize the energy spectrum of neutrons produced by the DD108 by measuring the particle ToF between the two detectors. The BC501A was positioned to ensure >1 m of water shielding between the DD108 and BC501A to suppress accidental coincidences due to line-of-sight neutrons from the generator interacting in the far detector. The face of the BC501A detector in line with the beam path was left unshielded to increase the efficiency of detection of neutrons from the true ToF path. All other sides of the BC501A detector were shielded by ~5 cm of Pb to reduce the accidental coincidence rate from ambient gamma rays interacting in the BC501A. A ~5 cm layer of borated polyethylene was constructed outside of the BC501A Pb shield to reduce the false coincidence rate produced by unwanted neutron shine off passive surfaces in the room.

The ideal signal events consist of a neutron leaving the neutron generator, scattering once in the NaI(Tl) detector, and then scattering in the far BC501A detector without scattering in passive materials during the journey. The deposited energy from neutron scatters off Na in the NaI(Tl) detector is given by Eq. 1.1, where m_A is atomic mass of Na. The neutron velocity is obtained by measuring the ToF between the NaI(Tl) and BC501A detectors. The energy of each neutron can be directly determined from its velocity as $E_{n,\mathrm{meas}} = 1/2mv^2$. Neutrons with the nominal expected mean energy for our experimental setup of 2.45 MeV are non-relativistic, traveling at 7% the speed of light. It takes these neutrons 46 ns to travel 1 m. The measured neutron energy using ToF between the two detectors, $E_{n,\mathrm{meas}}$, is lower than the energy of the neutron incident on the NaI(Tl) detector, E_n, due to the energy deposited in the NaI(Tl). Eq. 1.2, Eq. 3.1, and Eq. 3.2 are used to account for the lost recoil energy assuming Na recoils, $E_{\mathrm{nr,Na}}$, and reconstruct E_n given $E_{n,\mathrm{meas}}$:

$$E_n = E_{n,\mathrm{meas}} + E_{\mathrm{nr,Na}}\,. \tag{3.1}$$

The true measured incident energy is given by

$$E_n = \frac{E_{n,\mathrm{meas}}}{1-\zeta}\,, \tag{3.2}$$

where m_A is the atomic mass of Na and ζ is given in Eq. 1.2. Events due to neutrons that scatter multiple times in the NaI(Tl) crystal contribute to a featureless ToF background that does not affect the determination of the single-scatter peak parameters [94, 95]. The experimental setup was not sensitive to elastic iodine recoils in the NaI(Tl) detector due to the lower energy transfer to these nuclei as expected from Eq. 1.1 and the lower nuclear recoil yield for iodine. There are several inelastic recoil modes for iodine, only one of which remains after the analysis cuts described in Sec. 3.3. The remaining mode is $^{127}\mathrm{I}(\mathrm{n},\mathrm{n}'\gamma)$ producing a 57.6 keV gamma ray also seen in Ref. [95].

The DAQ setup is shown in Fig. 3.7. The PMTs in the NaI(Tl) and BC501A detectors were biased to 1.1 kV and -1.2 kV, respectively. After $\times 10$ amplification, the NaI(Tl) and BC501A signals were digitized at 1 GHz using an 8 bit Lecroy LT583 oscilloscope in sequence mode. The reported pulse heights and pulse areas for all plots are in terms of the signal seen at the digitizer. The NaI(Tl) signal was digitized on Ch1 and Ch3, while the BC501A signal was digitized on Ch2 and Ch4. The dynamic ranges of Ch1 and Ch2 were independently tuned to be optimal based on the observed signal sizes in both detectors. Ch3 and Ch4 provided an alternative dynamic range for both detectors to allow greater flexibility in recorded signal size and voltage resolution given the 8 bit digitizer. The analysis did not require the use of Ch3 or Ch4 other than for basic data quality cuts. The scope was externally triggered based upon the overlap coincidence of a 400 ns gate pulse from the NaI(Tl) and a 200 ns gate pulse from the BC501A. A discriminator was used to set hardware thresholds of $\sim$20 mV and $\sim$150 mV for the NaI(Tl) and BC501A signals, respectively, for the signal heights as measured at the digitizer. Each sequence of 50 triggers was pulled from the oscilloscope

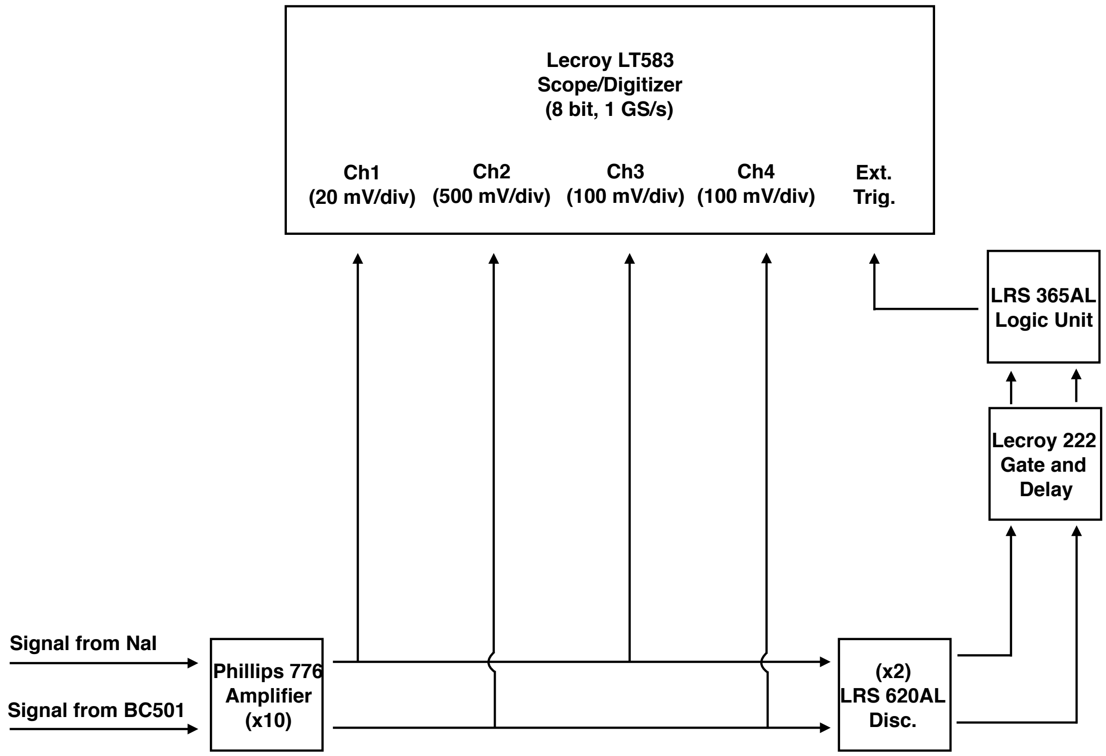

Figure 3.7: A diagram of the data acquisition logic and digitizers used for the neutron time-of-flight measurement. The signals from the NaI(Tl) and BC501A detectors were both digitized in two separate channels with alternative dynamic range. Ch3 and Ch4 were only used for data quality cuts.

to a control computer via Ethernet and saved to disk. This coincidence setup provides a trigger regardless of signal arrival order from the two detectors, which allows verification of the expected flat accidental coincidence background. The data taking parameters are listed in Table 3.1.

3.3 Measurement of the neutron time-of-flight spectrum

We provide a detailed overview of the analysis process and report results for Target orientation A in Sec. 3.3.1. The same analysis process is repeated for Target orientation B, and the results are summarized in Sec. 3.3.2. Identical cuts and algorithms were used for the analysis of datasets for both DD108 target orientations.[2]

[2]The code used for this analysis is located in the Brown Particle Astrophysics Group's GitHub organization [65] with the relative path "brownpa_code/jv_code/neutron_generator_spectrum/".

Table 3.1: The experimental parameters used for neutron time-of-flight data acquisition.

Parameter	Value
NaI(Tl) PMT high-voltage	1.1 kV
BC501A PMT high-voltage	-1.2 kV
NaI(Tl) discriminator threshold	20 mV
BC501A discriminator threshold	150 mV
Signal amplification	$\times 10$
Digitization frequency	1 GHz
Digitization resolution	8 bit

3.3.1 DD108 target orientation A

A total of 2.5×10^5 coincidence triggers were acquired in this configuration and used for the analysis. The t_0 of every NaI(Tl) and BC501A pulse was determined by the point where the pulse rose to 10% of its maximum value. The time difference between the t_0 of the pulses in each coincident event was used to measure the ToF. This is referred to as "raw ToF" in the text. The offset due to pulse shape differences in NaI(Tl) and BC501A was calibrated out using the raw ToF location of the gamma ray coincidence peak. The calibrated time scale is referred to as "corrected ToF."

Basic data quality cuts were applied. A duplicate event cut was applied to remove all instances of duplicated events in the dataset. This cut accepts 98.5% of all acquired events. These rare duplicate events are generated when the acquisition computer pulls the same sequence from the oscilloscope twice because a new memory buffer is not yet full. A cut was applied to ensure the measured t_0 time for the NaI(Tl) signal in Ch1 was within ± 5 ns of that measured for Ch3 to remove events where there was a clear failure of the pulse timing algorithm. This cut accepts 95.8% of all acquired events. Events where the mean or standard deviation of the baseline in any channel is $> 3\sigma$ from the average quantity for that channel are removed. The baseline cut 93.4% of all acquired events. The combination of the duplicate event cut, the pulse timing cut, and the baseline cut has a total acceptance of 84.5% of all acquired events. ToF values of $-1000 < \text{ToF} < 1000$ ns were accepted in the analysis, which covers the 600 ns total coincidence window width in the acquisition logic.

A pulse height cut was applied to ensure pulses from the NaI(Tl) detector were between 30–140 mV, as measured at the oscilloscope. The limits on NaI(Tl) pulse size reduce contamination from background gamma rays while maintaining high efficiency for neutron scatters producing coincident events in both detectors as can be seen in Fig. 3.8. The upper limit on NaI(Tl) pulse size also functions to remove potential events involving multiple neutron scatters in the NaI(Tl) crystal. Neutrons produced by the D-D source that scatter in both the NaI(Tl) and BC501A detectors are visible in the horizontal band at ∼115 ns. Residual background gamma ray events that produce signals in both the NaI(Tl) and BC501A detectors are represented in the horizontal band at roughly -20 ns. The vertical band of accidental coincidences at ∼20 mV is just above the discriminator threshold. The vertical band observed between 80 and 100 mV is produced by 57.6 keV gamma rays from $^{127}\mathrm{I}(\mathrm{n}, \mathrm{n}'\gamma)$ inelastic scatters.

A pulse height cut was applied to ensure pulses from the BC501A detector were between 500 and 3600 mV, as measured at the scope. The cut bounds the BC501A pulse height in Ch2 were set to ensure effective discrimination on the low end while avoiding the saturation on the high end. The raw ToF vs. BC501A pulse pulse height in Ch2 is shown in Fig. 3.9.

The pulse-shape discrimination (PSD) capabilities of the BC501A detector were used to differentiate between neutron and gamma ray events passing all other cuts, with the results shown in Fig. 3.10. The event traces were smoothed using a low-pass Butterworth filter with a cutoff frequency of 50 MHz before determining the area and height of each pulse. The resulting quantities are referred to as filtered area and filtered height. The filtered quantities are used for PSD only.

A Gaussian was fit to the gamma ray coincidence peak obtained after selecting electron recoil events in the BC501A to obtain the t_0 calibration, as shown in Fig. 3.11. The measured raw ToF values are corrected using this calibration of the location of the gamma ray peak and the expected 10.3 ns gamma ray ToF between the NaI and BC501A. The calibration of the ToF scale using gamma ray coincidences corrects for any unwanted time offset between the NaI(Tl) and BC501A channels due to cable lengths, signal delays in electronics, and, most significantly, the variation

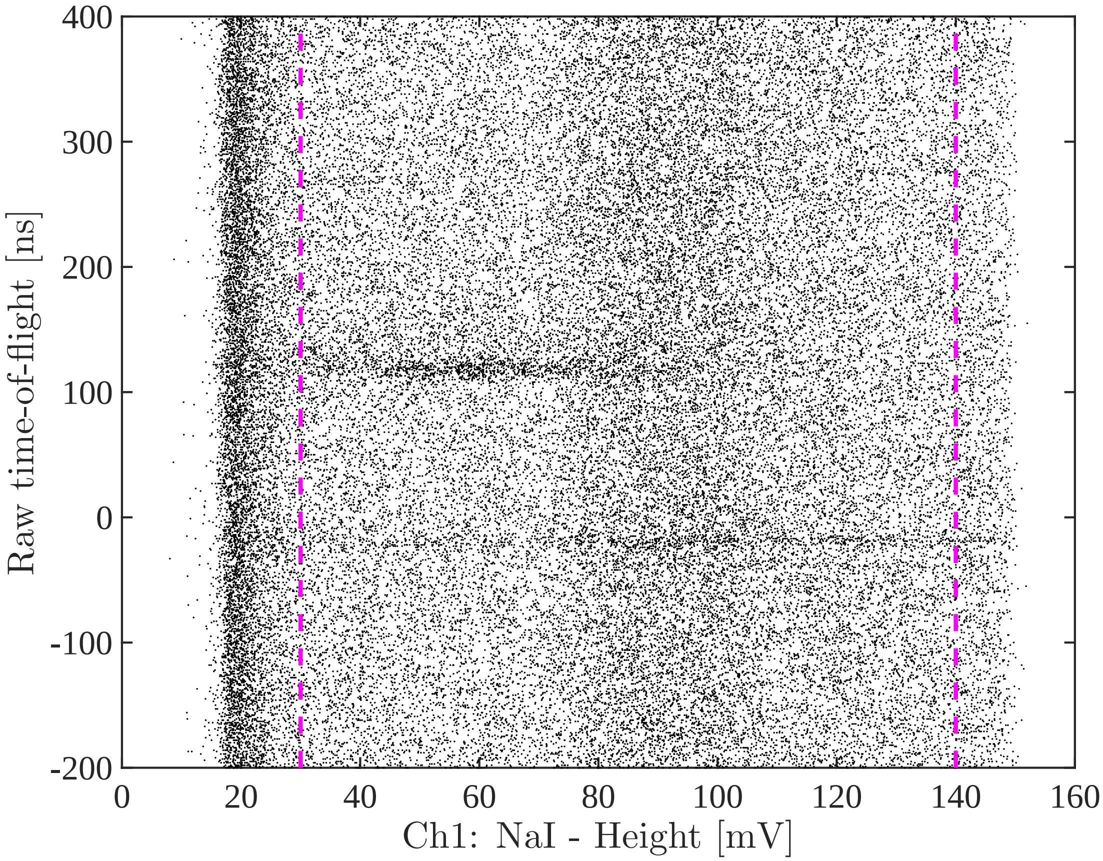

Figure 3.8: Target orientation A. The raw ToF vs. NaI(Tl) pulse height distribution is shown for events passing the area and data quality cuts. The lower and upper analysis thresholds at 30 and 140 mV, respectively, are represented by the vertical dashed magenta lines. This figure is produced before correcting the ToF based upon the known gamma ray propagation time between detectors.

in the algorithmic determination of pulse start time t_0 for the different pulse shapes provided by the NaI(Tl) and BC501A detectors. The measured variance of the gamma ray coincidence peak provides an estimate of the contribution to the intrinsic ToF resolution from detector size, angular acceptance, electronics, and analysis algorithms. The corrected ToF distributions for neutron and gamma ray events are shown in Fig. 3.12.

A non-Gaussian tail at high ToF due to neutron energy loss in passive material has been noted in other similar neutron scattering experiments [94, 95]. To accommodate the expected high ToF tail, the modified Crystal Ball function in Eq. 3.3 was fit to the observed neutron corrected ToF spectrum [96–99]. The Crystal Ball function is a smooth function composed of a Gaussian stitched

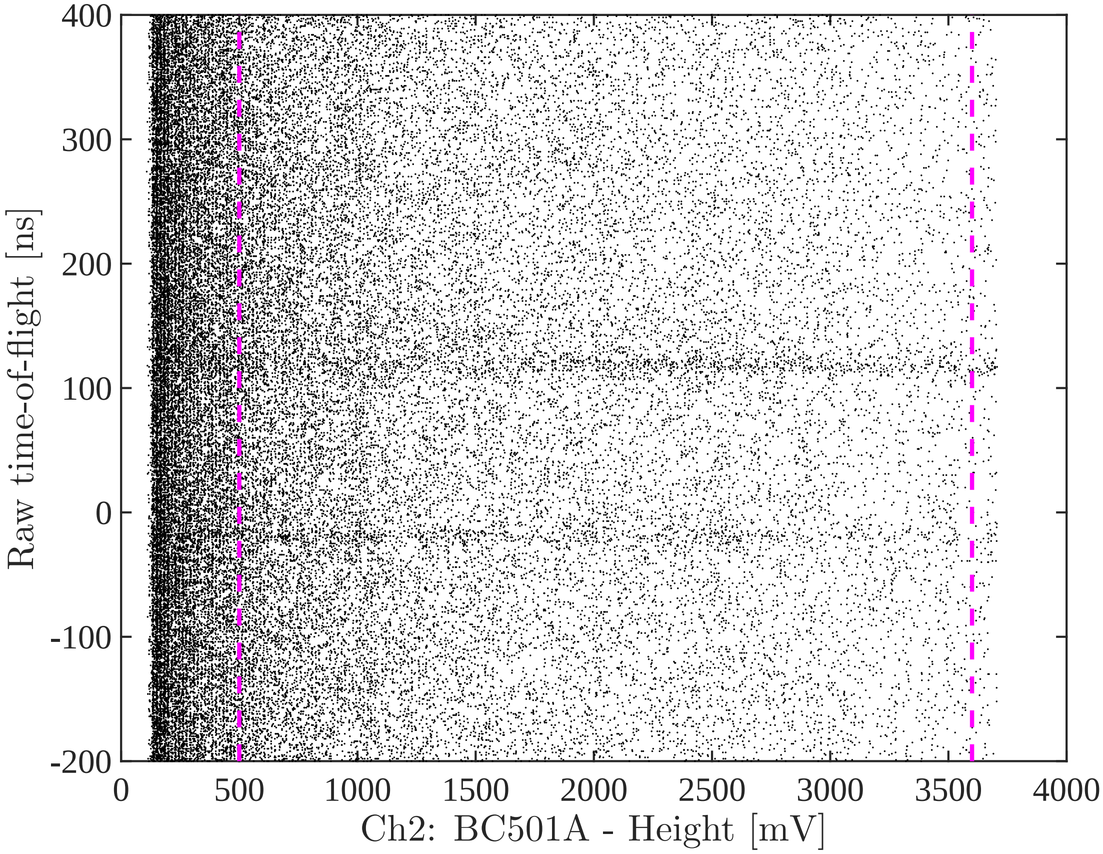

Figure 3.9: Target orientation A. The raw ToF vs. BC501A pulse height distribution for events passing the area and data quality cuts. The lower and upper analysis thresholds at 500 and 3600 mV, respectively, are represented by the vertical dashed magenta lines. This figure is produced before correcting the ToF based upon the known gamma ray propagation time between detectors.

together with a power law tail:

$$y = \begin{cases} N \exp\left[\frac{-(x-\mu)^2}{2\sigma^2}\right] + C\,, & \text{if } \frac{x-\mu}{\sigma} < -\alpha\,, \\ \\ N \frac{\left(\frac{n}{|\alpha|}\right)^n \exp\left(\frac{-\alpha^2}{2}\right)}{\left(\frac{n}{|\alpha|} - |\alpha| + \frac{x-\mu}{\sigma}\right)^n} + C\,, & \text{if } \frac{x-\mu}{\sigma} \geq -\alpha\,. \end{cases} \tag{3.3}$$

We modified the signs and inequalities to produce a tail at high ToF, rather than low ToF. The Gaussian mean and width are given by μ and σ, respectively. The parameter α controls location of transition from the Gaussian to the power law tail. The parameter n controls the slope of the power law, and N is an arbitrary overall scaling factor. We accommodate the flat accidental coincidence

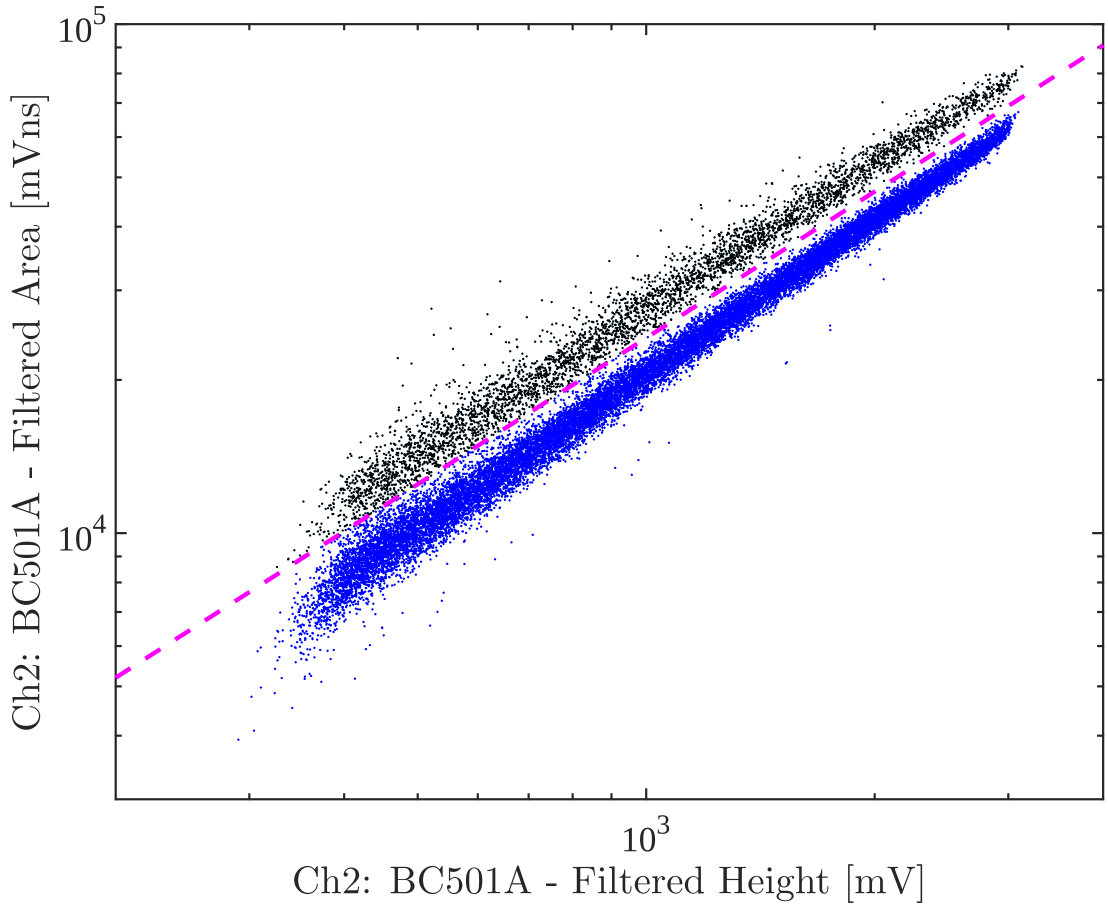

Figure 3.10: Target orientation A. The BC501A discrimination decision boundary in the area vs. height parameter space for events passing all cuts is represented by the dashed magenta line. Gamma ray events are depicted in blue while neutron events are depicted in black. The decision boundary is given by $y = 33x^{0.955}$.

background with the parameter C.

This functional form provides a reproducible, algorithmic determination of the location of the transition between the underlying Gaussian neutron energy spectrum produced by the DD108 and the tail of events at higher corrected ToF. The Gaussian mean and variance parameters in the Crystal Ball function fit shown in Fig. 3.13 were used to characterize the underlying energy spectrum from the DD neutron generator.

The mean neutron corrected ToF was measured to be 148.2 ± 0.4 ns with a resolution (σ/μ) of 3%. Eq. 3.2 combined with $E_{n,\text{meas}} = 1/2mv^2$ provides a mean neutron energy produced by the D-D source of 2.401 ± 0.012 (stat) ± 0.060 (sys) MeV. The total systematic uncertainty has contributions

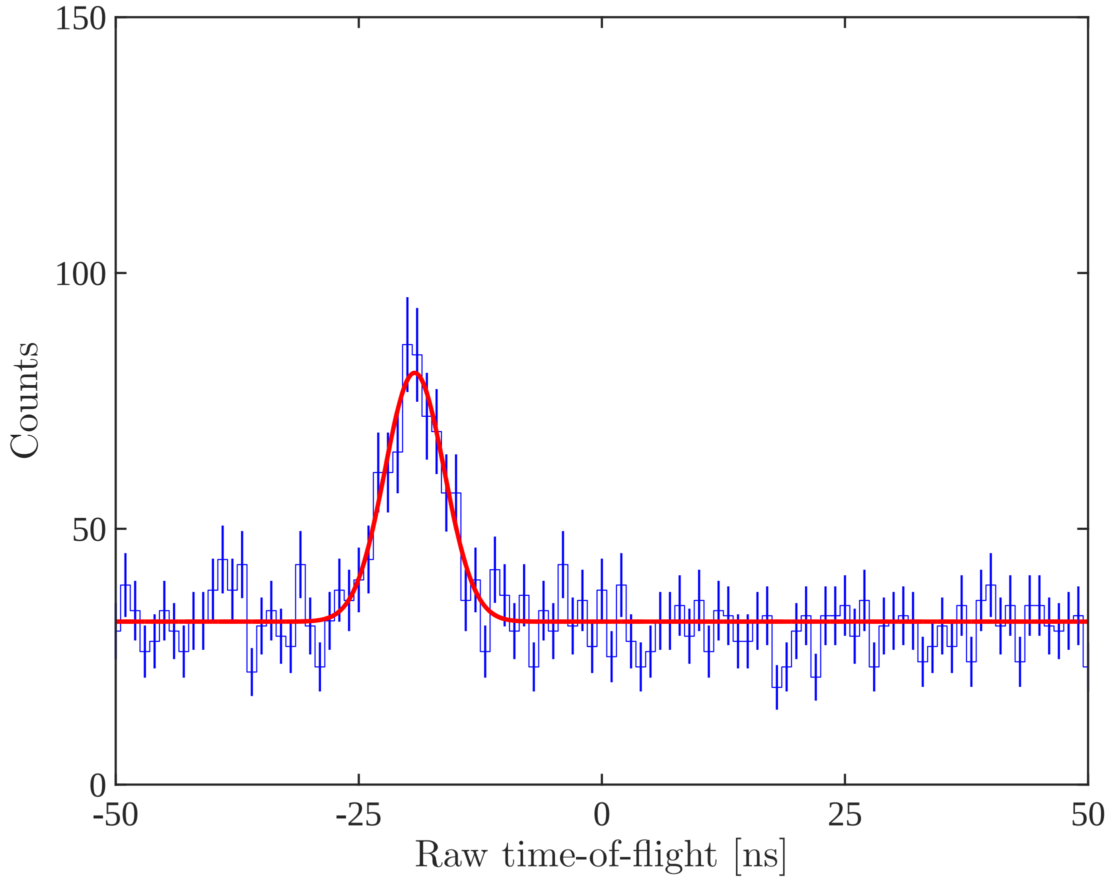

Figure 3.11: Target orientation A. The Gaussian fit to the gamma ray ToF spectrum is indicated by the solid red line. The gamma ray ToF was measured to be -19.3 $\pm$ 0.3 ns with a measured sigma of 3.1 $\pm$ 0.3 ns. Uncertainties are statistical. The fit region has χ^2/dof = 83.9/95 yielding a p-value of 0.78. Bins at the extremes of the fit domain with an expectation of fewer than 10 counts were combined when calculating χ^2.

from the uncertainties in the propagation distance between the detectors, the fixed angle of scatter, the angular acceptance of the collimation tubes, and most significantly the finite detector size and position. The systematic uncertainty due to the choice of several analysis parameters was estimated by varying these parameters and repeating the analysis. The systematic uncertainty due to the choice histogram bin width was estimated by repeating the analysis using 2 ns wide bins instead of the default 1 ns wide bins. The systematic uncertainty due to the choice of fit region was estimated by expanding the neutron ToF fit region from 100–250 ns to 50–300 ns. The systematic uncertainty due to position of the 140 mV NaI(Tl) pulse height cut was estimated by repeating the analysis using an upper pulse height cut of 80 mV/ns. This alternative upper NaI(Tl) pulse height cut was

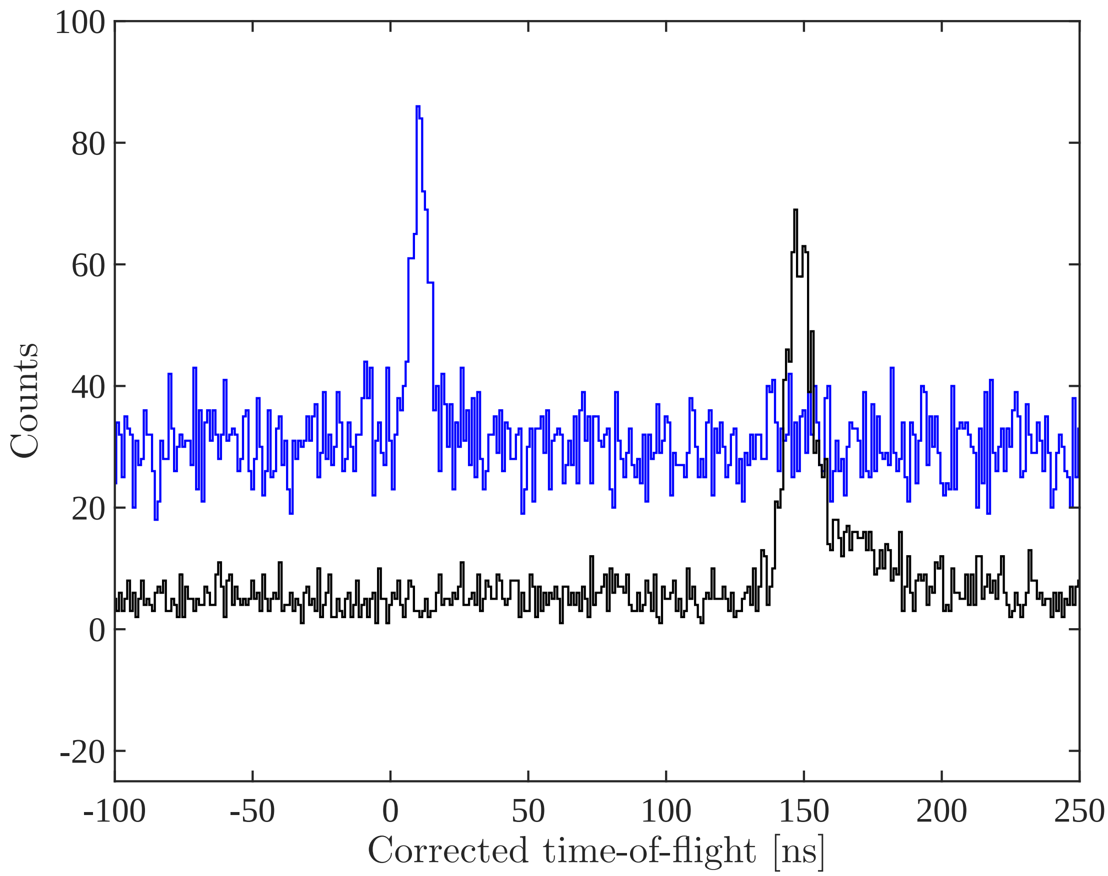

Figure 3.12: Target orientation A. The individual ToF spectra for gamma ray (blue) and neutron (black) events passing all cuts are shown as selected in Fig. 3.11. The ToF axis has been calibrated using the Gaussian fit to the gamma ray peak and the known gamma ray propagation time of 10.3 ns between detectors.

chosen to remove the majority of $^{127}\mathrm{I}(\mathrm{n}, \mathrm{n}'\gamma)$ events. All uncertainties are reported in Table 3.2.

The measured variance of the gamma ray ToF distribution shown in Fig. 3.11 provides an estimate of the contribution from our our experimental setup to the observed resolution. This experimental contribution was subtracted from the neutron ToF distribution variance to provide the most accurate determination of the intrinsic variance of the neutron energy distribution produced by the DD108. The fit determination of α, the transition between Gaussian and power law tail, in the Crystal Ball function is correlated with the parameter estimate of σ, the standard deviation of the Gaussian component. The additional uncertainty due to this correlation is included in the reported statistical uncertainty for σ. The standard deviation of the energy distribution of neutrons produced by the

Table 3.2: Target orientation A. The statistical and systematic uncertainties on the mean energy of neutrons produced by the DD108 neutron generator are shown in columns two and three, respectively.

Source of Uncertainty	Statistical [%]	Systematic [%]
n and γ peak fits	0.5	-
Detector position	-	2.4
Scattering angle	-	0.5
Choice of bin width	-	0.6
Choice of fit region	-	0.02
NaI(Tl) upper area cut	-	0.04
Total	0.5	2.5

Table 3.3: Target orientation A. The statistical and systematic uncertainties on the standard deviation of the neutron energy distribution produced by the DD108 neutron generator are shown in columns two and three, respectively.

Source of Uncertainty	Statistical [%]	Systematic [%]
n and γ peak fits	13	-
Detector position	-	2.4
Scattering angle	-	0.5
Choice of bin width	-	7
Choice of fit region	-	1.0
NaI(Tl) upper area cut	-	18
Total	13	19

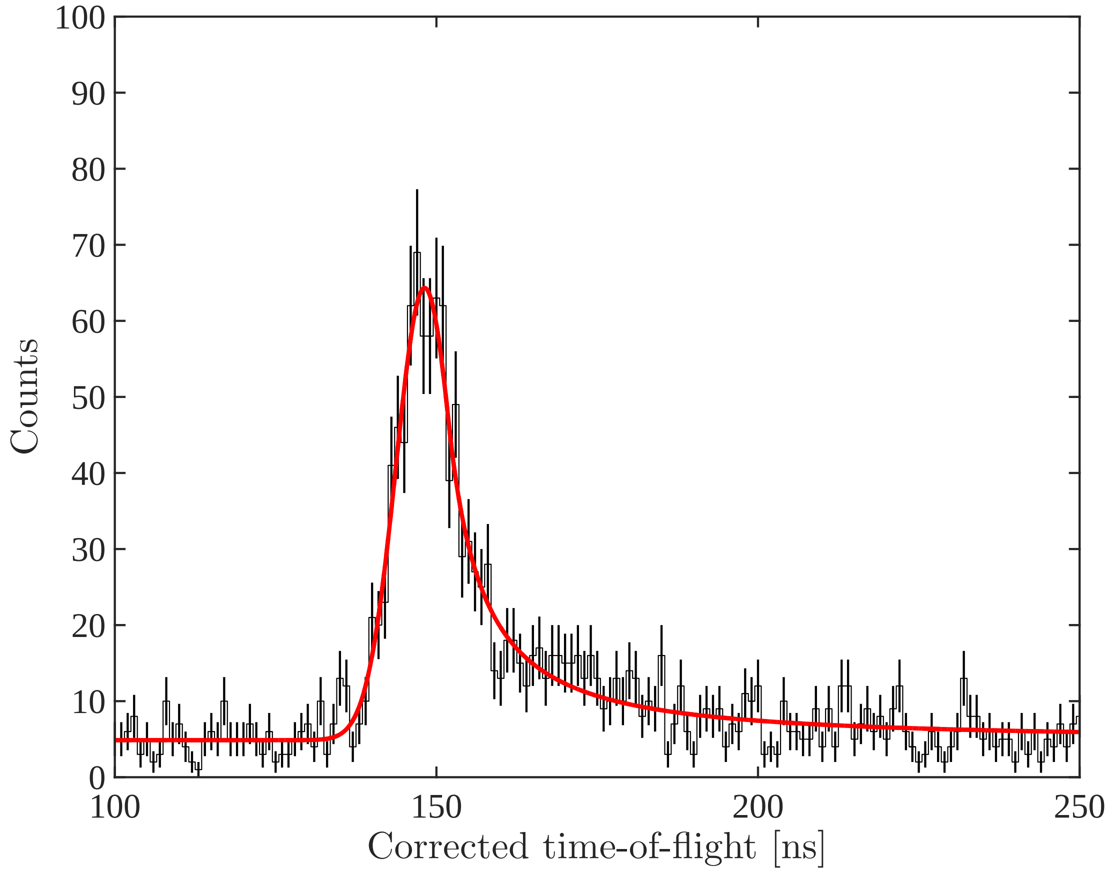

Figure 3.13: Target orientation A. The Crystal Ball function fit to the neutron ToF spectrum is indicated by the solid red line. The fit region has $\chi^2/\text{dof} = 23.7/25$ yielding a p-value of 0.54. Bins at the extremes of the fit domain with an expectation of fewer than 10 counts were combined when calculating χ^2.

DD108 source was measured to be 0.105 ± 0.014 (stat) ± 0.020 (sys) MeV after subtraction of the gamma ray peak variance. The uncertainties are reported in Table 3.3. The corresponding σ/μ of the neutrons produced by the D-D generator is 4.4 ± 0.6 (stat) ± 0.8 (sys) %.

3.3.2 DD108 target orientation B

A total of 5×10^5 coincidence triggers were acquired in this configuration and used for the analysis. The cuts and analysis steps are identical to those in Sec. 3.3.1. The same data quality cuts were applied to the data as used in Sec. 3.3.1. The duplicate event cut, pulse timing verification cut, and baseline cut accept 99.0%, 95.8%, and 94.0% of all acquired events, respectively. The combination of the duplicate event cut, the pulse timing cut, and the baseline cut has a total acceptance of 89.7% of all acquired events.

The equivalent figures containing the ToF vs. NaI pulse height scatter plot, the ToF vs. BC501A pulse height scatter plot, the BC501A discrimination decision boundary, the Gaussian fit to the Gamma spectrum, and the respective gamma ray and neutron corrected ToF spectra are shown in Fig. 3.14, Fig. 3.15, Fig. 3.16, Fig. 3.17, and Fig. 3.18, respectively.

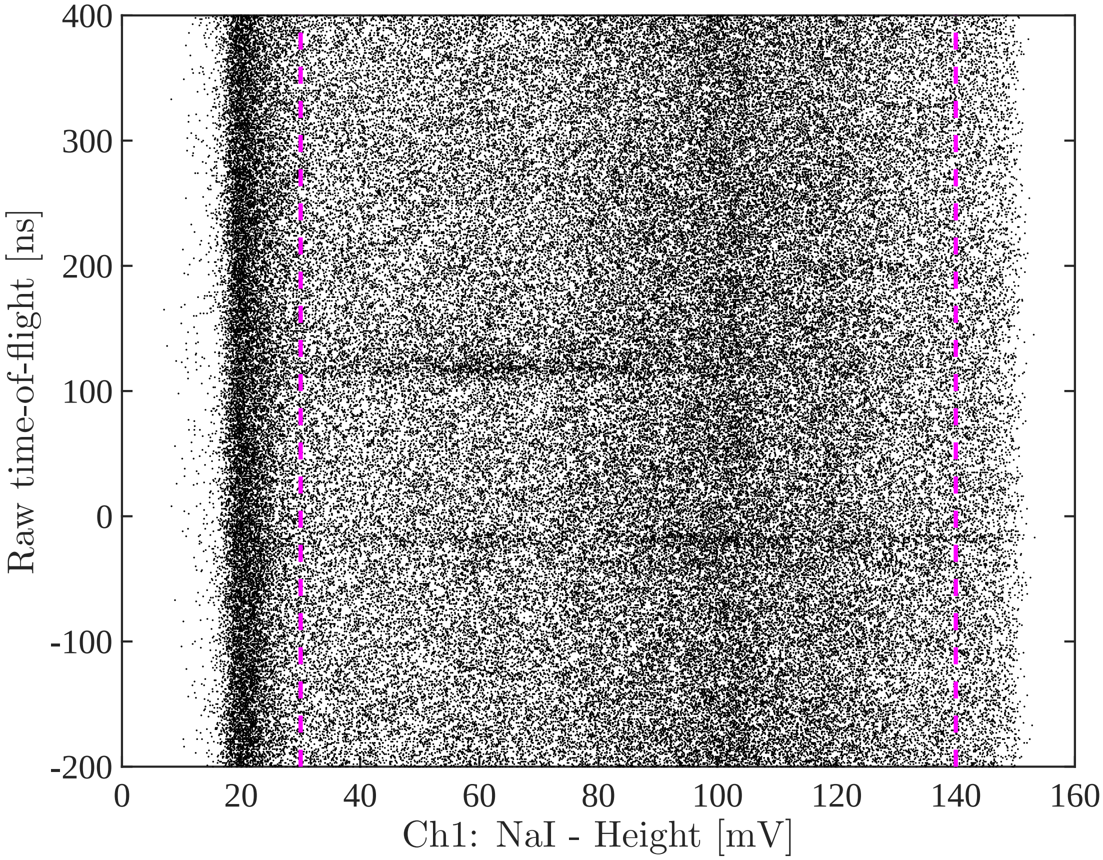

Figure 3.14: Target orientation B. The raw ToF vs. NaI(Tl) pulse height distribution is shown for events passing area and data quality cuts. The lower and upper analysis thresholds at 30 and 140 mV, respectively, are represented by the dashed magenta lines.

The final corrected ToF spectrum for neutron events passing all cuts is shown in Fig. 3.19. The mean neutron corrected ToF was measured to be 147.4 ± 0.4 ns with a resolution of 2.5%. This corresponds to a measured neutron energy of 2.426 $\pm$ 0.013 (stat) $\pm$ 0.08 (sys) MeV incident on the NaI(Tl) detector. The systematic uncertainties are calculated identically to Sec. 3.3.1 and are

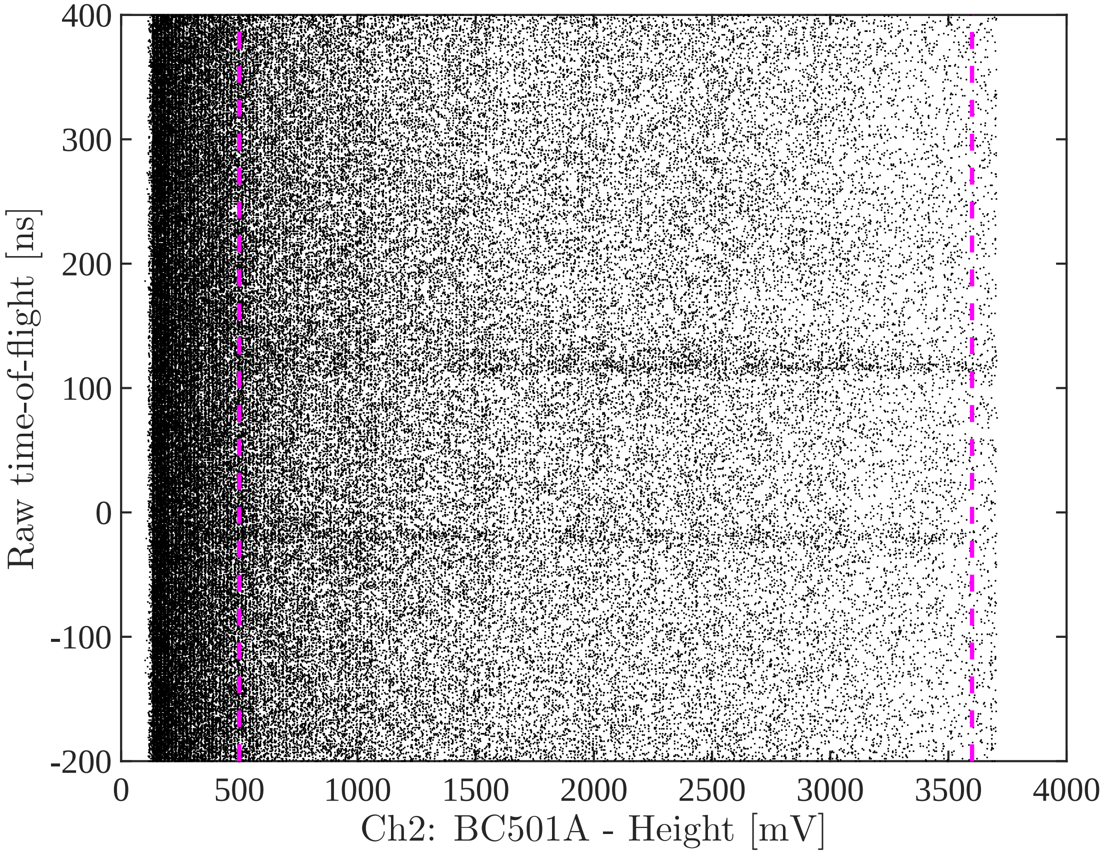

Figure 3.15: Target orientation B. The raw ToF vs. BC501A pulse height distribution for events passing area and data quality cuts. The lower and upper analysis thresholds at 500 and 3600 mV, respectively, are represented by the vertical dashed magenta lines.

shown in Table 3.4. The measured mean of the neutron energy spectrum produced using Target orientation B is in agreement with the value measured using Target orientation A.

The standard deviation of the underlying neutron energy spectrum was again calculated identically as in Sec. 3.3.1. The standard deviation of the energy distribution of neutrons produced by the DD108 source was measured to be 0.067 $\pm$ 0.020 (stat) $\pm$ 0.019 (sys) MeV after subtraction of the gamma ray peak variance. The uncertainties are listed in Table 3.5. This corresponds to a σ/μ of the neutron energies produced by the D-D generator of 2.7 $\pm$ 0.8 (stat) $\pm$ 0.8 (sys) %. The measured width of the neutron energy spectrum produced using Target orientation B is in agreement with the value measured using Target orientation A.

Table 3.4: Target orientation B. The statistical and systematic uncertainties on mean energy of neutrons produced by the DD108 neutron generator are shown in columns two and three, respectively.

Source of Uncertainty	Statistical [%]	Systematic [%]
n and γ peak fits	0.5	-
Detector position	-	2.4
Scattering angle	-	0.5
Choice of bin width	-	0.8
Choice of fit region	-	0.02
NaI(Tl) upper area cut	-	1.8
Total	0.5	3

Table 3.5: Target orientation B. The statistical and systematic uncertainties on the standard deviation of the neutron energy distribution produced by the DD108 neutron generator are shown in columns two and three, respectively.

Source of Uncertainty	Statistical [%]	Systematic [%]
n and γ peak fits	30	-
Detector position	-	2.4
Scattering angle	-	0.5
Choice of bin width	-	13
Choice of fit region	-	0.5
NaI(Tl) upper area cut	-	25
Total	30	28

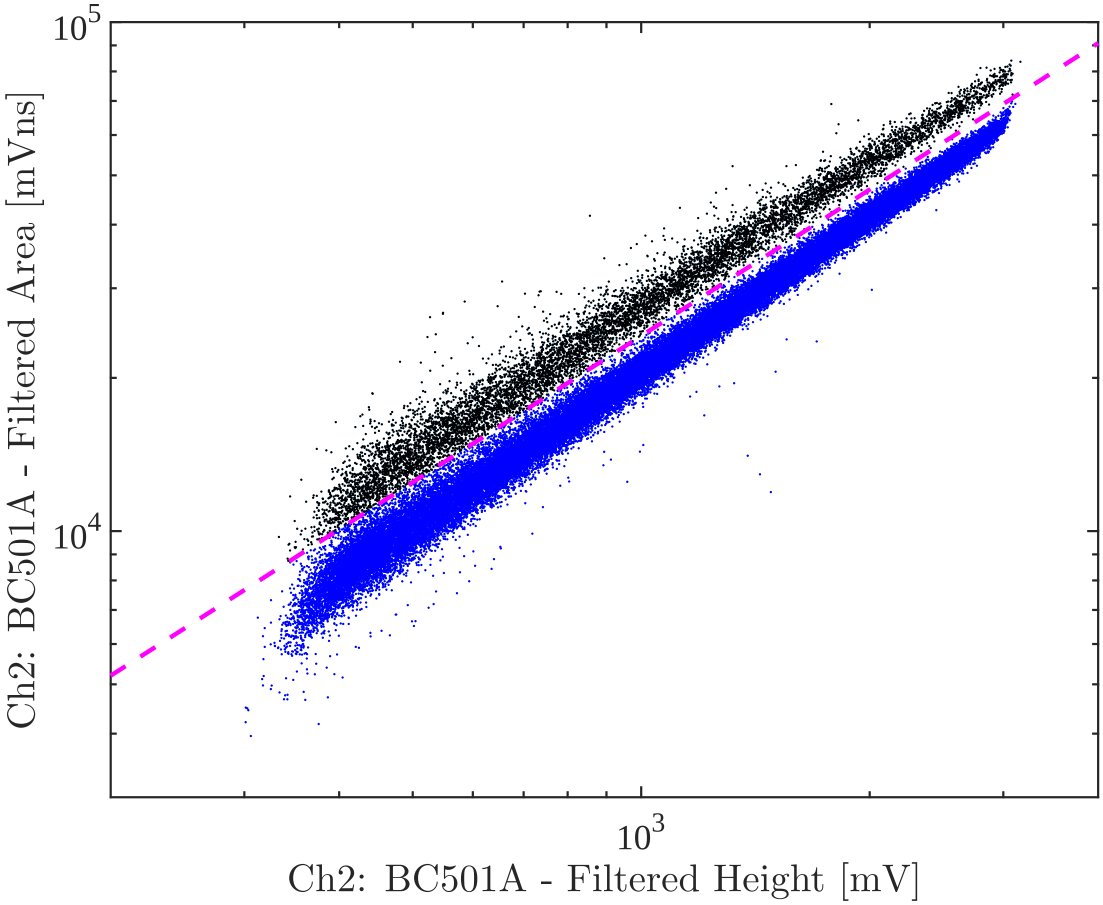

Figure 3.16: Target orientation B. The BC501A discrimination decision boundary in the area vs. height parameter space for events passing all cuts is represented by the dashed magenta line. Gamma ray events are depicted in blue, while neutron events are depicted in black. The decision boundary is given by $y = 33x^{0.955}$.

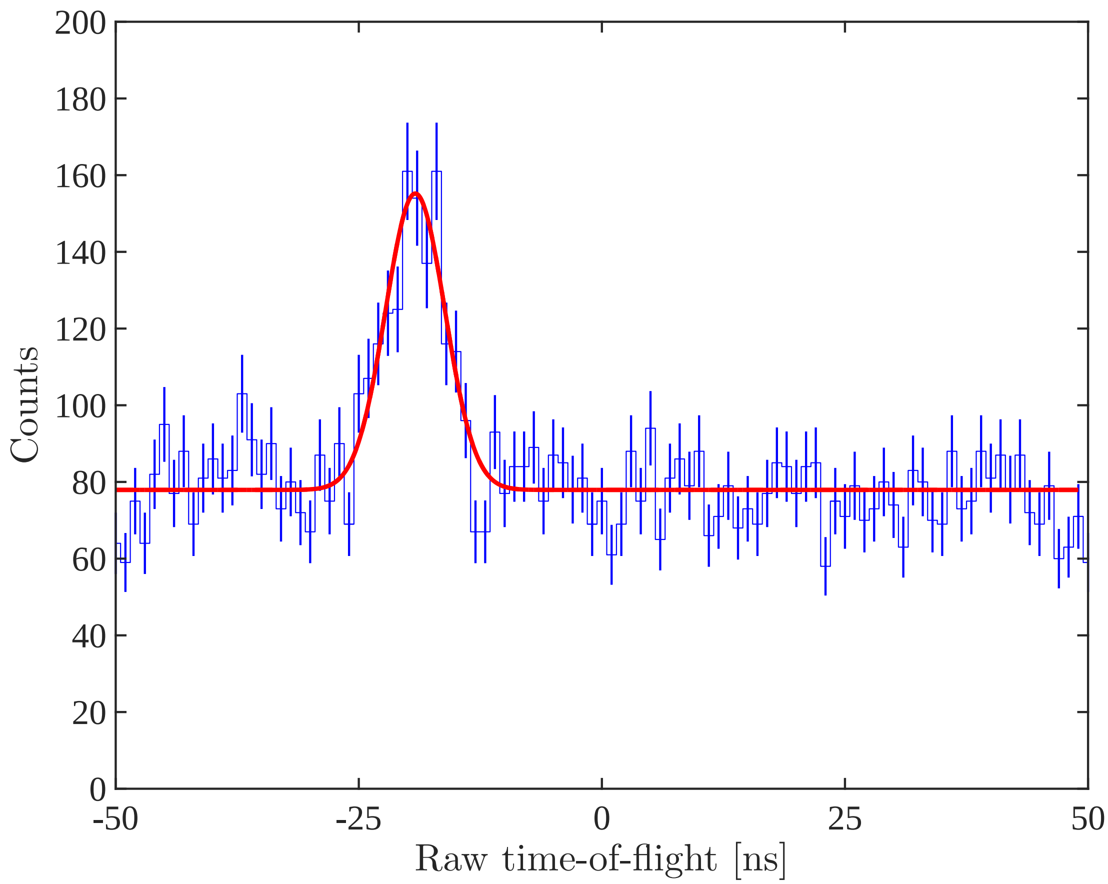

Figure 3.17: Target orientation B. The Gaussian fit to gamma ray ToF spectrum is indicated by the solid red line. The gamma ray ToF was measured to be -19.2 ± 0.3 ns with a measured sigma of 3.1 ± 0.3 ns. Uncertainties are statistical. The fit region has $\chi^2/\text{dof} = 111.2/95$ yielding a p-value of 0.12. Bins at the extremes of the fit domain with an expectation of fewer than 10 counts were combined when calculating χ^2.

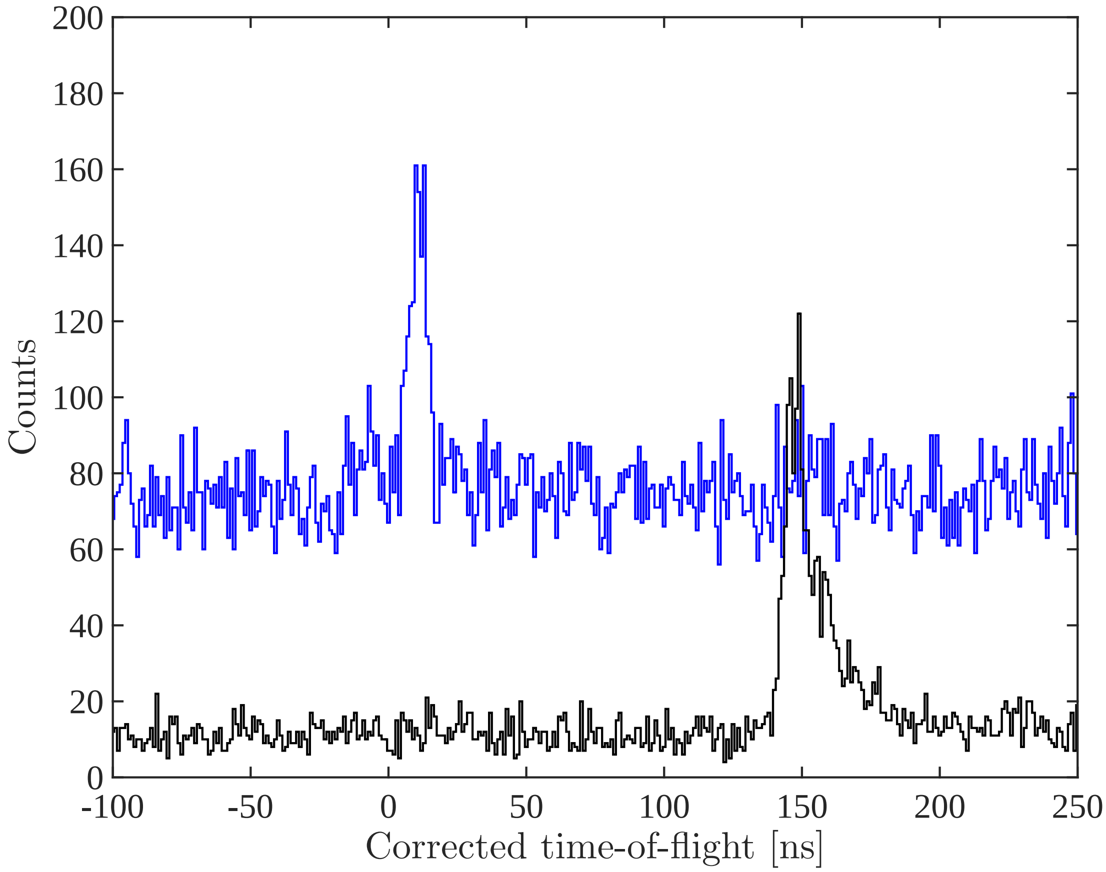

Figure 3.18: Target orientation B. The individual ToF spectra for gamma ray (blue) and neutron (black) events passing all cuts as selected in Fig. 3.17. The ToF axis has been calibrated using the Gaussian fit to the gamma ray peak and the known gamma ray propagation time of 10.3 ns between detectors.

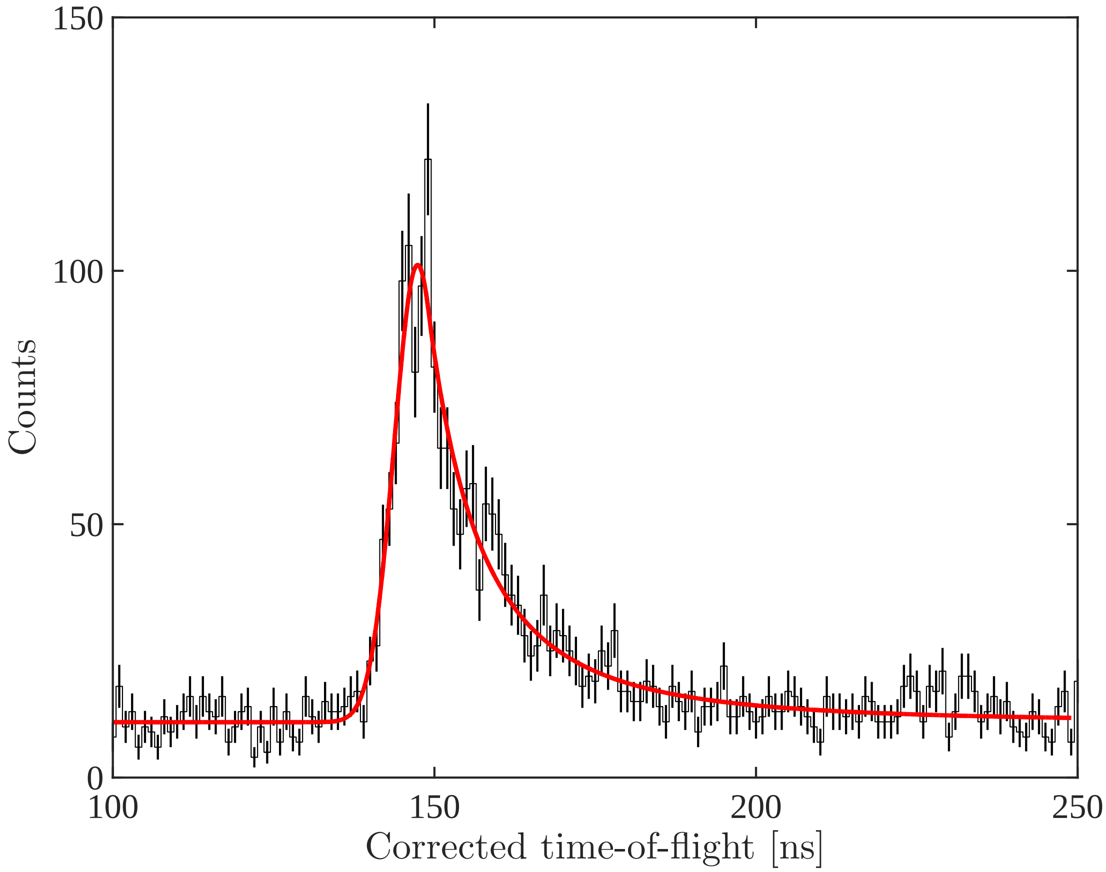

Figure 3.19: Target orientation B. The Crystal Ball function fit to the neutron ToF spectrum is indicated by the solid red line. The fit region has $\chi^2/\text{dof} = 159.3/143$ yielding a p-value of 0.17. Bins at the extremes of the fit domain with an expectation of fewer than 10 counts were combined when calculating χ^2.

Chapter 4

Calibration of the Nuclear Recoil Response of the LUX Detector

This chapter contains a detailed discussion of the D-D source setup used to measure the response of liquid xenon to nuclear recoils in the LUX detector. The new calibration technique proposed in Ch. 1 was used to perform a direct, absolute, *in situ* measurement of the light and charge yields for nuclear recoils. The DD108 neutron generator hardware characterized in Ch. 3 was used for the LUX calibration. We first outline the experimental setup at SURF in Sec. 4.1. An overview of underground operations during the Run03 nuclear recoil calibration is provided in Sec. 4.2. A direct measurement of the neutron generator flux using the same operating conditions used for the LUX calibration is described in Sec. 4.3. Plots of the neutron beam are shown in Sec. 4.4. A detailed description of the LUX nuclear recoil band measurement is provided in Sec. 4.5.

4.1 Experimental setup at SURF

An Adelphi Technology, Inc. DD108 neutron generator was used as the mono-energetic neutron source. It was operated externally to the LUX water tank shield with neutrons being introduced into the LUX detector via a narrow air-filled pipe, which displaced water producing a collimation path.

4.1.1 Neutron conduit infrastructure inside the LUX water tank

An air-filled neutron conduit was suspended from hand winches located in the crawlspace between the top of the LUX water tank and the floor of the upper level in the Davis Cavern. A photograph of the hand winches installed below the floor of the upper level is shown in Fig. 4.1. The neutron conduit was constructed using schedule 80 polyvinyl chloride (PVC). The conduit has a length of 377 cm from endcap-to-endcap as measured during installation and spans the horizontal distance from the outer water tank wall to the outer surface of the LUX cryostat. A summed water-filled gap of 6 cm is present beyond the two ends of the conduit. The inner-diameter (ID) is 4.9 cm and the outer-diameter (OD) is 6.0 cm. The tube has a stainless steel T-bar spine with sides 6.4 cm $\times$ 6.4 cm and 1.3 cm thick. The total length of the stainless steel spine was 298.5 cm. The spine provides ballast as well as a rigid source of support to prevent bowing of the neutron conduit. The distance from the outer tube end to the outer spine end was 35.5 cm and the distance from the inner tube end to the inner spine end was measured to be 45.0 cm. The tube is suspended using two winches attached to fixed floor gratings in the upper Davis Cavern. The support cable is stainless steel wire rope with a diameter of 2.38 mm. All stainless steel components were passivated to prevent corrosion before use in the water tank. A photograph of the neutron conduit raised in line with the LUX cryostat during deployment is shown in Fig. 4.2.[1] The neutron conduit was stored out of line with the TPC during the WIMP search campaign.

[1] A photograph of the inside of the water tank after all commissioning activities were complete was shown in Fig. 2.10.

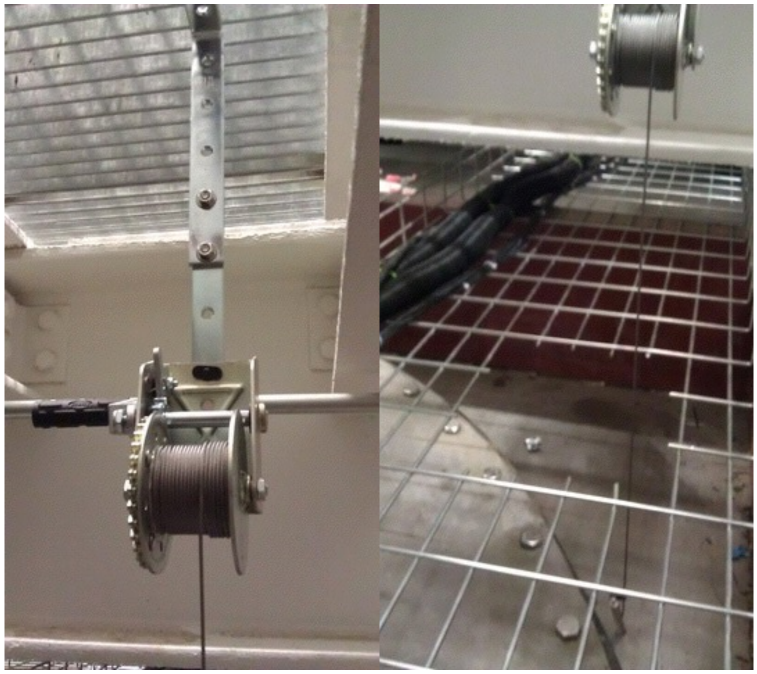

Figure 4.1: A photograph of the two neutron conduit hand winches installed above the LUX water tank in August 2012. The hand winches were mounted to the grated floor of the upper level in the Davis Cavern.

Two vertical PVC guide tubes were attached to the crossbeam of the LUX detector stand. These vertical guide tubes catch the neutron conduit as it is raised in line with the LUX cryostat. The guide tubes restrict the range of potential movement in the conduit due to convection currents in the water tank. In practice, no significant time-varying movement in the conduit occurred as verified by the neutron event rates and shape of the observed beam profile in the detector.

4.1.2 Neutron generator infrastructure outside the LUX water tank

The neutron generator was deployed outside the LUX water tank on the lower level in the Davis Cavern. The details of neutron generation inside the D-D source are described in Sec. 3.1. A photograph of the setup during the commissioning phase before the borated polyethylene shielding was installed is shown in Fig. 4.3. The generator head was mounted on a Genie lift Superlift Advantage SLA-5 to allow adjustment of the vertical and horizontal position of the D-D neutron source. The neutron generator electronics rack containing the high-voltage power supplies, turbopump controller,

Figure 4.2: A photograph of the neutron conduit raised in line with the LUX cryostat in August 2012. This photograph was taken before the installation of the vertical PVC guide tubes and before the water tank was filled. The neutron tube as shown here was raised to the maximum vertical extent allowed by the detector stand crossbeam. The mating between the PVC neutron conduit and the stainless steel T-bar spine is shown. The stainless steel wire rope suspension can be seen between the hose clamps used to secure the conduit to the spine.

pressure readouts, safety interlocks, and computer control interface was installed on scaffolding to accommodate the 2 m-long, 125 kV high-voltage cable connecting the voltage supply to the neutron generator beam target.[2] The 125 kV high-voltage cable was modified by the vendor for a custom connection to the neutron generator beam target. A chiller is located underneath the scaffolding to ensure a sufficient egress path around the neutron generator hardware. The chiller provides active cooling to the beam target, turbopump, magnetron, and plasma chamber by circulating 3M Fluorinert (FC-3283) coolant through these components. During the calibration campaign, the neutron generator was raised into position using the Genie lift and aligned with the beam pipe in the water tank using the procedure described in Sec. 4.2.2.1. A photograph of the neutron generator in the raised position is shown in Fig. 4.4. During calibration operations, a 3 m exclusion zone around the generator assembly was erected using temporary barriers to restrict access behind the LUX water tank. Personnel access to the entire upper level of the Davis Cavern was allowed during D-D source operation. The floor of the upper level in the Davis Cavern was greater than 3 m from the D-D source, satisfying the exclusion distance requirement.

4.1.3 Environmental health and safety

A detailed operations procedure was written to guide use of the DD108 neutron generator for the calibration of the LUX experiment. This document includes procedures for the alignment of the neutron tube in the water tank, lifting the neutron generator into place using the Genie lift, and operating the neutron generator [100]. A number of complementary engineering and administrative controls were developed to ensure safe operation of the neutron generator calibration system.

The primary administrative control is the creation of a 3 m exclusion zone around the generator during underground operation. The exclusion zone mitigates the major radiation, electrical, and mechanical hazards. The neutron generator hardware features several automatic safety interlocks

[2] The high-voltage cable length was kept short to limit the stored power in the cable. This was done to prevent possible high-voltage supply damage in the event of breakdowns in the target chamber. A current limiting high-voltage resistor was later obtained from the vendor to protect the power supply.

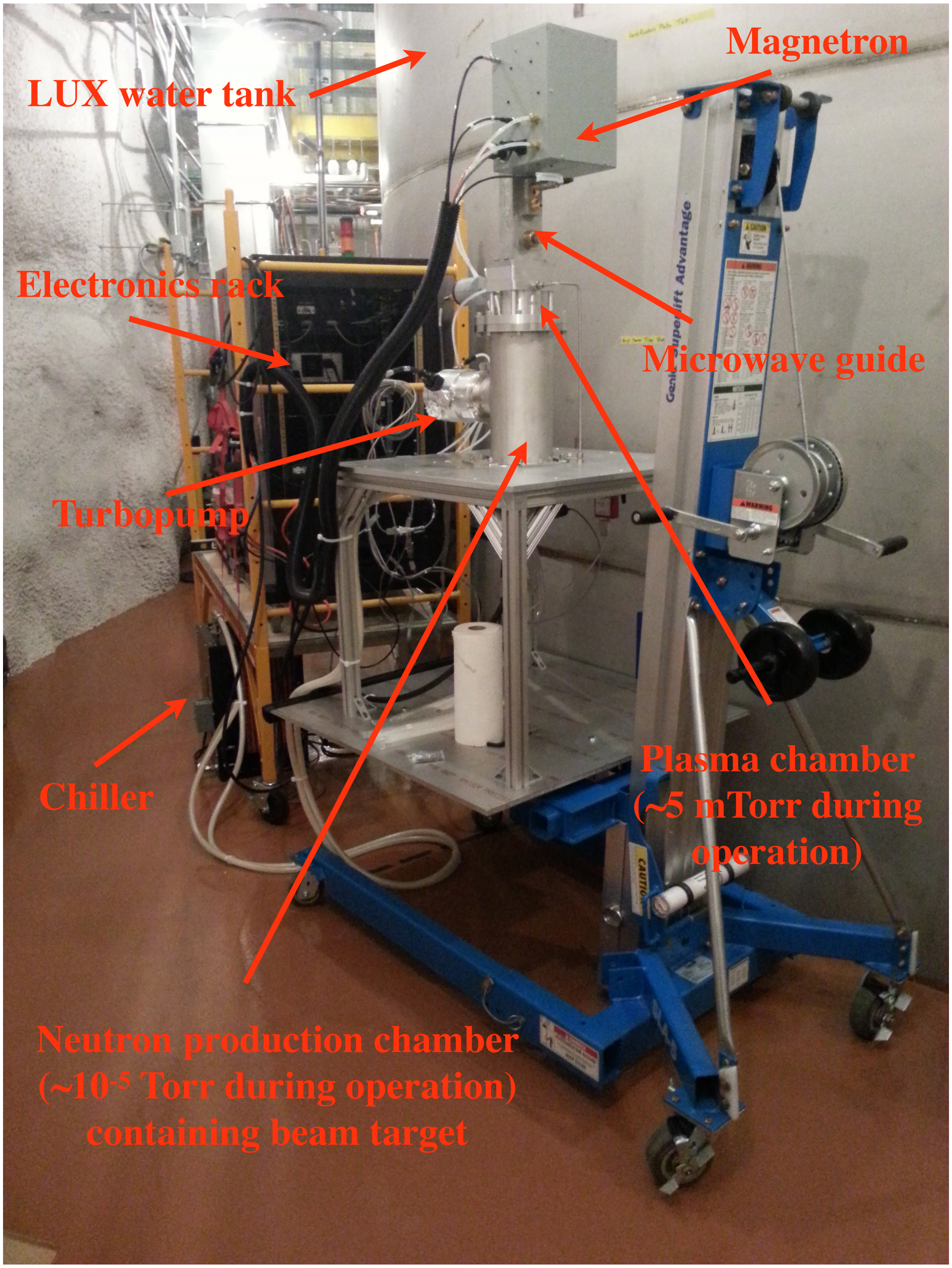

Figure 4.3: A photograph of the neutron generator hardware setup during commissioning at SURF before the borated polyethylene shielding was constructed around the generator head. The Genie lift is in the lowered position. Major components are labeled in red.

Figure 4.4: A photograph of the neutron generator hardware setup during commissioning at SURF after the borated polyethylene shielding was constructed around the generator head. The Genie lift is in the raised position approximately at the height used for the Run03 nuclear recoil calibration. The ethereal figure behind the author is the SURF EH&S manager—a frequent presence during the initial D-D source commissioning.

monitoring the coolant flow, magnetron temperature, and magnetron enclosure door. In addition, there is a personal protection key that must be inserted before high-voltage can be applied. An emergency shutoff switch exists outside of the exclusion zone, which allows immediate shutoff of the neutron generator high-voltage (and thus neutron production) in the event remote communication with the system is lost.

4.1.3.1 Radiation safety

The absorbed dose for any type of radiation is defined as the absorbed energy per unit mass.[3] This has historically been given in units of the rad, which is defined to be 100 ergs/g. The SI unit for the absorbed dose is the gray (Gy), which is defined as 1 J/kg. The relation between these units of absorbed dose is then 1 Gy = 100 rad. The health effects of energy deposition from radiation in living tissue is dependent on the density of energy deposition along the particle track. This density of energy deposition, or linear energy transfer, varies depending upon the type of radiation. This is quantified by defining an energy-dependent quality factor for a given type of radiation. The product of the quality factor and the absorbed dose provides the dose equivalent—allowing a direct comparison of the human dose delivered by various types of radiation. The dose equivalent has historically been given in terms of the unit rem ("radiation equivalent man"), which is defined as the absorbed dose in rad multiplied by the quality factor. The SI unit of dose equivalent is the sievert (Sv), which is defined as the absorbed dose in gray multiplied by the quality factor. The relation between these units of dose equivalent is 1 Sv = 100 rem. As is common in the radiation safety field, we use the units of rem in this thesis to report measured dose equivalent.

The primary safety concern is due to the prompt neutron flux from the neutron generator. The nominal maximum neutron production rate from the D-D source is 10^8 n/s. Under some operating parameters, the neutron production rate can be increased up to $\sim 3 \times 10^8$ n/s (see Ch. 3). This corresponds to a human dose rate of $\sim$300 mrem/hour (3 mSv/hour) at 1 m from the beam target

[3] This paragraph is based upon Ch. 2 of Ref. [10]. More information on units of radiation dose can be found there.

in the center of the assembly—enough to provide a yearly dose of natural radiation exposure in a few hours. A combination of borated polyethylene shielding around the neutron generator head and a physical 3 m exclusion zone was used to reduce the neutron dose in worker accessible areas to below the 2 mrem/hour (20 μSv/hour) limit for general public exposure set by the Nuclear Regulatory Commission (NRC) [101]. Radiation area warning signs were posted before generator neutron production was started to warn unauthorized personnel not to enter the area.

Whenever the operating parameters of the neutron generator were modified, a portable 9 inch diameter Bonner sphere (Ludlum 2241-4) was used to assay the neutron dose rate at a series of predefined locations in the Davis Campus to verify they met the 2 mrem/hour (20 μSv/hour) benchmark. the neutron generator was operated at a much lower flux for the Run03 nuclear recoil calibration as required by LUX detector event rate considerations—around 2.5×10^6 n/s. In practice, the neutron dose rate in worker accessible areas was far below the safety benchmark. An alarmed Ludlum 375 area monitor connected to a Ludlum 42-30H Bonner sphere was installed to continuously report the dose rate outside the 3 m exclusion zone near the neutron generator operator's station.

There are several sources of gamma and x-ray production during a D-D calibration campaign. The dominant reaction producing gamma rays from the source itself is ^{3}H(d, γ)^{4}He. These gamma rays have an energy of 23.84 MeV, but they are suppressed by a factor of $\sim$$10^{-7}$ relative to the neutron production rate [90]. This corresponds to roughly 10 γ/s when operating at the nominal maximum DD108 neutron yield of 10^8 n/s, which is negligible compared to environmental gamma rates from uranium, thorium, and potassium in the cavern [30]. Gamma ray production from neutron capture on materials in the cavern is more significant. Thermal neutron capture on hydrogen (LUX water tank and DD108 shielding) produces 2.22 MeV gamma rays. Borated polyethylene is used as a shielding material due to the high thermal neutron capture cross-section on boron. The ^{10}B(n, α) reaction has a thermal-neutron cross-section of 3840 barns; the resulting ^{7}Li nucleus is left in an excited state 94% of the time leading to the emission of a 0.48 MeV gamma ray [10]. The high capture cross-section of borated polyethylene shielding helps to prevent the spread of thermalized neutrons to other areas of the underground laboratory.

Electrons liberated by ion impacts on the target can back-stream across the 125 kV potential in the neutron generator and produce bremsstrahlung x-rays upon interaction with structural materials [92]. The V-shaped beam target is surrounded by a shroud electrode biased to a slightly higher voltage in order to prevent x-ray production by collecting the back-streaming electrons. A 4 mm thick Pb shield encapsulates the target chamber to reduce residual x-ray production by >99.99%.

The LUX water tank is an effective shield for gamma rays and x-rays produced during generator operation. A gamma ray and x-ray counter was used to assay the dose rate around the exclusion zone while the D-D source was operating at 10^7 n/s. The measured gamma ray and x-ray dose rate during D-D source operation was indistinguishable from the background dose rate of $\sim$10 μrem/hour. This is $\times$200 lower than the NRC general public benchmark of 2 mrem/hour. The background gamma ray rate near the neutron generator within the exclusion zone was measured at various times during the calibration campaign to check for significant neutron activation of materials in the cavern environment—no change in background gamma rates was observed.

The $^2\mathrm{H}(\mathrm{d,p})^3\mathrm{H}$ cross-section is similar to the neutron production cross-section. Tritium production inside the neutron generator was considered from a radiation safety perspective; protection of equipment was also considered. Most tritium is expected to remain embedded in the titanium/copper beam target, but a fraction could escape via the pump exhaust. The neutron generator vendor reported that 7 kBq (200 nCi) of tritium is released from the generator for every 8 hours of operation. The EPA regulation for tritium in drinking water is 20 nCi/liter; a typical office water cooler could contain more tritium than the generator releases in 8 hours [102]. As an additional precaution requested by SURF for both personnel safety and the protection of low-background experiments, the exhaust of the neutron generator pump was vented outside of the laboratory space into the mine drift.

The 2.5 GHz microwave radiation produced by the magnetron used to create the deuterium plasma may escape the magnetron enclosure through cable penetrations and mechanical seams. The microwave intensity was measured to be an average 7.4 mW/m^2 at a distance of 1 m from the neutron generator during operation. The maximum intensity over the 30 s measurement interval was recorded to be 10.2 mW/m^2. We covered all seams in the magnetron assembly with aluminum electromagnetic interference reducing tape and repeated the measurement. After the application of aluminum tape, the average (maximum) microwave intensity was measured to be 1.8 mW/m^2 (4.3 mW/m^2) at a distance of 1 m from the neutron generator during operation—a $\times 3$ reduction. For comparison, we measured the microwave intensity at 1 m from a microwave oven using the same device. The microwave oven produced an average and maximum measured intensity of 500 μW/m^2 and 1.5 mW/m^2, respectively. It was determined that no aluminum tape was necessary for the LUX installation. The 3 m exclusion zone ensured that no workers or experiments sharing the same space were exposed to microwaves at a level greater than released by a standard kitchen microwave oven.

4.1.3.2 Electrical safety

The 3 m exclusion zone used to address radiation safety concerns also serves to mitigate the major electrical safety concerns. The primary electrical safety concern is the 125 kV, 5 mA high-voltage used to provide the acceleration potential inside the neutron generator target chamber. All other sources of high-voltage used by the generator are $\leq$5 kV. The magnetron is powered by a 5 kV, 120 mA (maximum values) Glassman EK power supply. The physical barriers enforcing the exclusion zone around the generator are in place whenever the 125 kV acceleration voltage is supplied to generator. There are no exposed components at high-voltage during generator operation. The exteriors of the generator head, generator mounting, electronics rack, high-voltage supplies, and Genie lift are directly connected to earth ground via a 2.54 cm wide stainless steel braid. The ground is verified by ensuring the residence between the neutron generator assembly and the LUX water tank is $<$1 Ω.

The stored energy in the generator system must be considered from a personnel safety standpoint. The capacitance of the generator head and 125 kV acceleration high-voltage cable was estimated to be ∼300 pF. This corresponds to a total stored energy of $E = 1/2CV^2 = 2$ J in the cable and generator head assembly. This is subdominant to the stored energy in the Glassman WK power supply itself—reported to be 14.5 J by the manufacturer. The high-voltage power supply and the remote DD108 generator control interface reports the measured voltage at the supply output. The risk due to stored energy was mitigated by ensuring the acceleration voltage had dropped to $\mathcal{O}(1\text{ kV})$ before entering the 3 m exclusion zone near the neutron generator.

4.1.3.3 Chemical safety

The chiller system uses 3M Fluorinert (FC-3283) coolant. It is non-toxic, non-flammable, and environmentally safe under normal operating conditions. Fluorinert can decompose at temperatures >200 C° into hazardous components—specifically hydrogen fluoride and perfluoroisobutylene. The coolant circulation and magnetron temperature interlocks immediately shut down the system in the event of a coolant system failure.

The Pb sheet used for x-ray shielding was not encapsulated to prevent worker exposure. The Pb was enclosed by the borated polyethylene after the hardware installation was completed. Latex or nitrile gloves were used when handling Pb.

4.1.3.4 Fire safety

The deuterium gas used as the deuterium source for the $^2\mathrm{H(d, n)}^3\mathrm{He}$ reaction was the largest potential fire hazard. A small quantity (50 liters) of deuterium gas was located underground during neutron generator operation to reduce this fire risk. The length of tubing used for deuterium gas transfer was minimized in the assembly. The maximum rate of deuterium use was 2 sccm as determined by the mass flow controller (MFC) used by the neutron generator. During the Run03 D-D calibration, a more typical deuterium flow rate was 0.3–0.4 sccm. A 50 liter bottle of deuterium gas was sufficient for a month-long calibration operating under these conditions.

The borated polyethylene castle constructed around the neutron generator head was an additional fire risk. To help mitigate the risk of fire due to the shielding material, all borated polyethylene was rated to meet the Underwriters Laboratories (UL) 94 H-B burn test. Plastics that obtain this rating are considered "self-extinguishing". This is the lowest UL rating meeting the self-extinguishing criteria. Future deployments, such as the LZ experiment, would do well to consider using one of the more stringent vertical burn ratings to ensure continuing approval by SURF.

The high-voltage power supply used to supply the acceleration potential for the deuterium ion beam is hardware limited to 125 kV and 5 mA. This corresponds to a maximum power of 600 W delivered to the titanium/copper target by the ion beam. The target is actively cooled by circulating 3M Fluorinert coolant through the internal structure of the V-shaped target. The magnetron, turbopump, and plasma chamber are also actively cooled using the same chiller system. Automatic safety interlocks shutoff the acceleration voltage if the coolant flow is disrupted or the magnetron temperature is too high.

In the event of a fire, the emergency shutoff button outside the exclusion zone provides a failsafe control to shut off the acceleration high-voltage. A local, audible, battery-powered smoke alarm was affixed to the top of the polyethylene castle to provide an early warning of fire. A CO_2 fire extinguisher was located on lower Davis outside the exclusion zone near the neutron generator.

4.1.3.5 Mechanical safety

The capacity of the Genie lift varies according to the distance between the load center of mass and the vertical mast. The neutron generator assembly (including shielding) provides a load of <227 kg at 48 cm out from mast. The rated capacity of lift at 46–61 cm from vertical mast is 454 kg. At the farthest allowable distance from the mast (107 cm), the load rating is 159 kg. The Genie lift was tested with a load of >181 kg at 107 cm from mast to verify the capability of the device before use with the neutron generator. A single piece of steel Unistrut with flat base pieces attached at both ends is used as a secondary support mechanism for the Genie lift during the neutron calibration campaigns. This provides an additional fixed source of support for the load in the raised position during long calibration campaigns. The Unistrut is rated to 1043 kg. The borated polyethylene castle is constructed with internal steel threaded rods running through the structure for additional support.

4.2 Underground D-D calibration operations

4.2.1 LUX detector operating parameters during the D-D calibration

The LUX xenon target PMTs were set to an average voltage of -1216 V. The average measured gain was 5.08×10^6, which corresponds to 20.3 mVns/phe. The individual PMTs numbered 5, 32, and 93 were left unbiased during the D-D source calibration campaign. PMTs 5 and 32 are in the top array and were shut off due to a high pulse rate and light emission (presumably due to electrical discharge), respectively. PMT 93 is in the bottom array and was unbiased due to repeated high-voltage supply current limit trips. The capacitive liquid xenon level sensors LS02 and LS05 were shut off during the calibration campaign due to observed crosstalk with the PMTs.

The nuclear recoil calibration program using a D-D neutron generator discussed in this thesis was performed at the end of the 2013 LUX WIMP search run using the same detector operational state, including identical DAQ/trigger conditions and frequent $^{83\mathrm{m}}$Kr-based calibrations for position-dependent S1 and S2 signal corrections [5]. For S2 signals produced by scatters in the beam line, the mean electron lifetime correction was $1.16 \times S2$ and the average (x, y) correction was $0.96 \times S2$. For S1 signals produced by scatters in the beam line, the mean (x, y, z) position correction was $1.06 \times S1$.

Data were corrected for any time variation between their direct measurement during the WIMP search period and the later D-D calibration period using the variation in $^{83\mathrm{m}}$Kr $S1$ and $S2$ peak positions. The D-D analysis uses a g_1 of 0.115 ± 0.004 and a g_2 of 11.5 ± 0.9. These values are within 1.7% and 4.6% of the WIMP search values [5], respectively. The single electron (SE) distribution was measured to have a mean value of 23.77 ± 0.01 phd during the D-D campaign with a standard deviation of 5.75 ± 0.01 phd. The electron extraction efficiency during the D-D calibration period was

0.48 ± 0.04. The average electron drift velocity was measured to be 1.51 ± 0.01 mm/μs corresponding to a 324 μs maximum drift time [24].

The systematic uncertainties in $S1$ and $S2$ due to time variation in the three-dimensional (3D) position-based corrections using $^{83\text{m}}$Kr were determined to be 0.6% and 2.5%, respectively. A small radial drift field component alters the path of drifting electrons in the liquid xenon, with a maximum inward radial deflection of 4.6 cm for electrons originating at the bottom of the TPC [5]. The magnitude of this radial component is smaller near the liquid surface where the neutron beam is positioned. The systematic uncertainties in $S1$ and $S2$ from the $^{83\text{m}}$Kr-based corrections due to these non-uniformities in the drift field were determined to be a bias of 0.5% in $S1$ and 2.5% in $S2$.

The LUX event rate was actively monitored during the Run03 D-D calibration campaign. The background event rate was ∼10 Hz during the Run03 WIMP search. The average event rate in the LUX detector during D-D source operation was ∼65 Hz. The event rate reported by the DDC-8 trigger system during the Run03 D-D calibration spanning October 27th, 2013 to November 23rd, 2013 is shown in Fig. 4.5. During periods of D-D source operation, the event rate in the plot is constant at ∼65 Hz. Injections of $^{83\text{m}}$Kr were performed every few days during the calibration campaign to monitor the electron lifetime and provide precise (x, y, z) position corrections. These injections can be seen as sharp increases in the event rate followed by an exponential decrease with a time constant of 2.64 hours. The first three D-D calibration datasets were acquired on October 31st. A pump failure leading to a partial softening of the vacuum in the outer cryostat contributed to a drop in the electron lifetime of 200 μs on November 1st. Neutron calibration data was suspended until the electron lifetime improved to >500 μs on November 11th. A complete list of the Run03 D-D calibration datasets used for the analysis is given in Appendix A.

The LUX trigger rate was alarmed using the LUX slow control system to indicate if there was a change in D-D source operation. Alarm thresholds were defined above and below (±50 Hz) the average event rate during stable operation. If the event rate strayed outside of the predefined limits, LUX shifters were immediately notified.

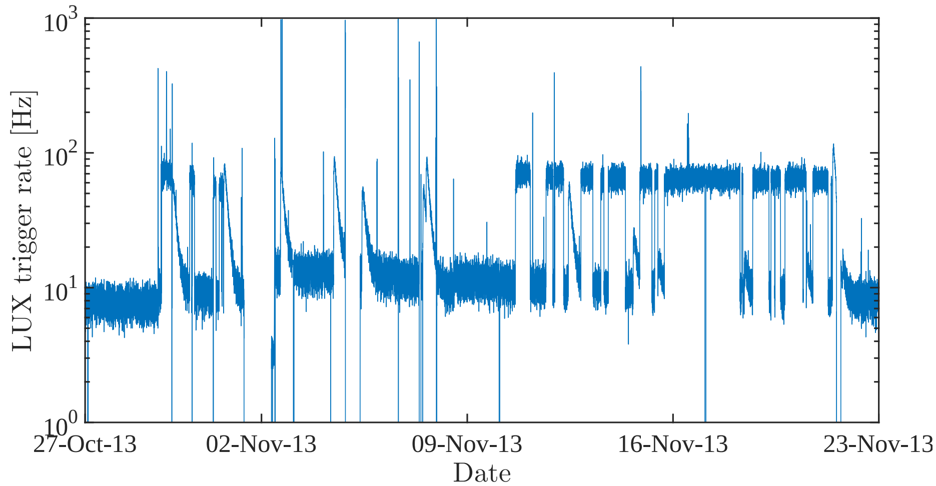

Figure 4.5: The recorded DDC-8 trigger rate in the LUX detector over the entire Run03 D-D calibration campaign.

4.2.2 DD108 neutron generator operation

The neutron generator was operated in pulsed mode during the Run03 D-D calibration campaign. The acceleration current was measured to be ∼0.11 mA. The plasma voltage was set to 4.8 kV with a 70 mA current limit. The measured plasma current was typically 6.3 mA during operation in this mode. The plasma pressure was measured to be 6.5 mTorr. The acceleration voltage was set to 80 kV. The TTL pulse used to control the neutron generator was not digitized into the data stream. Subsequent LUX calibrations did digitize the TTL pulse used to control the neutron generator and applied the techniques outlined in Ch. 1 using the resulting neutron bunch width time structure information [103]. The neutron generator was operated using a 5.2% duty cycle (105 μs on, 1895 μs off). The first three neutron calibration datasets corresponding to a total of 3.7 live hours were acquired using a slightly different duty cycle—a 6% duty cycle (120 μs on, 1880 μs off). An incident neutron flux of 78 ± 8 n cm^{-2} s^{-1} was measured on the exterior of the water tank near the entrance to the calibration conduit using a 9 inch diameter Bonner sphere as reported in Sec. 4.3. Assuming an isotropic source[4], this corresponds to $(2.5 \pm 0.3) \times 10^6$ n/s into 4π solid angle. These conditions provided a 60–70 Hz trigger rate in the LUX detector. For comparison, the typical WIMP search

[4]Actually, the D-D neutron flux varies by approximately a factor of two as a function of angle [26], but the isotropic assumption provides a convenient normalization.

data trigger rate was ∼10 Hz. A total of 107.2 live hours of D-D neutron data was acquired and used for the analysis.

Approval for remote operation of the neutron generator was obtained from SURF with the requirement that no personnel were in the Davis cavern. The steps for remote operation are outlined in the LUX critical procedure for neutron generator operation [100].

4.2.2.1 Alignment of D-D neutron generator for LUX calibration

After the neutron conduit was lowered into position in line with the LUX detector and the neutron generator was moved to be roughly in line with the neutron conduit, the fine adjustment of the neutron generator position was performed. The entire Genie lift assembly supporting the neutron generator was moved along a grid both vertically and horizontally in 0.5 cm increments. After each change of neutron generator position, neutron production was started. The trigger rate was recorded using the DDC-8 trigger system and averaged for 120 s at each position. The final D-D source position was determined by maximizing the trigger rate in both the horizontal and vertical axes. The results from a Run04 alignment with the conduit at ∼16 cm below the liquid xenon surface are shown in Fig. 4.6 (vertical) and Fig. 4.7 (horizontal).

4.3 Measurement of the DD108 neutron production rate

The neutron flux produced by the neutron generator was measured *in situ* in the underground cavern using the same DD108 operating parameters used for the LUX nuclear recoil yield calibration. This calibration of the neutron flux in the direction of the collimation conduit allows the absolute normalization of the expected number of neutron events in the LUX detector. This provides a strong normalization constraint for the yield measurement, reducing statistical uncertainty, and demonstrates that the correct number of events are observed given the measured yields.

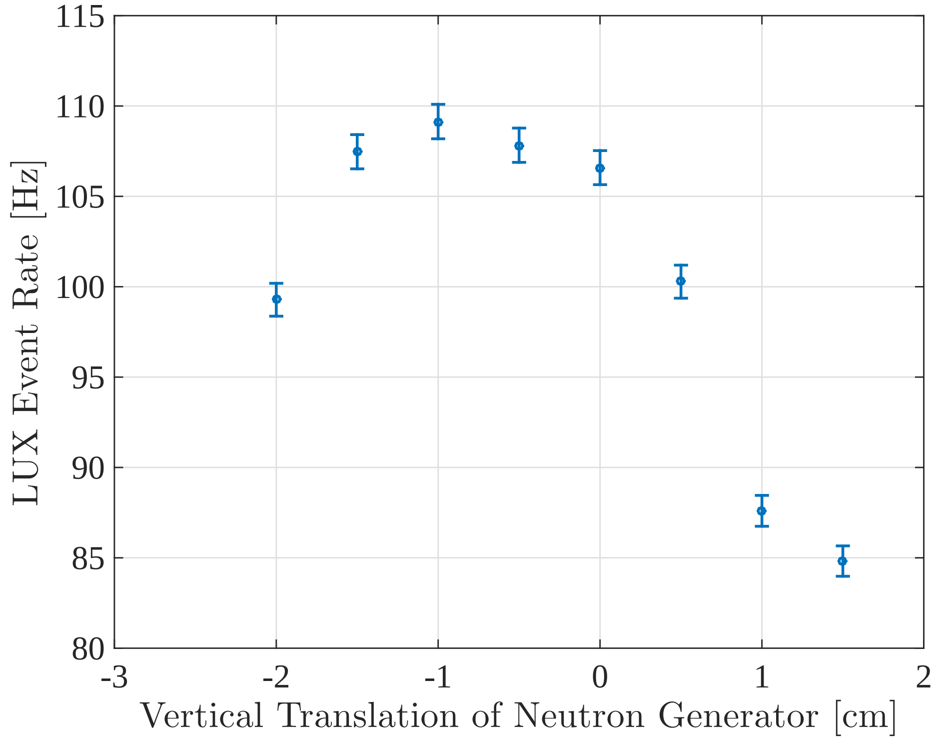

Figure 4.6: Vertical neutron generator alignment data from the first Run04 D-D calibration with the neutron conduit ~16 cm below the liquid xenon level. The final neutron generator position is chosen to maximize the observed event rate in the LUX detector as measured by the DDC-8 trigger system. The error bars are statistical (1σ).

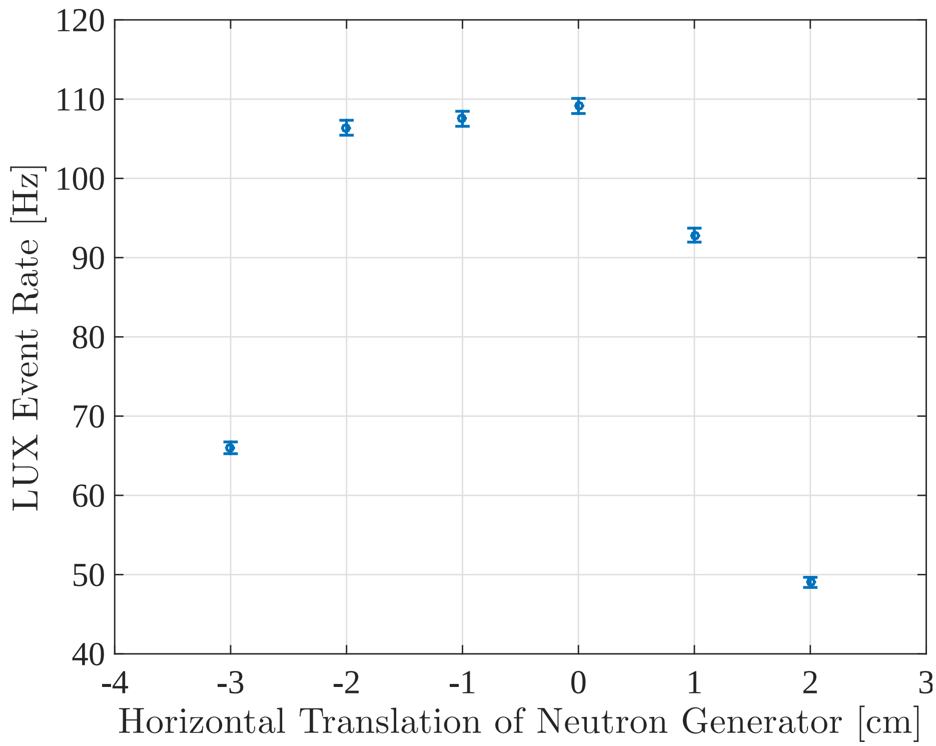

Figure 4.7: Horizontal neutron generator alignment data from the first Run04 D-D calibration with the neutron conduit ∼16 cm below the liquid xenon level. The final neutron generator position is chosen to maximize the observed event rate in the LUX detector as measured by the DDC-8. The error bars are statistical (1σ).

4.3.1 Calibration of the absolute Bonner sphere response

A Bonner sphere is a thermal neutron detector encased in a spherical moderator. The diameter of the spherical moderator determines the neutron energy for which the Bonner sphere is most sensitive. We used a Ludlum model 2241-4 Bonner sphere to measure the absolute neutron flux from the neutron generator. This unit uses a 2 atm ^{3}He proportional counter to detect neutrons moderated by a 22.86 cm (9 inch) diameter cadmium-loaded polyethylene sphere. The relative response of the Bonner sphere is a function of neutron energy, with the energy of maximum response determined by the diameter of the moderator as shown in Fig. 4.8. The 22.86 cm diameter of the unit used for this work was chosen to ensure maximum sensitivity to 2.45 MeV neutrons produced by the $^2\mathrm{H(d,n)}^3\mathrm{He}$ reaction. Additionally, the response vs. energy for Bonner spheres of this diameter closely approximates the energy-dependent human dose from neutron radiation as shown in Fig. 4.9. This similar energy dependence allows the count rate observed using detectors of this size to be linearly mapped to the human dose rate for a large range of neutron energies. This provides a convenient dose monitor for EH&S use.

The Ludlum 2241-4 was calibrated by the vendor using ^{241}Am/Be, an (α, n) source with a feature-rich continuous neutron energy spectrum with a mean energy of ∼4 MeV [106]. The Ludlum calibration documentation reports a calibration factor of 100 cpm per mrem/hour with an uncertainty of 20% for ^{241}Am/Be fast neutrons. Due to the bandpass-like response curve of the Bonner sphere with a maximum near 2.45 MeV, we expect the sensitivity to the mono-energetic neutrons produced by the neutron generator to be higher than would be assumed using this calibration factor. We used a ^{252}Cf spontaneous fission source to perform a more precise calibration of the absolute response of the Bonner sphere as a function of energy. The source was manufactured by Frontier Technology Corp. with serial number: FTC-Cf-Z2467. After taking into account the 2.645 year half life, the source contained 5.2 μg of ^{252}Cf, which provided $(1.20 \pm 0.05) \times 10^7$ n/s corresponding to a human dose rate of 11.4 mrem/hour at a distance of 1 m from the source as reported by the

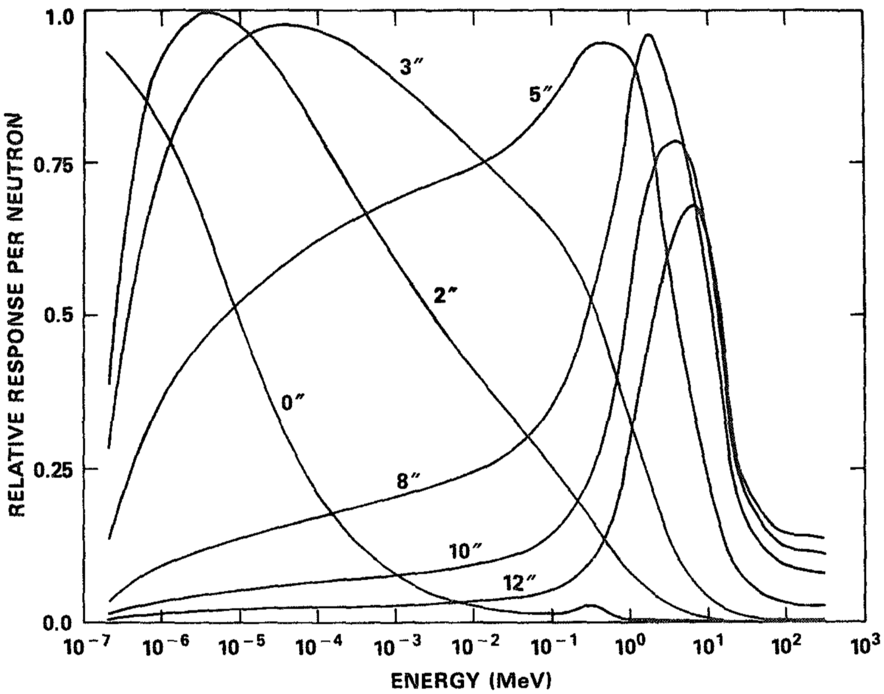

Figure 4.8: Relative neutron detection efficiency vs. energy for a variety of Bonner sphere moderator diameters. Figure reproduced from Ref. [10] (originally from Ref. [104]).

vendor—consistent with Ref. [107]. The ^{252}Cf neutron spectrum has a mean energy of 2.13 MeV and the shape is often approximated by the form:

$$\Phi(E_n) \propto \frac{1}{E_n} e^{(-E_n/T)}\,, \tag{4.1}$$

where $T = 1.42$ MeV [108, 109].

The Bonner sphere and source were positioned on a table away from any material that could contribute significant neutron shine. With a 1 m separation between source and detector, 1876 ± 43 counts were observed in 1 min corresponding to a count rate of 31.3 ± 0.7 counts/s. This exercise was repeated with a 2 m separation between source and detector, where 475 ± 22 counts were observed in a 1 min counting period, giving a count rate of 7.9 ± 0.4 counts/s. The ratio of the 2 m to the 1 m measurement is 0.253 ± 0.013, which is consistent with the expected r^{-2} scaling. We expect a flux of 96 ± 4 n cm^{-2} s^{-1} at 1 m from the source based upon the known activity reported in the vendor

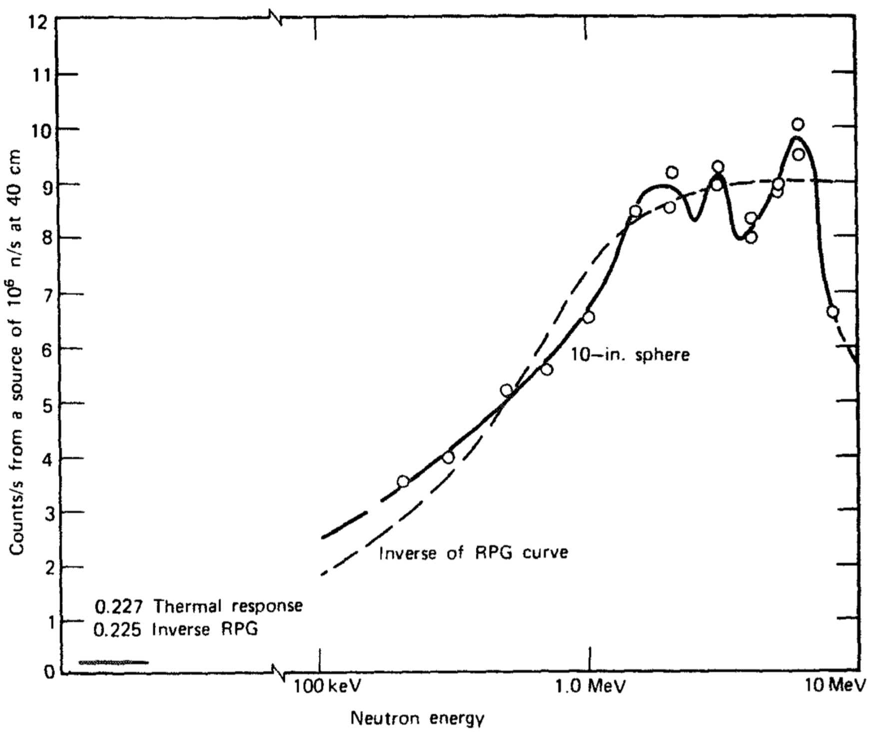

Figure 4.9: Response of a similarly sized (10 inch) Bonner sphere vs. energy. The energy-dependent human neutron dose from neutrons is overlaid labeled as "inverse of RPG curve". Figure reproduced from Ref. [10] (originally from Ref. [105]).

documentation. We define the instrument's response, R, in units of cm^2 to be the conversion factor between the neutron flux at the detector, Φ, and the measured count rate:

$$\text{measured counts [n/s]} = R\Phi\,. \tag{4.2}$$

The Bonner sphere response to the ^{252}Cf source, averaged between the 1 m and 2 m measurements, was calculated to be $R = 0.328 \pm 0.013$ cm^2.

The results from three simulation-based studies reporting the response of a 22.86 cm (9 inch) Bonner sphere as determined by simulation are shown in Fig. 4.10. The Hsu *et al.* [110] and Jing *et al.* [111] studies used Bonner spheres with a ^{3}He proportional counter at the center of the moderator with a target pressure of 2 atm and 4 atm, respectively. The Garny *et al.* [111] study used gold activation foils for thermal neutron detection at the center of the Bonner spheres. While the absolute response reported in these studies varies depending upon the characteristics of the thermal neutron detector, the relative shape of the response is determined based upon the radius of the moderating material surrounding the detector. The results in Fig. 4.10 are normalized to show the similarity of the relative response.

The normalized response curves shown in Fig. 4.10 were scaled by the measured response of the Ludlum 2241-4 Bonner sphere as determined using the ^{252}Cf source. The scaling used to determine the absolute response curves was obtained by multiplying the relative response curves by the ^{252}Cf spectrum probability density function defined in Eq. 4.1. The integral of the resulting function was compared to our measured response of the Ludlum 2241-4 Bonner sphere to a ^{252}Cf source to determine the scale factor in cm^2. The absolute response of our Bonner sphere as determined using this procedure is shown in Fig. 4.11. The calibrated average response curve shown in Fig. 4.11 was used to determine the absolute response of the Bonner sphere to the mono-energetic 2.45 MeV neutrons produced by the D-D neutron generator. Our calibrated average Bonner sphere response for 2.45 MeV neutrons is 0.38 ± 0.07 cm^2.

The Bonner sphere reports the measured equivalent dose as calculated using its internal 100 cpm/(mrem hour)

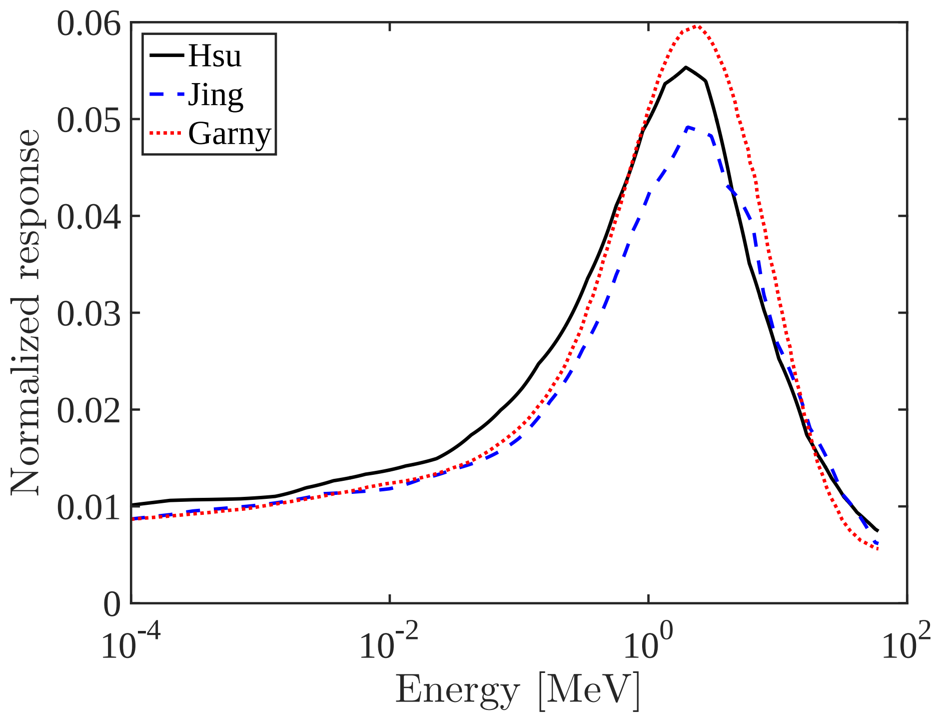

Figure 4.10: Three response curves for 22.86 cm (9 inch) Bonner spheres as digitized from Ref. [110] (solid black), Ref. [112] (dashed blue), and Ref. [111] (dotted red). The absolute response results reported in these references are normalized to provide the relative response over the neutron energy range of interest.

conversion factor verified by the vendor using a ^{241}Am/Be neutron source. Based upon the results of our calibration using ^{252}Cf, we expect that the Bonner sphere will report a dose that is systematically high by 50–80% when measuring monoenergetic 2.45 MeV neutrons. The scaler functionality of the device is unaffected by this systematic effect as it does not use the internal cpm to dose conversion factor.

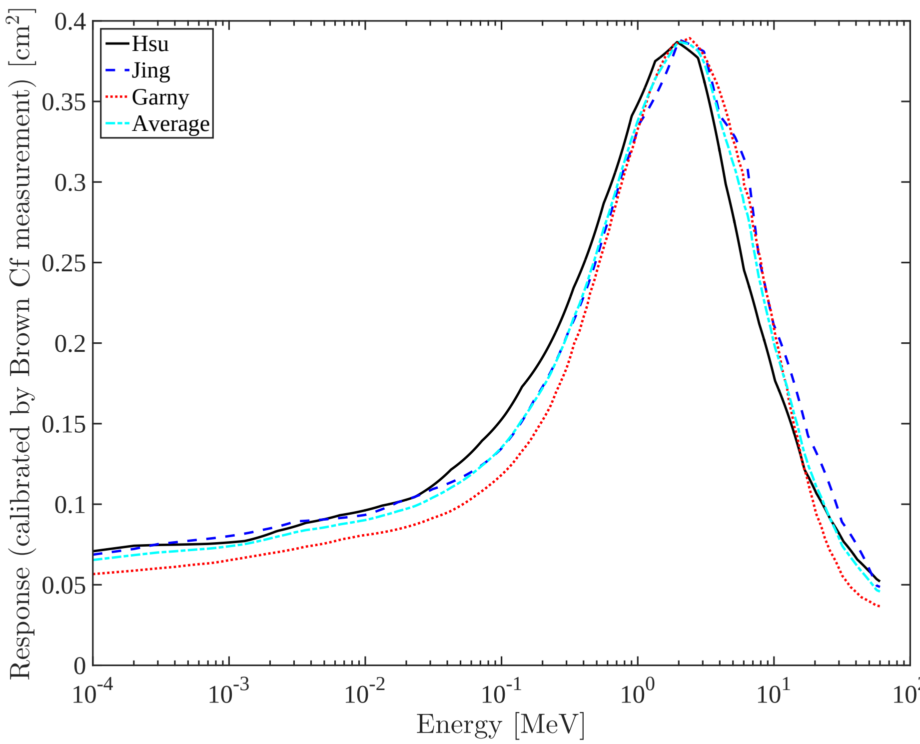

Figure 4.11: The same three response curves from Fig. 4.10 scaled to describe the absolute response of the Ludlum 2241-4 Bonner sphere using our measured ^{252}Cf count rate. The averaged response from the three curves is shown by the cyan dash-dotted line.

4.3.2 Measurement of the neutron flux in the Davis Cavern

The same Ludlum 2241-4 Bonner sphere was used to measure the neutron production rate of the D-D source during the LUX Run03 D-D calibration campaign. The center of the Bonner sphere was positioned 50 cm from the neutron production surface inside the DD108 apparatus as shown in Fig. 4.12. The neutron generator operating parameters were identical to the parameters used during the Run03 D-D calibration campaign.

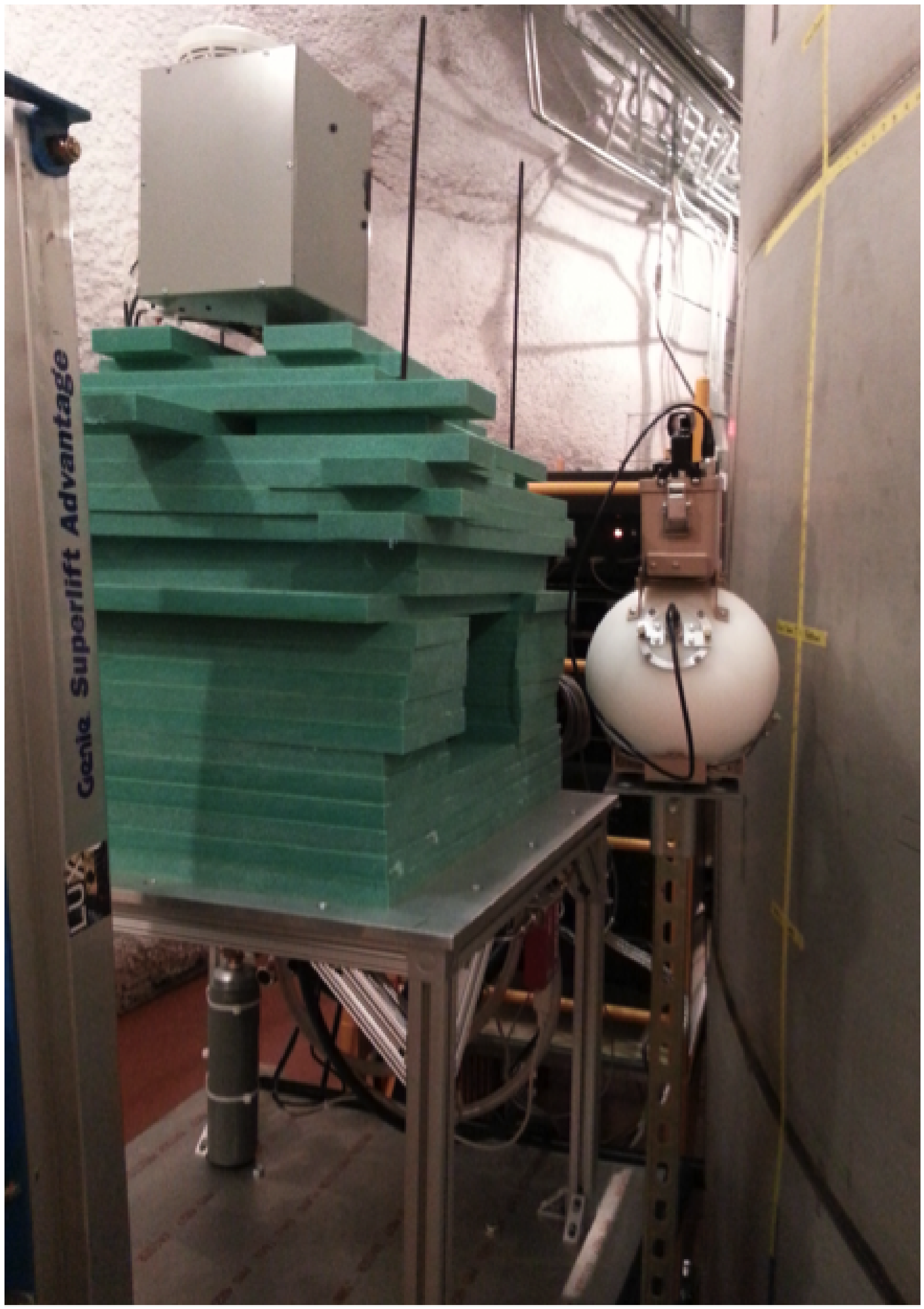

Figure 4.12: The experimental setup for the *in situ* measurement of the neutron generator flux during the LUX D-D nuclear recoil calibration campaign. The neutron flux in the direction of the neutron collimation conduit was measured using the Ludlum 2241-4 Bonner sphere on the steel stand.

We used the scaler functionality on the Bonner sphere to measure 3585 counts in a 2 minute interval. This corresponds to an observed count rate of 29.9 ± 0.5 counts/s. The calibrated average Bonner sphere response was combined with the observed count rate according to Eq. 4.2 to measure a neutron flux of $78 \pm 8\ \mathrm{n\,cm^{-2}\,s^{-1}}$ at a distance of 50 cm from the D-D source. This corresponds to a neutron rate of $(2.5 \pm 0.3) \times 10^6$ n/s fired into 4π solid angle, assuming an isotropic neutron flux. This value includes a 10% systematic uncertainty in the neutron generator rate as specified in the Bonner sphere calibration sheets provided by the vendor. We avoid introducing the vendor's quoted 20% systematic uncertainty in the "calibration factor" used for the device's internal mrem/hour conversion by measuring the absolute number of counts using the scaler functionality.

4.4 The neutron beam

The experimental setup at the LUX TPC is shown in Fig. 4.13. A convenient coordinate system used in the subsequent chapters on the D-D calibration analysis is defined here. The orientation of the Cartesian coordinates x', y', z' are defined by the neutron beam pipe axis and the vertical axis of the detector. The neutron beam spans a geometrical chord that is offset from the TPC diameter. The coordinate y' is along the beam pipe direction with zero at the point where the beam enters the liquid xenon active region. The coordinate x' is transverse to the beam pipe axis in the horizontal plane. The x' and y' coordinates defined by the beam direction differ from the more traditional x and y coordinates, which are centered in the middle of the TPC, by the translation and rotation defined by

$$\begin{bmatrix} x' \\ y' \end{bmatrix} = \begin{bmatrix} \cos\theta_{\mathrm{rot}} & -\sin\theta_{\mathrm{rot}} \\ \sin\theta_{\mathrm{rot}} & \cos\theta_{\mathrm{rot}} \end{bmatrix} \begin{bmatrix} x - 7.1\ \mathrm{cm} \\ y + 23.0\ \mathrm{cm} \end{bmatrix}, \tag{4.3}$$

where $\theta_{\mathrm{rot}} = -5.1°$. The coordinate z' is perpendicular to the beam pipe axis in the vertical plane. It is nearly identical to the traditional z (ionization drift) coordinate indicating the distance from the liquid surface. The neutron beam entry point into the liquid xenon volume is 0.9 cm above the exit point. This corresponds to an angle of $\sim$1° with respect to the liquid xenon surface.[5] A distance of 47.4 cm along y' separates the entry and exit points. This notation is further used in this thesis such that $S2[y'_1]$ and $S2[y'_2]$ represent the S2 signal size from the first and second neutron-xenon scattering vertices in the y' direction along the beam line, respectively. This notation is illustrated in more detail in the following figures. The z (drift time) vs. y' distribution of single-scatter events is shown in Fig. 4.14.

During the D-D calibration campaign, the center of the conduit was raised to be 16.1 cm below the liquid xenon surface in the TPC and leveled to 1° with respect to the liquid surface as shown in Fig. 4.14. This z position of the beam was chosen to provide a short distance to the liquid surface

[5] The small angle of the neutron conduit with respect to the liquid xenon surface was due to the precision of the neutron conduit leveling process.

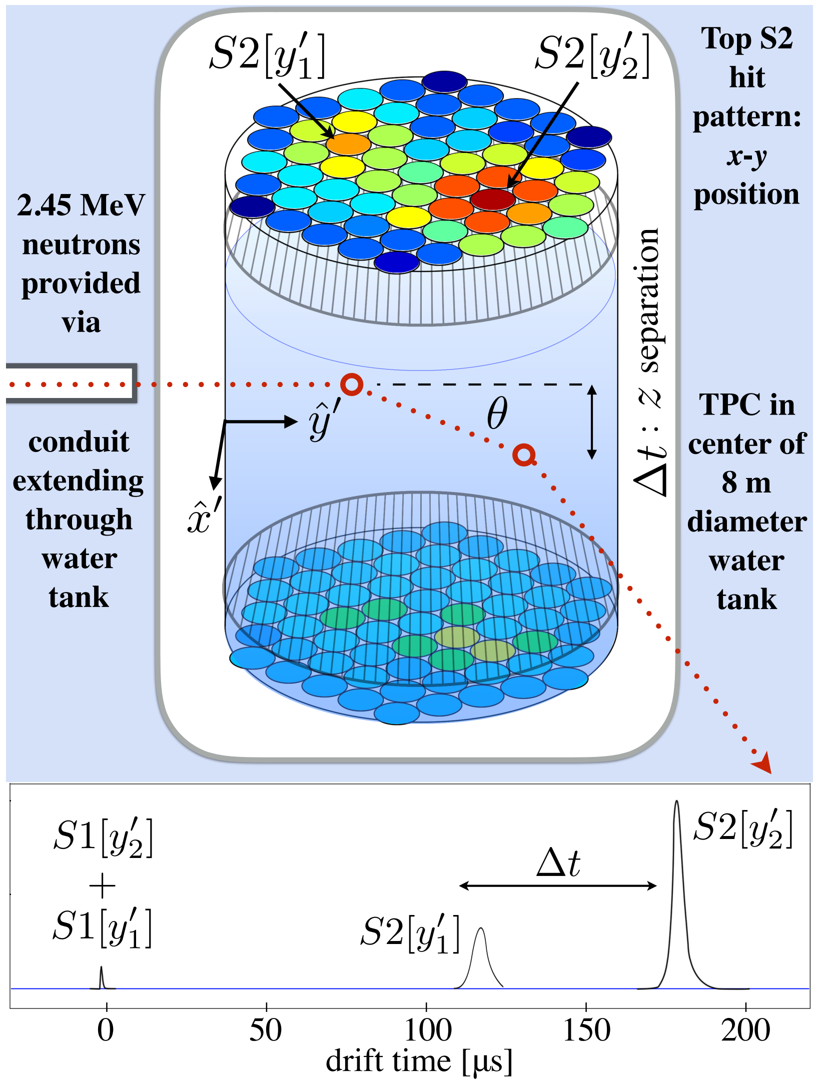

Figure 4.13: Conceptual diagram of the LUX D-D calibration experimental setup. The LUX TPC is visible in the center of the 8 m diameter, 6 m tall water shield. The LUX cryostat boundary is depicted as the thick gray line around the TPC. The monoenergetic 2.45 MeV neutrons are collimated through an air-filled conduit spanning the distance from the water tank wall to the LUX detector cryostat. The x' coordinate is coming out of the paper, and the y' coordinate is in line with the beam. This figure illustrates a potential event used for the Q_y analysis: a neutron (red dotted line) enters the active liquid xenon volume, scatters twice, and then leaves the target media. The resulting time-integrated hit pattern is shown on the PMT arrays. The bottom frame shows an event record of this neutron interaction sequence (for illustration only). The PMT hit pattern provides (x', y') information, while the drift time separation provides precise reconstruction of the z position of each vertex.

in order to increase the fraction of low-multiplicity neutron scatters in the dataset. The x vs. y projection is shown in Fig. 4.15. As in Fig. 4.14, the shine due to neutrons scattering in passive detector materials can be seen localized where the beam enters the liquid xenon. The source of neutron production inside the neutron generator was positioned 46 ± 2 cm outside of the LUX water tank in line with the neutron conduit during the calibration.

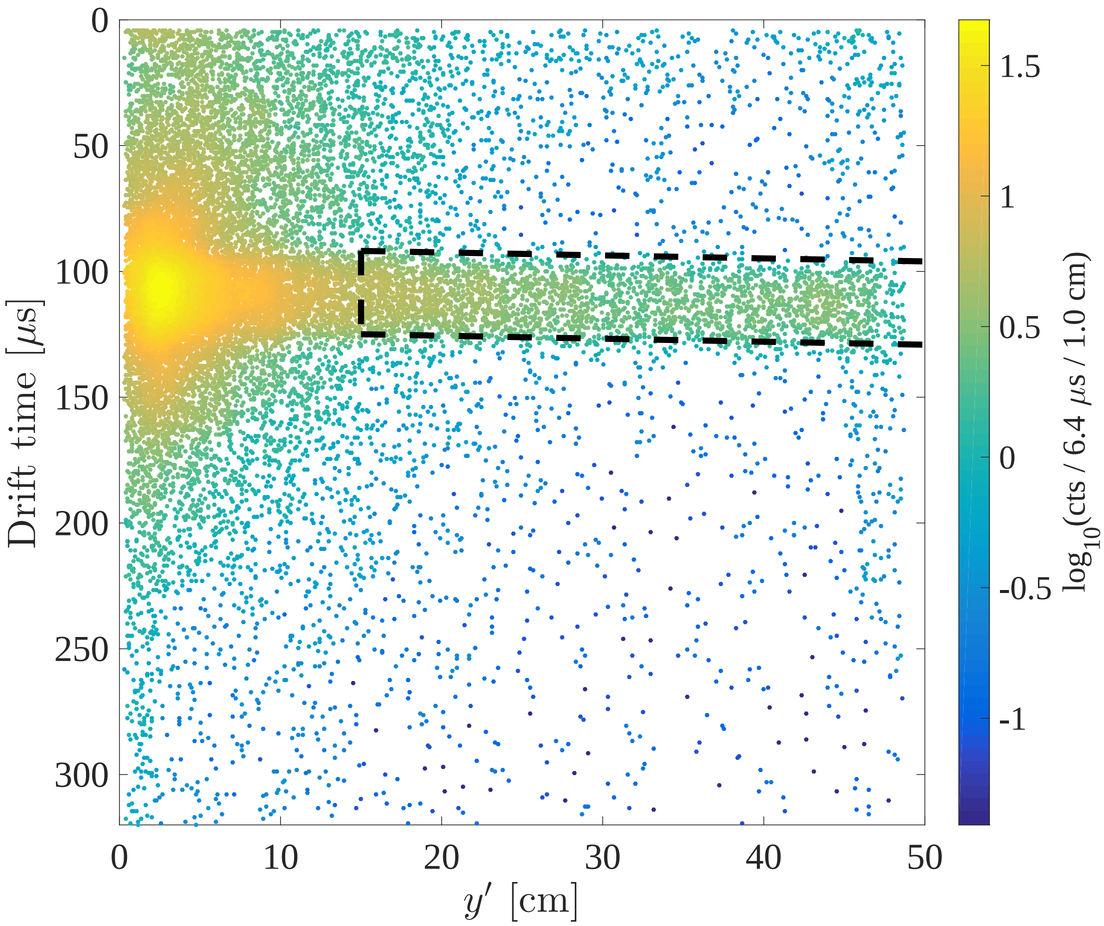

Figure 4.14: The z (drift time) vs. y' distribution of single-scatter events passing all nuclear recoil area selection and data quality cuts. The neutron beam pipe is aligned outside of the plot to the left in line with the beam at a drift time of 107 μs. A cut of $0 < x' < 10$ cm was used to select scatters in a narrow x' slice around the projection of the neutron beam into the liquid xenon. This plot contains the full 107.2 live hours of 2013 D-D data. The shine due to neutrons scattering in passive detector materials can be seen localized where the beam enters the liquid xenon. The black dashed line shows the approximate location of the neutron beam energy purity cuts. The neutron shine near the beam entry point is asymmetric in this plot due to the event selection criteria; only single-scatter events are accepted and the 12.6 cm total mean free path for neutrons makes it more probable for a neutron to exit out of the top of the xenon volume than the bottom.

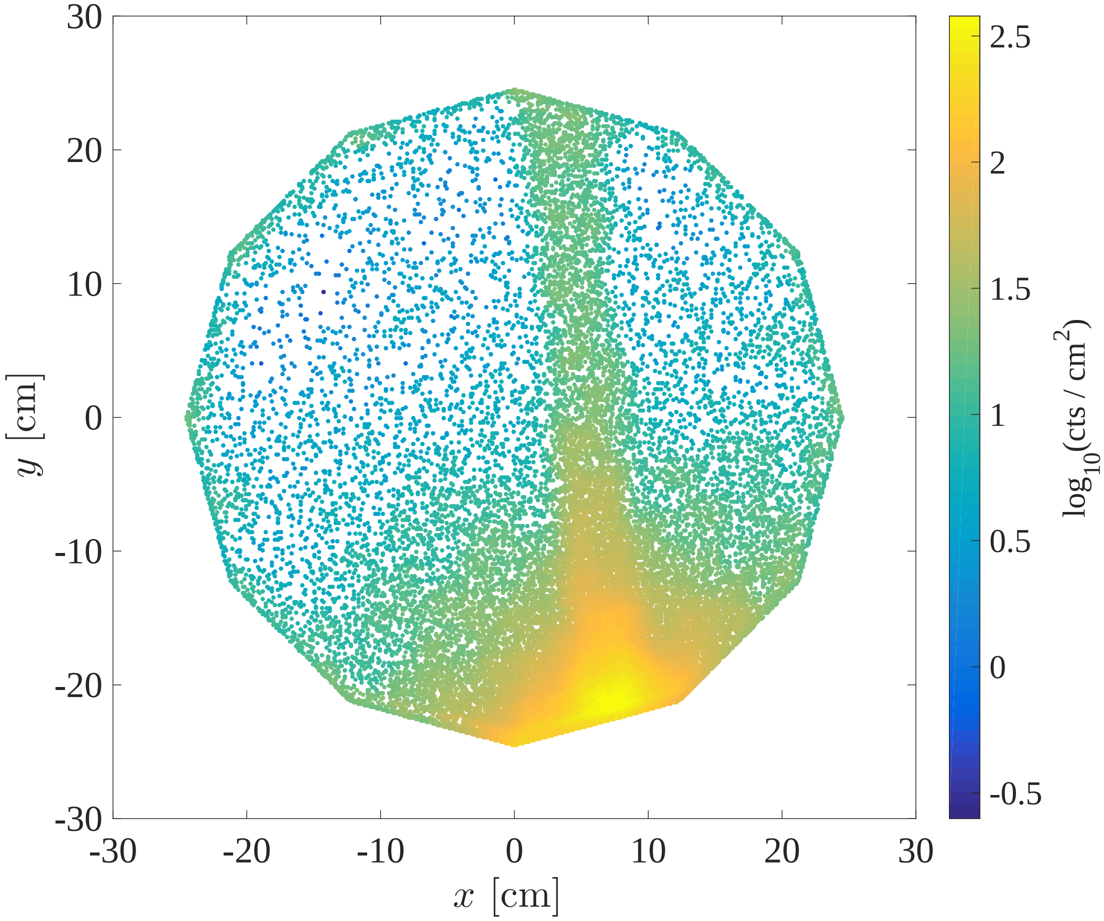

Figure 4.15: The x vs. y distribution of single-scatter events passing all nuclear recoil area selection and data quality cuts. The neutron beam pipe is aligned outside of the plot to the left in line with the beam at a drift time of 107 μs. A cut of 80 $<$ drift time $<$ 130 μs was used to select scatters in a narrow z slice around the projection of the neutron beam into the liquid xenon. This plot contains the full 107.2 live hours of 2013 D-D data. The shine due to neutrons scattering in passive detector materials can be seen localized where the beam enters the liquid xenon.

4.4.1 Ensuring neutron beam energy purity

The energy spectrum of the specific DD108 hardware was characterized at Brown University prior to use in the LUX calibration as described in Ch. 3.[6] The mean neutron energy was measured to be 2.40 ± 0.06 MeV, consistent with the expected 2.45 MeV within experimental uncertainties. The expected mean neutron energy of 2.45 MeV was used for the LUX nuclear recoil signal yield data analysis with an uncertainty of 2%.

Monte Carlo simulation studies using LUXSim/GEANT4 [43, 113] indicate that after selecting events using a cylindrical analysis volume in line with the neutron beam in the TPC, 95% of accepted events are produced by neutrons with energies within 6% of the initial energy at the D-D source [30]. This position cut requires that the first scatter has a reconstructed location of $y' > 15$ cm and is within the 4.9 cm diameter of the neutron beam projection in the detector active region.[7] These position-based analysis cuts are referred to as the "neutron energy purity cuts" in the following chapters. Any residual electron recoil contamination due to neutron capture or inelastic scatters in passive materials was identified and removed in the data analysis [30].

A view parallel with the neutron beam is shown in Fig. 4.16 and Fig. 4.17. The effectiveness of the neutron energy purity cuts is demonstrated in these figures. In Fig. 4.16, the cut $y' > 0$ is applied. The neutron shine from scatters in passive detector materials is seen surrounding the circular collimated beam profile of 4.9 cm diameter. In Fig. 4.17, the cut $y' > 15$ is applied. The effect of the 15 cm event position cut into the liquid xenon along the neutron beam line is immediately obvious. Events due to neutrons that previously scattered in passive detector materials are removed, and the corresponding shine around the collimated circular beam profile is reduced.

[6] The LUX calibration used an identical shielding structure and source configuration defined as "Target Orientation A" in Ch. 3.

[7] It is possible to relax this cut to increase the number of events used in the analysis (not done here). This comes at the cost of an increased spread in the energy of incident neutrons.

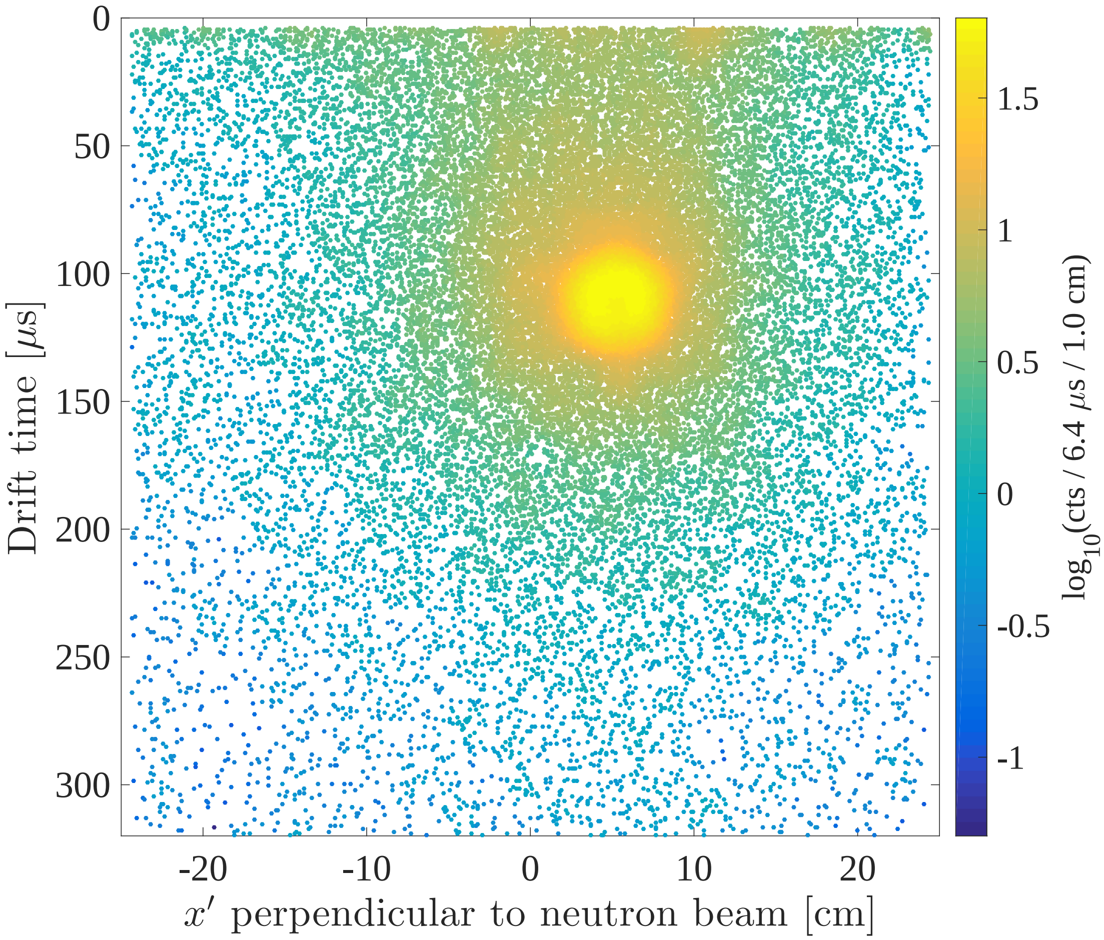

Figure 4.16: The z (drift time) vs. x' distribution of single-scatter events passing all nuclear recoil area selection and data quality cuts. This point of view is parallel with the neutron beam. This plot uses all events with $y' > 0$; it contains the full 107.2 live hours of 2013 D-D data. The shine due to neutrons scattering in passive detector materials can be seen around the circular beam profile.

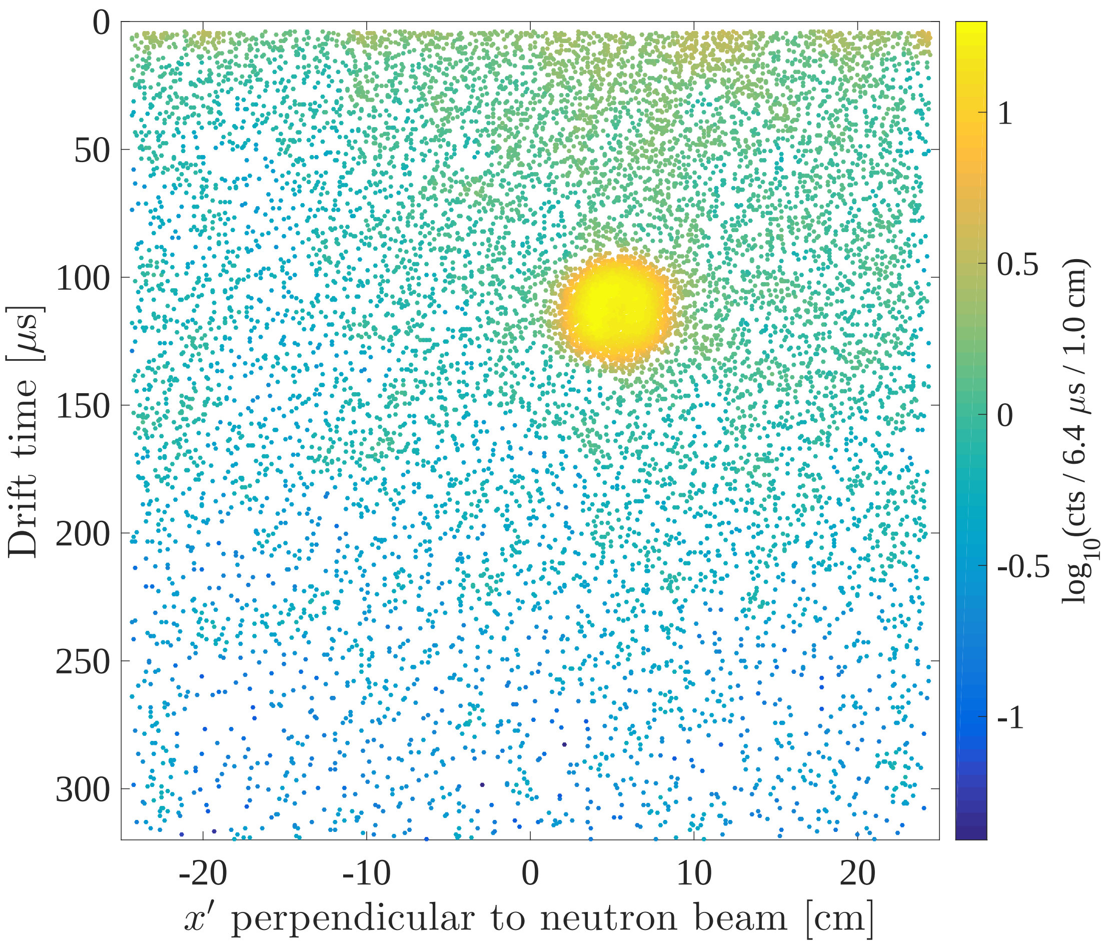

Figure 4.17: The z (drift time) vs. x' distribution of single-scatter events passing all nuclear recoil area selection and data quality cuts. This point of view is parallel with the neutron beam. This plot uses all events with $y' > 15$; it contains the full 107.2 live hours of 2013 D-D data. The shine due to neutrons scattering in passive detector materials seen in Fig. 4.16 has been cut away by the $y' > 15$ cut.

4.5 LUX nuclear recoil band

The ratio of the ionization to scintillation signal (nuclear recoil band) is used to discriminate between nuclear and electron recoils in liquid xenon TPCs. In this section, we use neutrons from the D-D source to define the nuclear recoil band over the $S1$ range used for the WIMP search analysis. Subsequently, a simulated nuclear recoil band is compared to data to demonstrate consistency of the nuclear recoil signal model used to generate $S1$ and $S2$ PDFs for the WIMP search profile-likelihood-ratio analysis [5, 57].

The nuclear recoil band was measured using the single-scatter event population in the D-D calibration dataset.[8] Events were selected using the following cuts. An S2 threshold at 164 phd was applied on the raw $S2$ area before position-correction for consistency with the LUX WIMP search [5]. An upper limit ensuring $S2 < 5000$ phd was applied. The nuclear recoil band analysis applied an upper limit on the raw digitized area outside of the identified S1 and S2 signals in the event record of 219 phd. This cut ensures quiet detector conditions and is described in more detail in Ch. 7. In contrast to the nuclear recoil yield analyses in later chapters, the incident neutron energy does not need to be precisely known for the nuclear recoil band measurement. The neutron beam energy purity cuts were not applied. A z cut of $80 <$ drift time < 130 μs was applied to select events around the neutron beam projection in the active region. A radial cut of $r < 21$ cm was used to avoid detector edge effects.

After all cuts, the remaining events with $S1_{\mathrm{spike}} < 50$ phd are shown in Fig. 4.18. This is the same $S1_{\mathrm{spike}}$ range used for the improved LUX WIMP search result [5]. The non-zero width of the vertical bands of events at low $S1_{\mathrm{spike}}$ is due to corrections for spike overlap in the per-channel waveforms as well as 3D position-based detector corrections. The mean $S1_{\mathrm{spike}}$ value is offset slightly from integer values due to the same corrections.

A Gaussian fit was performed to the $\log_{10}(S2/S1_{\mathrm{spike}})$ distribution in each 1.1 phd-wide bin

[8] The code used for this analysis is located in the Brown Particle Astrophysics Group's GitHub organization [65] with the relative path "jverbus_lux_scratch/NeutronGeneratorAnalysis/nr_band/".

along the $S1_{\mathrm{spike}}$ axis. The Gaussian centroid and 90% one-sided limit for each bin, depicted in black in Fig. 4.18, were determined based upon the fit parameters. The bins were positioned to ensure the observed vertical bands of events at low $S1_{\mathrm{spike}}$ were centered in their corresponding bin. It is worth noting the significant improvement in the single detected photon resolution at low $S1_{\mathrm{spike}}$ compared to traditional $S1$ area-based techniques, which are subject to the intrinsic single photoelectron resolution ($\sigma_{\mathrm{sphe}} = 0.37$ in the case of LUX).

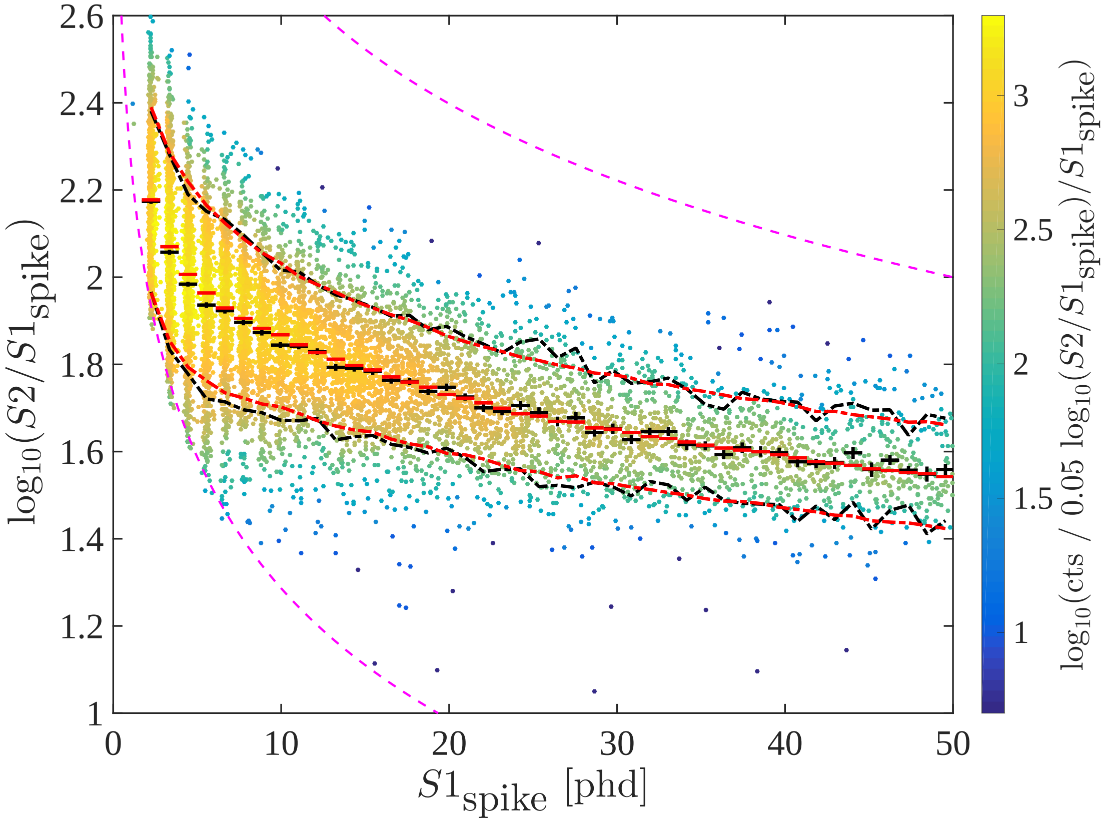

Figure 4.18: The measured D-D neutron events used to define the LUX nuclear recoil band are shown in the scatter plot. There are 9864 events remaining after all cuts with $S1_{\mathrm{spike}} < 50$. The black data points are the Gaussian fit mean values for each $S1_{\mathrm{spike}}$ bin. The red data points are corresponding Gaussian fit mean values for the simulated nuclear recoil band produced using the model described in Sec. 9.2. The black and red dot-dashed lines indicate the 90% one-sided limits from data and simulation, respectively. The magenta dashed lines indicate the lower S2 threshold at ∼164 phd raw S2 and the upper S2 limit at 5000 phd. Error bars are statistical only.

In dual-phase liquid xenon TPCs, multiple-scatter events misidentified as single-scatters due to interactions in the reverse field region below the cathode produce events at artificially low

$\log_{10}(S2/S1_{\mathrm{spike}})$ [31, 32]. Compared to more traditional nuclear recoil band calibrations using ^{252}Cf or ^{241}Am/Be, there is a relative absence of these pathological events at low $\log_{10}(S2/S1_{\mathrm{spike}})$ due to the well-defined neutron beam position near the liquid xenon surface away from the sub-cathode ionization signal dead region.

A LUXSim/GEANT4-based simulation using a Lindhard-based NEST model fit to the LUX D-D results (described in Sec. 9.2) was used to produce single-scatter event waveforms for comparison with the measured nuclear recoil band. These waveforms were passed through the data processing pipeline used for the D-D calibration data. The same cuts and analysis used for nuclear recoil band data were applied to the resulting reduced simulation waveforms. The average (maximum) deviation of the band-fit centroid between simulation and data is 0.010 (0.029) in $\log_{10}(S2/S1_{\mathrm{spike}})$ space over the 0–50 phd $S1_{\mathrm{spike}}$ range. The average standard deviation of the band agrees with a mean (maximum) absolute deviation of 0.009 (0.039) in $\log_{10}(S2/S1_{\mathrm{spike}})$ space over the 0–50 phd $S1_{\mathrm{spike}}$ range. The simulated nuclear recoil band is consistent with D-D calibration data within the systematic uncertainty intrinsic to the simulation process. This simultaneous agreement of the model described in Sec. 9.2 with the measured Q_y, L_y, and nuclear recoil band demonstrates the consistency of the signal model used to generate the LUX WIMP search limit with data [5]. As an additional check, we verified the WIMP search limit is unchanged for all reported WIMP masses by the small variation in the nuclear recoil band between data and simulation.

Representative individual Gaussian fits to data for the lowest, middle, and highest $S1_{\mathrm{spike}}$ bins are shown in Fig. 4.19. The middle and high-energy bins are well fit using a Gaussian, but non-Gaussian behavior is observed at low $S1_{\mathrm{spike}}$. This non-Gaussian behavior is expected due to the low number of signal carriers produced at the interaction site as well as the effect of the 164 phd $S2$ threshold. The simulated distribution of events in each NR band is represented by the red shaded histogram in Fig. 4.19. The LUXSim simulation captures the non-Gaussian behavior at low $S1$ and provides an accurate model of the nuclear recoil band in the profile likelihood ratio analysis used for the WIMP search results [5, 57].

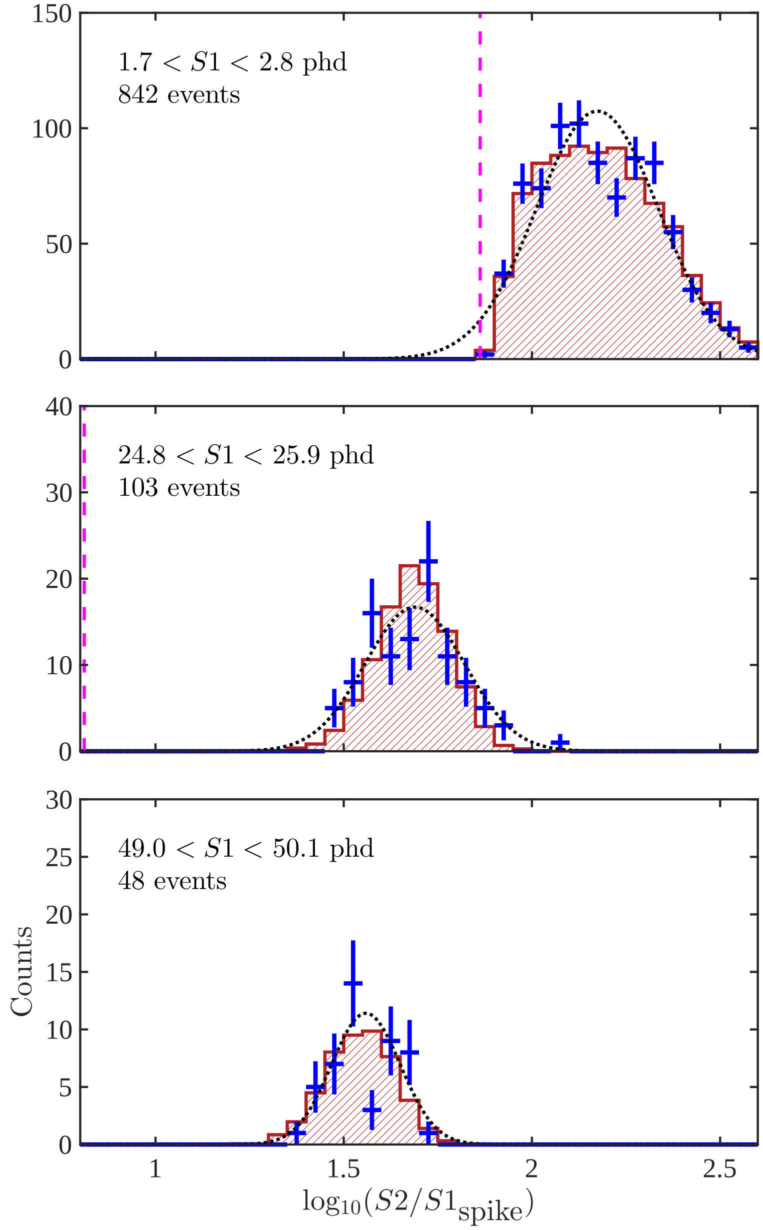

Figure 4.19: Comparison of representative bins used for nuclear recoil band comparison between data and simulation. The lowest, middle, and highest bins in $S1_{\mathrm{spike}}$ are shown. The blue crosses show the distribution of events in data. The black dotted line shows a Gaussian fit to the blue data points. The red shaded histogram represents simulated nuclear recoil band profile. The simulation histogram was generated using 9324 events, 3067 events, and 1924 events in the three graphs; this corresponds to a statistical uncertainty on the maximum value of the red histogram in each graph of 3%, 4%, and 5%, respectively. As expected, non-Gaussian behavior is observed in the first $S1_{\mathrm{spike}}$ bin. The magenta dashed line indicates the approximate location of the S2 threshold. The single bin with three counts in the bottom frame is not statistically unreasonable; the χ^2/dof for the Gaussian fit in that bin is 9.9/5, which gives a p-value of 0.08.

Chapter 5

Measurement of the Low Energy Liquid Xenon NR Ionization Yield

The ionization yield was measured as a function of nuclear recoil energy from 0.7 to 24.2 keV_{nr} using neutrons that scatter twice in the active liquid xenon volume.[1] This analysis uses the full 107.2 live hours of Run03 D-D neutron data acquired as outlined in Ch. 4.

5.1 Absolute measurement of recoil energy from reconstructed double-scatter events

For double-scatter neutron events, the scattering angle between the first and second interaction vertices was calculated based upon the reconstructed (x, y, z) position of each vertex. The scattering angle in the center-of-mass frame, θ_{CM}, is related to the recoil energy associated with the first vertex as shown in Eq. 1.1 (reproduced here):

[1]The code used for this analysis is located in the Brown Particle Astrophysics Group's GitHub organization [65] with the relative path "jverbus_lux_scratch/NeutronGeneratorAnalysis/qy/".

$$E_{\mathrm{nr}} = E_n \frac{4 m_n m_{\mathrm{Xe}}}{(m_n + m_{\mathrm{Xe}})^2} \frac{1 - \cos(\theta_{\mathrm{CM}})}{2}, \tag{5.1}$$

where m_{Xe} is the average atomic mass of Xe, m_n is the mass of the neutron, and E_n is the energy of the incident neutron. The relationship between θ_{CM} and the scattering angle in the laboratory frame, θ_{lab}, is given by Eq. 1.3 (reproduced here):

$$\tan\theta_{\mathrm{lab}} = \frac{\sin\theta_{\mathrm{CM}}}{m_n/m_{\mathrm{Xe}} + \cos\theta_{\mathrm{CM}}}. \tag{5.2}$$

This absolute determination of the recoil energy combined with the observed $S2$ from the first vertex provides a direct Q_y calibration. A conceptual schematic of this type of event is shown in Fig. 4.13. The (x, y) position was determined using the algorithm described in Ref. [38]. The z position was measured using the ionization electron drift time. The variable θ_{lab} was reconstructed using the measured 3D positions of the first and second interaction vertices. The ionization yield measurement used individual events with a reconstructed nuclear recoil energy between 0.3 and 30 keV$_{\mathrm{nr}}$, which corresponds to a neutron scattering angle range of 7° to 79°. For comparison, the recoil energy spectrum endpoint produced by 180° neutron scatters corresponds to a nuclear recoil energy of 74 keV$_{\mathrm{nr}}$.

5.2 Recoil energy measurement uncertainties

The statistical uncertainty associated with the (x, y) position reconstruction is dependent upon the size of $S2$. The typical statistical error in the reconstructed x and y coordinates was typically no more than ∼1 cm for the signal sizes used for this analysis, with a maximum statistical error of ∼2 cm at the 36 phd raw $S2$ threshold. The systematic uncertainties in the reconstructed x and y positions were estimated to be 0.0–0.7 cm, with the best estimate of 0.35 cm. The z position of each scatter vertex has a statistical uncertainty of ∼0.1 cm [37]. After neutron energy purity cuts, the incident direction of neutrons producing accepted events was parallel within 1° of the beam direction based upon the solid angle presented by the collimation conduit. An estimated position uncertainty on the beam entry position into the TPC of 0.6 cm in x' and z' was included in the per-event energy determination.

The error in the measured nuclear recoil energy at the first scattering vertex in an individual double-scatter event was estimated by propagating the error on the x, y, and z coordinates through to the reconstructed angle. Events with larger distances between vertices and/or majority components in the z direction have a smaller fractional error in the event energy. The per-event uncertainties on the reconstructed recoil energy were used to weight the events in order to optimize the fractional error on the mean reconstructed energy of a particular keV_{nr} bin. The weighting scheme is described in detail in Ch. 6.

A detailed study was made of the way in which event reconstruction populates the measured nuclear recoil energy bins. Events with true energy outside a given bin can bleed inside, due to the non-zero resolution of the angle based measurement. This is an example of Eddington bias [114, 115] and must be accounted for in the analysis.[2] This effect broadens the width of the measured charge distribution in a given bin. If additionally the underlying spectrum is falling (rising), there is more (less) bleeding into the bin from lower (higher) energies, causing a negative (positive) bias in the mean measured charge per unit recoil energy with respect to the true yield. Due to the S2 threshold, there are more high-energy events that can be reconstructed down into a given low-energy bin than there are lower-energy events that can be reconstructed up into the same bin. A Monte Carlo simulation of multiple scatter neutron events in the LUX detector was used to quantify and generate corrections for these effects due to position reconstruction uncertainty and to verify the angular reconstruction algorithms used for the data analysis. The Monte Carlo also includes $S2$ resolution effects due to fluctuations associated with signal creation and recombination as modeled by NEST v1.0. The electron lifetime and extraction efficiency effects are binomially applied and also contribute to the simulated $S2$ resolution. The simulation is described in detail in Ch. 6 and the

[2] Eddington bias is commonly confused with the more widely known Malmquist bias, which is a related effect [116].

associated systematic uncertainties are reflected in the results reported in Table 5.1. It is important to note that the Eddington bias correction was only applied to the mean recoil energy of the event population in each bin. As a consequence, for the results reported in this section, the defined recoil energy bin boundaries and per-event reconstructed recoil energies are reported before any Eddington bias correction.

5.3 Double-scatter event selection

The double scatter event structure was described in Sec. 5.1. Scintillation from both interaction sites was observed as a single combined S1 signal because the maximum time-of-flight of a 2.45 MeV neutron between scattering vertices in the LUX active region is $\sim$30 ns, which is similar to the time constant associated with the S1 pulse shape in liquid xenon. Similar to normal single-scatter TPC operation, the S1 pulse was used to provide a start-time t_0 in the double-scatter analysis allowing the reconstruction of the z' position of both scatters with respect to the liquid surface.

The analysis threshold for S2 identification is raw $S2 > 36$ phd (1.5 extracted electrons) prior to position-dependent corrections. This is a lower threshold than was used for the WIMP search analysis [5], which is possible due to the small number of accidental coincidence events that can pass as legitimate double-scatters. An estimate of the number of accidental coincidence double-scatter events is provided in Sec. 5.4.

Multiple neutron interactions at similar z can be misidentified as single interaction vertices if there is significant overlap in the S2 waveforms. The intrinsic S2 pulse width for a single neutron interaction site is due to the length of the detector's luminescent gas gap. There is an additional z' dependent contribution to the intrinsic S2 signal width due to the longitudinal diffusion of electrons drifting in the liquid xenon [117]. A cut on the root-mean-square of the charge arrival time (RMS width) within S2 pulses was used to preferentially reject overlapping S2 signals. The optimum value of this upper limit on the RMS width was determined to be 775 ns via simulation. This cut accepts 99% of true single-interaction vertices, while rejecting 69% of combined multiple-interaction vertices. The remaining events containing S2 pulses composed of combined multiple interaction vertices contribute to the background of events described in Sec. 5.4.

The reconstructed (x', y') position of the first scatter vertex satisfied the neutron energy purity cuts discussed in Sec. 4.1. Forward scatter events were selected by ensuring that the second scatter has a y' position deeper into the liquid xenon along the beam path than the first scatter. The Euclidean distance ρ was defined as the separation of scatter vertices in physical 3D space. A cut ensuring $\rho > 5$ cm removed events with dominant systematic bias in angle reconstruction due to position reconstruction uncertainties.

Maximum signal size cuts on $S1$ and $S2$ were used to reject electron recoil events. The thresholds for these cuts were conservatively informed using NEST v0.98 and NEST v1.0 for electron recoil and nuclear recoil signal yields, respectively [86, 118]. The cut $S1 < 300$ phd accepts >99% of D-D neutron double-scatter events. The cut $S2 < 5000$ phd, applied to both scatters in each event, accepts >99% of all D-D neutron S2 pulses while rejecting all 39.6 keV_{ee} gamma rays from inelastic neutron scatters on ^{129}Xe. The next lowest-energy gamma ray resulting from an inelastic scatter is due to the 80.2 keV_{ee} excitation of ^{131}Xe, which is well outside of the parameter space of interest.

A cut on $S2[y'_2]$ was used to ensure a high efficiency for the detection of the combined S1 signal. A requirement was imposed that $S2[y'_2] > 225$ phd. This minimum cut on $S2[y'_2]$ ensured a 90% efficiency for detecting the combined S1 for double-scatter events due to the summed $S1$ contribution from the second scatter alone. This cut accepts > 70% of underlying double-scatter nuclear recoils before other cuts are applied and is flat as a function of the energy deposited at the first scattering vertex.

For double-scatter events with both vertices within the projection of the neutron conduit, there can be ambiguity as to which vertex occurred first. A cut on $S2[y'_2] < 1500$ phd was effective in removing events in which a first scatter with $\theta \sim 180$ degrees is followed by a second scatter in the cylinder of the beam at smaller y'. Monte Carlo studies demonstrated that this cut accepts 89% of good candidate D-D neutron forward scatter events while rejecting 95% of potential events where the vertices may have been incorrectly ordered by the analysis.

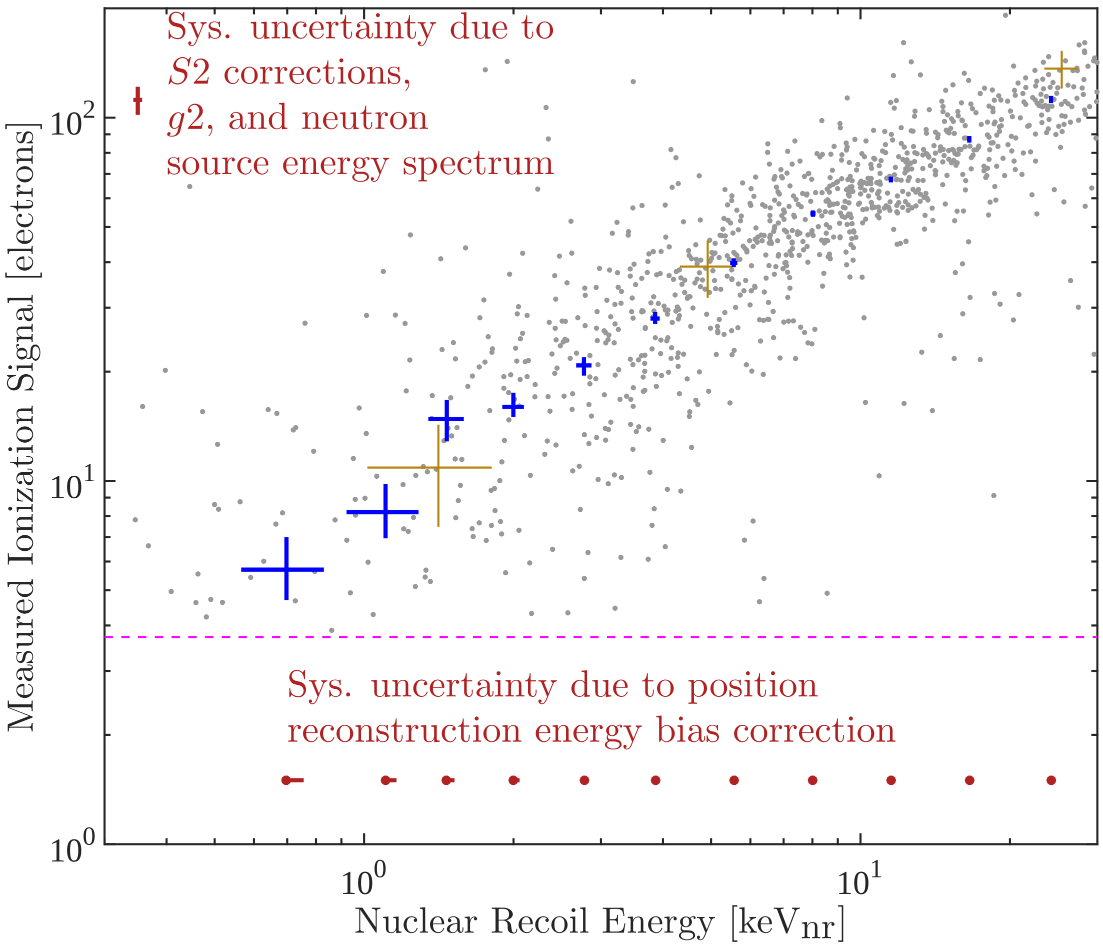

Figure 5.1: The gray points represent the measured ionization signal for each of the 1031 events remaining after all cuts in the double-scatter dataset. The gold crosses illustrate the estimated error associated with the most precisely measured individual events, both in ionization signal (y error) and reconstructed energy (x error). The measured ionization signal for each bin is represented by the blue crosses. As discussed in Sec. 5.2, the mean recoil energy of the event population in each bin, represented by the location of the blue crosses on the horizontal axis, has been corrected for Eddington bias. The red error bars at the bottom of the plot represent the systematic uncertainty associated with this Eddington bias correction.

5.4 Data analysis

The per-event ionization signal is defined as the number of electrons escaping recombination with ions at the interaction site, n_e, for a given recoil energy deposition. The ionization signal was determined for each event by dividing the position-corrected $S2$ by the electron extraction efficiency and by the measured single electron size. The uncertainty on the single electron size is subdominant ($\ll$1%) to other uncertainties in the Q_y analysis. The 1031 events remaining after the application of all cuts are shown as gray points in Fig. 5.1. These events were divided into eleven keV$_{\rm nr}$ bins. The two lowest-energy bins span the regions from 0.3–0.65 keV$_{\rm nr}$ and 0.65–1.0 keV$_{\rm nr}$, respectively. The remaining nine bins are logarithmically spaced from 1–30 keV$_{\rm nr}$. Histograms of the measured distribution of electrons escaping the interaction site for each bin are shown in Fig. 5.2.

In order to determine the energy dependence of the charge yield, the analysis took full account of the statistical fluctuations associated with the ionization signal measurement and their interaction with the S2 threshold. Given an input mean number of ionization electrons that escape recombination, a Monte Carlo based model was used to generate the expected probability distribution of the number of reconstructed electrons at the interaction site. The model is composed of an underlying Poisson distribution convolved with a Gaussian to account for the observed resolution of the ionization distribution. Detector-specific effects including SE size and S2 threshold are included in the model. Liquid xenon purity and electron extraction efficiency effects were applied binomially to the modeled number of ionization electrons to determine the distribution of observed electrons in the xenon gas.

The most significant contribution to the resolution of the ionization distribution is Eddington bias. This arises from uncertainty in reconstructed energy due to the position reconstruction effects described in Sec. 5.1. The expected ionization resolution after Eddington bias effects were addressed was confirmed to have an energy dependence $\propto 1/\sqrt{E_{\rm nr}}$ via simulation (Ch. 6). The resolution in the model, set using the variance of the Gaussian convolution, was determined by fitting the signal model to the seven highest-energy Q_y bins where S2 threshold effects are minimal as shown in Fig. 5.2. An $a/\sqrt{E_{\rm nr}}$ functional form was fit to the measured ionization resolution for these seven bins as shown in Fig. 5.3. The value of the parameter $a \pm \sigma_a$ was measured to be 0.64 ± 0.06 $\sqrt{\rm keV_{nr}}$. The mean of the signal model distribution was an unconstrained nuisance parameter during this maximum-likelihood

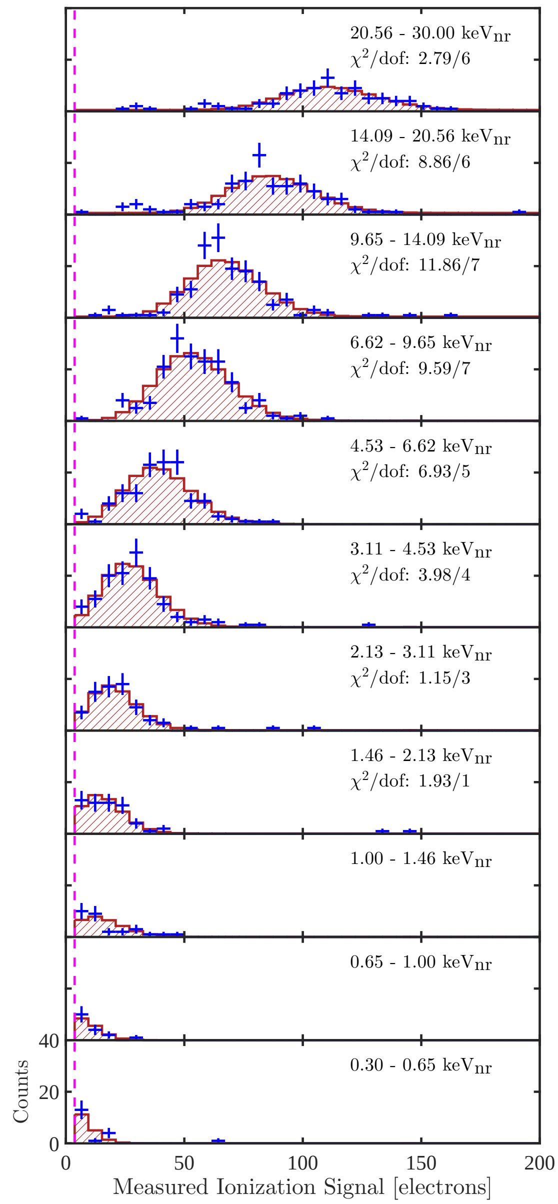

Figure 5.2: Histogram of the measured ionization signal with the best-fit model for each nuclear recoil energy bin. As discussed in Sec. 5.2, the bin boundaries are defined based upon the per-event reconstructed nuclear recoil energy before the Eddington bias correction. Data is shown by the blue crosses with Poisson error bars. The red shaded histogram is the model best-fit to the data in each bin. The best-fit parameters were determined using an unbinned optimization. The ionization signal bins are for visualization and were used to calculate χ^2/dof values for energy bins where dof > 0. The magenta line represents the approximate location of the S2 threshold. The axes limits are the same for each graph.

fit to extract the resolution. The resulting additional uncertainty from this nuisance parameter is reflected in the reported error bars.

After determining the nuclear recoil energy dependence of the energy resolution, the final signal model was fit to each bin. The resulting ionization signal distribution and best-fit model for each bin is shown in Fig. 5.2. The ionization signal model was fit to the observed ionization distribution for each bin using an extended unbinned maximum likelihood optimization, with the modeled resolution implemented as a constrained nuisance parameter [119]. The log-likelihood for the optimization is

$$\ln L = - (N_s + N_b) - \ln (N!) + \ln \left[\frac{1}{\sqrt{2\pi}\sigma_R} e^{-\frac{(R-R_0)^2}{2\sigma_R^2}} \right] + \sum_{i=1}^{N} \ln \left[N_s p_s(x_i|n_e, R) + N_b p_b(x_i) \right], \quad (5.3)$$

where the parameters N_s, N_b, n_e, and R are varied in the optimization. The index i iterates over each event x_i in the particular $\mathrm{keV_{nr}}$ bin, and N is the total observed number of events in the bin. The parameter N_s is the number of signal events, and N_b is the number of background events in the fit. The parameter of primary interest is n_e, the measured number of ionization electrons escaping recombination with ions at the interaction site. The parameter R is the resolution of the reconstructed electron distribution at the interaction site. The parameters n_e and R are inputs to the signal model PDF $p_s(x_i|n_e, R)$, where R functions as a nuisance parameter constrained by the measured resolution best-fit to the seven highest-energy bins as shown in Fig. 5.3. This constraint on R is enforced using the parameters R_0 and σ_R in Eq. 5.3 for each reconstructed energy bin. For each recoil energy bin, these resolution parameters are

$$R_0 = a/\sqrt{E_{\mathrm{nr}}} \quad (5.4)$$

and

$$\sigma_R = \sigma_a/\sqrt{E_{\mathrm{nr}}}\,. \tag{5.5}$$

The parameters a and σ_a were defined earlier based upon the fit in Fig. 5.3.

Events outside the main peak were accommodated by a flat continuum background PDF $p_b(x_i)$. The best-fit number of background events, N_b, accounts for less than 6% of the area in the first nine $\mathrm{keV_{nr}}$ bins and less than 20% in the three highest-energy bins. The classes of events contributing to this background are discussed in Sec. 5.5.

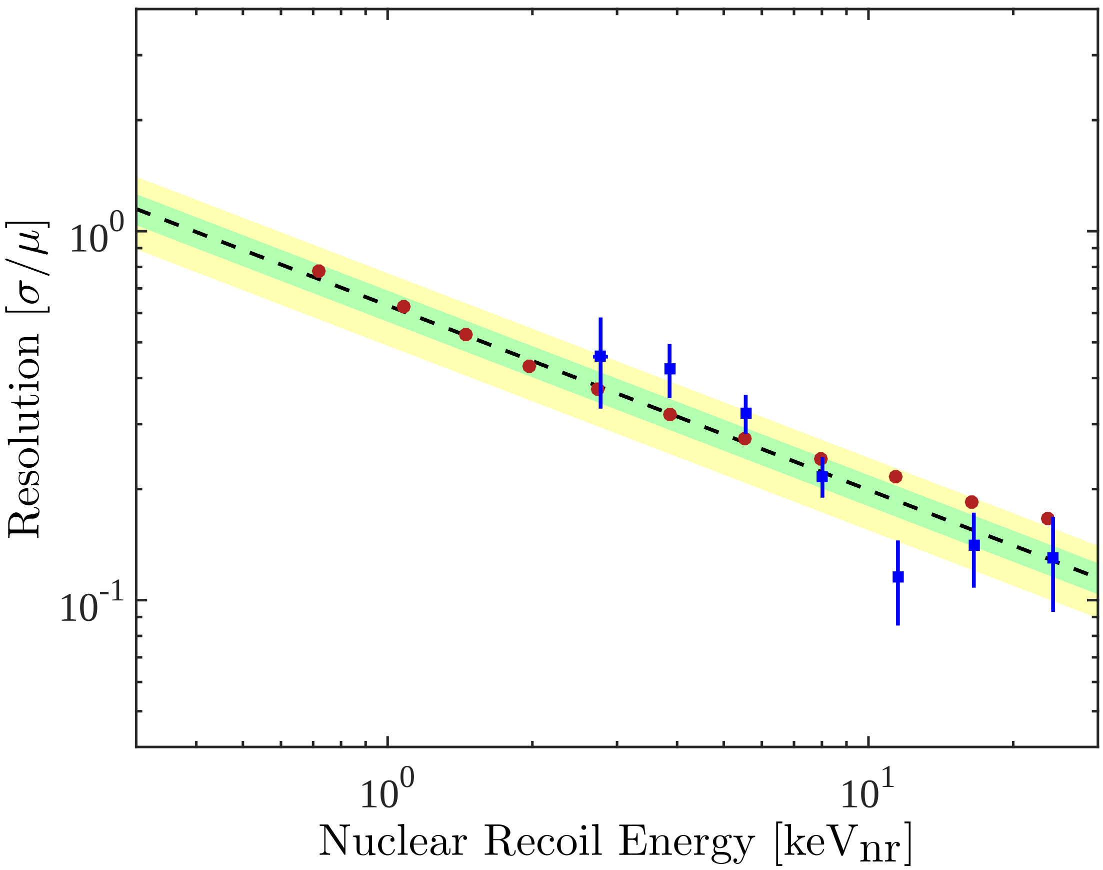

Figure 5.3: The measured resolution, R, of the ionization distributions in the seven highest-energy bins of the double-scatter dataset are represented by the blue squares. The estimated uncertainty in the resolution due to the extraction efficiency is a constant 4% for all energies. The error bars are symmeterized for the fit following the procedure in Ref. [120]. The simulated resolution of the ionization distribution produced by a NEST v1.0 Monte Carlo with modeled position reconstruction uncertainties is represented by the red circles. The black dashed line represents the best-fit to the blue squares given by $R_0 = 0.64/\sqrt{E_{\mathrm{nr}}}$. The fit has a $\chi^2/\mathrm{dof} = 10.6/6$, which corresponds to a p-value of 0.12. The one and two sigma contours on the parameter a are shown in green and yellow, respectively.

The ionization signal model best-fit for each of the eleven bins is shown in Fig. 5.1. The corresponding measured ionization yield is shown in Fig. 5.4. The ionization yield was calculated from the mean ionization signal shown in Fig. 5.1 by dividing each point by the reconstructed nuclear recoil energy to obtain electrons per keV$_{\rm nr}$. The measured ionization yield and associated per-bin uncertainties are shown in Table 5.1.

Table 5.1: Measured ionization yield for nuclear recoils in liquid xenon at 180 V/cm and associated 1σ statistical uncertainties. The systematic uncertainty in energy due to the position reconstruction Eddington bias correction is denoted by $\Delta E_{\rm nr}/E_{\rm nr}$. This uncertainty in energy is represented in Fig. 5.4 by a slanted error bar due to the anti-correlation of the location of the Q_y data points on the vertical axis.

$E_{\rm nr}$ (keV$_{\rm nr}$)	Q_y (e$^-$/keV$_{\rm nr}$)	$\Delta E_{\rm nr}/E_{\rm nr}$ (%)
0.70 ± 0.13	$8.2^{+2.4}_{-2.1}$	$^{+8}_{-2}$
1.10 ± 0.18	$7.4^{+1.9}_{-1.7}$	$^{+5}_{-1.9}$
1.47 ± 0.12	$10.1\ ^{+1.5}_{-1.6}$	$^{+3}_{-1.3}$
2.00 ± 0.10	$8.0^{+0.9}_{-0.6}$	$^{+2}_{-1.3}$
2.77 ± 0.10	$7.5^{+0.5}_{-0.6}$	$^{+2}_{-0.7}$
3.86 ± 0.08	$7.3^{+0.3}_{-0.3}$	$^{+1.3}_{-0.5}$
5.55 ± 0.09	$7.2^{+0.2}_{-0.2}$	$^{+0.7}_{-0.2}$
8.02 ± 0.10	$6.8^{+0.2}_{-0.17}$	$^{+0.16}_{-0.05}$
11.52 ± 0.12	$5.88^{+0.12}_{-0.13}$	$^{+0.13}_{-0.3}$
16.56 ± 0.16	$5.28^{+0.11}_{-0.13}$	$^{+0.2}_{-0.7}$
24.2 ± 0.2	$4.62^{+0.13}_{-0.10}$	$^{+0.4}_{-1.0}$

To verify the consistency of the measured yields with the observed absolute event rate, we performed a LUXSim/GEANT4 based neutron double-scatter simulation using the NEST model described in Sec. 9.2 [122, 123]. This simulation used a model of the full calibration conduit geometry with the neutron source external to the water tank. Simulated per-channel waveforms were produced for each Monte Carlo event. The simulated waveform data were reduced using the standard experimental LUX D-D data processing and analysis pipeline.

The event rate in each Q_y analysis bin is shown in Fig. 5.5 for both data and simulation. The

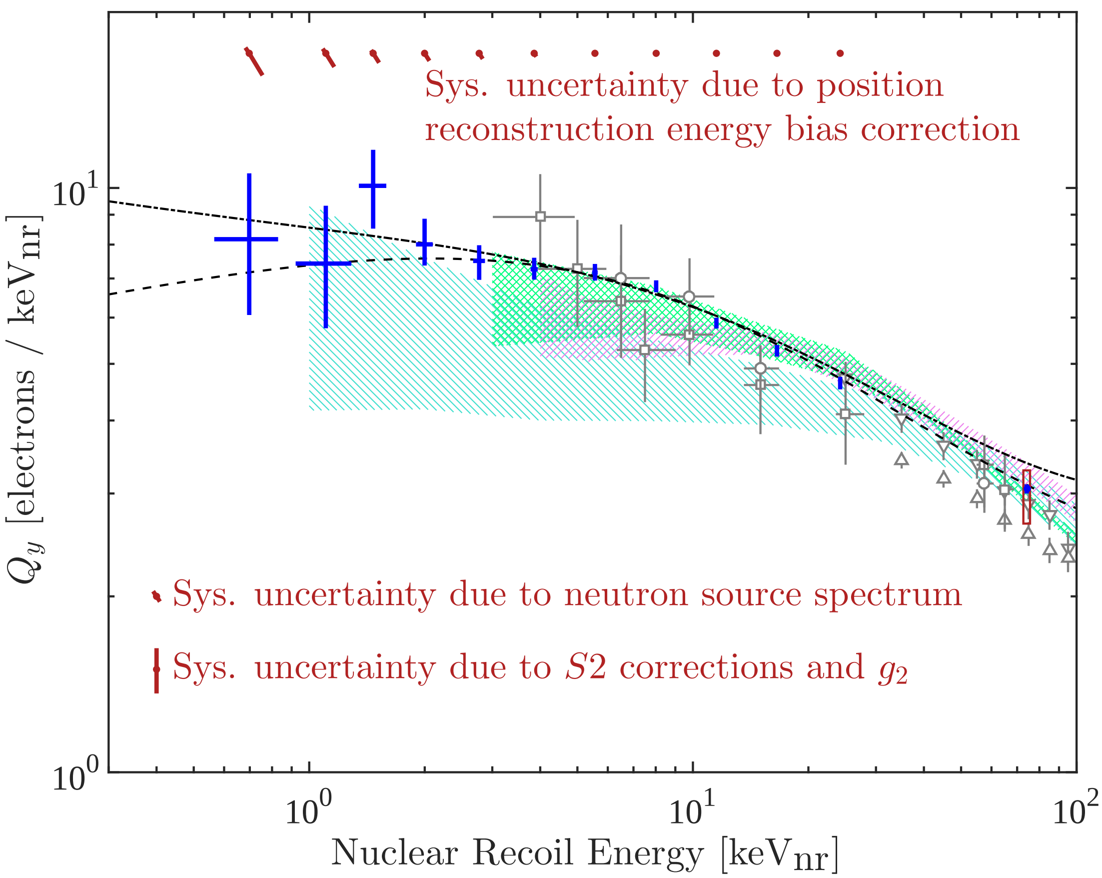

Figure 5.4: The LUX measured low-energy ionization yield at 180 V/cm is represented by the blue crosses. The red error bars at the bottom left of the plot represent systematic uncertainties with a constant scaling across all points, including the uncertainty in the mean neutron energy from the D-D source, $S2$ position-based corrections, and the LUX measured g_2. The red error bars at the top of the plot represent the systematic uncertainty associated with the Eddington bias correction for the mean energy of each bin due to position reconstruction uncertainties as determined by simulation. The red box represents the associated systematic uncertainty on the measured endpoint yield at 74 keV$_{\mathrm{nr}}$. The gray data points represent other angle based measurements with an absolute (keV$_{\mathrm{nr}}$) energy scale. The gray squares (□) and circles (◯) correspond to measurements at 1 kV/cm and 4 kV/cm, respectively [18]. The gray triangles were measured at 0.3 kV/cm (▽) and 0.1 kV/cm (△) [121]. The hatched bands represent simulated spectrum based measurements with a best-fit (keV$_{\mathrm{nr}}$) energy scale. The purple single right-hatched (///) band was measured at an average field of 3.6 kV/cm [15]. The teal single left-hatched (\\\\) band corresponds to a measurement at 730 V/cm [70]. The green cross-hatched band was measured at 530 V/cm [16]. The dashed (dot-dashed) black line corresponds to the Lindhard-based (Bezrukov-based) LUX best-fit NEST model as described in Sec. 9.2.

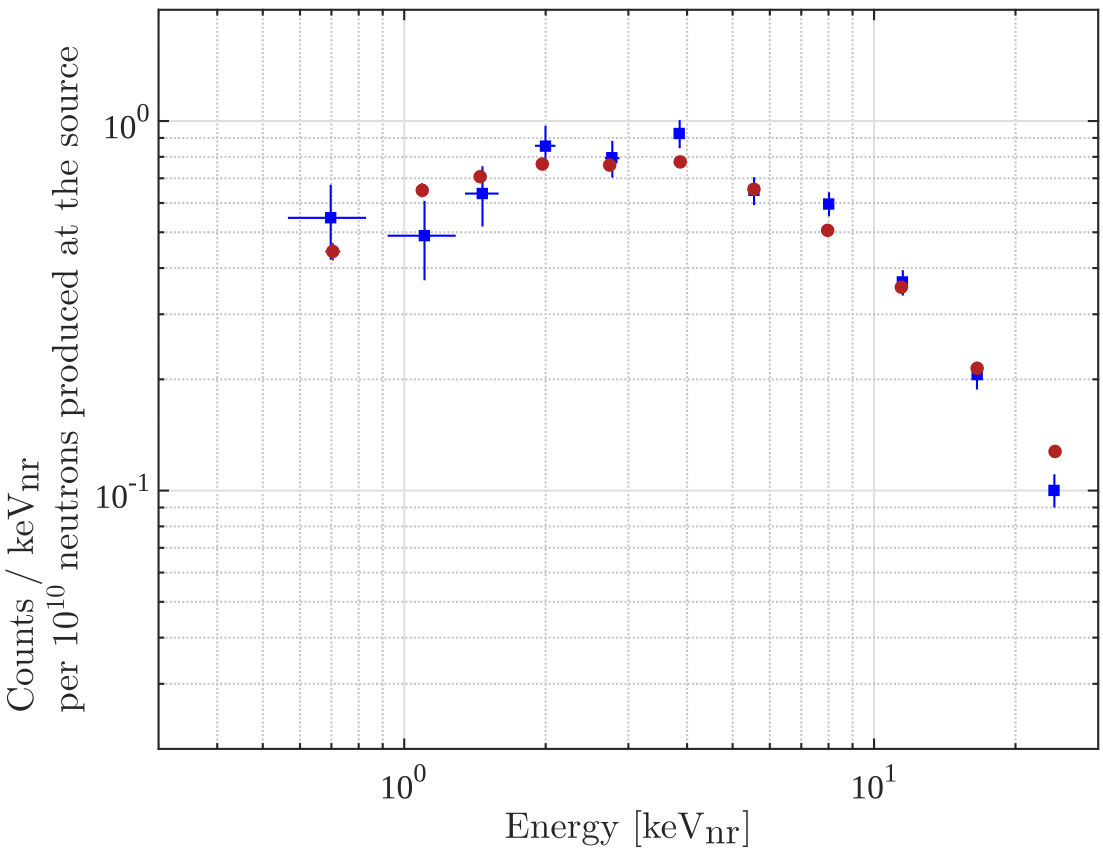

Figure 5.5: The observed rate of double-scatter neutron events in the Q_y analysis is represented by the blue squares. An identical analysis of simulated waveforms produced by LUXSim/GEANT4 using the LUX measured nuclear recoil signal yields was performed. The results are shown as red circles. The simulation statistical error bars are smaller than the size of the data points unless otherwise depicted. The results are normalized by the number of neutrons produced by the D-D source outside the water tank. The χ^2/dof value is 14.6/10 based upon statistical uncertainties only, which yields a p-value of 0.15.

data and simulation results were normalized by the total number of neutrons produced at the D-D source outside the water shield. For consistency with the other yield results, the simulation data points were updated to use the more modern angular scattering cross-sections from the JENDL-4 nuclear databases instead of G4NDL3.14. The absolute value of the correction factor was $\leq$1% for energy bins up to 5.55 keV$_{\mathrm{nr}}$ and was a maximum of 5% at 24.2 keV$_{\mathrm{nr}}$. The best agreement was achieved assuming an isotropic neutron source rate of 2.6×10^6 n/s for the data normalization, which is in agreement with the independently measured source rate of $(2.5 \pm 0.3) \times 10^6$ n/s. This agreement between the data and simulation in both absolute rate and shape confirms the consistency of the LUX D-D measured yields and the number of events seen in the double-scatter data at nuclear recoil energies as low as 0.7 keV$_{\mathrm{nr}}$.

5.5 Background and uncertainties

There are five classes of events that contribute to the continuum background observed outside of the signal peaks in Fig. 5.2. The common quality of continuum background events is that the measured angle is not directly related to the true recoil energy at the first scattering vertex.

i. The first class consists of three or more scatter events classified as two scatter events. These occur when the pulse finding algorithm combines two S2 pulses that are close in z position. The S2 pulse width cut preferentially removes events with combined S2 signals, while having an average acceptance of 94% for legitimate double-scatters after all other cuts are applied. The corresponding acceptance of legitimate double-scatter events with a first vertex nuclear recoil energy of $<$2 keV$_{\mathrm{nr}}$ and $<$1 keV$_{\mathrm{nr}}$ is 86% and 80%, respectively.

ii. The second class contains events that have $>$2 scatters, but only two of the scatters are above the 36 phd raw S2 threshold. As for the first class of events, if this was a dominant effect the observed mean path length between scatters would be longer than expected based upon the predicted mean free path of 2.45 MeV neutrons in liquid xenon. The measured mean path between double scatter events was demonstrated to be consistent with simulation using the total and elastic scattering cross-sections from JENDL-4 as shown in Sec. 6.5.

iii. The third class consists of events that scatter once within the neutron beam projection in the TPC, then scatter in passive detector materials, and then finally scatter again in the active liquid xenon volume. This is effectively a 3+ scatter event that is identified as a two scatter event.

iv. The fourth class of events is the accidental coincidence of delayed electron emission (SE or small S2) classified as the first scatter, with a legitimate single-scatter neutron event classified as the second scatter. The measured background rate of random small S2 pulses indicates that $\ll$0.1% of events in the Q_y dataset after the analysis volume constraints and pulse area thresholds for $S2[y_1']$ and $S2[y_2']$ are this type of accidental coincidence.

v. The fifth class of events are produced by the small number of incident neutrons that have lost a significant fraction of their energy in passive detector materials but pass the energy purity cuts. The nuclear recoil energy bins are determined by scattering angle, so this is a unidirectional effect that could produce a $\sim$5% excess of events at lower ionization signal in a given bin. It is possible that some evidence of this effect is seen in the high-energy bins in Fig. 5.2. It is worth noting that due to the absolute angle based energy scale neutrons that have lost energy in passive materials can only suppress the measured charge yield.

Table 5.1 contains the statistical errors for the reconstructed energy and the measured Q_y as returned by the maximum-likelihood optimization. The reported errors on the measured Q_y values were extracted from the log-likelihood contour accounting for variations in all four parameters in the fit. The third column contains the systematic uncertainty in energy due to the Eddington bias correction. Systematic uncertainties common to all bins in the low-energy ionization yield measurement and endpoint Q_y measurement are listed in Table 5.2.

The systematic uncertainty in Q_y due to the S2 threshold was confirmed to be subdominant to other quoted uncertainties by varying the modeled threshold by 10% and repeating the fitting procedure. The low-energy Q_y analysis was repeated using a smaller fiducial analysis volume ensuring that $r < 21$ cm and $30 <$ drift time < 290 μs to test potential systematic effects associated with the choice of analysis volume. The results of this check for systematic effects are within the quoted 1σ statistical uncertainties in Table 5.1. The systematic uncertainty in the reconstructed energy due to the variation in the atomic mass and cross-section over xenon isotopes with significant natural abundance was estimated to be <2% for all energies [124].

Table 5.2: Uncertainties common to the Q_y measurement both at low energies and at the D-D recoil energy spectrum endpoint. The second column lists systematic uncertainties associated with the mean reconstructed ionization signal n_e. The third column lists systematic uncertainties associated with the mean reconstructed energy E_{nr}. Quoted uncertainties are symmetric ($\pm$) unless otherwise indicated.

Source of Uncertainty	$\Delta n_e/n_e$ (%)	$\Delta E_{\mathrm{nr}}/E_{\mathrm{nr}}$ (%)
SE size	$\ll$1	-
e^- extraction efficiency	8	-
$S2$ correction (3D position)	2.5	-
$S2$ correction (non-uniform field)	$^{+0}_{-2.5}$	-
Mean neutron energy from source	-	2
Total	$^{+8}_{-9}$	2

Chapter 6

Study of Position Reconstruction Effects on the Low-Energy Nuclear Recoil Ionization Yield Measurement

This chapter provides additional supplementary information on the energy reconstruction technique used for the low-energy nuclear recoil ionization yield measurement in Ch. 5. In addition, some of the simulation based studies contained within this chapter are relevant to the single-scatter signal yield analyses reported in Ch. 7 and Ch. 8.

In Sec. 6.1 of this chapter, we first outline the calculations used for the reconstruction of the scattering angle in double-scatter neutron events and for the estimation of the associated uncertainties. We include the calculation of the per-event energy, and the weighting scheme used to determine the mean recoil energy in each bin of the Q_y analysis. In Sec. 6.2, we describe the expected bias in recoil energy reconstruction arising from position reconstruction uncertainties. In Sec. 6.3, we provide an outline of the simulation framework created to study these bias effects. In Sec. 6.4 and Sec. 6.5, we use the targeted simulation to verify analysis algorithms and demonstrate consistency between simulation and data. In Sec. 6.6, we use the simulation to study the effect of physical boundaries of the liquid xenon volume on the observed underlying neutron recoil energy spectrum. In Sec. 6.7, the simulation-based corrections for the described bias effects due to position reconstruction are reported.

6.1 Nuclear recoil energy reconstruction from scattering angle

The (x, y) position of each scattering vertex is measured from the S2 hit-pattern in the top PMT array using the Mercury algorithm [38]. The z position of each scattering vertex is determined based upon the measured drift time between the S1 and S2 pulses using the measured 1.51 mm/μs electron drift velocity. More detail on the observed signals and event reconstruction is presented in Sec. 2.3.1.

The positions of the first and second neutron interactions are reconstructed for the double-scatter event population used in the Q_y analysis described in Ch. 5. The measure of the scattering angle gives an absolute determination of the recoil energy at the first scattering vertex according to Eq. 1.1, which allows for the direct calibration of the observed S2 signal for that vertex. This technique provides a direct, absolute measurement of the recoil energy and associated uncertainties for each event. The Q_y analysis obtains maximal statistical leverage when determining the mean recoil energy of each bin by preferentially weighting the most precisely measured events.

6.1.1 Per-event nuclear recoil energy reconstruction from scattering angle

For a given neutron double-scatter event used in the Q_y analysis described in Ch. 5, the scattering angle was calculated by defining vectors along the neutron path before and after the first scatter in the liquid xenon:

$$\begin{aligned} \vec{v}_1 &= \vec{x}_1 - \vec{x}_0 \\ \vec{v}_2 &= \vec{x}_2 - \vec{x}_1 \,, \end{aligned} \tag{6.1}$$

where $\vec{x}_0 = (x_0, y_0, z_0)$, $\vec{x}_1 = (x_1, y_1, z_1)$, and $\vec{x}_2 = (x_2, y_2, z_2)$. The vector $\vec{x}_0$ is the position of the neutron beam entrance into the liquid xenon active region: $(x_0, y_0, z_0) = (7.1, -23.0, -16.1)$ in units of cm. The vector $\vec{x}_1$ is the position of the first scatter and $\vec{x}_2$ is the position of the second scatter. The scattering angle in the lab frame at the first scattering vertex was then directly determined using the law of cosines:

$$\theta_{\mathrm{lab}} = \cos^{-1}\left(\frac{\vec{v}_1 \cdot \vec{v}_2}{|\vec{v}_1||\vec{v}_2|}\right) \,, \tag{6.2}$$

where θ_{lab} is the scattering angle between the first and second scatter positions in the lab frame. We then used Eq. 1.1 to determine the energy deposited at the first scattering vertex. As discussed in Sec. 1.1, the deviation between θ_{lab} and θ_{CM} for neutron induced nuclear recoils in xenon is <2% for all scattering angles.

6.1.2 Uncertainty on the per-event recoil energy reconstruction

The uncertainties in the x and y scattering vertex positions were parameterized as a function of raw $S2$ and are used in the analysis in this chapter. The calculation of the position reconstruction uncertainty for each event and the corresponding calculation of recoil energy are described in this section.

6.1.2.1 Uncertainty on reconstructed vertex position

While the x and y positions are directly returned by the Mercury algorithm for each scattering vertex in Cartesian coordinates, the uncertainties in position are returned in polar coordinates. We translate the reported per-event uncertainties into the standard Cartesian coordinate system using the following described prescription.

The radial position uncertainty, σ_r, is defined as the uncertainty in the reconstructed vertex position along the radial direction in the TPC as determined using the χ^2 contour obtained during the optimization performed by the Mercury algorithm. This σ_r quantity is the average of the "sd_radius_inf" and "sd_radius_sup" distances shown in Fig. 6.1. The polar uncertainty, σ_{polar}, is the uncertainty in the direction perpendicular to the radial direction obtained using the same procedure. These variables do not correspond to the 1σ uncertainties in the polar coordinates; instead they represent the semi-major and semi-minor axes of the ellipse that is populated by 68% of events [125].

The mean value of the σ_r and σ_{polar} uncertainties as returned by the Mercury algorithm are monotonically decreasing as function of raw $S2$. A lookup table was generated based upon a detailed study of the raw $S2$ dependence of the polar and radial uncertainties [126]. This lookup table is used for efficient simulation of position reconstruction effects and is used in the simulation described in Sec. 6.3.

The definitions in Eq. 6.3 describe the conversations between the polar and rectangular coordinate systems:

$$\begin{aligned} x &= r\cos\phi \\ y &= r\sin\phi \\ r &= \sqrt{x^2+y^2} \\ \phi &= \tan^{-1}\left(\tfrac{y}{x}\right) \\ \sigma_\phi &= \tfrac{\sigma_{\text{polar}}}{r}\,. \end{aligned} \tag{6.3}$$

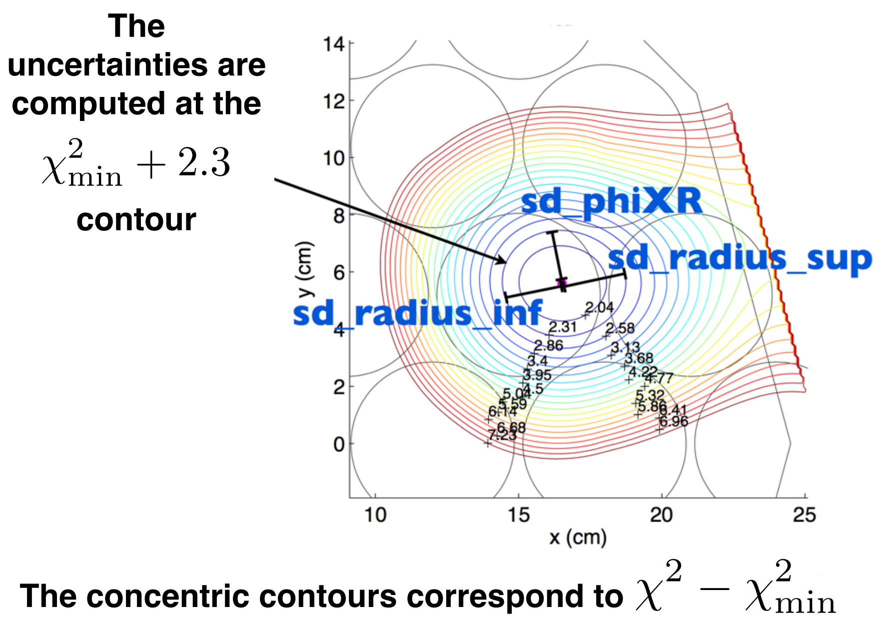

Figure 6.1: The 1σ uncertainties in position returned by the Mercury algorithm. Our radial uncertainty, σ_r, is the average of the radial uncertainty toward the wall (sd_radius_sup) and the radial uncertainty toward the center of the detector (sd_radius_inf). Our polar uncertainty is given by "sd_phiXR". This figure courtesy of Claudio Silva from the LUX collaboration.

We convert from σ_{polar}, which is in units of cm, to σ_ϕ, which has units of radians. The variable σ_ϕ is dependent upon the radial position of the event in the TPC. Taking the derivative of the equations for x and y with respect to r and ϕ yields

$$\begin{aligned}\tfrac{dx}{dr} &= \cos\phi \\ \tfrac{dx}{d\phi} &= -r\sin\phi \\ \tfrac{dy}{dr} &= \sin\phi \\ \tfrac{dy}{d\phi} &= r\cos\phi\,. \end{aligned} \tag{6.4}$$

We convert the uncertainties for each event from polar coordinates to rectangular coordinates via the relations in Eq. 6.5. The factor of 1/2 is due to the conversion from the uncertainty in the semi-major and semi-minor axes of the contour containing 68% of events to standard 1σ uncertainties in the x and y coordinates [126].

$$\begin{aligned}\sigma_x^2 &= \tfrac{1}{2}\left[\left(\tfrac{dx}{dr}\right)^2\sigma_r^2 + \left(\tfrac{dx}{d\phi}\right)^2\sigma_\phi^2\right] \\ \sigma_y^2 &= \tfrac{1}{2}\left[\left(\tfrac{dy}{dr}\right)^2\sigma_r^2 + \left(\tfrac{dy}{d\phi}\right)^2\sigma_\phi^2\right]\,. \end{aligned} \tag{6.5}$$

The uncertainties in the reconstructed x and y positions are shown in Fig. 6.2 as a function of raw $S2$. For S2 signals produced by 2.45 MeV D-D neutrons, the x and y coordinates typically have a $\sim$1 cm 1σ statistical uncertainty. At the raw $S2 > 33$ threshold, the 1σ statistical uncertainty in the reconstructed x and y positions increases to $\sim$2 cm For comparison, the uncertainties in the principal axes of the $\chi^2_{\text{min}}+2.3$ contour, σ_r and σ_{polar}, as directly reported by the Mercury algorithm are also included in the figure.

The uncertainty in the reconstructed z position of the interaction has an estimated 1σ statistical uncertainty of 0.1 cm [37]. The (x, y, z) uncertainty in $\vec{x}_0$, the center of the entry point for the projection of the neutron tube into the active region of the LUX detector, was estimated to be 0.6 cm in each dimension by fitting the beam profile in the D-D data [127].

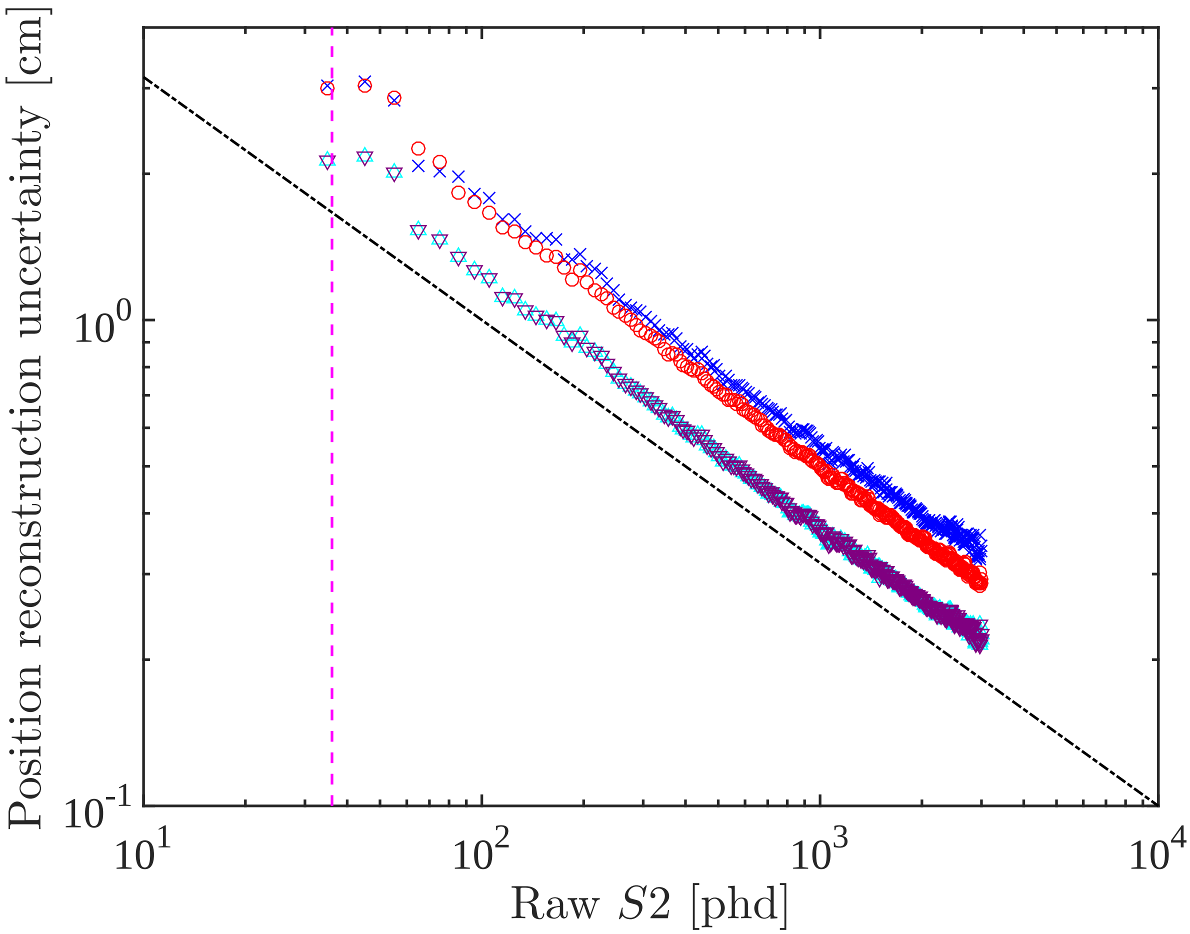

Figure 6.2: The average statistical uncertainty in reconstructed position as a function of raw $S2$ size as determined by the Mercury algorithm. The blue ($\times$) and red ($\circ$) data points correspond to the statistical uncertainty in principal axes along the radial (σ_r) and polar (σ_{polar}) directions, respectively, of the $\chi^2_{\text{min}} + 2.3$ contour containing 68% of events. The cyan ($\triangle$) and purple ($\bigtriangledown$) data points are produced by transforming the polar coordinate uncertainties using Eq. 6.5 and correspond to σ_x and σ_y, respectively. The black dot-dashed line is the function $A/\sqrt{S2}$ (using raw $S2$). This line is intended to be a visual reference for the slope of the data only. The scaling factor A was arbitrarily set to 10 for this comparison. The magenta dashed line indicates the location of the 36 phd raw $S2$ threshold used for the Q_y analysis. The underlying data was provided by Claudio Silva.

In addition to the statistical position reconstruction uncertainties, we add an additional systematic component to σ_r and σ_{polar}. The best estimate of this systematic component is $\sigma_{(x,y)} = 0.35$ cm [126]. For several of the analyses reported in this chapter, we vary $\sigma_{(x,y)}$ from 0.00–0.70 cm to include an estimate of the uncertainty in position reconstruction systematic. The additional systematic uncertainty values used were determined by a detailed study of the position reconstruction algorithm.

6.1.2.2 Uncertainty on angle and recoil energy reconstruction

The uncertainty in the reconstructed scattering angle for each double-scatter event (and thus reconstructed recoil energy) can be calculated by directly propagating the uncertainty in the reconstructed (x, y, z) position of both neutron interaction sites through Eq. 6.2 using standard error propagation techniques. To do this, we define the individual components of $\vec{v}_1$ and $\vec{v}_2$ as

$$\begin{aligned}\vec{v}_1 &= (a_1, b_1, c_1) = (x_1 - x_0, y_1 - y_0, z_1 - z_0)\\ \vec{v}_2 &= (a_2, b_2, c_2) = (x_2 - x_1, y_2 - y_1, z_2 - z_1)\,.\end{aligned} \tag{6.6}$$

We then rewrite Eq. 6.2 in Cartesian coordinates:

$$\theta_{\text{lab}} = \cos^{-1}\left(\frac{a_1 a_2 + b_1 b_2 + c_1 c_2}{\sqrt{a_1^2 + b_1^2 + c_1^2}\sqrt{a_2^2 + b_2^2 + c_2^2}}\right). \tag{6.7}$$

The choice of coordinates in Eq. 6.7 serves to allow for a more straightforward calculation in the coming steps. The associated uncertainties in $\vec{v}_1$ and $\vec{v}_2$ can be calculated using

$$\begin{aligned}\sigma_{\vec{v}_1} &= \sqrt{\sigma_{x_0}^2 + \sigma_{x_1}^2}\,\hat{x} + \sqrt{\sigma_{y_0}^2 + \sigma_{y_1}^2}\,\hat{y} + \sqrt{\sigma_{z_0}^2 + \sigma_{z_1}^2}\,\hat{z}\\ \sigma_{\vec{v}_2} &= \sqrt{\sigma_{x_1}^2 + \sigma_{x_2}^2}\,\hat{x} + \sqrt{\sigma_{y_1}^2 + \sigma_{y_2}^2}\,\hat{y} + \sqrt{\sigma_{z_1}^2 + \sigma_{z_2}^2}\,\hat{z}\,.\end{aligned} \tag{6.8}$$

We use the relations in Eq. 6.8 to calculate the uncertainty on θ_{lab} as

$$\sigma_{\theta_{\text{lab}}} = \sqrt{\left|\sigma_{\vec{v}_1} \odot \frac{d\theta}{d\vec{v}_1}\right|^2 + \left|\sigma_{\vec{v}_2} \odot \frac{d\theta}{d\vec{v}_2}\right|^2}\,, \tag{6.9}$$

where the $\odot$ operation indicates component-wise multiplication and results in a vector. The derivative of θ_{lab}, as shown in Eq. 6.7, with respect to a_1 is

$$\frac{d\theta_{\text{lab}}}{da_1} = \frac{-1}{\sqrt{1-\left(\frac{\vec{v}_1\cdot\vec{v}_2}{|\vec{v}_1||\vec{v}_2|}\right)^2}}\left(\frac{a_2}{|\vec{v}_1|^2|\vec{v}_2|^2} - \frac{a_1(\vec{v}_1\cdot\vec{v}_2)}{|\vec{v}_1|^3|\vec{v}_2|^1}\right). \tag{6.10}$$

This can be rewritten to include all three dimensions by symmetry:

$$\begin{aligned}\frac{d\theta_{\text{lab}}}{d\vec{v}_1} &= \frac{-1}{\sqrt{1-\left(\frac{\vec{v}_1\cdot\vec{v}_2}{|\vec{v}_1||\vec{v}_2|}\right)^2}}\left(\frac{\vec{v}_2}{|\vec{v}_1|^2|\vec{v}_2|^2} - \frac{\vec{v}_1(\vec{v}_1\cdot\vec{v}_2)}{|\vec{v}_1|^3|\vec{v}_2|^1}\right)\\ \frac{d\theta_{\text{lab}}}{d\vec{v}_2} &= \frac{-1}{\sqrt{1-\left(\frac{\vec{v}_1\cdot\vec{v}_2}{|\vec{v}_1||\vec{v}_2|}\right)^2}}\left(\frac{\vec{v}_1}{|\vec{v}_1|^2|\vec{v}_2|^2} - \frac{\vec{v}_2(\vec{v}_1\cdot\vec{v}_2)}{|\vec{v}_1|^1|\vec{v}_2|^3}\right).\end{aligned} \tag{6.11}$$

The uncertainty on the reconstructed nuclear recoil energy at the first neutron scattering vertex is then given by combining Eq. 6.9 and Eq. 6.11.

$${\sigma_{E_{\text{nr}}}}^2 = \left[\frac{2\sigma_{E_n} m_n m_{\text{Xe}}}{(m_n+m_{\text{Xe}})^2}(1-\cos\theta_{\text{lab}})\right]^2 + \left[\frac{2E_n m_n m_{\text{Xe}}}{(m_n+m_{\text{Xe}})^2}\sin\theta_{\text{lab}}\sigma_{\theta_{\text{lab}}}\right]^2. \tag{6.12}$$

6.1.3 Reconstruction of the mean nuclear recoil energy in each bin

The mean energy of each bin—and thus the horizontal axis position of each corresponding data point—used for the Q_y analysis described in Ch. 5 is determined using a weighted average to maximally leverage the individual double-scatter events with the most precisely measured nuclear recoil energy. The individual weight given to each event, w_i, is determined by the reciprocal of the squared 1σ uncertainty on the reconstructed recoil energy for the event, $\sigma_{E_{\text{nr}},i}$, as calculated using Eq. 6.12:

$$w_i = \frac{1}{\left(\sigma_{E_{\text{nr}},i}\right)^2}. \tag{6.13}$$

The best estimate of the mean bin energy, $\langle E_{\text{nr}}\rangle$, is then determined by taking the weighted average over all events in the given bin of reconstructed recoil energy:

$$\langle E_{\text{nr}}\rangle = \frac{\sum_i\left(w_i E_{\text{nr},i}\right)}{\sum_i w_i}, \tag{6.14}$$

where $\sum_i$ denotes a sum across all events and $E_{\mathrm{nr},i}$ is the per-event reconstructed recoil energy given by Eq. 1.1. The uncertainty on the weighted mean energy in each bin, $\sigma_{\langle E_{\mathrm{nr}} \rangle}$, is then calculated as

$$\sigma_{\langle E_{\mathrm{nr}} \rangle} = \frac{1}{\sqrt{\sum_i w_i}} \, . \tag{6.15}$$

The dominant effect contributing to $\sigma_{E_{\mathrm{nr}},i}$ is the uncertainty in the reconstructed (x, y) positions of the two neutron interactions. In particular, the error in the (x, y) position of the first scatter vertex is the most significant contributor to the overall error in the reconstructed event recoil energy. This is intuitive because uncertainty in the first scattering vertex affects the accuracy of both vectors $\vec{v}_1$ and $\vec{v}_2$, while variation in the second scattering vertex only affects the determination of $\vec{v}_2$.

The events that are weighted most heavily in the mean recoil energy calculation are those with the smallest estimated uncertainty in the reconstructed energy. There are two qualities that determine the most precisely measured events. First, and most significantly, due to the dominant (x, y) reconstruction uncertainty, double-scatter vertices that are primarily separated along the more precisely measured z (drift time) dimension have a smaller uncertainty on the measured scattering angle. Second, events with a larger distance between the first and second scattering vertices have a longer lever arm to determine the scattering angle relative to the magnitude of the uncertainty in the reconstructed vertex positions. As a consequence of these effects, we expect that the most precisely measured events preferentially scatter within the z–y' plane and have long path lengths between the first and second neutron interactions.

The distance between vertex positions for for all double-scatter events used in the Q_y analysis from Ch. 5 are shown for each bin in Fig. 6.3 (0.3–1.5 keV$_{\mathrm{nr}}$), Fig. 6.4 (1.5–4.5 keV$_{\mathrm{nr}}$), Fig. 6.5 (4.5–14.1 keV$_{\mathrm{nr}}$), and Fig. 6.6 (14.1–30 keV$_{\mathrm{nr}}$). The left column of plots shows the projection onto the Δx vs. Δy plane while the right column of plots shows the corresponding projection onto the Δz vs. Δy plane for each bin. The variable Δx is defined as $x_2 - x_1$; Δy and Δz are defined similarly. The color scale indicates the uncertainty in the reconstructed nuclear recoil energy as calculated using Eq. 6.12. The color scale is the same for each graph. The five events with the smallest uncertainty in recoil energy for each bin are circled in red. As expected, the most precisely measured events typically have large $|\Delta z|$ and a long path length between the first and second scatter vertices.

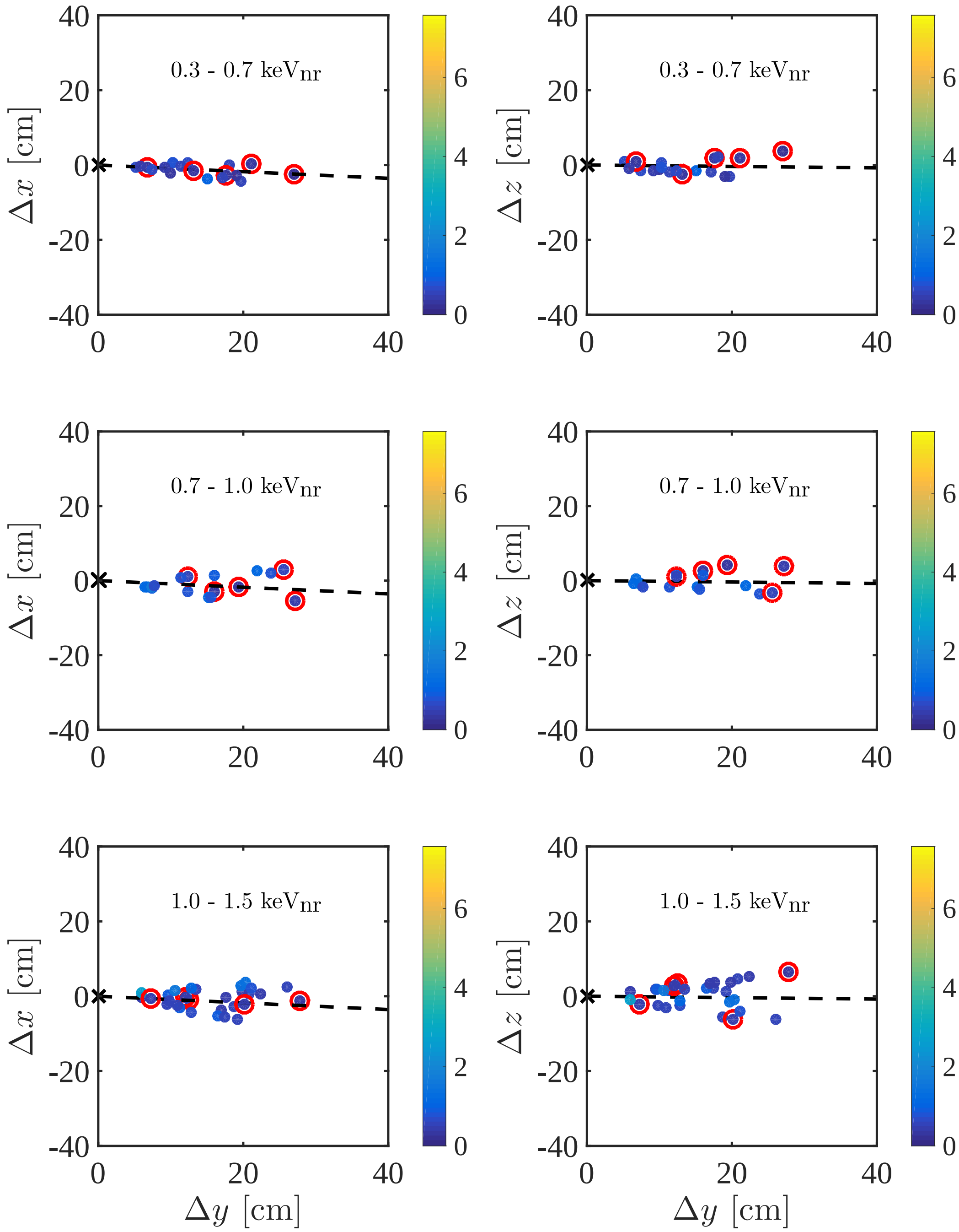

Figure 6.3: Scatter plots showing the x, y, and z separation of the interaction vertices in the double-scatter event population used for the Q_y analysis. All events are translated in space so that the first scatter is at the origin as shown by the black $\times$. The black dashed line represents the center of the neutron conduit projection into the liquid xenon. The first three reconstructed nuclear recoil energy bins spanning the range 0.3–1.5 keV$_{\mathrm{nr}}$ are shown in this plot. The left column of plots shows the projection onto the Δx vs. Δy plane. The right column of plots shows the projection onto the Δz vs. Δy plane. The color bar represents the per-event uncertainty in the reconstructed energy in units of keV$_{\mathrm{nr}}$. The color bar scale is identical for each plot. The red circles surround the five events with the most precisely measured recoil energy.

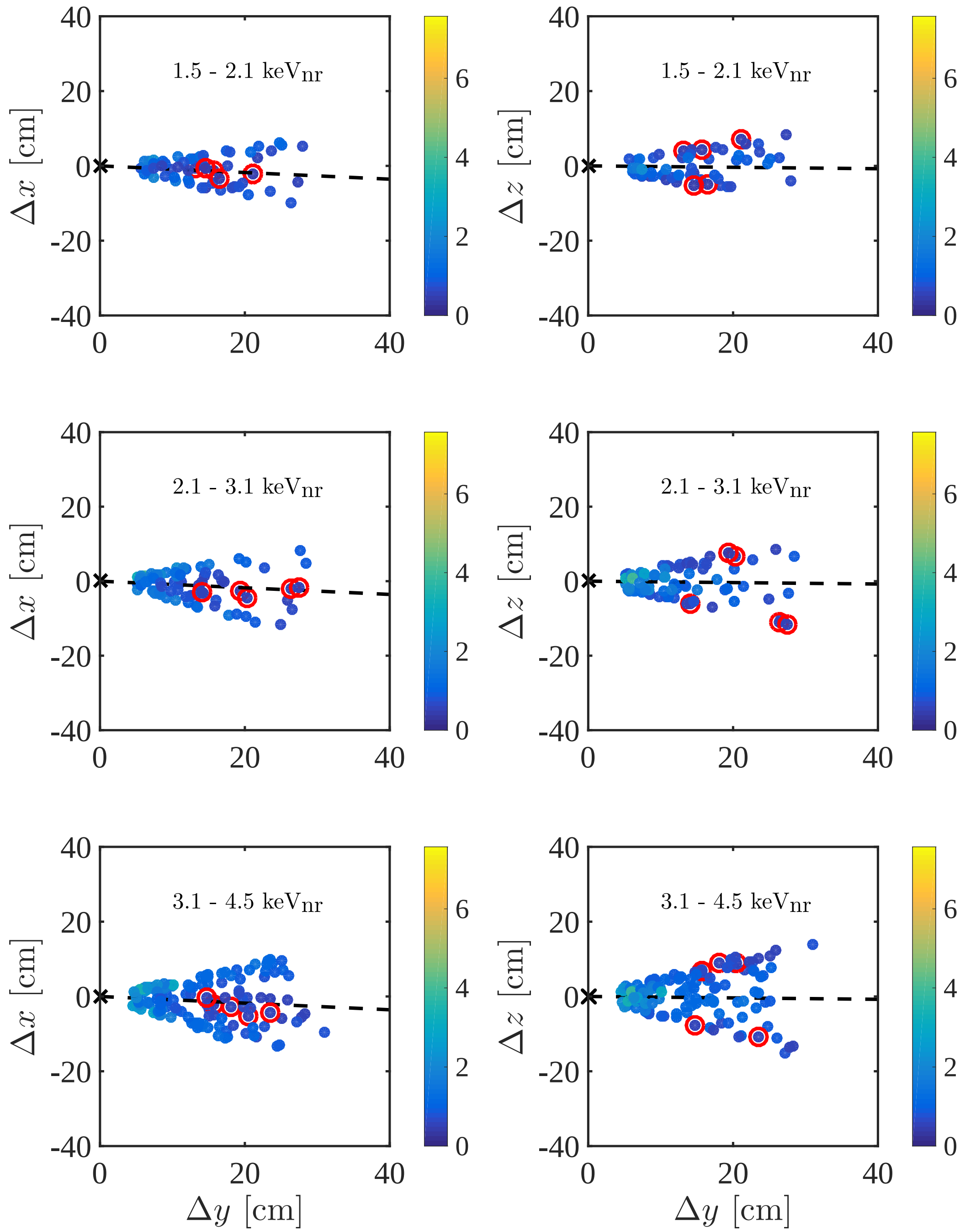

Figure 6.4: (Same as Fig 6.3, except for energy range of bins.) The three reconstructed nuclear recoil energy energy bins spanning the range 1.5–4.5 keV$_{\rm nr}$ are shown in this plot.

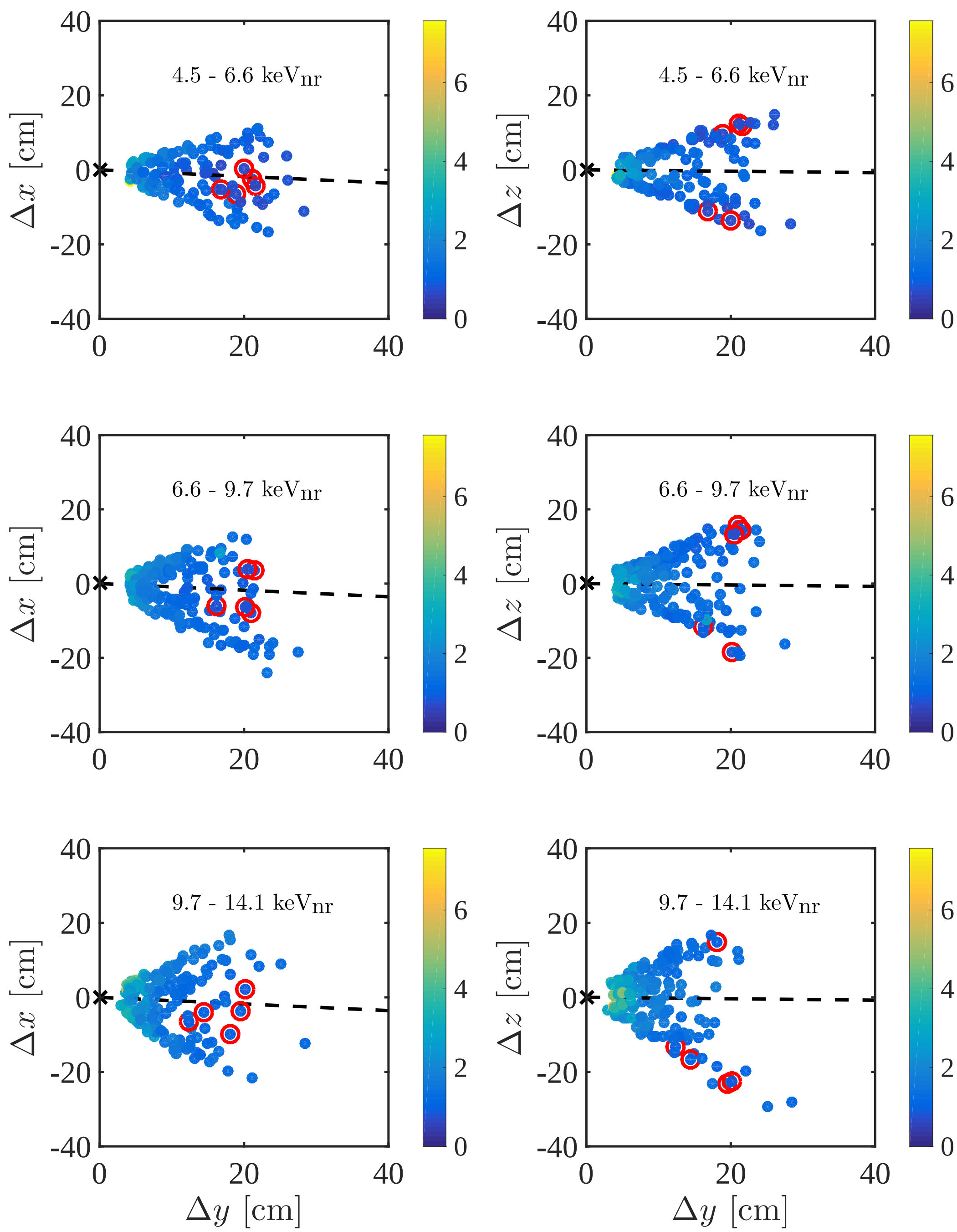

Figure 6.5: (Same as Fig 6.3, except for energy range of bins.) The three reconstructed nuclear recoil energy energy bins spanning the range 4.5–14.1 keV$_{\mathrm{nr}}$ are shown in this plot.

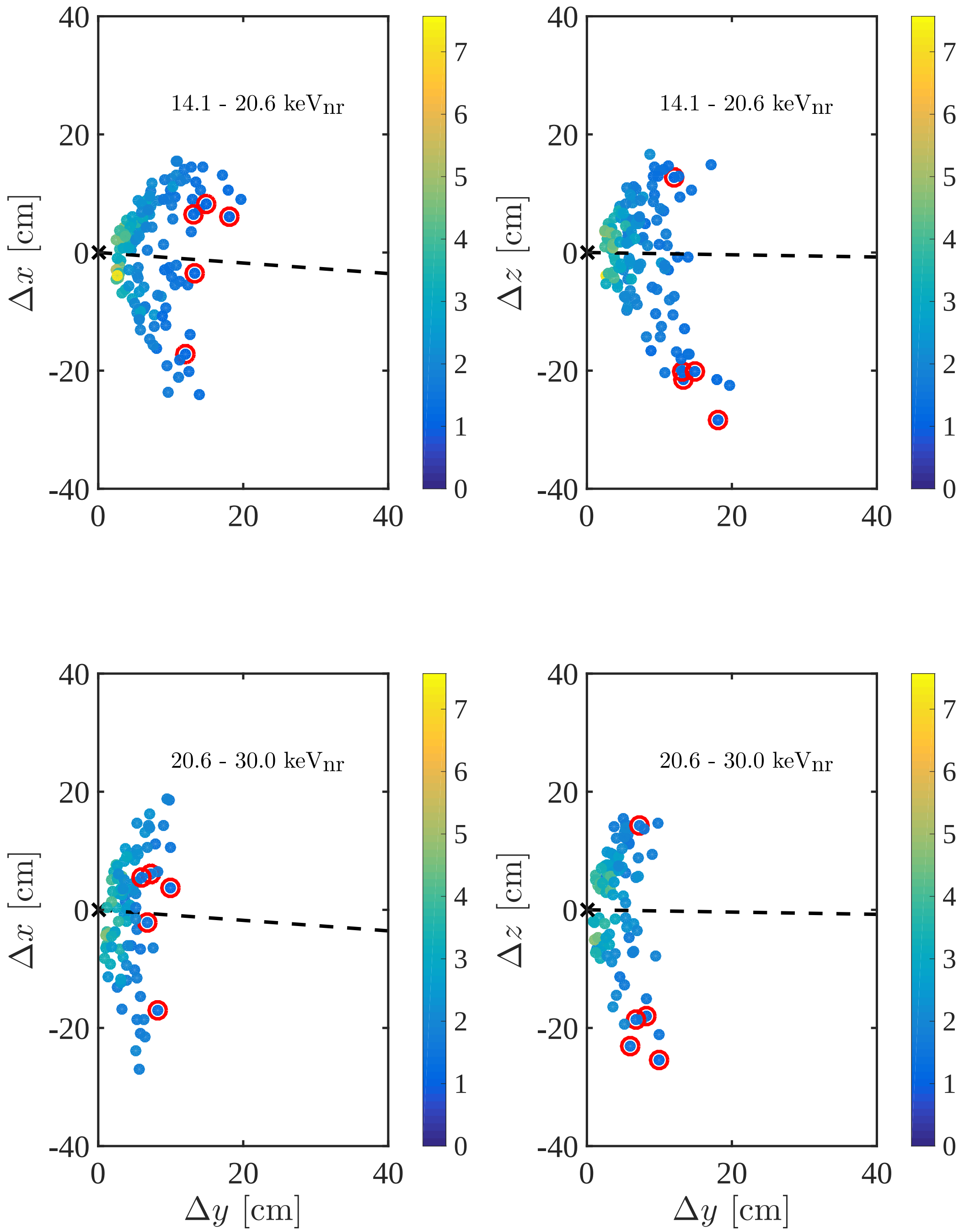

Figure 6.6: (Same as Fig 6.3, except for energy range of bins.) The three reconstructed nuclear recoil energy energy bins spanning the range 14.1–30 keV$_{\mathrm{nr}}$ are shown in this plot.

6.2 Bias effects due to position reconstruction uncertainty

There are two systematic effects modifying the population of events in a given reconstructed recoil energy bin in the Q_y analysis that must be characterized and accommodated. Both effects result from the per-event uncertainty in the scattering-angle-based recoil energy measurement due to the error in the reconstructed neutron interaction vertex positions. These systematic effects are the result of Eddington bias [114–116]. In the following sections, a short introduction to Eddington bias and the expected effects in the double-scatter Q_y analysis is provided. In Sec. 6.3, we describe a Monte Carlo simulation used to study these effects, and in Sec. 6.7 we report the resulting bias corrections used in the Q_y data analysis in Ch. 5.

6.2.1 Eddington bias

In general for a bin-based analysis, the observed distribution of events in a particular bin is dependent upon the per-event statistical uncertainty in the observed variable. Some of the events measured in a given bin truly belong to neighboring bins to the left or right, but due to statistical fluctuations from measurement uncertainty they are mis-reconstructed into the particular bin of interest. This bleeding of observed events into a given bin is an example of Eddington Bias. In addition to broadening the true distribution of measured quantities in the given reconstructed energy bin, if the underlying spectrum of events is falling (rising), there is more (less) bleeding into the bin from lower (higher) energies, negatively (positively) biasing the mean quantity in the bin relative to the true mean. There is an additional asymmetrical bias in the population of observed events if the particular bin of interest is near a detection threshold [128].

The Q_y analysis in Ch. 5 uses bins of nuclear recoil energy as reconstructed from scattering angle. The observed population of events in each bin is affected by Eddington bias due to the statistical uncertainty in the reconstructed nuclear recoil energy due to the position resolution discussed in Sec. 6.1. Events of higher and lower true recoil energy are mis-reconstructed into a given nuclear recoil energy bin defined by a range of scattering angles.

6.2.1.1 Expected effects of Eddington bias on the width of observed ionization distribution

For each nuclear recoil energy bin in the Q_y analysis, the observed distribution of the ionization signal of all events is broadened by Eddington bias. Events that bleed into a given reconstructed energy bin with a true event recoil energy that is lower (higher) than the bin minimum (maximum) typically are associated with smaller (larger) S2 signals. As a consequence, the resulting spread in the observed $S2$ distribution—and corresponding number of measured electrons escaping the interaction site—is wider. To determine the energy dependence of this broadening of the observed ionization signal distribution, the effect is simulated using the Monte Carlo framework described in Sec. 6.3. The simulated results are reported in Sec. 6.7.1. In data, the recoil energy dependence of the observed ionization distribution resolution ($R = \sigma/\mu$) is extracted from the double-scatter data using the $R = a/\sqrt{E_{nr}}$ functional form that agrees with the simulated results. The signal model used to extract the Q_y data points in Ch. 5 uses this measured dependence of R on recoil energy to accommodate the broadening due to Eddington Bias.

6.2.1.2 Expected effects on the reconstructed mean bin energy

The mean nuclear recoil energy calculated for a given bin in the Q_y data analysis may be shifted due to the same Eddington bias process. For bins near the recoil energy threshold of 0.3 keV_{nr}, there are more events with a higher true energy that are mis-reconstructed down into a given bin than there are events with a lower true energy that are mis-reconstructed up into the given bin. The opposite is true for high-energy bins in the Q_y analysis near the maximum reconstructed recoil energy limit of 30 keV_{nr} used in the analysis. This process produces a bias in the observed mean energy, as calculated using the method outlined in Sec. 6.1.3, relative to the true mean recoil energy in the bin. As for the sister process outlined in Sec. 6.2.1.1, the simulation described in Sec. 6.3

is used to quantify this effect and the results are reported in Sec. 6.7.2. The bias in the measured mean bin energy in the low-energy Q_y analysis is corrected using these results and the associated systematic uncertainty in Q_y due to this correction is reported in Sec. 5.4.

6.3 Neutron scattering Monte Carlo simulation

A targeted Monte Carlo simulation of single and double-scatter elastic nuclear recoil events in the LUX detector was created to study the bias effects described in Sec. 6.2. These geometry based effects were simulated to inform the width of the ionization distribution for use in the Q_y signal model, and to quantify a correction factor for any bias in the reconstructed recoil energy from angle. The simulation was also used to verify the code base used to reconstruct scattering angles, mean nuclear recoil energies, and associated uncertainties. The simulation results were used to check for any potential biases in the observed true nuclear recoil spectrum due to the interaction of event position selection and the physical boundary conditions presented by the walls of the TPC. Finally, the simulated distribution of the observed distance between scattering vertices was demonstrated to be consistent with data. The simulation and these results are presented in the following sections.

6.3.1 Simulation technique

The custom, Matlab-based simulation uses an infinite volume of liquid xenon within which appropriate physical detector boundary conditions are enforced.[1] The LUX detector active liquid region is approximated by a 50 cm diameter, 50 cm drift volume in the simulation. The neutrons originate at the detector boundary in the simulation with the profile set by the 4.9 cm inner diameter neutron conduit. The initial direction of the simulated neutrons is set to be parallel with the neutron beam as measured in data. The simulation uses the procedure outlined in the following steps to simulate single-scatter and double-scatter nuclear recoil events.

[1] The simulation code base is located in the Brown Particle Astrophysics Group's GitHub organization [65] with the relative path "jverbus_lux_scratch/NeutronGeneratorAnalysis/angular_scattering_simulation/".

i. Randomly generate the nuclear recoil energies for the first and second scatter positions in the liquid xenon based upon the 2.45 MeV angular scattering cross-section from the JENDL-4 nuclear database [33]. The angular scattering cross-section used is averaged over all significant isotopes based upon the elastic scattering cross-section and the total isotopic abundance in natural xenon. All data analyses in this thesis use either single-scatter or double-scatter events in the TPC. For the single-scatter (double-scatter) analyses, a second (third) scatter is simulated. The requirement that this final scatter is outside of the detector boundary conditions ensures that the simulated neutron leaves the detector active volume.

ii. We simulate the true Monte Carlo positions of the first, second, and third scattering vertices. The distance between scatters is determined by the JENDL-4 total and elastic scattering cross-sections as appropriate. The true scattering angle at each vertex is calculated based upon the known recoil energy deposited at each vertex.

iii. The observed signals ($S1$ and $S2$) as well as the true number of photons and electrons escaping the interaction site (n_p and n_e) are calculated for each neutron interaction using NEST v1.0, which was the most recent NEST version before the update based upon the LUX D-D results discussed in Sec. 9.2 and Refs. [2, 59].

iv. The observed (x, y, z) position of each scattering vertex is calculated by varying the true (x, y, z) position of each scatter using the known position reconstruction resolution. The resolution for (x, y) used for this step is set based upon the results discussed in Sec. 6.1.2. The z coordinate resolution is taken to be 0.1 cm [37].

v. The deposited energy at the first scattering vertex is reconstructed from the scattering angle measured after position resolution effects are applied. This step uses the same scattering angle to nuclear recoil energy reconstruction algorithm (Sec. 6.1) used for the Q_y measurement data analysis in Ch. 5.

After following the steps listed above, cuts are made on the scatter multiplicity within the TPC boundaries to select simulation events corresponding to single or double-scatters. Position based cuts are applied to select scattering geometries corresponding to those used for the Q_y, L_y, and nuclear recoil band data analyses described in Ch. 5, Ch. 7, and Sec. 4.5, respectively. Similarly, the $S1$ and $S2$ thresholds and other pulse area based limits are applied as appropriate for each data analysis case to the observed simulation signals generated using NEST v1.0. All simulation parameters controlling detector conditions and signal response are set to be identical to those described in Ch. 2 with the exception of g_2, which is tuned to a value of 0.54 to ensure the simulated nuclear recoil band generated using NEST v1.0 matches the band mean as measured using D-D data in Sec. 4.5. Finally, where appropriate, the S2 waveform separation efficiency in the LUX data processing pipeline is applied using a function dependent upon the z separation, Δz, of the first and second-scatter vertices [129]:

$$\text{separation efficiency} = \frac{1}{1 + e^{-24.1(\Delta z - 0.561)}} \,. \tag{6.16}$$

For more details on these cuts, please refer to the chapters discussing the corresponding data analysis, or refer to the simulation code itself.

We simulated 10^7 single-scatter events and 10^7 double-scatter events for the results presented in this chapter. A 1% sample of the simulated single-scatter event population remaining after all cuts and position resolution effects for the L_y analysis are applied is shown in Fig. 6.7 and Fig. 6.8. The single-scatter events inside the neutron beam projection in the TPC are shown in blue. The red interaction vertices located outside the TPC boundaries are virtual "second scatters" used as a record keeping device in the simulation.

The corresponding 1% sample of simulated double-scatter events remaining after all cuts and position resolution effects for the low-energy Q_y analysis are applied is shown in Fig. 6.9 and Fig. 6.10. The first and second interactions in the forward scatter events passing all cuts are shown in blue and red, respectively. As in the single-scatter simulation, the final scatter must be outside the TPC boundaries to ensure the neutron escapes after scattering twice. For the double-scatter simulation

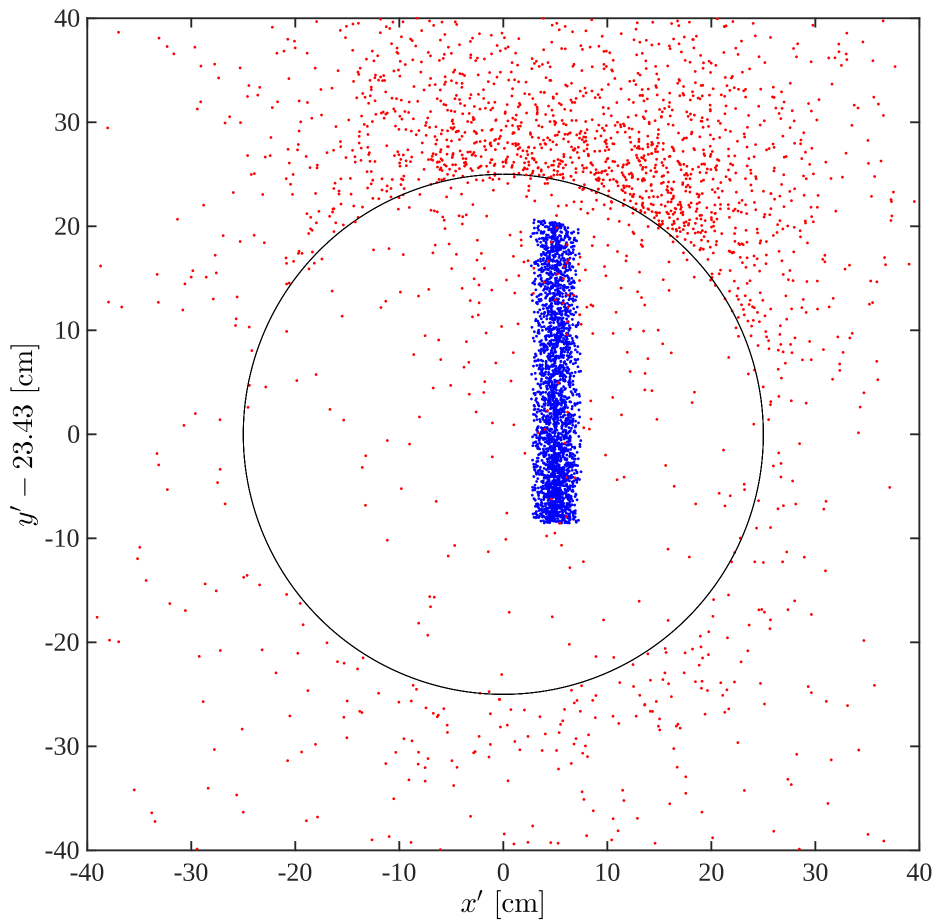

Figure 6.7: Top view of the simulated single-scatter events passing all cuts used for the L_y analysis. The single-scatter event population is shown in blue. The TPC boundaries are represented by the black circles depicted 10 cm apart in z. The red points are the virtual "second scatters" outside of the TPC boundaries used to ensure the neutron escapes the TPC without scattering twice. For clear visualization, this figure shows 1% of simulation events passing all cuts.

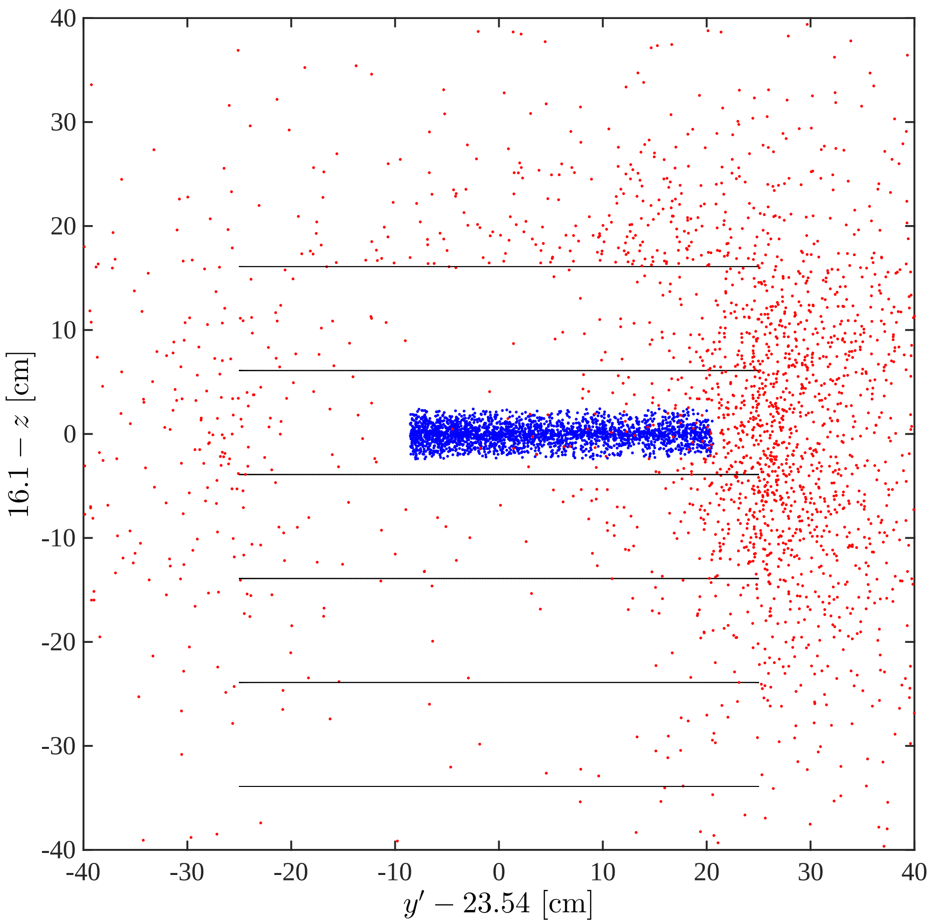

Figure 6.8: Side view of the simulated single-scatter events passing all cuts used for the L_y analysis. The single-scatter event population is shown in blue. The TPC boundaries are represented by the black circles depicted 10 cm apart in z. The red points are the virtual "second scatters" outside of the TPC boundaries used to ensure the neutron escapes the TPC without scattering twice. For clear visualization, this figure shows 1% of simulation events passing all cuts.

plots, these virtual "third scatters" are represented by the black crosses ($\times$). Again, these third scatters show the distribution with which escaping neutrons leave the TPC boundaries.

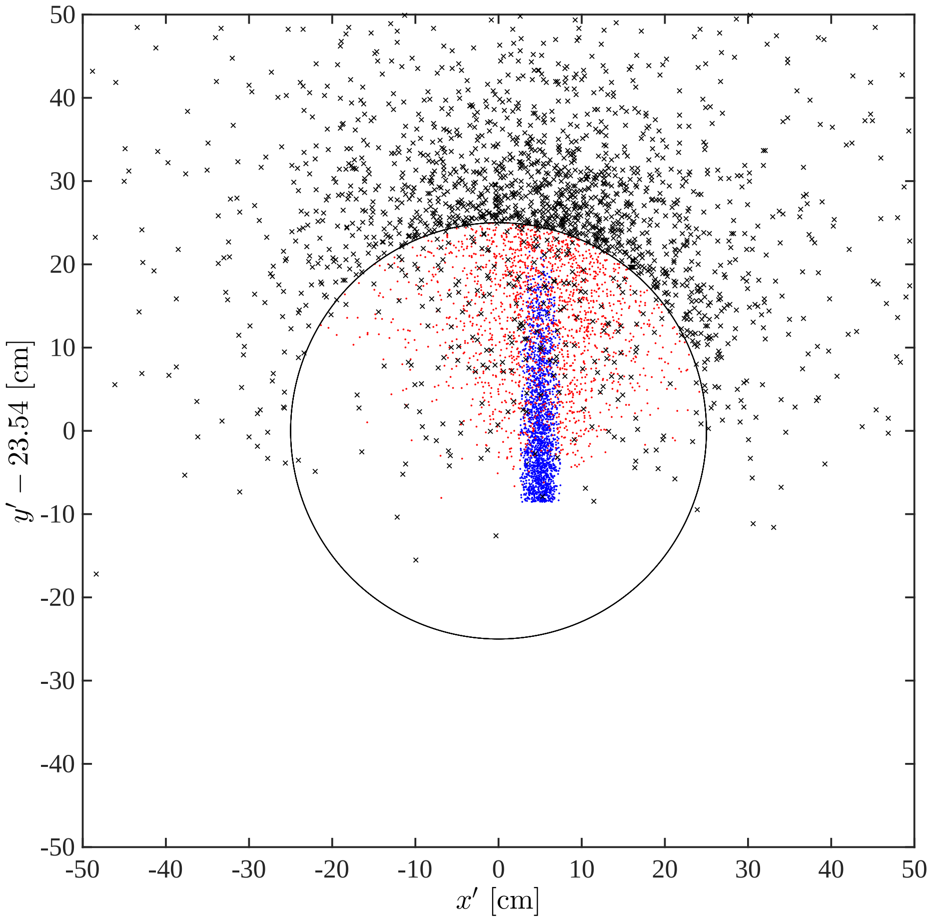

Figure 6.9: Top view of the simulated double-scatter events passing all cuts. The first scatters are blue and the second scatters are red. The TPC boundaries are represented by the black circles depicted 10 cm apart in z. The black $\times$ are the virtual "third scatters" outside of the TPC boundaries used to ensure the neutron escapes the TPC after scattering twice. For clear visualization, this figure shows 1% of simulation events passing all cuts.

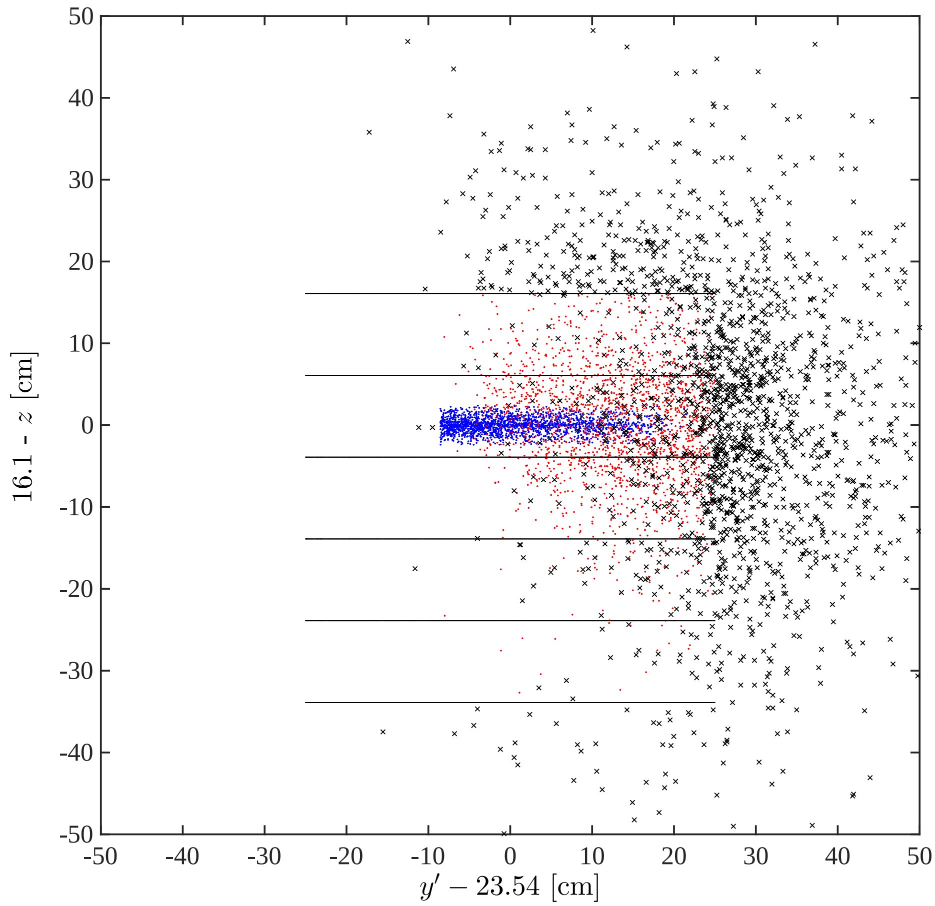

Figure 6.10: Side view of the simulated double-scatter events passing all cuts. The first scatters are blue and the second scatters are red. The TPC boundaries are represented by the black circles depicted 10 cm apart in z. The black $\times$ are the virtual "third scatters" outside of the TPC boundaries used to ensure the neutron escapes the TPC after scattering twice. For clear visualization, this figure shows 1% of simulation events passing all cuts.

6.3.2 Comparison of nuclear database differential cross-section evaluations

As a short aside, we compare the calculated elastic nuclear recoil energy distribution for a number of alternative nuclear databases. As discussed in Ch. 7, we use the database with the most modern evaluation, JENDL-4, for the low-energy L_y and endpoint yield measurements [130]. The evaluated recoil energy distributions are shown in Fig. 6.11 for eight nuclear databases including JENDL-4. The angular scattering cross-sections for each isotope were weighted by the total elastic scattering cross-section and the natural abundance in xenon. We show the same recoil spectra, divided by the spectrum produced using JENDL-4 in Fig. 6.12 to quantify the relative deviation between databases. In Fig. 6.12, the maximum deviation between the database used for the low-energy L_y and endpoint yield analyses is $\times 2.3$ at 35 keV$_{\mathrm{nr}}$. The maximum deviation at 1 keV$_{\mathrm{nr}}$ is $\times 0.9$. In both cases, the largest separation is between JENDL-4 and the ENDF/B-VII.1 evaluation [45].

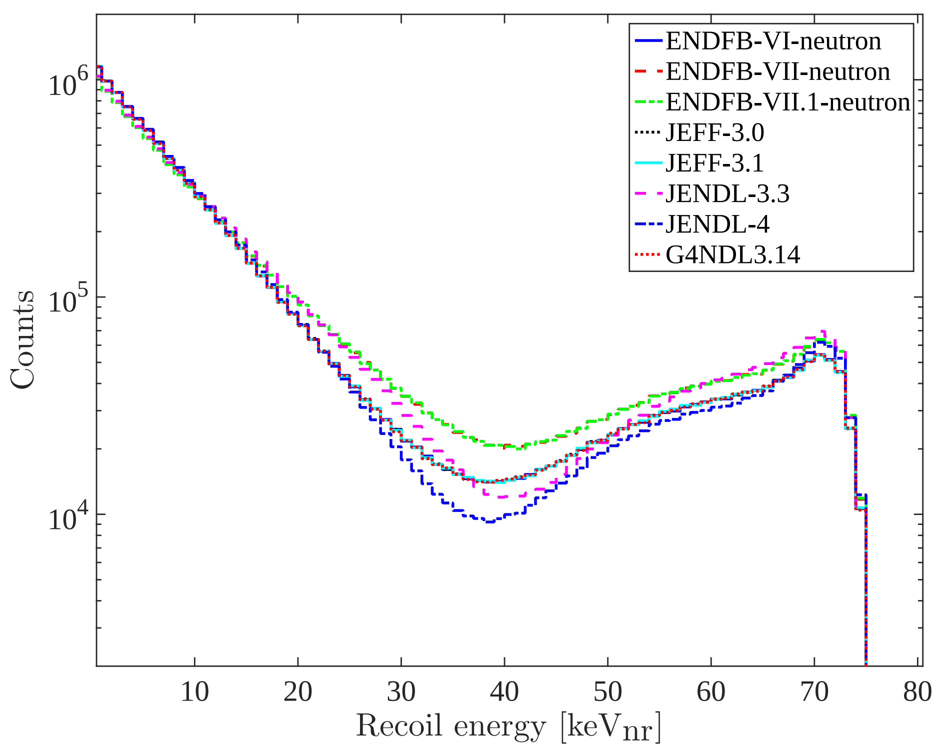

Figure 6.11: The elastic nuclear recoil energy distribution generated using various nuclear databases for comparison. The recoil energy distribution for each database was weighed based upon the total elastic scattering cross-section and the isotopic abundance in natural xenon.

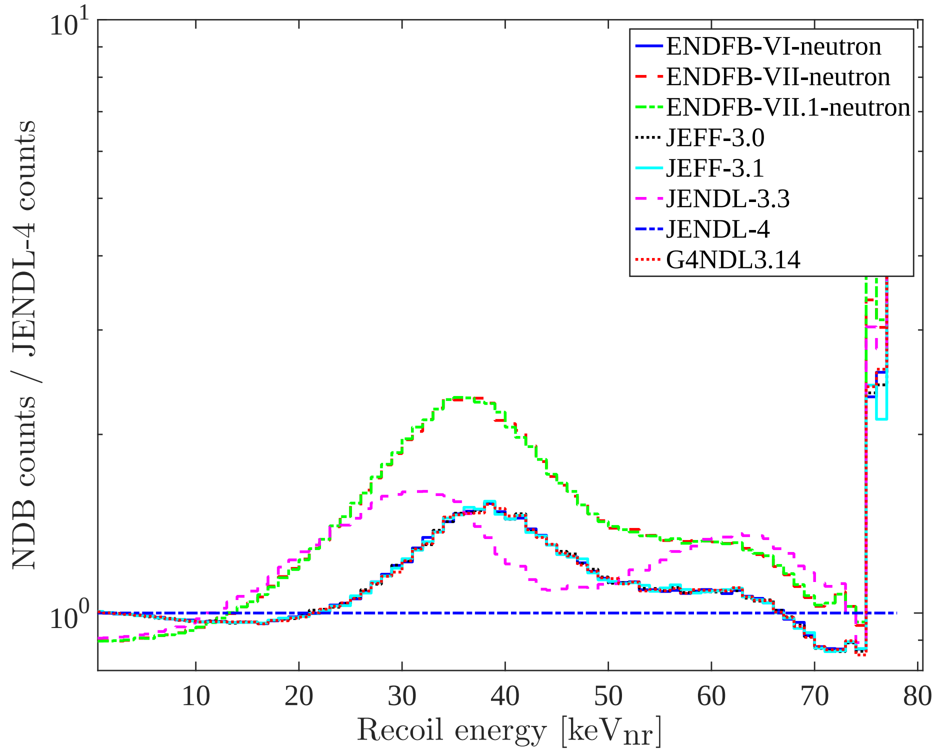

Figure 6.12: The elastic nuclear recoil energy distribution generated using various nuclear databases for comparison divided by the JENDL-4 recoil spectrum.

The low-energy L_y analysis normalizes the simulated nuclear recoil spectrum to the observed spectrum in data using the region $900 < S2 < 1500$. This corresponds roughly to an observed recoil energy of 20–30 keV$_{\rm nr}$. In Fig. 6.13, we normalized the spectra shown in Fig. 6.12 using this energy range. The data points reported in the low-energy L_y result lie within the 0–20 keV$_{\rm nr}$ region. Within this region, the maximum difference between the expected number of counts from different databases varies by $\times 0.62$ at 1 keV$_{\rm nr}$. It is clear that there are two groups of nuclear databases examined here in terms of their behavior relative to JENDL-4 at low-energies. The first group deviates maximally by $\times 0.92$ and includes JEFF-3.0, JEFF-3.1, ENDF/B-VI, and G4NDL3.14. The second group has the largest deviation of $\times 0.62$ at 1 keV$_{\rm nr}$ and consists of ENDF/B-VII, ENDF/B-VII.1, and (at low-energies) JENDL-3.3.

As described in Sec. 7.4, the JENDL-4 evaluation—in addition to being the most modern—is the most conservative for the L_y result at low-energies. The JENDL-4 database predicts the largest

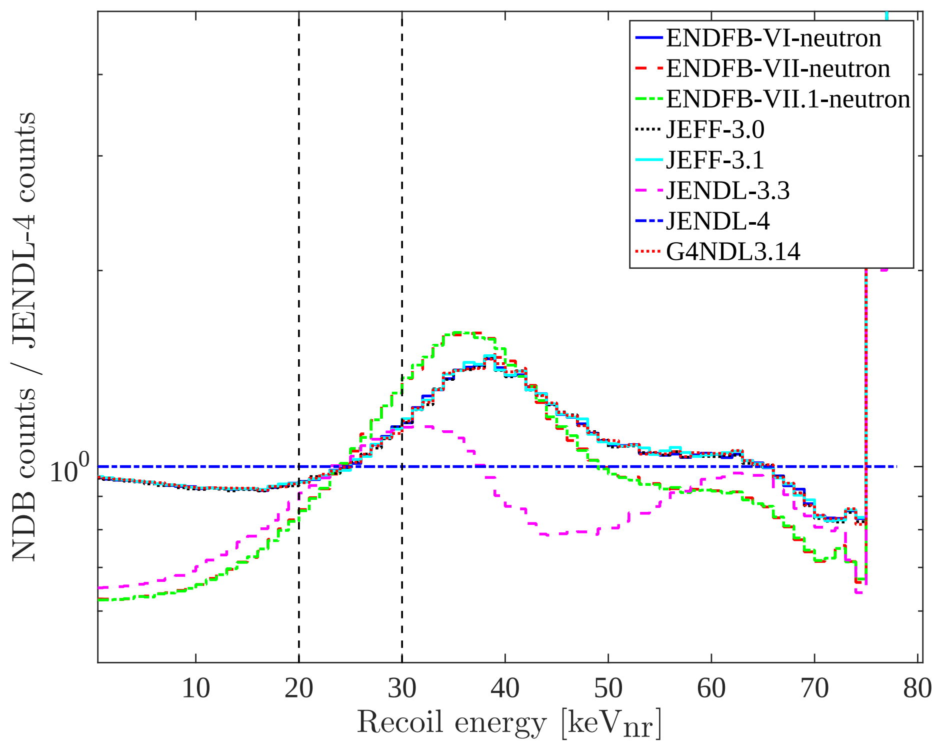

Figure 6.13: The elastic nuclear recoil energy distribution generated using various nuclear databases for comparison divided by the JENDL-4 recoil spectrum. All recoil spectra are normalized between 20–30 keV$_{\mathrm{nr}}$, which corresponds to the normalization region of the simulated spectrum used for the low-energy L_y analysis.

number of events at low-energies given the normalization used for the analysis. If the underlying differential cross-section used for the analysis overpredicts the number of expected events at low-energies, the optimization will favor a lower L_y to compensate. Additionally, as described in Sec. 7.4, the L_y analysis was repeated using the JEFF-3.1 and ENDF/B-VII.1 recoil spectra to quantify the systematic uncertainty in the light yield due to the choice of nuclear database. The uncertainty in the endpoint yields due to the choice of nuclear database is also quantified and reported as described in Ch. 8.

6.4 Verification of the scattering angle reconstruction algorithm

The simulated double-scatter events were used to verify the algorithms for the reconstruction of the scattering angle and mean bin recoil energy used for the Q_y result reported in Ch. 5. The simulated events were binned according to the reconstructed nuclear recoil energy with the same 11 bins as for the Q_y data analysis. The two lowest-energy bins span the regions from 0.3–0.65 $\mathrm{keV_{nr}}$ and 0.65–1.0 $\mathrm{keV_{nr}}$, respectively. The remaining nine bins are logarithmically spaced from 1–30 $\mathrm{keV_{nr}}$. The mean true Monte Carlo simulated recoil energy was compared to the mean measured scattering angle-based reconstructed nuclear recoil energy for each bin.

The mean reconstructed recoil energy was measured using the prescription described in Sec. 6.1. For this verification, the simulation used perfect position reconstruction resolution in x, y, and z. The reconstructed quantities include the effect of the raw $S2 > 36$ phd threshold. All other event selection cuts used for the Q_y data analysis were applied. The comparison between the mean true Monte Carlo simulated energy and the reconstructed energy based upon scattering angle for each bin is shown in Fig. 6.14.

There is excellent agreement between the true Monte Carlo simulation mean recoil energy for each bin and the recoil energy reconstructed from scattering angle for all energy bins. The largest

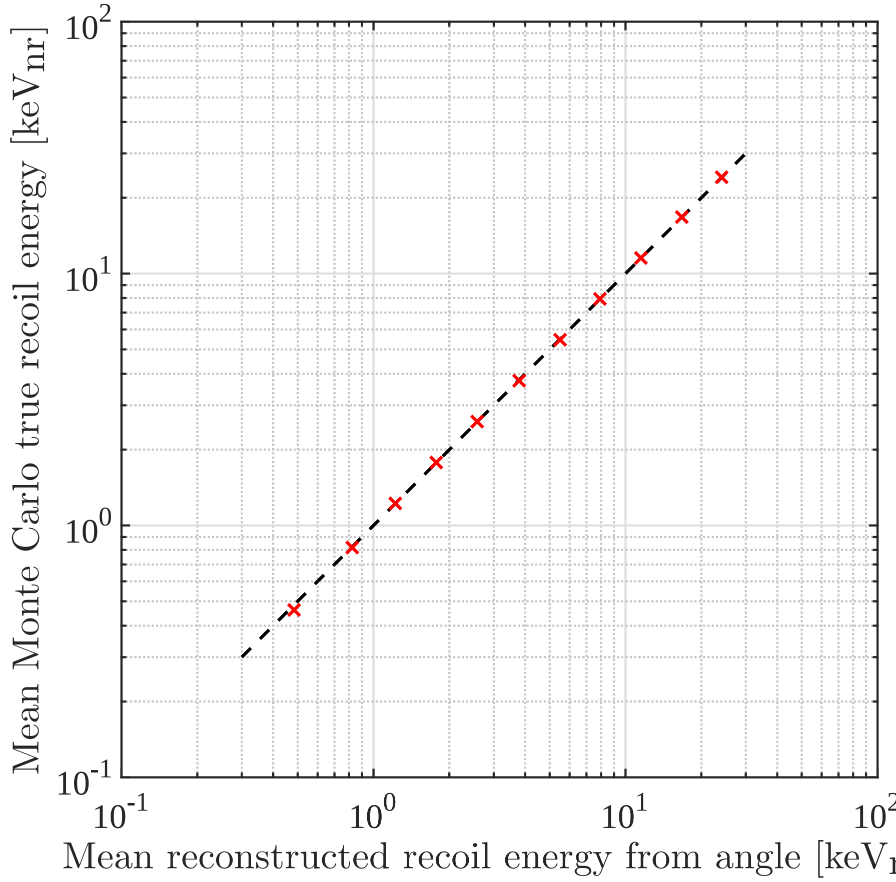

Figure 6.14: The red crosses ($\times$) show the mean true Monte Carlo simulation nuclear recoil energy vs. the mean recoil energy reconstructed from angle before the (x, y, z) position resolution is applied to the first and second scatter vertex positions in the simulation. The black dotted line is the ideal case of a one-to-one mapping between the true Monte Carlo simulation recoil energy and the value reconstructed from angle. The small offset of the lowest-energy point from the ideal black dotted line is due to the raw $S2 > 36$ phd threshold.

discrepancy is 5% for the lowest-energy 0.48 keV$_{\rm nr}$ data point. This test confirms the implementation of the algorithms described in Sec. 6.1 correctly reconstructs the average recoil energy in each bin used used for the Q_y analysis. The 5% deviation seen in the lowest-energy point is due to S2 threshold effects on the reconstructed quantities. These threshold effects are included in the overall bias correction factor for each bin calculated in Sec. 6.7.2, where they are subdominant.

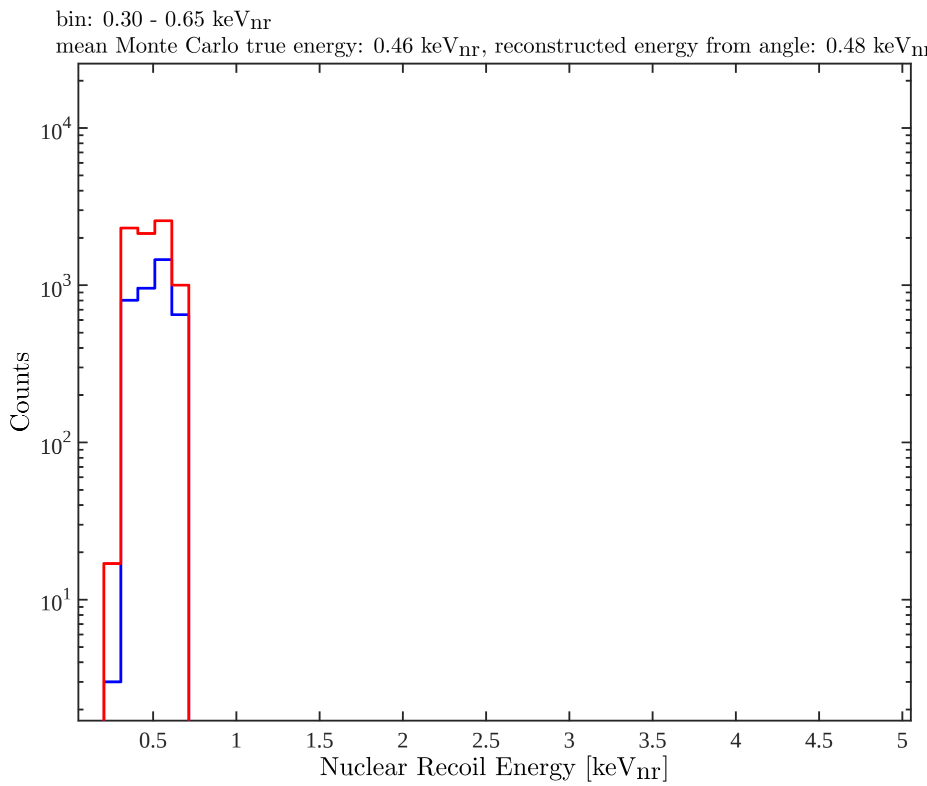

Figure 6.15: The Monte Carlo simulation true recoil energy distribution is shown in red and the simulated reconstructed recoil energy distribution is shown in blue for the lowest 0.3–0.65 keV$_{\rm nr}$ energy bin in the Q_y analysis before position resolution effects are applied in the simulation. The blue reconstructed histogram has fewer events and rolls off at low energies due to the raw $S2 > 36$ phd threshold.

Histograms of the true and reconstructed recoil energies for the lowest-energy 0.3–0.65 keV$_{\rm nr}$ bin are shown in Fig. 6.15. The discrepancy between the true Monte Carlo simulation distribution shown in red with the reconstructed recoil energy distribution shown in blue is due only to the acceptance of the raw $S2 > 36$ phd threshold. As one would expect with when using true Monte Carlo simulation (x, y, z) positions, there is no contamination from events with a true energy outside the reconstructed energy bin. After all cuts are applied—when calculating the scattering angle using the true Monte Carlo simulation vertex positions—the acceptance of the S2 threshold in the 0.3–0.65 $\mathrm{keV_{nr}}$ bin, 0.65–1.0 $\mathrm{keV_{nr}}$ bin, 1.00–1.46 $\mathrm{keV_{nr}}$, and 1.46–2.13 $\mathrm{keV_{nr}}$ bin is estimated to be 48%, 76%, 91%, and 97%, respectively.

6.5 Verification of the path length between neutron scatters

The physical (x, y, z) distance between double-scatter vertices in simulation was compared to data. The distribution of the measured distance between scatters for both data and simulation is shown in Fig. 6.16. The simulation included position resolution effects with an additional systematic uncertainty of +0.35 cm $\sigma_{(x,y)}$ as described in Sec. 6.1.2. The excellent agreement over the full domain of interest from 5–50 cm agreement between data and simulation demonstrates the consistency of the simulation geometry, position cuts, and S2 threshold. Additionally, if a significant fraction of interaction vertices were below threshold in data due to a crashing Q_y at low-energies, the measured separation between observed vertices would increase. There is no evidence of the described effect in Fig. 6.16.

6.6 Study of detector geometry effects on the observed neutron single-scatter recoil energy spectrum

The physical boundaries of the detector's liquid xenon active region can modify the underlying nuclear recoil spectrum depending upon the position cuts used for the fiducial analysis volume. These effects are due to the requirement of exactly one neutron scatter in the fiducial volume for the low-energy L_y analysis in Ch. 7. In particular, the distance a neutron must travel to escape the liquid xenon after interacting once inside the fiducial volume used for the L_y analysis varies as a function of direction due to the physical boundaries of the detector. The 50 cm linear dimension

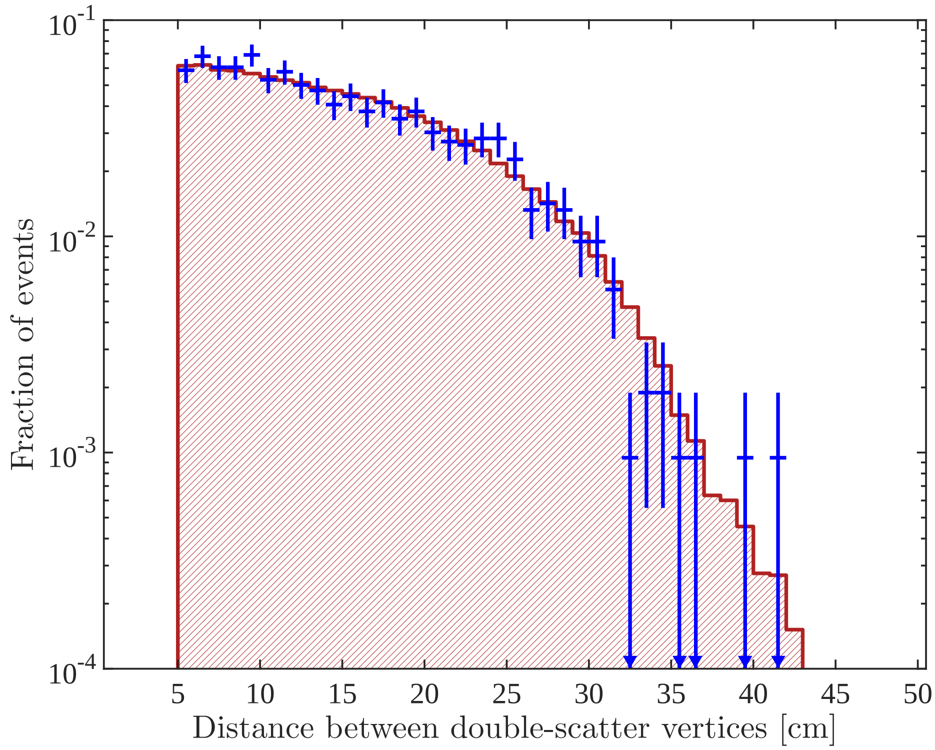

Figure 6.16: A histogram of the measured distance between double-scatter vertices in data and simulation. The blue data points were generated using 1031 events between 0.3 and 30 $\mathrm{keV_{nr}}$ in the low-energy ionization yield dataset described in Ch. 5. The red shaded histogram represents the distribution of distances between double-scatter events in simulation.

of the LUX TPC is around $\times 4$ the total mean free path of 2.45 MeV neutrons in liquid xenon (13 cm). This variation in xenon path length as a function of the outgoing neutron direction produces a scattering angle dependent efficiency for the observation of single-scatter events. The resulting observed neutron energy spectrum is modified due to these detector wall effects compared to the recoil spectrum expected based solely on nuclear physics—in our case the JENDL-4 nuclear database.

The change in the observed nuclear recoil energy spectrum due to these detector wall effects is significant for the fiducial volume used for the nuclear recoil band measurement in Sec. 4.5. This is not an issue for the nuclear recoil band measurement which does not require the energy spectrum to be mono-energetic or precisely measured, but it does provide a clear demonstration of this effect. As there is no need to ensure the energy purity of the incident neutrons unlike the signal yield measurements, the nuclear recoil band measurement uses a radially symmetric, cylindrical fiducial analysis volume with $r < 21$ cm and $80 <$ drift time < 130 μs. The underlying energy spectra from JENDL-4 averaged over all isotopes and the resulting observed spectrum after nuclear recoil band analysis volume cuts are shown in Fig. 6.17.

The radial position cut that accepts events as close as 4 cm to the detector wall is responsible for the deviation between the observed spectrum (red) and that based upon nuclear physics alone (blue). The asymmetry in the path a neutron must travel after scattering once in the fiducial analysis volume for the nuclear recoil band produces a maximum deviation factor of $\sim$3 at the 74 keV$_{\mathrm{nr}}$ endpoint. The overabundance of observed events at high-energy is expected based upon upon the typically smaller path a backscattered neutron must take to escape the liquid xenon without scattering again. The suppression of low-energy events is due to the converse effect for forward neutron scatters.

The low-energy L_y, low-energy Q_y, and endpoint yield analyses use a different fiducial volume, which only accepts neutron interactions in line with the neutron beam. The $y' > 15$ cm cut used in these analyses significantly reduces the deviation between the underlying JENDL-4-based nuclear recoil energy spectrum and the observed spectrum for these yield measurements. This is because

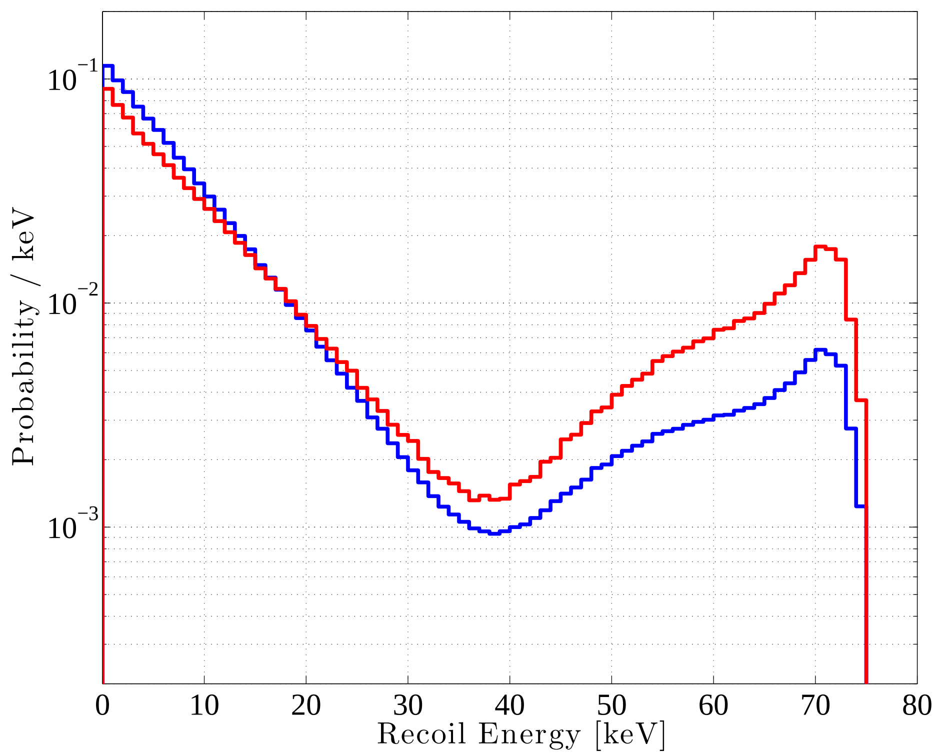

Figure 6.17: The effect of the physical detector boundaries on the underlying observed energy spectrum of events passing the nuclear recoil band fiducial volume cuts. The underlying nuclear recoil energy spectrum from JENDL-4 averaged over all isotopes using their natural abundance and elastic scattering cross-section is shown in blue. The corresponding spectrum after applying the nuclear recoil band fiducial analysis volume cuts is shown in red. No signal detection thresholds are applied to either histogram to clearly isolate the effect due to position cuts.

the y' cut ensures the first neutron interaction is >15 cm into the liquid xenon, so the majority of the neutron interactions occur in the center of the detector where there is a roughly equal amount of xenon in the direction of forward-scatters, back-scatters, and 90° scatters exiting through the top of the liquid xenon column. These conditions conspire to ensure that neutrons that scatter once in the fiducial analysis volume have a similar distance to travel through the liquid xenon to escape the active volume regardless of scattering angle.

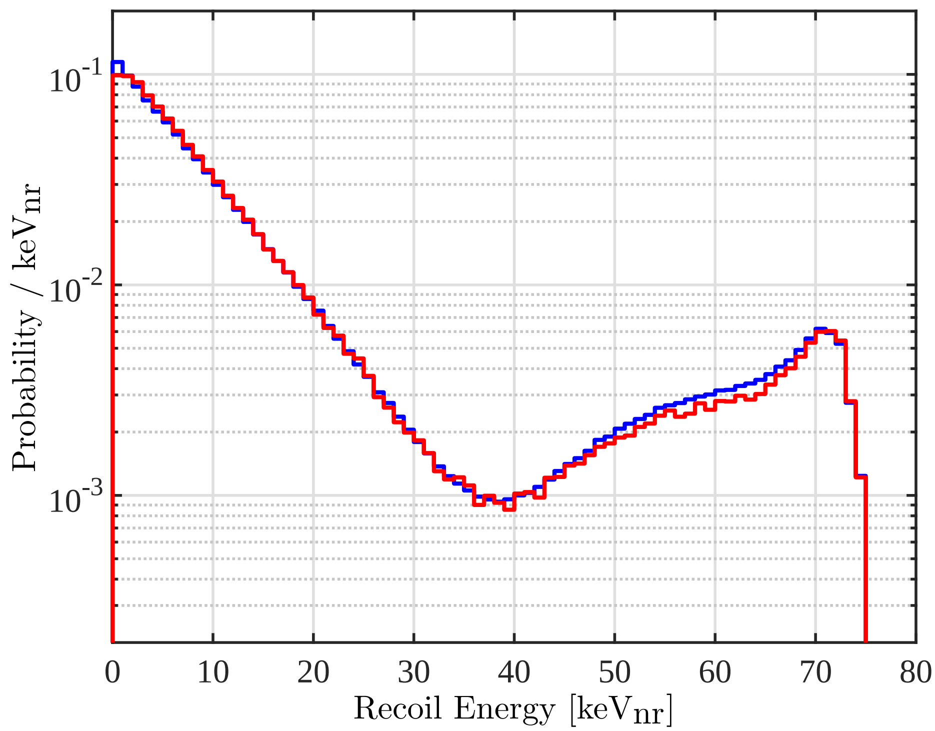

Figure 6.18: The effect of the physical detector boundaries on the underlying observed energy spectrum for single-scatter neutron events in line with the neutron beam with $y' > 15$ cm. This fiducial volume cut is used for the low-energy L_y and recoil spectrum endpoint yield measurements. The underlying nuclear recoil energy spectrum from JENDL-4 averaged over all isotopes using their natural abundance and elastic scattering cross-section is shown in blue. The corresponding spectrum after applying the fiducial analysis volume cuts is shown in red. No signal detection thresholds are applied to either histogram to clearly isolate the effect due to position cuts.

The result is shown in Fig. 6.18. The maximum deviation between the observed energy spectrum after position cuts (red) and the initial spectrum produced using JENDL-4 (blue) is everywhere less than 20%. In the forward scattering regime used for the low-energy L_y measurement, the deviation is typically no more than a few percent with a maximum low-energy deviation of 14% for the <1 keV_{nr}

bin—similar to the uncertainty in the nuclear database at 1 $\mathrm{keV_{nr}}$ as estimated in Sec. 6.3.2. In general, the deviation due to the described wall effects is subdominant to the quoted uncertainty between nuclear databases, which have a maximum deviation of $\sim 2\times$ for 90° scatters as shown in Sec. 6.3.2. It should be noted that the low-energy Q_y analysis technique used in Ch. 5 does not assume any particular form for the underlying neutron-nucleus recoil spectrum, and the observed spectrum is in good agreement with data as reported in Sec. 5.4.

6.7 Corrections for Eddington bias effects due to position reconstruction uncertainty

We used the Monte Carlo simulation infrastructure described in this chapter to characterize the expected systematic effects due to Eddington Bias in the low-energy Q_y result. In Sec. 6.7.1, the increased resolution (σ/μ) of the observed ionization distribution in the Monte Carlo simulation is shown to be consistent with data. In Sec. 6.7.2, we generate corrections for the bias in the mean reconstructed nuclear recoil energy, which are directly applied in the Q_y data analysis in Ch. 5.

6.7.1 Width of the observed ionization distribution

As discussed in Sec. 6.2, the observed ionization signal distribution in data is broadened due to Eddington bias. In this section, we quantify the expected resolution of the observed ionization signal distribution accounting for these bias effects using the simulation described in Sec. 6.3. For a given nuclear recoil energy bin used for the Q_y analysis, the resolution of the Monte Carlo simulation true ionization distribution can be compared to the ionization distribution from the reconstructed Monte Carlo simulation events after position resolution effects have been applied. The ionization signal model used for the low-energy Q_y measurement described in Ch. 5 was fit to the simulated ionization distribution after position reconstruction effects. The resolution parameter, R, in Eq. 5.3 fit was left unconstrained in this fit. The optimal resolution was determined for each bin using the same unbinned maximum-likelihood algorithm used for the Q_y data analysis in Ch. 5. The fit to the ionization distribution in the bin spanning the range 0.3–0.65 keV_{nr} is shown in Fig. 6.19. The fit in the last bin spanning the range 20.56–30.00 keV_{nr} is shown in Fig. 6.20.

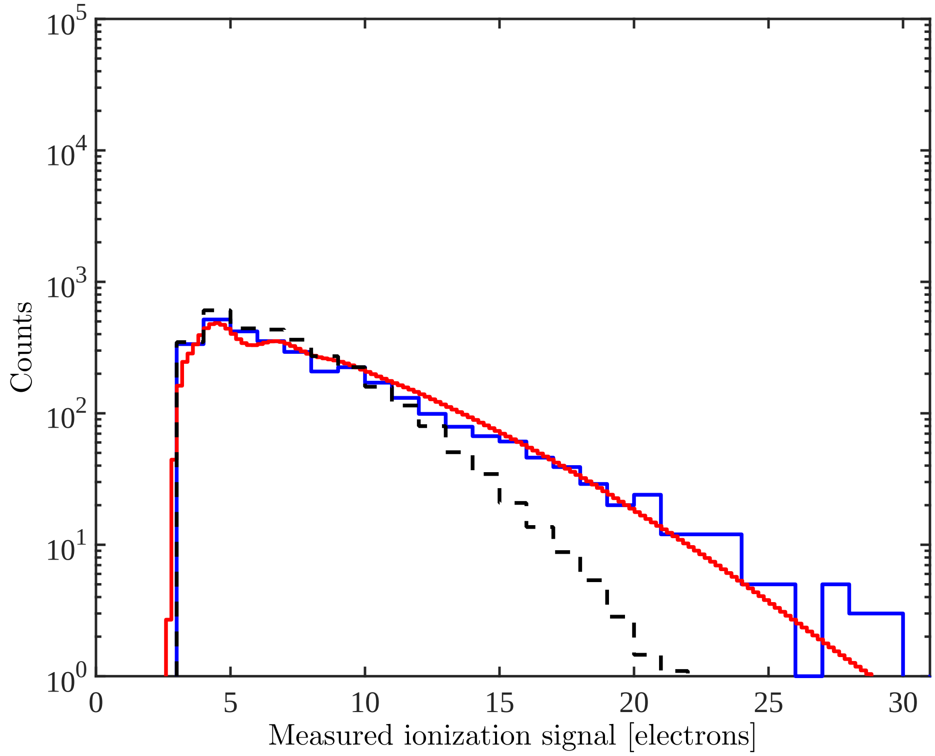

Figure 6.19: The reconstructed ionization distribution falling into the 0.3–0.65 keV_{nr} bin is shown in blue. The best-fit ionization signal model with $R = 0.78$ is represented by the red curve. For comparison, the dotted black line is the output of the signal model assuming a standard Poisson distribution with the same mean. The soft S2 threshold is applied between 3–4 measured electrons.

Similar fits were performed for each recoil energy bin in simulation in order to extract the resolution of the ionization distribution accounting for Eddington bias effects. The simulation was run three times to quantify the systematic uncertainty in the result due to varying assumptions about the precision of the detector's position reconstruction algorithm. Each iteration used a different additional systematic position reconstruction uncertainty added in quadrature with the statistical uncertainties as described in Sec. 6.1.2. The baseline additional systematic position reconstruction uncertainty was taken to be 0.35 cm. The other two simulation runs used additional systematic uncertainties of 0.00 cm and 0.70 cm. These results are shown in Table 6.1.

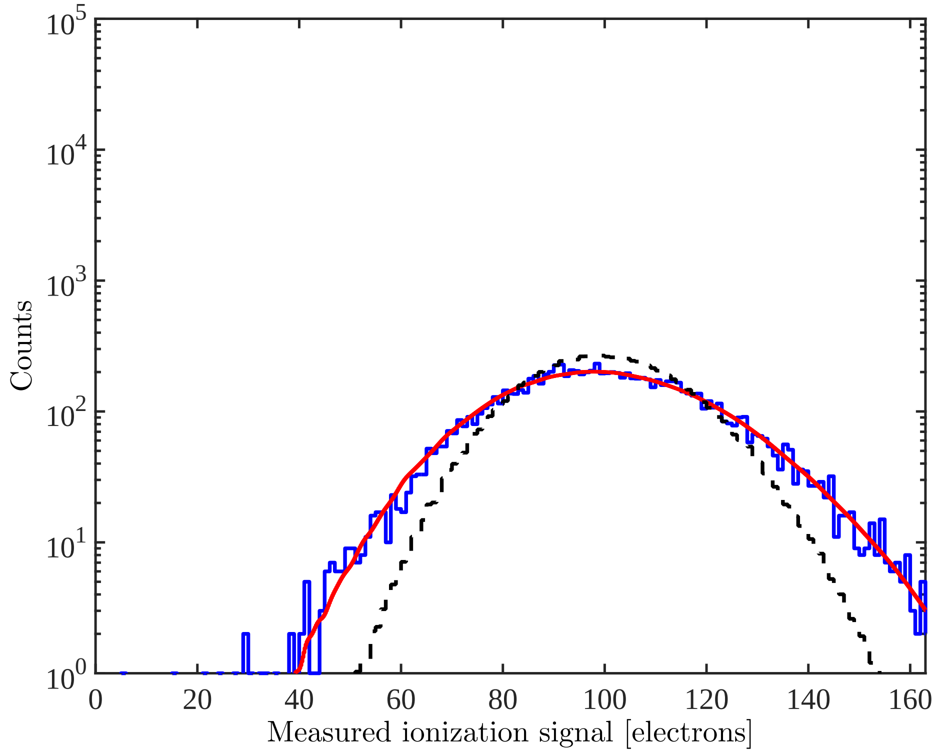

Figure 6.20: The reconstructed ionization distribution falling into the 20.56–30.00 $\mathrm{keV_{nr}}$ bin is shown in blue. The best-fit ionization signal model with $R = 0.17$ is represented by the red curve. For comparison, the dotted black line is the output of the signal model assuming a standard Poisson distribution with the same mean.

Table 6.1: The resolution (R) of the ionization distribution in each recoil energy bin used for the Q_y measurement. These values are determined from high statistics simulation and the uncertainties are $\mathcal{O}(0.01)$ in R. The first column contains the bin limits in units of reconstructed recoil energy from scattering angle. The simulated resolution of the observed ionization signal distribution is given in the proceeding columns. The second column contains resolution values as calculated when the true Monte Carlo neutron interaction positions are used in the simulation. These values correspond to the red diamonds Fig. 6.21. Columns three through five correspond to the bias correction calculated when position reconstruction is included in the simulation. These position reconstruction uncertainties include the statistical position reconstruction uncertainty as well as an additional systematic component of +0.00 cm $\sigma_{(x,y)}$, +0.35 cm $\sigma_{(x,y)}$, and +0.70 cm $\sigma_{(x,y)}$, respectively, according to the prescription described in Sec. 6.1.2. The +0.35 cm $\sigma_{(x,y)}$ case in column four corresponds to the red circles in Fig. 6.21. The statistical uncertainty in the number of simulated events in the lowest-energy bin is 1.8%, which corresponds to an uncertainty in R of $\sim$0.01.

Q_y bin [keV$_{\mathrm{nr}}$]	No (x,y) uncertainty R (σ/μ)	(+0.00 cm $\sigma_{(x,y)}$) R (σ/μ)	(+0.35 cm $\sigma_{(x,y)}$) R (σ/μ)	(+0.70 cm $\sigma_{(x,y)}$) R (σ/μ)
0.30–0.65	0.56	0.79	0.78	0.84
0.65–1.00	0.41	0.59	0.62	0.64
1.00–1.46	0.32	0.51	0.52	0.54
1.46–2.13	0.28	0.43	0.43	0.46
2.13–3.11	0.24	0.36	0.37	0.39
3.11–4.53	0.21	0.31	0.32	0.33
4.53–6.62	0.18	0.27	0.27	0.29
6.62–9.65	0.16	0.23	0.24	0.26
9.65–14.09	0.15	0.21	0.22	0.23
14.09–20.56	0.14	0.18	0.18	0.20
20.56–30.00	0.14	0.16	0.17	0.18

A comparison of the simulated resolution with the resolution measured in data is shown in Fig. 6.21. This figure includes the simulated values from column four in Table 6.1 (circles), which use the best estimate of the position reconstruction resolution. The observed resolution without Eddington bias from column two (diamonds) are included for comparison. The blue crosses show the resolution as measured using the double-scatter data in Sec. 5.4. The increase in resolution between the diamonds and the circles illustrates the dominant contribution from Eddington bias to the observed resolution of the ionization distributions used for the Q_y analysis. The energy of the data points is corrected for Eddington bias following the procedure described in Sec. 6.7.2 and is the reason for the observed variation between the position of the diamonds and circles along the horizontal axis.

6.7.1.1 Future measurement of the ionization signal width due to signal generation and recombination fluctuations

A future analysis could quantify the contribution from recombination fluctuations to the variance of the distribution of electrons freed from the interaction site using this information. This procedure is somewhat similar to the related process used to measure recombination fluctuations for electron recoils in the LUX tritium data [72, 131]. In our case, the added complication due to using double-scatter events requires special treatment of the Eddington bias effects. Also, due to the overlap of S1 signals from both interactions in the double-scatter events, we would need to target the charge signal from the first scatter vertex only for this analysis.

6.7.1.2 Verification of the fitting algorithm used to extract the mean ionization signal

As a cross-check on the fitting algorithm, we compare the mean Monte Carlo true number of electrons in each reconstructed recoil energy bin to the reconstructed number of electrons in simulation using the ionization signal model with a resolution set by the values of column three of Table 6.1. This column contains the observed resolution of the ionization signal distribution as simulated using

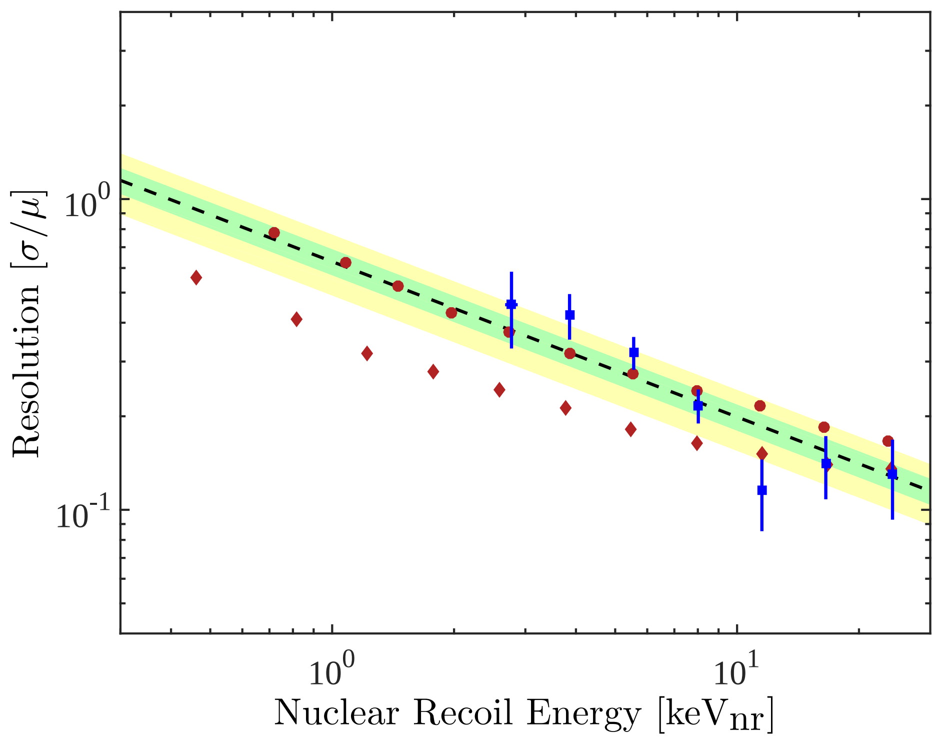

Figure 6.21: This figure is identical to Fig. 5.3 except for the addition of the red diamonds ($\diamondsuit$), which depict the reconstructed resolution of the ionization electron distribution in simulation using the true Monte Carlo positions for each vertex. The measured resolution, R, of the ionization distributions in the seven highest-energy bins of the double-scatter dataset are represented by the blue squares ($\square$). The simulated resolution of the ionization distribution produced by a NEST v1.0 Monte Carlo with modeled position reconstruction uncertainties is represented by the red circles ($\circ$). The black dashed line represents the best-fit to the blue squares given by $R_0 = 0.64/\sqrt{E}$. The fit has a χ^2/dof = 10.6/6, which corresponds to a p-value of 0.12. The 1σ and 2σ contours on the parameter a are shown in green and yellow, respectively.

the best estimate of the position reconstruction effects. The result is shown in Fig. 6.22. The maximum deviation between the reconstructed and Monte Carlo simulation true value is ∼1%. This is subdominant to other uncertainties in the low-energy Q_y analysis and is a verification of the algorithm used to reconstruct the mean number of ionization electrons.

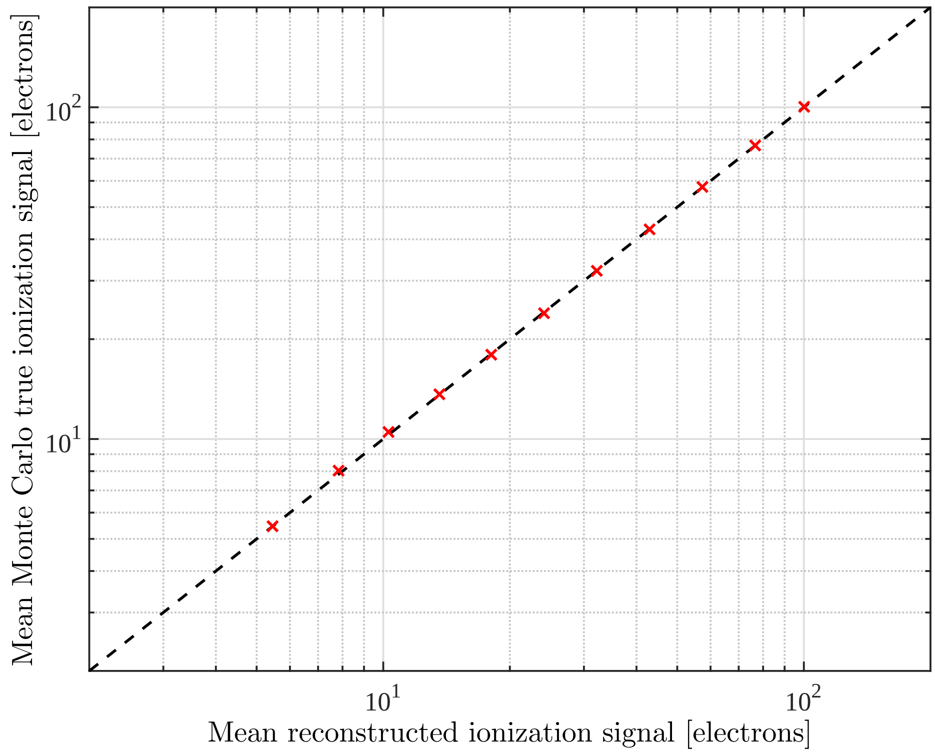

Figure 6.22: The red points are the Monte Carlo true mean ionization signal vs. the mean reconstructed ionization signal in a given reconstructed nuclear recoil energy bin after the (x, y, z) position uncertainties are applied to the first and second scatter vertex positions in the simulation. The black dotted line is the ideal case of a one-to-one mapping between the Monte Carlo truth values before position resolution effects and the reconstructed values after position resolution effects are applied.

6.7.2 Bias on the mean reconstructed nuclear recoil energy measured from scattering angle

The estimated per-event uncertainty in the neutron double-scatter event recoil energy reconstruction, including effects from position resolution, was used to leverage the most precisely measured events when determining the mean energy of each bin used in the analysis. As described in Sec. 6.2, there is an additional systematic effect due to Eddington bias that must be accounted for when estimating the mean bin energies. Using the double-scatter simulation described in Sec. 6.3, we quantify this bias in the mean reconstructed nuclear recoil energy for each bin. The correction factors for this effect are reported in this section.

The event distribution of the true Monte Carlo simulation nuclear recoil energies and the reconstructed nuclear recoil energies from angle for three representative bins are shown in Fig. 6.23, Fig. 6.24, and Fig. 6.25. These three bins include the lowest-energy and highest-energy, as well as a bin in the middle of the logarithmic spacing scheme.

The first bin shown in Fig. 6.23 can be directly compared with the result in Fig. 6.15 to observe the effect of Eddington bias on the lowest energy bin used for the Q_y measurement. In contrast to Fig. 6.15, the true Monte Carlo simulation recoil energy values bleed outside of the reconstructed energy bin in Fig. 6.23. This spread of true Monte Carlo simulation energies is solely due to Eddington bias produced by the uncertainty in the reconstructed (x, y, z) of the neutron interactions in the detector. The asymmetric bias in the red true Monte Carlo simulation recoil energy distribution can be clearly seen in this low-energy bin. This asymmetry is due to S2 threshold effects and, most significantly, the limited solid angle "phase space" available for low-energy (and thus small angle) neutron scatters. This can be intuitively understood: for this low-energy bin with boundaries 0.30–0.65 keV$_{\mathrm{nr}}$ (7°–11°), there are more events with true scattering angle >11° that can be mis-reconstructed down into this bin than scatters with true scattering angle <7° that can be mis-reconstructed up in energy into the given bin.

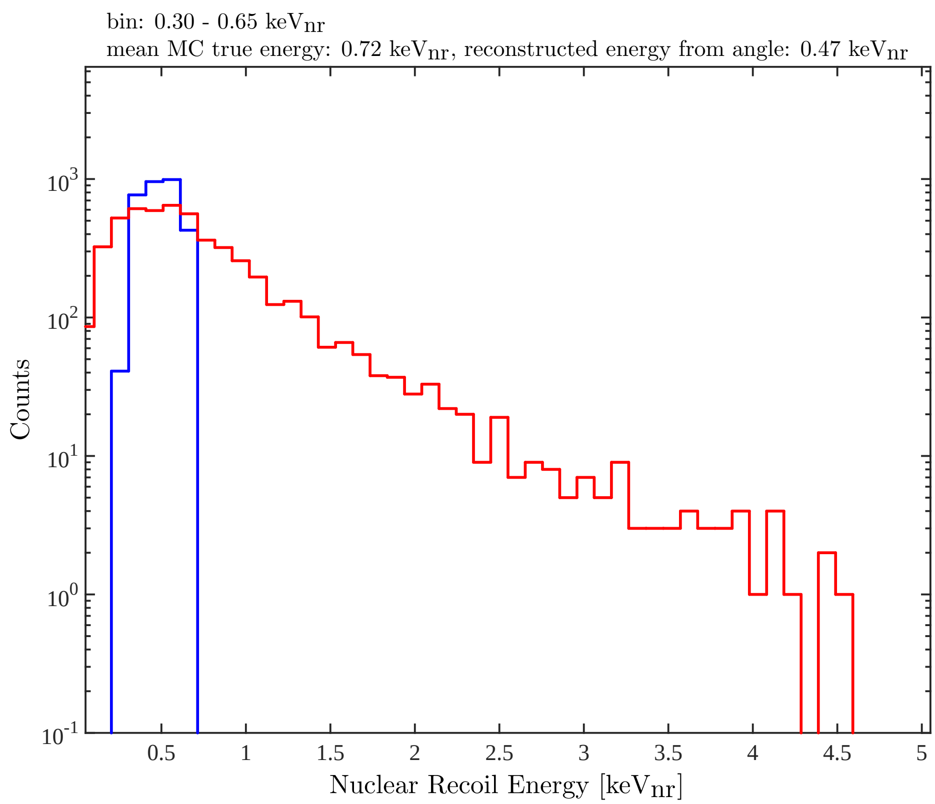

Figure 6.23: The Monte Carlo simulation true energy distribution (red) and the simulated reconstructed nuclear recoil energy distribution (blue) for the lowest 0.30–0.65 keV$_{\mathrm{nr}}$ energy bin in the Q_y analysis. This figure was produced after position resolution effects are applied in the simulation. This represents a $\times 1.53$ shift in the mean reconstructed energy of the bin relative to the true Monte Carlo energy and is taken into account in the correction factor reported in Table 6.2.

The same Eddington bias effects are present in Fig. 6.24 and Fig. 6.25. The spread in the true Monte Carlo simulation nuclear recoil energy for the events in a given reconstructed energy bin extends outside the reconstructed recoil energy bin boundaries. The asymmetric effects seen in Fig. 6.23 become smaller in magnitude as the bin energy increases. The direction of the bias changes for the high-energy bins due the upper limit on the scattering angle of 90° presented by the requirement for the low-energy Q_y analysis that the neutrons forward scatter. This effect can be seen in the highest-energy bin shown in Fig. 6.25. The maximum energy for a forward scatter is roughly 37 keV$_{\text{nr}}$, which ensures that there are fewer events with higher true energy outside mis-reconstructed down into the reconstructed energy bin than there are lower true energy events that are mis-reconstructed up into the reconstructed energy bin.

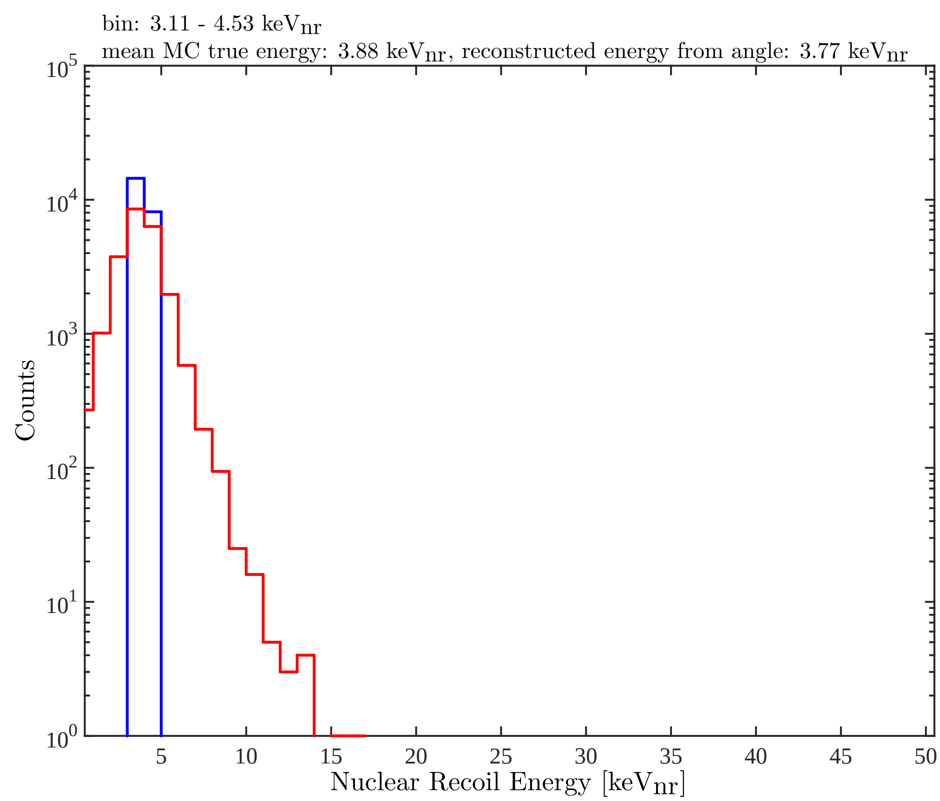

Figure 6.24: The Monte Carlo simulation true energy distribution (red) and the simulated reconstructed nuclear recoil energy distribution (blue) for the lowest 3.11–4.53 keV$_{\text{nr}}$ energy bin in the Q_y analysis. This figure was produced after position resolution effects are applied in the simulation. This represents a $\times 1.03$ shift in the mean reconstructed energy of the bin relative to the true Monte Carlo simulation recoil energy and is taken into account in the correction factor reported in Table 6.2.

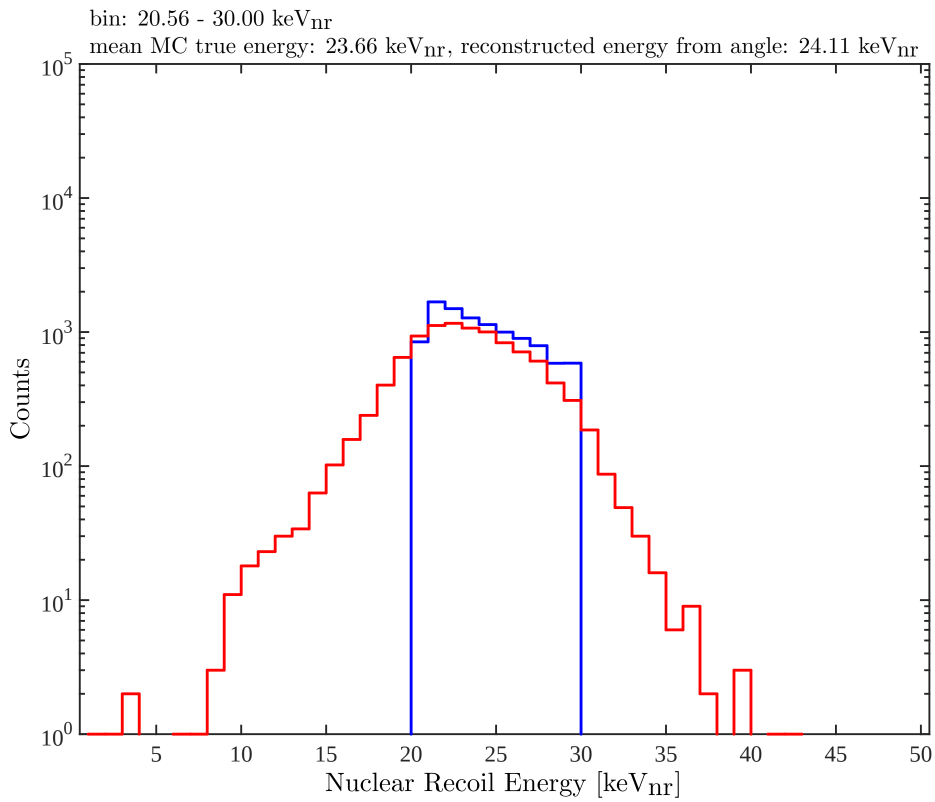

Figure 6.25: The Monte Carlo simulation true energy distribution (red) and the simulated reconstructed nuclear recoil energy distribution (blue) for the lowest 20.56–30.00 keV$_{\rm nr}$ energy bin in the Q_y analysis. This figure was produced after position resolution effects are applied in the simulation. This represents a $\times 0.98$ shift in the mean reconstructed energy of the bin relative to the true Monte Carlo simulation recoil energy and is taken into account in the correction factor reported in Table 6.2.

The energy reconstruction bias due to position resolution effects is shown in Fig. 6.26. The corresponding correction factor applied to produce the corrected mean bin recoil energies, $\left\langle E_{\rm nr,\,corrected}\right\rangle$, of the low-energy Q_y result in Ch. 5 is given by column four in Table 6.2. This correction factor γ is applied to the weighted mean recoil energy of each bin from Eq. 6.14:

$$\left\langle E_{\rm nr,\,corrected}\right\rangle = \gamma \left\langle E_{\rm nr}\right\rangle \tag{6.17}$$

The systematic uncertainty in this correction, reported in the Q_y result, is determined by comparing the effects of the baseline case where +0.35 cm of $\sigma_{(x,y)}$ is added to the +0.00 cm $\sigma_{(x,y)}$ and +0.70 cm $\sigma_{(x,y)}$ cases shown in columns three and five, respectively, of Table 6.2. In all cases, the

$\sigma_{(x,y)}$ uncertainty is added in quadrature to the radial and polar uncertainty terms in Eq. 6.5.

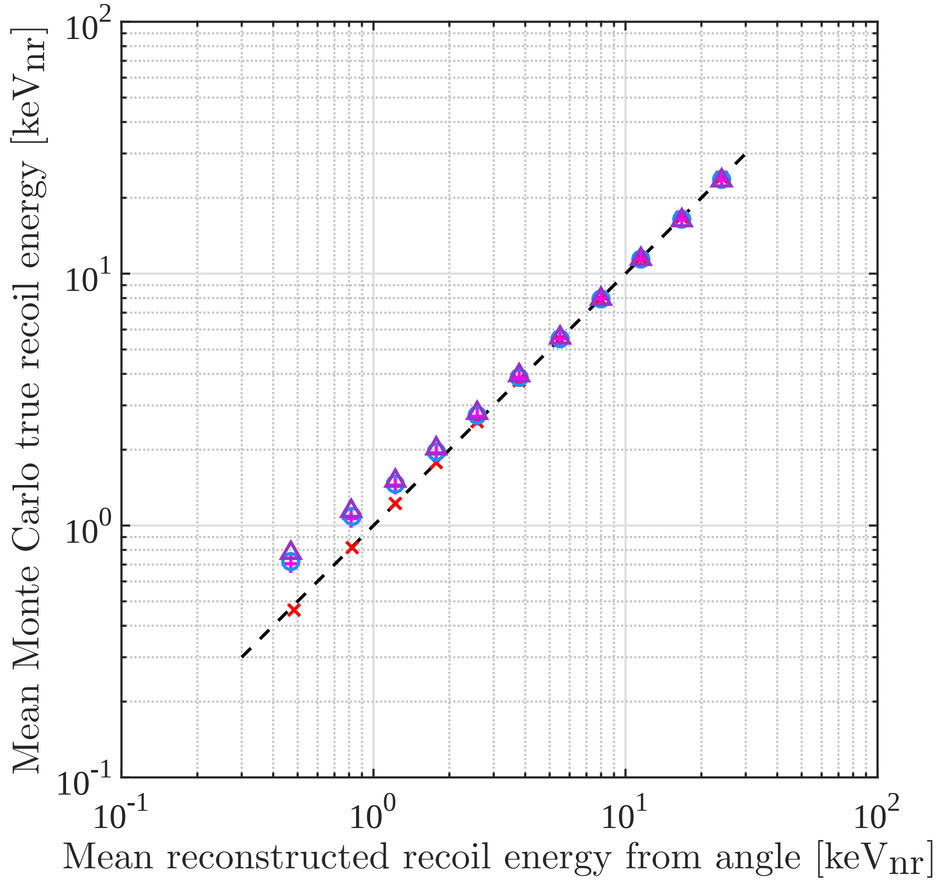

Figure 6.26: The effect of Eddington bias on the reconstructed recoil energy from angle for each bin used for the Q_y analysis. The red crosses ($\times$) show the mean true Monte Carlo nuclear recoil energy vs. the mean recoil energy reconstructed from angle before the (x, y, z) position resolution is applied to the first and second scatter vertex positions in the simulation (same as Fig. 6.14). The magenta plus signs ($+$), blue circles ($\circ$), and purple triangles ($\triangle$) show the mapping between true and reconstructed recoil energy after position reconstruction uncertainties are applied. The plus signs, blue circles, and purple triangles correspond to an additional systematic uncertainty in position beyond that calculated using Fig. 6.2 of +0.00 cm $\sigma_{(x,y)}$, +0.35 cm $\sigma_{(x,y)}$, +0.70 cm $\sigma_{(x,y)}$, respectively. The black dotted line is the ideal case of a one-to-one mapping between the true Monte Carlo simulation recoil energy and the reconstructed energy.

We confirmed that uncertainty in the position of the first neutron interaction is the dominant contributor to Eddington bias effects, as expected in the discussion in Sec. 6.1.3, by systematically repeating the simulation and analysis process. For each iteration, we injected position reconstruction uncertainty only along the specific coordinate under study, and only for one simulated scattering vertex—of the two in a double scatter—at a time. The result of this process indicates that the

Table 6.2: The Eddington bias correction applied to the mean measured recoil energy in the Q_y analysis. The first column contains the bin limits in units of reconstructed recoil energy from scattering angle. The ratio of the true Monte Carlo simulation recoil energy to the reconstructed recoil energy from scattering angle (correction factor γ) is given in columns two through five. The second column contains the correction as calculated when the true Monte Carlo neutron interaction positions are used in the simulation. These values correspond to the red crosses is Fig. 6.26. Columns three through five correspond to the bias correction calculated when position reconstruction are included in the simulation. These position reconstruction uncertainties include the statistical position reconstruction uncertainty, as well as an addition systematic component of +0.00 cm $\sigma_{(x,y)}$, +0.35 cm $\sigma_{(x,y)}$, and +0.70 cm $\sigma_{(x,y)}$, respectively, added according to the prescription described in Sec. 6.1.2. Column four is used for the mean bias correction applied to the Q_y data points, while columns three and five are used to estimate the uncertainty on the correction.

Q_y bin [keV$_{\mathrm{nr}}$]	No (x, y) uncertainty [keV$_{\mathrm{nr}}$ / keV$_{\mathrm{nr}}$]	(+0.00 cm $\sigma_{(x,y)}$) [keV$_{\mathrm{nr}}$ / keV$_{\mathrm{nr}}$]	(+0.35 cm $\sigma_{(x,y)}$) [keV$_{\mathrm{nr}}$ / keV$_{\mathrm{nr}}$]	(+0.70 cm $\sigma_{(x,y)}$) [keV$_{\mathrm{nr}}$ / keV$_{\mathrm{nr}}$]
0.30–0.65	0.95	1.47	1.53	1.65
0.65–1.00	0.99	1.30	1.32	1.39
1.00–1.46	1.00	1.18	1.19	1.24
1.46–2.13	1.00	1.10	1.11	1.14
2.13–3.11	1.00	1.05	1.06	1.08
3.11–4.53	1.00	1.02	1.03	1.04
4.53–6.62	1.00	1.01	1.01	1.02
6.62–9.65	1.00	1.00	1.00	1.00
9.65–14.09	1.00	0.99	0.99	0.99
14.09–20.56	1.00	0.99	0.98	0.98
20.56–30.00	1.00	0.98	0.98	0.97

dominant systematic contribution is from the $\sigma_{x'}[y'_1]$ uncertainty with some minor contribution from $\sigma_{y'}[y'_2]$. It is clear from this study that there is negligible contribution to the observed recoil energy bias from the $\sigma_{y'}[y'_1]$, $\sigma_{x'}[y'_2]$, $\sigma_z[y'_1]$, and $\sigma_z[y'_2]$ uncertainties. As always, y'_1 represents the first scatter vertex along the neutron beam projection and y'_2 represents the second scatter vertex along the beam line.

Chapter 7

Measurement of the Low-Energy Liquid Xenon Nuclear Recoil Scintillation Yield

The LUX Q_y result provides a precise *in situ* measurement of the charge yield as a function of energy, which defines the $S2$ response as a function of recoil energy scale within the 0.7–74 keV$_{\rm nr}$ range. A single-scatter signal model that simultaneously provides simulated $S1$ and $S2$ distributions was developed as described in Sec. 7.2. The ionization yield in the model was fixed to the measured Q_y from Ch. 5. The single-scatter (one S1 and one S2) event population was then used to calibrate the $S1$ yield using the observed $S2$ as a measure of energy. The L_y in the model was varied and the output compared to data to extract the best-fit scintillation yield for 1.08–12.8 keV$_{\rm nr}$ nuclear recoils. The absolutely measured g_1 value is used to directly report the light yield in the absolute units of photons / keV$_{\rm nr}$.

We use the model described in Sec. 7.2 to measure the light yield for energies as low as 1.08 keV$_{\rm nr}$, where a fraction of the events are above the S1 and S2 detection thresholds.[1] The main challenges in this regime are ensuring that the thresholds and resolution are well modeled for both $S1$ and $S2$. The LUX S1 and S2 threshold behavior is well understood [5, 59] and is included in the simulation used for best-fit parameter estimates. Uncertainty in the measured L_y due to uncertainties in the modeled S1 and S2 thresholds are quantified and discussed in Sec. 7.4. The $S1$ resolution is dominated by Poisson fluctuations in the number of detected photons due to the g_1 value of 0.115. The $S2$ resolution due to the Fano factor associated with quanta production, recombination fluctuations, and detector effects (purity, electron extraction) is constrained by the results in Ch. 5 and is consistent with the Poisson expectation of the model over the energy range spanned by the reported L_y data points. The shape of the $S2$ vs. $S1$ distribution in data and simulation is compared in Fig. 7.1.

7.1 Single-scatter event selection

The single-scatter pulse pairing requires an identified S1 pulse preceding an identified S2 pulse. The S1 identification threshold requires a coincidence of 2 PMTs each with signal >0.25 phd. The S2 analysis threshold required that raw $S2 > 55$ phd to reduce the number of potential accidental coincidence events. This S2 threshold is higher than used for the low-energy Q_y analysis described in Ch. 5 to ensure rejection of accidental coincidences masquerading as single-scatters. This source of potential contamination is quantified in Sec. 7.4. The LUX WIMP search analysis used a higher raw $S2 > 164$ phd threshold due to the longer exposure and lower signal to accidental coincidence background event ratio. The origin and measured residual number of accidental coincidence events are discussed later in Sec. 7.3. The same maximum area thresholds used in the low-energy Q_y analysis are applied to $S1$ and $S2$.

The lower S2 threshold than what was used for the WIMP search analyses provides an increased

[1] The code used for this analysis is located in the Brown Particle Astrophysics Group's GitHub organization [65] with the relative path "jverbus_lux_scratch/NeutronGeneratorAnalysis/ly/".

efficiency for detection of single-scatter events associated with low-energy nuclear recoils. The efficiencies for detecting 1 keV_{nr} and 2 keV_{nr} nuclear recoils were estimated after all analysis cuts to be 4% and 25%, respectively. In addition to this increased detection efficiency due to the lower S2 threshold, the underlying true nuclear recoil spectrum produced by 2.45 MeV neutrons in liquid xenon is a sharply falling function of energy from 0–30 keV_{nr}, which provides an additional enhancement in the relative number of low-energy events.

The neutron beam energy purity cuts were applied ensuring that only single-scatters within the 4.9 cm beam pipe projection with $y' > 15$ cm were accepted. A radial position cut ensuring $r < 21$ cm was applied.

Data quality cuts were applied to remove events due to accidental triggers in the period of delayed electron extraction, photoionization of impurities in the liquid xenon, or other photoelectric feedback effects following large S2 pulses that can span many subsequent event windows. An upper limit on the total raw pulse area in the event record outside of the identified S1 and S2 of 219 phd was applied. A cut ensuring that there are no SE or S2 pulses in the event record before the identified single-scatter S1 pulses was applied to ensure quiet detector conditions in the period preceding the identified single scatter. These requirements are independent of the nuclear recoil energy of the event, and accept 83% of non-accidental events after all other cuts are applied. The same upper limit on the width of S2 pulses used in the Q_y analysis was enforced to reject multi-site events at similar z'.

After all event selection, position, and data quality cuts for the scintillation yield analysis were applied, a population of 1931 events remained in the neutron beam projection analysis volume. The single-scatter event population is exceptionally clean with only a few events ($\ll$1%) lying outside the main distribution as can be seen in Fig. 7.1.

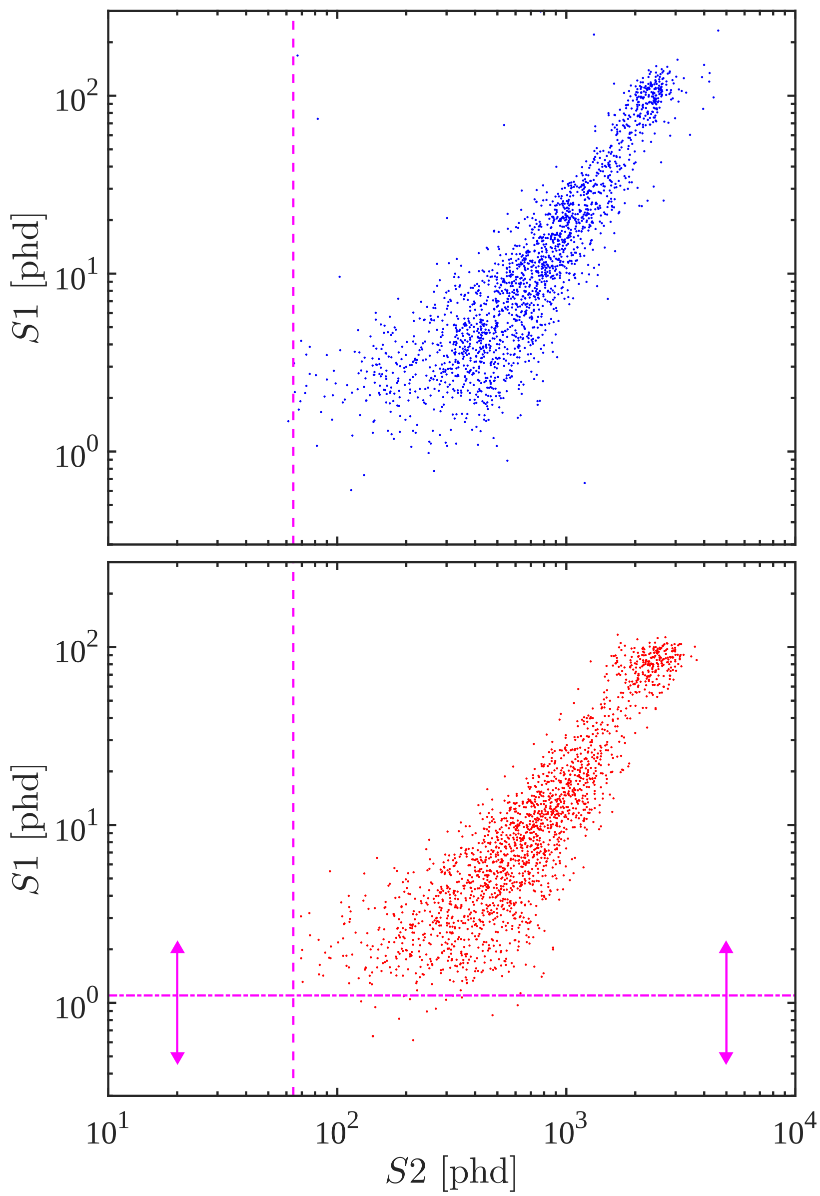

Figure 7.1: $S1$ vs. $S2$ single-scatter distribution for the L_y measurement. The 1931 events in data after all L_y analysis cuts are shown in this plot in blue in the upper frame. The non-uniformity of the distribution is due to the shape of the differential scattering cross-section (see Ch. 6 and Ch. 8). For comparison, a randomly selected sample consisting of the same number of simulated events, produced by the Lindhard-based NEST model described in Sec. 9.2, is shown in red in the lower frame. The raw $S2 > 55$ phd threshold is represented by the vertical dashed magenta line in corrected $S2$ space ($\sim$64 phd). All shown simulated events pass the two S1 photon coincidence requirement. An additional hard cutoff on the simulated $S1$ is applied as shown by the horizontal dot-dashed magenta line. This cutoff is varied over the range indicated by the magenta arrows, and the analysis is repeated to estimate the systematic uncertainty due to S1 threshold effects.

7.2 Signal model used for single-scatter simulation

A Monte Carlo model of the S1 and S2 signal production was used to generate a simulated single-scatter event population to compare to the observed single-scatter events in data passing the cuts described in Sec. 7.1. The ionization yield in the model was fixed to match the LUX D-D measured Q_y [122]. The modeled scintillation yield can be arbitrarily scaled using the free parameter ξ. The model includes anti-correlation between $S1$ and $S2$ as well as fluctuations in exciton and ion creation, recombination, and biexcitonic quenching. The variation of the scintillation yield in the model is achieved by scaling the number of photons produced at the interaction site before these fluctuation effects are applied. The JENDL-4.0 nuclear database was used to generate the underlying single-scatter nuclear recoil energy spectrum [33].

The S1 threshold in the model required that two individual photons are detected with a combined area greater than 1.1 phd. These threshold rules were chosen to match the efficiency of the LUX S1 threshold. The single-scatter event distribution after the application of this threshold is shown in Fig. 7.1. The corresponding $S2$ spectrum is shown by the shaded red histogram in Fig. 7.2. Systematic uncertainties associated with this model are discussed in Sec. 7.4.

7.3 Data analysis

The selected single-scatter events were collected into bins of $S2$, and the resulting mean photon yield for each bin was extracted by comparing the $S1$ distribution of events in the $S2$ bin to the model described in Sec. 7.2. The resulting $S2$ spectrum is shown in Fig. 7.2 for both data and simulation. The first bin spans the range $50 < S2 < 100$ phd and the subsequent eight bins are 100 phd wide. The simulation was normalized to match the total number of counts observed in data between 900–1500 phd, while the L_y measurement was made using the $S2$ range between 50–900 phd. This ensured that the normalization between simulation and data was performed outside of the region used to produce L_y data points. The higher energy normalization range from 900–1500 phd corresponds to roughly 20–30 keV$_{\rm nr}$, while the L_y measurement region from 50–900 phd contains events with a recoil energy of 0–20 keV$_{\rm nr}$. These $S2$ ranges for the L_y measurement and normalization regions were chosen to match the recoil energy range used for the forward-scatter based low-energy Q_y measurement, which accepts events with a maximum recoil energy of 30 keV$_{\rm nr}$. The transition between the measurement and normalization regions at an $S2$ of 900 phd was chosen to ensure the measured L_y data points fall within the 0.7–24.2 keV$_{\rm nr}$ recoil energy range, where the ionization yield is absolutely defined by the low-energy Q_y measurement described in Ch. 5. As the L_y bin boundaries are defined by $S2$ values, the corresponding mean recoil energy for each L_y bin is not expected to match the measured nuclear recoil energy of the Q_y data points.

The best-fit light yield for each $S2$ bin was obtained via a maximum-likelihood based optimization of the simulated $S1$ spectrum. The log-likelihood function is given by Eq. 7.1, where the parameters are ξ, N_s, N_b, and g_1. The constant N is the total number of events in the $S2$ bin of interest in data. It does not vary during the optimization so the $\ln(N!)$ term can be dropped. The parameter ξ is a scaling factor used to vary the light yield in the model used for simulation during the optimization. The parameter N_s is the number of signal events expected from simulation based upon the normalization at higher energies. This value of N_s is fixed for each iteration of the ξ parameter. The parameter N_b is the number of events in a floating flat background PDF component; this is typically $\sim$1% and no more than $\sim$10% of total events. The parameter g_1 is the S1 photon detection efficiency, which is allowed to float as a nuisance parameter within the constraints set by the measured value of 0.115 ± 0.004. This treatment of g_1 as a constrained nuisance parameter incorporates the systematic uncertainty due to the photon detection efficiency into the reported uncertainties resulting from the four dimensional log-likelihood contour.

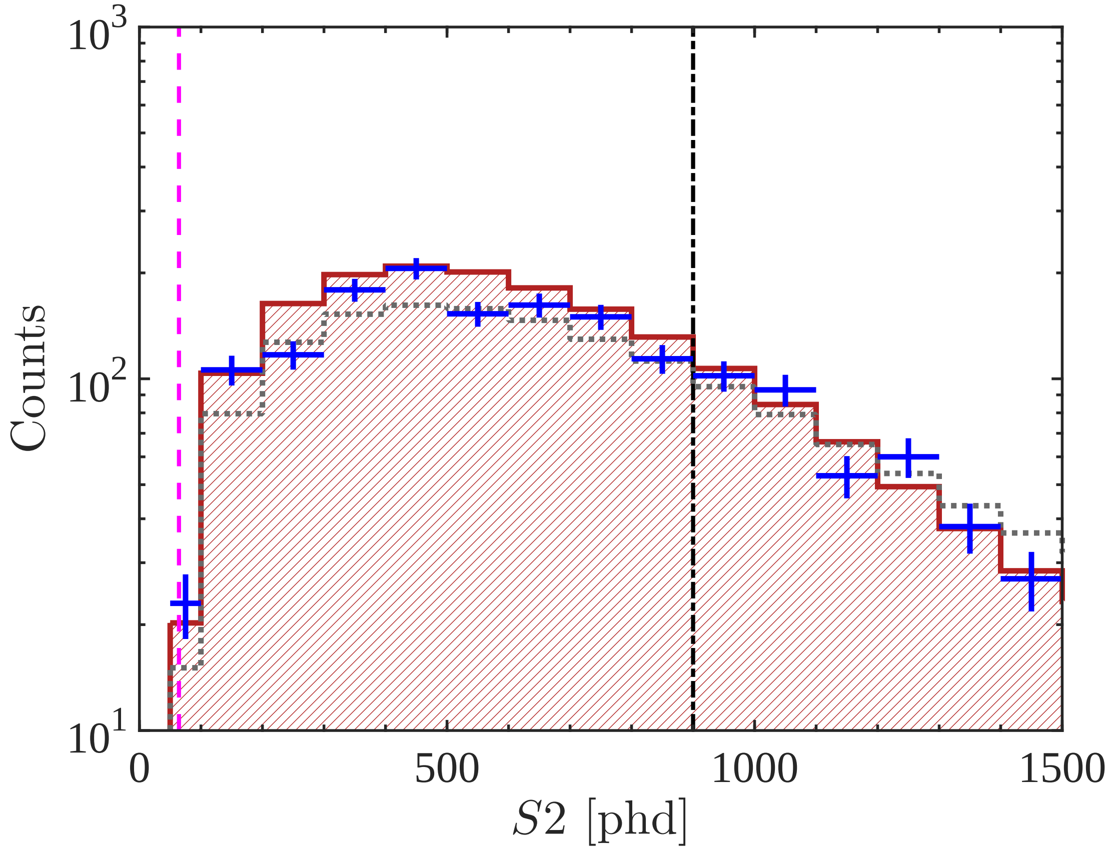

Figure 7.2: The single-scatter $S2$ spectrum from data after all L_y analysis cuts are applied is shown in blue. The blue error bars are statistical. The corresponding simulated $S2$ spectrum is represented by the shaded red histogram. The simulated $S2$ spectrum produced using an alternative nuclear database (ENDF/B-VII.1 [45]) is shown by the gray dotted line. The statistical uncertainty on the simulated spectra is negligible. The black dot-dashed line at 900 phd $S2$ demarcates the measurement region from the normalization region. The simulation is normalized to match the total number of counts observed in data between 900–1500 phd, while the L_y points are determined using the events in the region $50 < S2 < 900$. The raw $S2 > 55$ phd threshold is represented by the vertical dashed magenta line in corrected $S2$ space ($\sim$64 phd).

$$\ln L =$$

$$- (N_s + N_b) + \ln (N!) + \ln \left[\frac{1}{\sqrt{2\pi}\sigma_{g_1}} e^{-\frac{(g_1 - g_{1,0})^2}{2\sigma_{g_1}^2}} \right] + \sum_{i=1}^{N} \ln \left[N_s p_s(x_i|\xi, g_1) + N_b p_b(x_i) \right]. \quad (7.1)$$

This optimization was performed for each of the nine $S2$ bins used to extract the L_y. The resulting estimated parameters of interest are the measured mean number of S1 photons leaving the interaction site, n_p, and the mean underlying recoil energy. The parameters of interest were extracted from the simulated event distribution once we obtained a fit to the observed $S1$ distribution for a given $S2$ bin. The corresponding L_y data point is centered on the mean energy of the underlying Monte Carlo events that populate the $S2$ bin.

The resulting measured scintillation yield for each of the nine bins is shown in Fig. 7.3. The LUX L_y measurement is shown in both absolute units of photons/keV$_{\mathrm{nr}}$ on the left axis and relative to the 32.1 keV$_{\mathrm{ee}}$ $^{83\mathrm{m}}$Kr light yield as measured at 0 V/cm on the right axis. It is worth noting that the left axis represents the first direct absolute measurement of the nuclear recoil scintillation yield. All previous measurements of the liquid xenon light yield have reported results in terms of $\mathcal{L}_{\mathrm{eff}}$, the observed light yield relative to that of 122 keV$_{\mathrm{ee}}$ gamma rays from a ^{57}Co calibration source.

We performed a cross-check of the observed event rate in data and simulation, similar to what was done for the low-energy Q_y analysis. A single-scatter LUXSim/GEANT4 based simulation of single-scatters was performed using the NEST model described in Sec. 9.2. The simulation output was used to produce per-channel waveform data that was processed using the LUX D-D analysis pipeline. A neutron source rate of $(2.6 \pm 0.8) \times 10^6$ n/s provides the optimal match between the absolute number of single-scatter events in simulation and data, which is in agreement with the independently measured neutron production rate of $(2.5 \pm 0.3) \times 10^6$ n/s. In addition, this absolute rate is consistent with the corresponding normalization of double scatter data in Ch. 5.

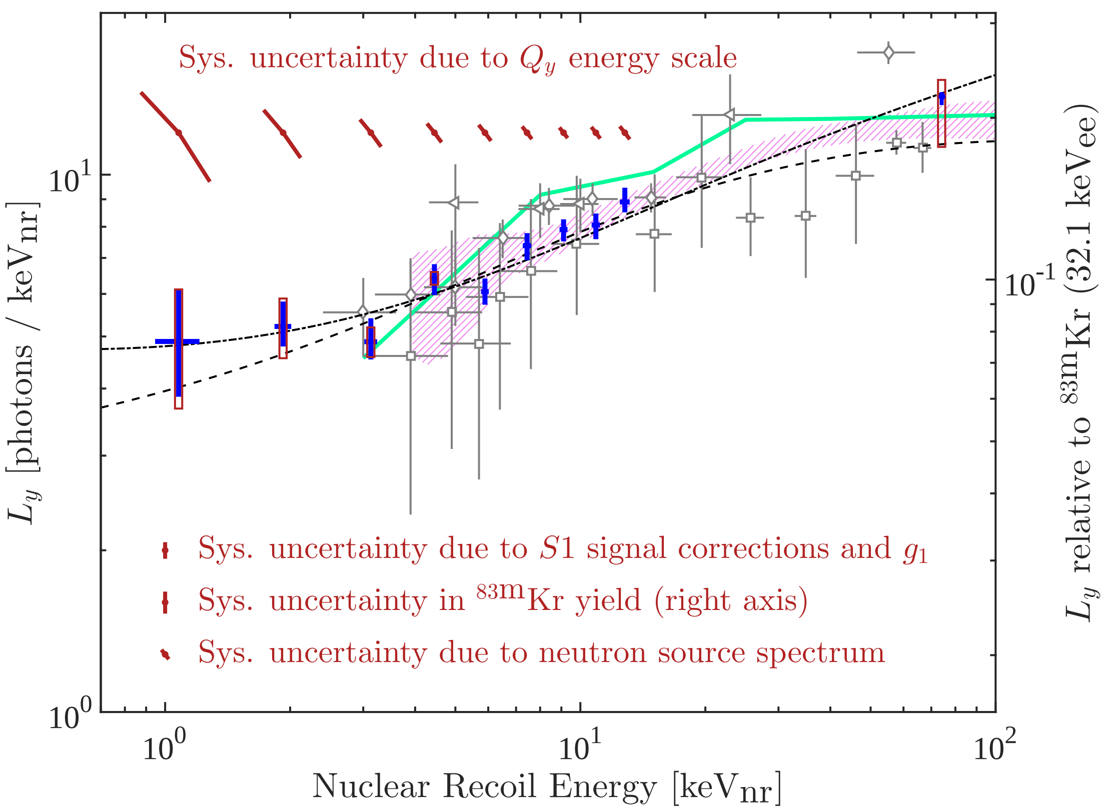

Figure 7.3: The LUX L_y measured at 180 V/cm is shown by the blue points. The left axis is the absolute yield L_y in units of photons/keV$_{\text{nr}}$ and the right axis is the L_y relative to the LUX *in situ* 32.1 keV$_{\text{ee}}$ $^{83\text{m}}$Kr yield at 0 V/cm. The red diagonal error bars at the top of the plot correspond to the 1σ systematic uncertainties on the determination of the energy scale from our measured Q_y. Inserted below the data, the top red systematic uncertainty marker on the left side of the plot corresponds to the scaling uncertainty due to g_1 and $S1$ signal corrections. The middle red systematic uncertainty marker is the uncertainty on the $^{83\text{m}}$Kr light yield as measured at 0 V/cm in LUX. This uncertainty is applicable to the right axis scale only. The bottom red systematic uncertainty marker corresponds to the uncertainty in the mean neutron energy produced by the D-D source. The red box indicates the systematic uncertainty in the endpoint L_y measurement at 74 keV$_{\text{nr}}$. The gray data points represent other angle based measurements with a keV$_{\text{nr}}$ energy scale. The $\mathcal{L}_{\text{eff}}$ measurements in Refs. [17] ($\triangleleft$), [18] ($\square$), and [19] ($\diamond$) were performed at 0 V/cm. The purple band [15] and thick green line [16] represent spectral fit based $\mathcal{L}_{\text{eff}}$ measurements with a keV$_{\text{nr}}$ energy scale corrected to 0 V/cm using an assumed value of S_{nr}. The dashed (dot-dashed) black line corresponds to the Lindhard-based (Bezrukov-based) LUX best-fit NEST model as described in Sec. 9.2.

This agreement between the observed data and expected absolute event rate using the model in Sec. 9.2 demonstrates the self-consistency of the measured yields with the observed number of events. Additionally, the agreement with the independently measured best-fit neutron rate at the source from the double-scatter Q_y analysis demonstrates consistency between the single-scatter and double-scatter analyses.

The relative scale (right vertical axis) in Fig. 7.3 is set using the measured ^{83m}Kr yield in LUX at 0 V/cm of 64 ± 3 photons/keV$_{ee}$. The internal, homogeneous ^{83m}Kr source is a more effective standard candle than the primary gamma ray produced by the traditional external ^{57}Co source used for $\mathcal{L}_{\rm eff}$ measurements due to the self-shielding properties of modern, large liquid xenon TPCs. ^{83m}Kr decays via the emission of a 32.1 keV$_{ee}$ conversion electron followed by a 9.4 keV$_{ee}$ conversion electron with a characteristic time separation of about 154 ns.[2] Previous measurements reported in terms of $\mathcal{L}_{\rm eff}$ were converted to L_y assuming a ^{57}Co absolute yield of 63 photons/keV$_{ee}$ at 0 V/cm [86, 133]. Conveniently in LUX, as was found in Ref. [85], the ^{83m}Kr yield at 32.1 keV$_{ee}$ and the ^{57}Co yield at 122 keV$_{ee}$ are in close agreement allowing easy direct comparison to previous L_y measurements using the right axis in Fig. 7.3.

The electron recoil light yield was also measured using ^{131m}Xe remaining in the liquid xenon from cosmogenic activation before the target media was transported underground. The ^{131m}Xe nuclei undergoes an isomeric transition depositing 163.9 keV$_{ee}$ with a half life of 11.8 days and provides an internal, homogeneous calibration source close in energy to the 122 keV$_{ee}$ gamma from ^{57}Co that has been used to calibrate smaller liquid xenon TPCs in the past. The light yield was measured to be 41.3 ± 1.1 photons/keV$_{ee}$ at 180 V/cm using this source. The light yield due to a 122 keV$_{ee}$ electron recoil at 180 V/cm is $1.12^{+0.08}_{-0.06}$ times higher than the yield expected at 164 keV$_{ee}$ according to NEST v0.98. After accounting for this yield translation from 163.9 keV$_{ee}$ to 122 keV$_{ee}$ and the expected $S_{ee}(\mathcal{E} = 180$ V/cm) field quenching factor for electron recoils of 0.74 [85, 121],

[2] Unlike the 9.4 keV$_{ee}$ component, the light yield of the 32.1 keV$_{ee}$ component is constant as a function of the time separation between the emission of conversion electrons and can be used as a standard candle [132].

we measure the electron recoil yield for a 122 $\mathrm{keV_{ee}}$ gamma to be 63^{+5}_{-4} photons/$\mathrm{keV_{ee}}$ at 0 V/cm. This measured yield in LUX is in agreement with the value of 63 photons/$\mathrm{keV_{ee}}$ at 0 V/cm used to convert previous $\mathcal{L}_{\mathrm{eff}}$ results to L_y.

Avoiding any assumptions about S_{nr} and S_{ee}, the LUX measured L_y in Fig. 7.3 is reported in absolute units at 180 V/cm. Previous results in the figure were measured at 0 V/cm or were corrected to 0 V/cm assuming various values of S_{nr} for the operating field—all of which ranged 0.92–1.0. The agreement of results from liquid xenon TPCs operating across a broad range of drift fields (0–3.6 kV/cm) in Fig. 7.3 indicates that the nuclear recoil light yield in liquid xenon is a weak function of the drift electric field.

7.4 Backgrounds and uncertainties

Accidental coincidences due to S2 signals produced by delayed extraction of ionization electrons and photoionization of impurities can masquerade as single-scatter events potentially contributing to a background in the lowest-energy L_y bin ($50 < S2 < 100$ phd). The overlapping photoelectrons due to the intrinsic PMT dark rate as well as stray photons contribute to the S1 signals in these accidental coincidence single-scatter events. These accidental coincidence events are rejected using a combination of two data quality cuts: the upper limit on the raw pulse area in the event window outside of the S1 and S2 signals, and the requirement that there are no single electrons or S2 signals before the S1 in the event record.

The number of accidental coincidence events remaining after the application of the two data quality cuts was quantified using off-beam single-scatter interactions as a sideband. The accidental coincidence events potentially contributing to a low-energy L_y analysis background were verified to occur with a flat distribution as a function of z. The neutron beam analysis volume was offset to $z = 33.9$ cm below the liquid surface, away from the true neutron beam center at $z = 16.1$ cm. Other than the analysis volume offset, an identical analysis was performed. Any events observed in the first $S2$ bin of the sideband analysis were conservatively assumed to be accidental coincidences. This conservative estimate of the accidental coincidence event contamination in the first L_y bin is 3.0 ± 1.7 events, which is within the 1σ uncertainty of the total number of events in this bin during the standard analysis.

The L_y data and per-bin statistical and systematic uncertainties are listed in Table 7.1. Uncertainties common across all bins in the low-energy and endpoint L_y measurements are listed in Table 7.2.

Table 7.1: The LUX measured scintillation yield for nuclear recoils in liquid xenon at an electric field of 180 V/cm and associated statistical uncertainties. The first two columns correspond to the blue low-energy L_y data points in Fig. 7.3. The fractional systematic uncertainty in energy due to the data-driven Q_y based energy scale is denoted by $\Delta E_{\rm nr}/E_{\rm nr}$. This uncertainty in energy is represented by the slanted red error bars at the top of the figure due to the anti-correlation of the location of the L_y data points on the vertical axis. The estimated fractional systematic uncertainty in n_p due to uncertainty in the S1 threshold is represented by $\Delta n_p/n_p$. This uncertainty is represented by the red boxes around the low-energy L_y data points. Quoted uncertainties are symmetric ($\pm$) unless otherwise indicated.

$E_{\rm nr}$ (keV$_{\rm nr}$)	L_y (ph/keV$_{\rm nr}$)	$\Delta E_{\rm nr}/E_{\rm nr}$ (%)	$\Delta n_p/n_p$ (%)
1.08 ± 0.13	$4.9^{+1.2}_{-1.0}$	19	25
1.92 ± 0.09	$5.2^{+0.6}_{-0.4}$	10	13
3.13 ± 0.11	$4.9^{+0.5}_{-0.4}$	6	6
4.45 ± 0.11	$6.4^{+0.4}_{-0.4}$	4	3
5.89 ± 0.13	$6.1^{+0.4}_{-0.3}$	3	-
7.44 ± 0.17	$7.4^{+0.4}_{-0.4}$	3	-
9.1 ± 0.2	$7.9^{+0.4}_{-0.4}$	3	-
10.9 ± 0.3	$8.1^{+0.4}_{-0.5}$	2	-
12.8 ± 0.3	$8.9^{+0.6}_{-0.4}$	3	-

The systematic uncertainty in L_y due to the S1 threshold model used in simulation is reported in Table 7.1. The contribution from the S1 threshold model to the systematic uncertainty in L_y was estimated by re-analyzing the data using the alternative $S1$ thresholds in the signal model, as indicated by the arrows in Fig. 7.1. The two alternative S1 thresholds require two photons to be detected in simulation with a combined area of 0.5 phd and 2.0 phd, respectively. The systematic uncertainty due to the modeled S1 threshold was conservatively estimated by quoting the maximum variation in L_y observed during this exercise. The average systematic uncertainty due to the measurement uncertainty in g_1 is quantified in Table 7.2.

The dominant effect contributing to the $S1$ resolution is Poisson fluctuation in the number of collected photons due to the g_1 value of 0.115. Resolution effects due to variations in the underlying Fano factor and recombination fluctuations were confirmed to be subdominant. Systematic effects due to S2 threshold uncertainty, which only affect the lowest recoil energy bin, were confirmed to be subdominant to the reported uncertainties for 10% variations in S2 threshold.

If the nuclear database used in the signal model overpredicts (underpredicts) the expected number of events at low energies the optimization will favor a lower (higher) L_y to compensate. The JENDL-4.0 library used in the model used to extract the L_y result is the most modern evaluation for neutron-xenon cross-sections for neutron energies of 2.45 MeV [130]. Seven other nuclear databases were studied to quantify the effect on the predicted number of events at low energies and the effect on the measured L_y when using older evaluations. Of the databases studied, ENDF/B-VII.1 and JENDL-4.0 represent the extremes in the angular scattering cross-section over the energy range of interest for this analysis between 0–30 keV_{nr} (roughly $S2 < 1500$ phd). In addition to being the most modern evaluation, the baseline JENDL-4.0 database is the most conservative for use in the light yield measurement as all other databases predict fewer events at low energies after normalization between 900–1500 phd $S2$. The $S2$ spectra produced via the signal model described in Sec. 9.2 using both the ENDF/B-VII.1 and JENDL-4.0 databases are shown in Fig. 7.2. The L_y analysis was repeated using the alternative ENDF/B-VII.1 database, which results in a measured L_y 25% larger at 1.1 keV_{nr}. The difference in measured L_y between databases decreases with increasing energy until it is subdominant to statistical uncertainties at 5.9 keV_{nr}.

As a cross-check, the L_y measurement was repeated using an alternative initial modeled light yield as the starting point for the optimization. The results of this cross-check were consistent with the baseline measurement within 1σ statistical uncertainties. The systematic uncertainty in the reconstructed energy due to the variation in the atomic mass and cross-section over xenon isotopes with significant natural abundance was estimated to be <2% for all energies [124].

Table 7.2: Uncertainties common to the L_y measurement both at low energies and at the D-D recoil energy spectrum endpoint. The second column lists systematic uncertainties associated with the mean reconstructed number of primary scintillation photons, n_p. The third column lists systematic uncertainties associated with the mean reconstructed energy. Quoted uncertainties are symmetric ($\pm$) unless otherwise indicated.

Source of Uncertainty	$\Delta n_p/n_p$ (%)	$\Delta E_{\rm nr}/E_{\rm nr}$ (%)
g_1	3.48	-
$S1$ correction (3D position)	0.6	-
$S1$ correction (non-uniform field)	$^{+0}_{-0.5}$	-
Mean neutron energy from source	-	2
Total	$^{+4}_{-4}$	2

Chapter 8

Measurement of the Liquid Xenon Scintillation and Ionization Yields at the D-D Nuclear Recoil Spectrum Endpoint

The maximum nuclear recoil energy produced in liquid xenon by the monoenergetic 2.45 MeV neutrons from the D-D source is given by Eq. 1.1. This provides a known endpoint feature in the $S1$ and $S2$ spectra produced by 180° scatters corresponding to the maximum recoil energy of 74 keV$_{\mathrm{nr}}$. The population of single-scatter events was used to extract L_y and Q_y using the nuclear recoil energy spectrum endpoint closely following the analysis procedure used in Ref. [28].[1]

As in the low-energy L_y analysis, the neutron beam energy purity cuts and a radial position cut of $r < 21$ cm were applied. A raw $S2$ analysis threshold of 164 phd was applied, well below the region of interest near the endpoint where the mean $S2$ is 2500 phd. An upper limit on the total digitized area in the event record outside of the identified S1 and S2, identical to the one used for the L_y analysis, was applied. As in the previous analyses, an upper limit on the S2 signal RMS width of 775 ns was enforced. As in the low-energy L_y measurement, we used the JENDL-4.0 nuclear database to generate the underlying nuclear recoil energy spectrum in the model used for optimization. The systematic uncertainty in the reconstructed energy due to the variation in the atomic mass and cross-section over xenon isotopes with significant natural abundance was estimated to be <2% for all energies [124].

8.1 Scintillation yield at nuclear recoil spectrum endpoint

To extract the light yield at 74 $\mathrm{keV_{nr}}$, we fit an S1 signal model to the $S1$ spectrum endpoint feature. The observed $S1$ spectrum was modeled using a constant L_y across the entire nuclear recoil energy range. Three parameters were varied in a binned maximum-likelihood optimization: the L_y value at the endpoint as the target parameter, F_1' as a resolution term, and the overall normalization of counts in the model. The $S1$ resolution as a function of the mean integer number of photons detected, n_{phd}, was set by

$$\sigma_{S1}(n_{\mathrm{phd}}) = \sqrt{n_{\mathrm{phd}}(F_1' + \sigma_{\mathrm{sphe}}^2)}\,, \tag{8.1}$$

where $\sigma_{\mathrm{sphe}} = 0.37$ is the mean single photoelectron resolution of the LUX PMTs [80]. The F_1' parameter was allowed to float as a nuisance parameter controlling effective $S1$ resolution in the

[1] The code used for this analysis is located in the Brown Particle Astrophysics Group's GitHub organization [65] with the relative path "jverbus_lux_scratch/NeutronGeneratorAnalysis/endpoint_yields/".

optimization and accommodating fluctuations in the observed signal. The most significant contribution to the F_1' resolution term is the detector's scintillation photon detection efficiency (g_1). The fluctuations associated with scintillation and recombination at the interaction site are subdominant.

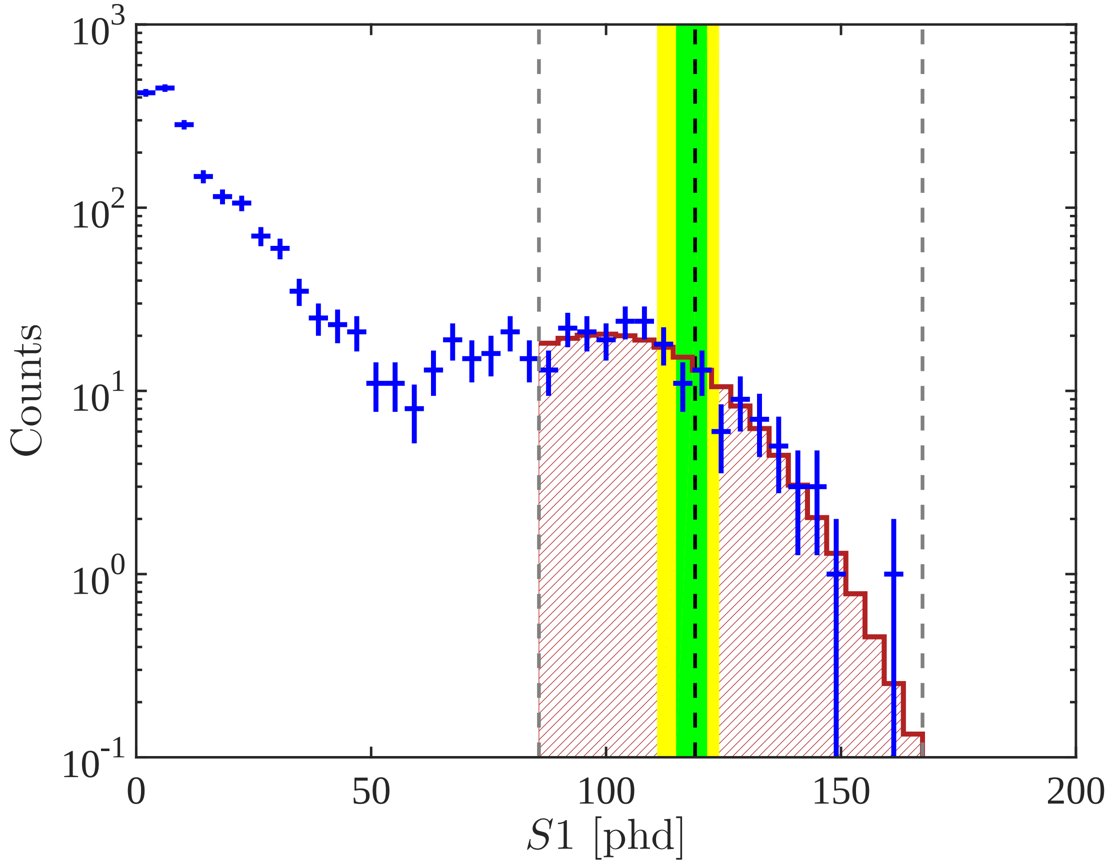

Figure 8.1: Result of the L_y endpoint optimization. The single-scatter $S1$ spectrum after all cuts is shown in blue. The horizontal error bar represents the bin width, and the vertical error bar represents the statistical uncertainty on the number of events in each bin. The best-fit endpoint model is represented by the red shaded histogram. The binned maximum-likelihood optimization was performed between the gray dashed lines. The fit has a $\chi^2/\mathrm{dof} = 7.5/9$ yielding a p-value of 0.59. The black dashed line is the best-fit endpoint in $S1$ space, with 1σ and 2σ statistical uncertainties represented by the green and yellow regions, respectively.

The results of the L_y measurement using the nuclear recoil spectrum endpoint are shown in Fig. 8.1. The L_y at 74 keV$_{\mathrm{nr}}$ was measured to be $14.0^{+0.3(\mathrm{stat})+1.1(\mathrm{sys})}_{-0.5(\mathrm{stat})-2.7(\mathrm{sys})}$ photons/keV$_{\mathrm{nr}}$ at 180 V/cm. The systematic uncertainties specific to the L_y measurement at the D-D recoil spectrum endpoint are listed in the right column of Table 8.1 and are represented by the red box around the blue endpoint in Fig. 7.3. Additional sources of systematic uncertainty that are common to both the endpoint and low-energy L_y measurement are listed in Table 7.2.

The L_y endpoint specific systematic uncertainties were determined by varying the associated model or analysis parameters and re-running the optimization. The systematic uncertainty due to the D-D neutron recoil energy spectrum used in the model was conservatively estimated by repeating the analysis assuming a completely flat recoil spectrum extending to 74 keV$_{\mathrm{nr}}$. The systematic uncertainty due to the assumption of a constant L_y was determined by repeating the analysis while modeling the L_y as a straight line. In this case, the slope of the modeled L_y was allowed to float as an additional nuisance parameter. The systematic uncertainties due to the choice of optimization region and bin size were estimated by separately repeating the analysis with a 20% larger optimization region and ×2 the number of bins, respectively.

Table 8.1: Uncertainties specific to the L_y measurement using the D-D nuclear recoil spectrum endpoint. Quoted uncertainties are symmetric (±) unless otherwise indicated.

Source of Uncertainty	Statistical (%)	Systematic (%)
Binned likelihood optimization	$^{+2}_{-3}$	-
Input recoil energy spectrum	-	6
Slope of L_y in model	-	$^{+5}_{-18}$
Choice of optimization region	-	1.8
Choice of bin size	-	0.4
Total	$^{+2}_{-3}$	$^{+8}_{-19}$

8.2 Ionization yield at nuclear recoil spectrum endpoint

An identical procedure to that used for the L_y endpoint was used to extract the Q_y using the same population of single-scatter events. The observed S2 signal spectrum was modeled using a flat Q_y across the entire D-D recoil energy range. Three parameters were varied in a binned maximum-likelihood optimization: the Q_y value at the endpoint as the target parameter, F_2' as a resolution term, and the overall normalization of counts in the model. The S2 resolution as a function of mean integer number of electrons extracted, $n_{e_{S2}}$, was determined by

$$\sigma_{\mathrm{S2}}(n_{e_{\mathrm{S2}}}) = \sqrt{n_{e_{\mathrm{S2}}}(\mu_{\mathrm{SE}}^2 F_2' + \sigma_{\mathrm{SE}}^2)}\,, \tag{8.2}$$

where μ_{SE} and σ_{SE} are the mean and standard deviation, respectively, of the observed SE distribution in the D-D dataset.

The F_2' parameter was allowed to float as a nuisance parameter controlling effective $S2$ resolution in the optimization and accommodating fluctuations in the observed signal. The most significant contributions to the F_2' resolution term are the fluctuations associated with ionization and recombination at the interaction site, as well as binomial detector effects due to the free electron lifetime and electron extraction efficiency.

The results of the Q_y measurement using the D-D recoil spectrum endpoint are shown in Fig. 8.2. The Q_y at 74 keV$_{\mathrm{nr}}$ was measured to be $3.06^{+0.05(\mathrm{stat})+0.2(\mathrm{sys})}_{-0.06(\mathrm{stat})-0.4(\mathrm{sys})}$ electrons/keV$_{\mathrm{nr}}$ at 180 V/cm. The systematic uncertainties specific to the Q_y measurement at the nuclear recoil spectrum endpoint are listed in Table 8.2 and are represented by the red box around the blue endpoint in Fig. 5.4. Identically to the procedure used for the L_y, the Q_y endpoint specific systematic uncertainties were determined by varying the associated model or analysis parameters and re-running the optimization. The systematic uncertainty due to the D-D neutron recoil energy spectrum used in the model was conservatively estimated by repeating the analysis assuming a completely flat recoil spectrum extending to 74 keV$_{\mathrm{nr}}$. The systematic uncertainty due to the assumption of a constant Q_y in the base measurement was determined by repeating the analysis while modeling the Q_y as a straight line. In this case, the slope of the modeled Q_y was allowed to float as an additional nuisance parameter. This is the dominant source of systematic uncertainty. The systematic uncertainty due to the choice of optimization region and bin size was estimated by separately repeating the analysis with a 20% larger optimization region and $\times 2$ the number of bins, respectively. Additional sources of systematic uncertainty that are common to both the endpoint and low-energy Q_y measurement are listed in

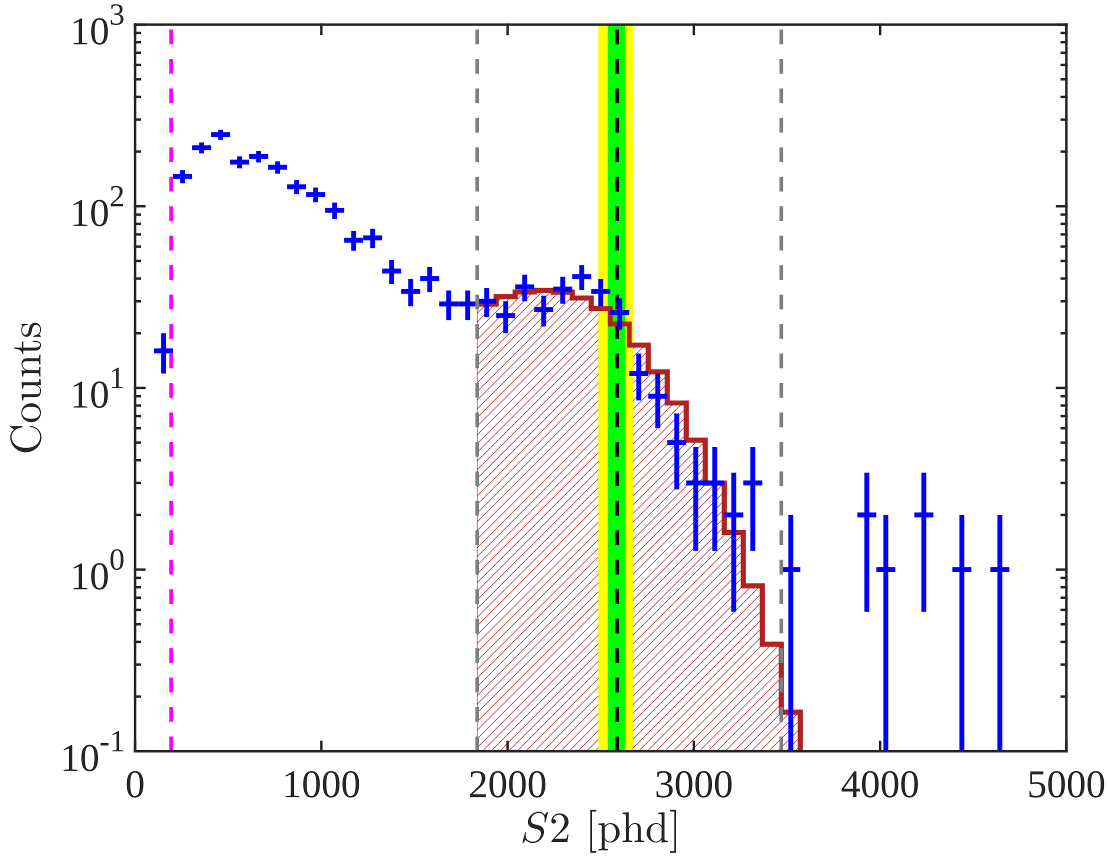

Figure 8.2: Result of the Q_y endpoint optimization. The single-scatter S2 spectrum after all cuts is shown in blue. The horizontal error bar represents the bin width, and the vertical error bar represents the statistical uncertainty on the number of events in each bin. The best-fit endpoint model is represented by the red shaded histogram. The binned maximum-likelihood optimization was performed between the gray dashed lines. The magenta dashed line depicts the location of the S2 threshold. The χ^2/dof is 14.7/9 yielding a p-value of 0.10. The black dashed line is the best-fit endpoint in S2 space, with 1σ and 2σ statistical uncertainties represented by the green and yellow regions, respectively. The six events observed outside of the fit range ($3500 < S2 < 5000$) could be due to multiple simultaneous S2 signals at the same z position combined in the event record, or contamination consisting of 39.6 keV$_{\mathrm{ee}}$ gamma rays from ^{129}Xe inelastic neutron scatters.

Table 5.2.

Table 8.2: Uncertainties specific to the Q_y measurement using the D-D recoil spectrum endpoint. Quoted uncertainties are symmetric ($\pm$) unless otherwise indicated.

Source of Uncertainty	Statistical (%)	Systematic (%)
Binned likelihood optimization	$^{+1.6}_{-2}$	-
Input recoil energy spectrum	-	5
Slope of Q_y in model	-	$^{+0.16}_{-11}$
Choice of optimization region	-	6
Choice of bin size	-	1.6
Total	$^{+1.6}_{-2}$	$^{+7}_{-13}$

Chapter 9

Impact of the Low-Energy Nuclear Recoil Calibration on LUX and Other Liquid Xenon Based Dark Matter Searches

In Sec. 9.1 of this chapter, we provide a summary of the LUX nuclear recoil measurements. After the yield measurements were finalized, two new versions of the NEST model were created using the simultaneous constraints provided by the measured Q_y, L_y, and nuclear recoil band results as described in Sec. 9.2. The first, more conservative, parameterization used for the recent LUX WIMP search results [5, 57] was based upon the Lindhard model [68]. An alternative parameterization was based upon the Bezrukov model using the Ziegler stopping power [87, 134]. Both the Lindhard- and Bezrukov-based models are consistent with the measured signal yields within experimental uncertainties over the entire recoil energy range for which results are reported.

In Sec. 9.3, we discuss the enhanced sensitivity to low-mass WIMPs of the LUX experiment resulting from this calibration. In Sec. 9.4, we discuss the effect of these nuclear recoil results on the expected observed rate of coherent elastic neutrino-nucleus scattering in liquid xenon TPCs. In Sec. 9.5, we discuss the theoretical limitations on low-energy nuclear recoil measurements in liquid xenon. In Sec. 9.6, we discuss the D-D calibration program for the next generation LUX-ZEPLIN dark matter detector.

9.1 Summary of results

We proposed a new type of *in situ* neutron calibration for large dual-phase noble liquid TPCs in Ch. 1. This calibration technique exploits the 3D position reconstruction capabilities of these detectors to measure the scattering angle between multiple interaction vertices in the detector from a single incident neutron, and thus absolutely determine the nuclear recoil energy on a per-event basis. This technique can provide a measurement of the charge and light yields of ultra-low-energy nuclear recoils in noble liquid TPCs with reduced experimental uncertainties compared to previous measurements in the field. This type of *in situ* neutron calibration can be used to provide a clear confirmation of the WIMP signal response at low masses in the modern generation of large TPC dark matter detectors.

In Sec. 1.3, we described several advanced strategies to enhance the physics reach of the neutron scattering kinematics-based calibration. First, using the pulsing capabilities of existing commercially available neutron generators to provide a well defined $\mathcal{O}(10~\mu\mathrm{s})$ neutron bunch width allows for z position reconstruction in the TPC without the traditionally required S1 to provide a t_0 for the event. This allows the rejection of >99% of accidental coincidence-based backgrounds simply from the reduction in duty cycle for <1 kHz repetition rate, and the measurement of events with S1 signals below threshold—including events with no observed S1 signal. The additional calibration statistics due to being able to measure the number of (no-S1, 1+ S2) events and (1 phe S1, 1+ S2) events can be used to measure L_y lower in energy with a better handle on systematic uncertainties due to threshold effects such as those described in Ref. [135]. Second, a quasi-monoenergetic 272 keV neutron source can be created using a passive deuterium-loaded material to reflect neutrons from the D-D generator. This technique provides a $\times 9$ reduction in neutron energy. The reflector neutron source provides an alternative set of calibration systematics and the potential to separate the S1 signals in time from multiple scatter vertices due to the $\times 3$ reduction in neutron velocity. These techniques could be exploited in a range of dark matter direct detection experiments that require low-energy monoenergetic neutrons with low gamma background including Ge and Si ZIP detectors, semiconductor ionization detectors, noble element single-phase, and dual-phase TPC detectors.

In Ch. 3, we measured the neutron energy spectrum of an Adelphi Technology, Inc. DD108 neutron generator at 90° relative to the deuterium ion beam direction. We characterized the outgoing neutron energy spectrum in two directions relative to the asymmetrical neutron production surface to determine the optimal orientation for the proposed nuclear recoil calibration. In both cases, the measured mean neutron energy is in agreement with the theoretical expectation of 2.45 MeV for this experimental setup. We also report the intrinsic resolution of the outgoing neutron energy distribution. The width (σ/μ) of the neutron distribution produced using Target orientation A and Target orientation B was measured to be 4.4 ± 0.6 (stat) $\pm$ 0.8 (sys) % and 2.7 ± 0.8 (stat) $\pm$ 0.8 (sys) %, respectively. The measured mean and width of the neutron energy distribution for Target orientation A and Target orientation B are in agreement within quoted uncertainties, indicating negligible dependence on rotation along the azimuthal direction. This characterization of the DD108 neutron spectrum confirmed the suitability of the device for the calibrations described in Ch. 1.

The low-energy ionization yield result described in Ch. 5 was obtained using the proposed technique to absolutely measure the nuclear recoil energy using the reconstructed angle between double-scatter events in the LUX TPC. The reported ionization yield has been measured a factor of $\times 5$ lower in energy than any other previous calibration with a kinematically-defined energy scale. The low-energy scintillation yield was measured using the single-scatter event population as described in

Ch. 7. The reported scintillation yield has been measured a factor of ×3 lower in energy than has been achieved previously, and is the first liquid xenon L_y result reported in the absolute units of photons/keV$_{\rm nr}$. The resulting light and charge yields are consistent with other recent measurements in the literature, as shown in Fig. 5.4 and Fig. 7.3.

The ratio of ionization to scintillation, commonly used in liquid xenon TPCs to discriminate between nuclear and electron recoils, was measured in Sec. 4.5. The collimated beam of neutrons from the D-D source provides a nuclear recoil band calibration with minimal contamination from multiple scintillation, single ionization events. All nuclear recoil measurements were performed at an electric field of 180 V/cm. In addition, the kinematically fixed 74 keV$_{\rm nr}$ endpoint of the nuclear recoil energy spectrum in liquid xenon was used to extract the charge and light yields as reported in Ch. 8. The measured signal yields at the recoil spectrum endpoint are also consistent with previously reported results at similar recoil energy.

9.2 NEST model fit to D-D data

To directly use the Q_y and L_y measurements in LUX simulation and analysis, we performed a fit of the NEST model to the data presented in this thesis [122].[1] We used a Metropolis-Hastings algorithm to sample a global likelihood function, in which the model was simultaneously constrained by the measurements of the nuclear recoil band mean (Sec. 4.5), light yield (Ch. 7 & 8), and charge yield (Ch. 5 & 8). The procedure followed the methodology described in Ref. [118]. The model parameterization and optimization are described in detail in Ref. [59], and the resultant NEST model is used in the analyses presented in Refs. [5, 57]. Here we discuss the implications for the physics of liquid xenon response at low energies.

[1]This section is part of a paper in preparation for publication [2]. I am the corresponding author of this paper. The analysis and text contained in this section was primarily generated by Brian Lenardo from UC Davis.

9.2.1 Nuclear recoil energy scale

In contrast to electronic recoils, recoiling nuclei lose a fraction of their energy to nuclear collisions, dissipating energy as heat rather than in processes leading to a detectable electronic signal. Reconstruction of nuclear recoil events, therefore, requires an understanding of these processes as a function of recoil energy. The formula for energy reconstruction can be written as

$$E = \frac{W(N_e + N_{\mathrm{ph}})}{L}\,, \tag{9.1}$$

where L is the fraction of energy that goes into detectable electronic channels [69]. Here, $W = 13.7$ eV is the average energy needed to create an exciton or electron-ion pair [66], N_e is the absolute number of ionization electrons, and N_{ph} is the absolute number of scintillation photons. Both N_e and N_{ph} represent the number of signal carriers before biexcitonic quenching effects, in contrast to n_e and n_p defined earlier in Ch. 5 and Sec. 7, which are the measured number of signal carriers that escape the interaction site.

The factor L is traditionally given by the Lindhard model [68, 69]. It is described by the formula

$$L = \frac{k\,g(\epsilon)}{1 + k\,g(\epsilon)}\,. \tag{9.2}$$

The parameter k is a proportionality constant between the electronic stopping power and the velocity of the recoiling nucleus. The quantity $g(\epsilon)$ is proportional to the ratio of electronic stopping power to nuclear stopping power, calculated using the Thomas-Fermi screening function. It is a function of the energy deposited, converted to the dimensionless quantity ϵ using

$$\epsilon = 11.5(E_{\mathrm{nr}}/\mathrm{keV_{nr}})Z^{-7/3}\,. \tag{9.3}$$

In these terms, $g(\epsilon)$ is given in Ref. [55] by

$$g(\epsilon) = 3\epsilon^{0.15} + 0.7\epsilon^{0.6} + \epsilon\,. \tag{9.4}$$

A commonly accepted value for the proportionality constant is $k = 0.166$, but this may range from 0.1 to 0.2 [69]. We utilize the Lindhard model in our nuclear recoil response model, allowing k to float in the fit to these data. The best-fit value from the global optimization is $k = 0.1735 \pm 0.0060$.

In addition to Lindhard's model, we explored an alternative model proposed in Ref. [87] that is more optimistic at energies below 2 keV$_{\mathrm{nr}}$. To do so, we begin with the generic form of L in Eq. 9.1:

$$L = \alpha \frac{s_e}{s_e + s_n} \,. \tag{9.5}$$

Here, s_e and s_n are the electronic and nuclear stopping powers, respectively, and α is a scaling parameter to model the cascade of collisions in a nuclear recoil event (best-fit is $\alpha = 2.31$ in the global optimization). The ratio s_e/s_n is analogous to g in Eq. 9.2. While the Lindhard model uses the Thomas-Fermi approximation to calculate s_n, we replace this with the empirical form from Ziegler et al. [134]:

$$s_n(\epsilon_{\mathrm{Z}}) = \frac{\ln(1 + 1.1383\,\epsilon_{\mathrm{Z}})}{2(\epsilon_{\mathrm{Z}} + 0.01321\,\epsilon_{\mathrm{Z}}^{0.21226} + 0.19593\,\epsilon_{\mathrm{Z}}^{0.5})} \,, \tag{9.6}$$

where $\epsilon_{\mathrm{Z}} = 1.068\epsilon$. The slight difference in energy scales is due to different assumed screening lengths in the calculation of the dimensionless energy.

To directly compare to data, we sum the measured light and charge to get a measured total quanta, $N_q = N_e + N_{\mathrm{ph}}$. This is accomplished by interpolating the measured light yield using an empirical power law fit, and adding the result to the charge yield at the measured energies. To avoid extrapolation of the light yield, we ignore the 0.70 keV$_{\mathrm{nr}}$ charge yield bin and consider only points above 1.08 keV$_{\mathrm{nr}}$, where both charge and light calibration data is available. The fractional statistical uncertainties in light yield are also empirically interpolated and added in quadrature to the statistical uncertainties in Q_y to estimate uncertainties in N_q. The result is plotted against the total quanta predicted by our best-fit nuclear recoil model and the standard Lindhard model in Fig. 9.1. We find excellent agreement with the unmodified Lindhard model in the low energy regime down to 1.1 keV_{nr}.

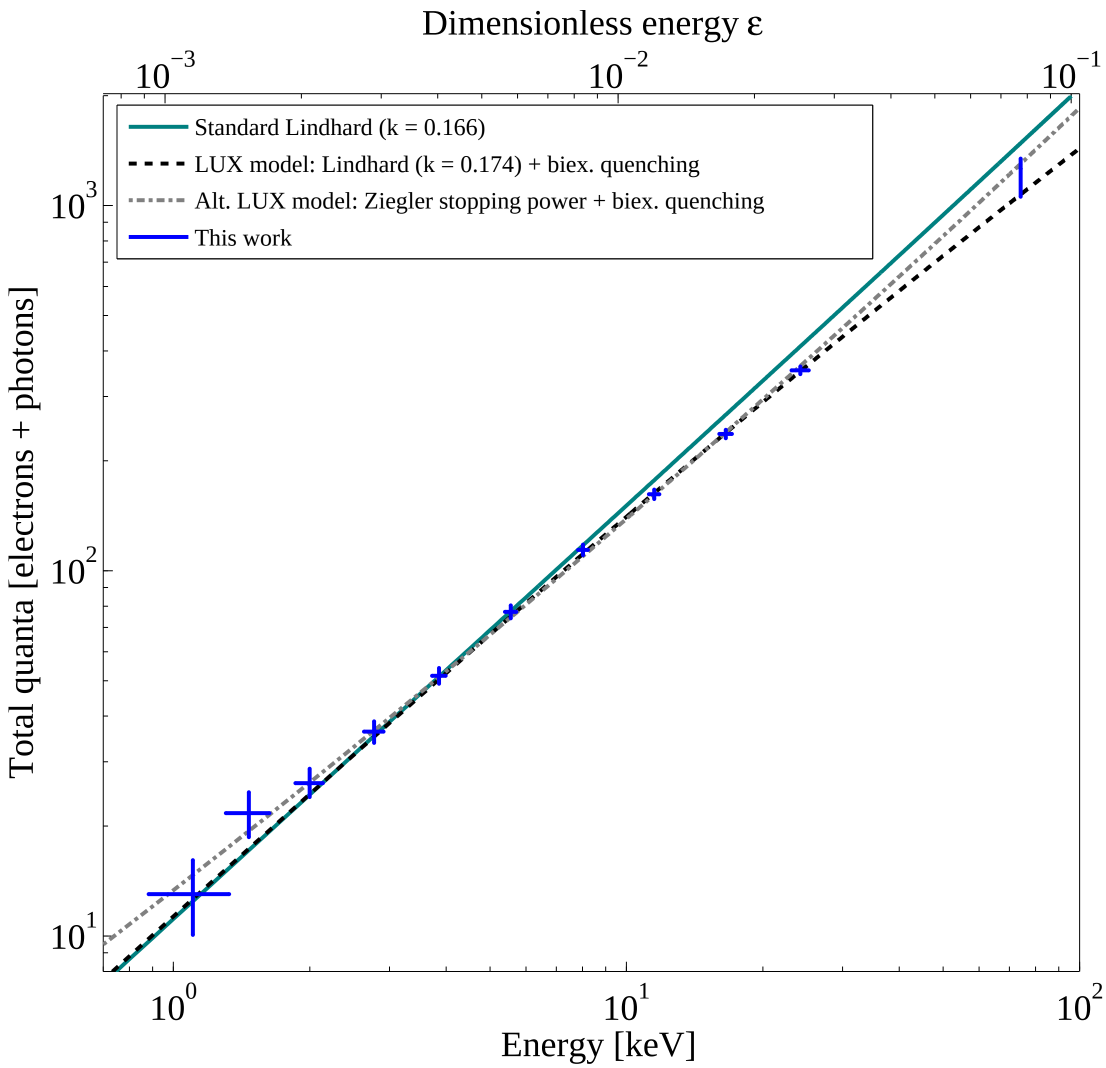

Figure 9.1: Total quanta, calculated by summing the measured light and charge yields. Predicted number of quanta using the new nuclear recoil models described in this work and the standard Lindhard model are shown. The disagreement between the new models and the standard Lindhard model at high energies is due to our inclusion of biexcitonic interactions. This reduces the number of quanta as the exciton density increases and better describes the data above 10 keV_{nr}. This figure was produced by Brian Lenardo.

The disagreement with the Lindhard model at high energies (>10 keV_{nr}) is attributed to biexcitonic effects, in which two excitons can interact to produce only one photon, or one photon and one electron (Penning ionization). Evidence for such effects in other experiments has been described in Refs. [18, 20]. We incorporate this into our model via the quenching factor

$$f_l = \frac{1}{1 + \eta\, s_e}\,, \tag{9.7}$$

where $s_e = 0.166\,\epsilon^{1/2}$ is the theoretical electronic stopping power for liquid xenon [87] and η is a free parameter allowed to float in the fit. This factor multiplies the total number of predicted photons, and a fraction of this is added to the total number of predicted ionization electrons to model Penning ionization. The optimal value obtained is $\eta = 13.2 \pm 2.3$. The fraction of biexcitonic collisions resulting in ionization is modeled as an additional free parameter. The inclusion of these effects allows our models to describe the data across the energy range spanned by D-D neutron induced recoils.

The new model using the Ziegler stopping power is found to be a better description of our data below 2 $\mathrm{keV_{nr}}$; however, it provides a slightly worse fit over the entire energy range (1–74 $\mathrm{keV_{nr}}$). Therefore, we employ the new Lindhard-based NEST model in LUX data analysis and simulation. As it is fit directly to the *in situ* calibration data, this model produces a robust description of liquid xenon response for the simulation and reconstruction of nuclear recoil events within the LUX detector.

More detail on this new NEST model is provided in Ref. [59], including the values of all best-fit model parameters. We show the ratio of the mean number of ionization electrons to scintillation photons produced by the final model in Fig. 9.2. This includes effects due to the initial ratio of excitons-to-ions, recombination, and biexcitonic quenching.

9.3 LUX dark matter WIMP search results

The first LUX spin-independent WIMP-nucleon cross-section limit using data acquired during the Run03 WIMP search was published in 2014 [24]. This first WIMP search result was announced in October of 2013 during the Run03 D-D calibration data taking period. As a consequence, the first WIMP search result was not able to benefit from the *in situ* measurement of the nuclear recoil

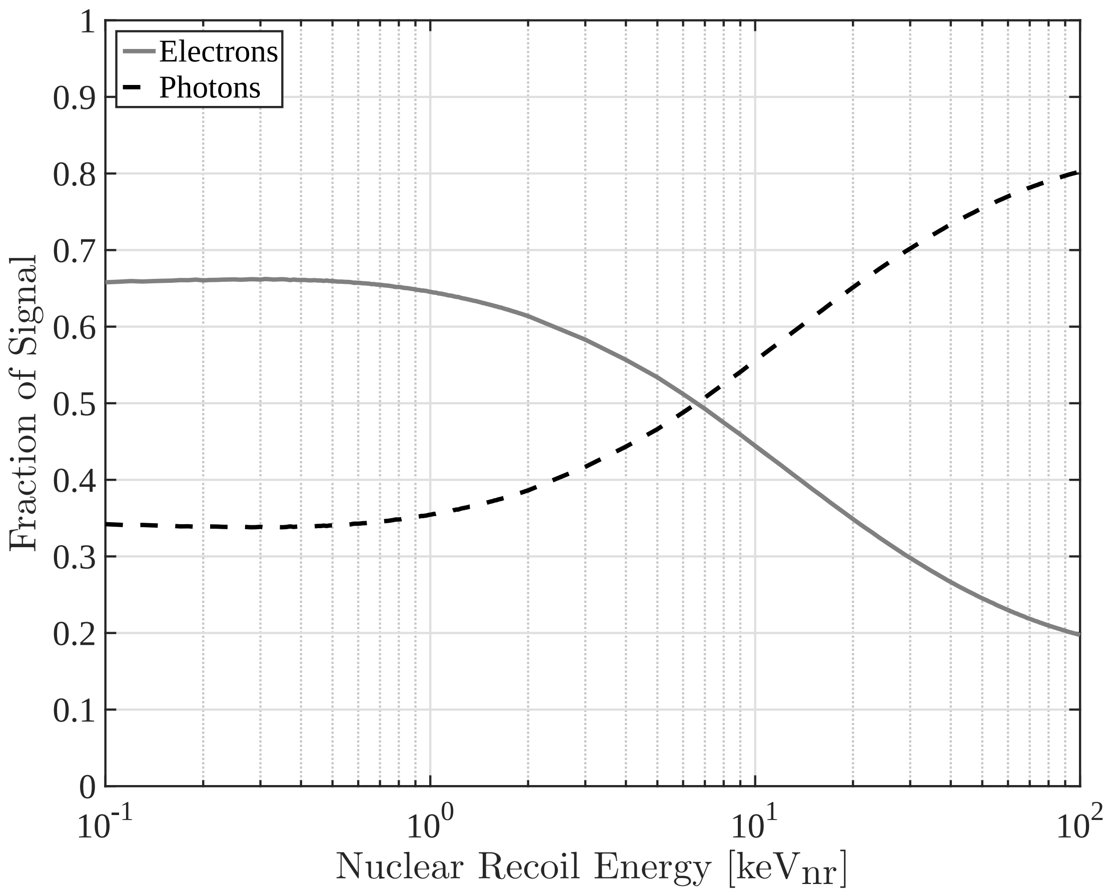

Figure 9.2: The fraction of electrons (solid gray) and photons (dashed black) produced by nuclear recoils in liquid xenon that escape the interaction site at 180 V/cm. This figure was generated using the Lindhard-based NEST model fit to the LUX D-D nuclear recoil data.

yields down to 1.1 $\mathrm{keV_{nr}}$. Instead, it conservatively assumed a hard cutoff in the liquid xenon signal response at 3 $\mathrm{keV_{nr}}$—at the time the lowest measured $\mathcal{L}_{\mathrm{eff}}$ data point with a kinematically-determined energy scale.

An improved LUX spin-independent limit was recently published in 2016 based upon a reanalysis of the same data acquired during the Run03 WIMP search period [5]. This improved limit result takes advantage of a more sophisticated understanding of the detector and several analysis improvements, including a single-detected-photon (phd) calibration for VUV photons, improved event reconstruction algorithms, a larger fiducial volume enabled by a revised background model that includes events originating on the detector walls, and a higher statistics tritium calibration. The most significant change to the limit at low-energies is due to the direct measurement of the nuclear recoil yields using D-D neutrons presented in this thesis.

The D-D neutron calibrations summarized in Sec. 9.1 define the nuclear recoil signal response in both channels (charge and light) from 1.1 to 74 $\mathrm{keV_{nr}}$, which covers the entire recoil energy range used for the LUX WIMP search. This allows the low-energy cutoff for nuclear recoil response to be lowered from 3 $\mathrm{keV_{nr}}$ to 1.1 $\mathrm{keV_{nr}}$ in the signal model in the profile-likelihood-ratio analysis used to generate the limit. The signal model for the improved analysis was updated to use the Lindhard-based NEST model described in Sec. 9.2. The measured signal yields, best fit NEST models, and efficiencies for nuclear recoil event detection are shown in Fig. 9.3.

The demonstration of signal yield in liquid xenon at recoil energies as low as 1.1 $\mathrm{keV_{nr}}$ directly results in improved LUX sensitivity to low mass WIMPs—a factor of $\times 7$ improvement in sensitivity for WIMPs of mass 7 GeV/c^2. In addition, as a direct result of this calibration, the lowest kinematically accessible WIMP mass has been reduced from 5.2 to 3.3 GeV/c^2 [5]. This result further excludes the low-mass WIMP interpretations of anomalous signals seen in several dark matter experiments [6–8]. The favored low-mass WIMP regions in the cross-section vs. WIMP mass parameter space for these anomalous signals was already excluded at 90% CL by the 2014 LUX result [24]. The improved LUX WIMP search result (in light of the low-energy nuclear recoil calibration using

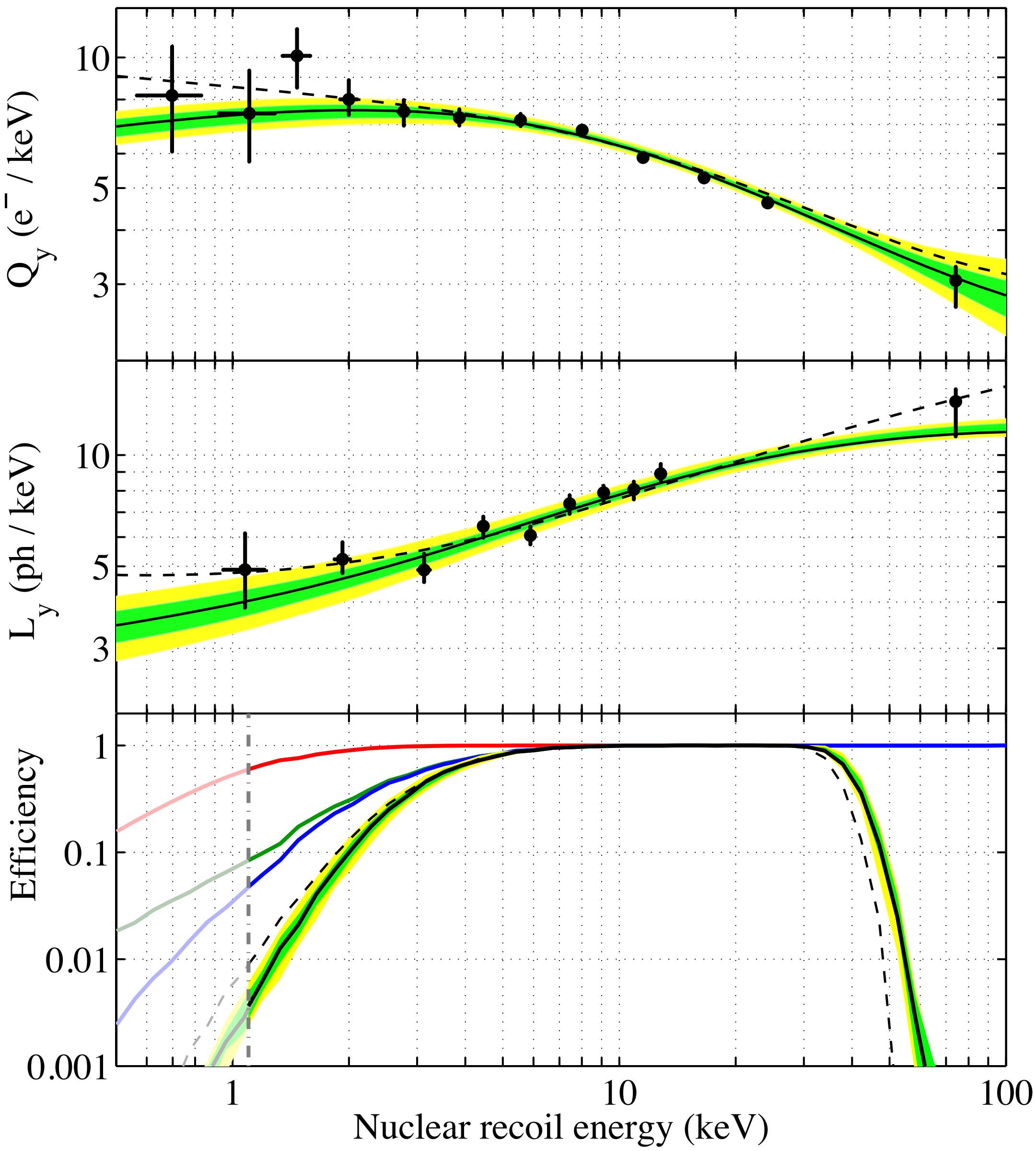

Figure 9.3: *Top, middle:* Yields of electrons and photons, respectively, for nuclear recoils in LUX, measured *in situ* with D-D neutrons. Error bars are statistical. *Bottom:* Efficiencies for nuclear recoil event detection, averaged over the fiducial volume and estimated using LUXSim with parameters tuned to D-D calibration. In descending order of efficiency—red: detection of an S2 ($\geq$2 electrons emitted); green: detection of an S1 ($\geq$2 PMTs detecting photons); blue: detection of both an S1 and an S2; black: detection passing thresholds in S1 and raw S2 size. The $(97.5 \pm 1.7)\%$ event-classification efficiency is applied as an additional, energy-independent scaling. The vertical line at 1.1 keV marks the low-energy cutoff applied in the signal model. *All panels:* Solid lines show the best fit of the Lindhard parametrization; shaded regions span its 1σ and 2σ uncertainty used for the final result. Dashed lines show the best fit of the alternate, Bezrukov nuclear recoil parametrization. This figure and caption were reproduced from Ref. [5].

D-D neutrons) confirms the initial exclusion claim, and increases the already strong disagreement with all existing low-mass WIMP signal interpretations from other dark matter experiments [5]. The 2014 (gray) and 2016 (black with green and yellow contour) LUX WIMP search results are shown in Fig. 9.4. The first LUX spin-dependent WIMP-nucleon cross-section result also benefited from the nuclear recoil yield measurements presented here [57].

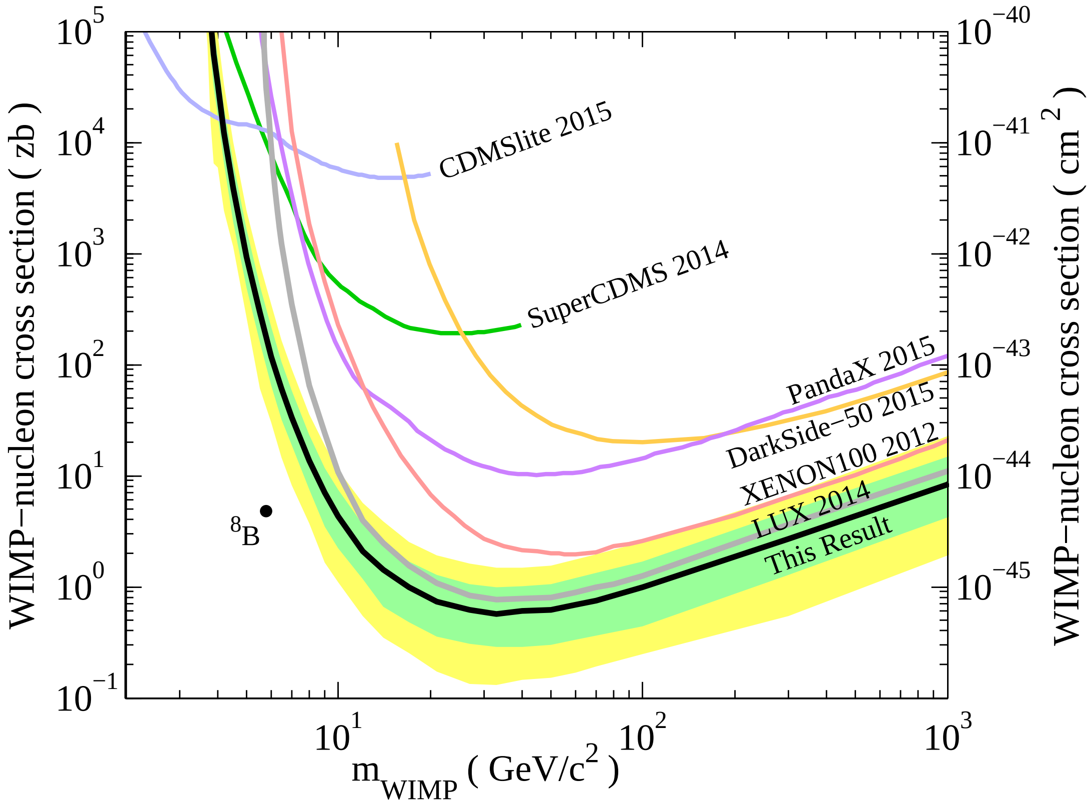

Figure 9.4: Upper limits on the spin-independent elastic WIMP-nucleon cross section at 90% CL. The observed limit is in black, with the 1- and 2-σ ranges of background-only trials shaded green and yellow (2016). Also shown are limits from the first LUX analysis (2014) [24] (gray), SuperCDMS [136] (green), CDMSlite [137] (light blue), XENON100 [9] (red), DarkSide-50 [29] (orange), and PandaX [138] (purple). The expected spectrum of coherent neutrino-nucleus scattering by ^{8}B solar neutrinos can be fit by a WIMP model as in Ref. [41], plotted here as a black dot. This figure and caption were reproduced from Ref. [5].

9.4 Coherent elastic neutrino-nucleus scattering

The standard model predicts coherent ($\propto A^2$) elastic neutrino-nucleus scattering (CENNS). Detailed reviews of the implications of this effect on dark matter experiments are available in Refs. [40, 41]. The CENNS interaction has not yet been observed; however, there are experiments underway that are dedicated to observing this effect [139]. Several sources of neutrinos may contribute to a CENNS signal, most notably: solar neutrinos originating in the sun, atmospheric neutrinos produced by cosmic rays in the earth's atmosphere, and diffuse supernova background neutrinos (remnants of past supernovae) [40]. The maximum nuclear recoil energy from a CENNS interaction is given by

$$E_{\mathrm{nr}}^{\mathrm{max}} = \frac{2E_\nu^2}{m_A + 2E_\nu}\,, \tag{9.8}$$

where E_ν is the energy of the neutrino and m_A is the mass of the target nucleus [41].

The most significant signal is expected to be due to ^{8}B solar neutrinos produced via the

$$^8\mathrm{B} \rightarrow {}^7\,\mathrm{Be}^* + e^+ + \nu_e \tag{9.9}$$

reaction in the sun [40]. The ^{8}B solar neutrino flux has been measured to be 5×10^6 cm^{-2} s^{-1} [140]. For detector threshold energies >100 eV$_{\mathrm{nr}}$, the expected underlying ^{8}B event rate is roughly 1000 scatters tonne^{-1} year^{-1}. This is nearly three orders of magnitude higher than other competing solar neutrino signals, and more than four orders of magnitude higher than the underlying CENNS rate from atmospheric and diffuse supernovae background neutrinos [41]. In practice, the expected observed event rates are much smaller due to detector efficiencies for observing the small nuclear recoils produced by ^{8}B neutrino scatters. The maximum ^{8}B neutrino energy is ∼15 MeV [140]. Using Eq. 9.8, we calculate a maximum recoil energy for ^{8}B events of 3.7 keV$_{\mathrm{nr}}$. The vast majority of such events are of lower recoil energy.

The newly demonstrated nuclear recoil signal response down to $\mathcal{O}$(1 keV$_{\mathrm{nr}}$) enables improved estimates of expected CENNS event rates in liquid xenon TPCs. In the case of ^{8}B, we estimate an underlying integrated neutrino CENNS rate in liquid xenon of 100 events tonne^{-1} year^{-1} for nuclear recoils of energy $\gtrsim$1 keV$_{\rm nr}$ using Fig. 3 of Ref. [41]. Given the 145 kg of xenon in the LUX fiducial volume and the 95 day exposure [5], we calculate an expectation of 3.8 ^{8}B CENNS interactions depositing 1 keV$_{\rm nr}$ or more in the target during the Run03 WIMP search. Assuming an average efficiency of 2% (from Fig. 9.3) for ^{8}B recoils between 1 keV$_{\rm nr}$ and the maximum of 3.7 keV$_{\rm nr}$, we calculate an expectation of 0.08 observed events. This back-of-the-envelope calculation should be taken with a grain of salt; there is a significant source of systematic error given the fast varying efficiency curve from 1–3.7 keV$_{\rm nr}$ in Fig. 9.3, and the also quickly varying differential event rate for ^{8}B CENNS scatters in xenon over the same energy range [41]—the 2% efficiency was an educated guess.

A much more systematic and detailed calculation of the expected ^{8}B was performed for Ref. [5], with a similar final result to our back-of-the-envelope calculation. The recent LUX WIMP search result had the expectation of observing 0.10 events due to ^{8}B solar neutrinos under the LUX Lindhard-based model, while the Bezrukov model provides an expectation of 0.16 observed events [5]. The uncertainty in the ^{8}B solar neutrino flux is $\pm$3% [140], but the dominant uncertainty in the predicted event rate is due to the uncertainty in the liquid xenon signal yields at low-energies. The variation between the Lindhard and Bezrukov predictions can be used to estimate the systematic uncertainty in the expected ^{8}B neutrino event rate due to the choice of xenon signal response model.

Using the same signal model based upon the LUX D-D nuclear recoil results, the expectation for the observed number of ^{8}B CENNS events in the next generation LZ dark matter experiment (described in Sec. 9.6) can be determined. We expect that LZ will observe 7 nuclear recoil events due to ^{8}B solar neutrinos during the planned 1000 live day exposure for the nominal operating conditions [141]. Optimistically, if the LZ photon detection efficiency reaches 12% and a 2-fold PMT coincidence is used (similar parameters to LUX), the expectation rises to 55 observed events in 1000 days [141].

9.5 Theoretical limits on measuring the nuclear recoil response in liquid xenon

The nuclear recoil calibration reported in this thesis measured the ionization and scintillation yield at recoil energies as low as 0.7 $\mathrm{keV_{nr}}$ and 1.1 $\mathrm{keV_{nr}}$, respectively. The combination of these individual Q_y and L_y data points provides a measurement of the total quanta produced by nuclear recoils that escape the interaction site for energies as low as 1.1 $\mathrm{keV_{nr}}$ as seen in Fig. 9.1. In this section, we discuss the theoretical limits on the measurement of the low-energy nuclear recoil response in liquid xenon.

The main limitations on the extension of the low-energy reach of this type of nuclear recoil calibration fall into three categories:

i. *Calibration strategy limitations:* The design of the calibration may fundamentally limit the low-energy reach.

ii. *Detector performance limitations:* The performance of the detector used for the calibration may not be sufficient. In particular, the detection efficiency for single photons and electrons needs to be large enough to allow the use of signals consisting of a few quanta produced at the particle interaction site.

iii. *Fundamental physics limitations:* The target media itself may not generate any measurable electronic excitation for energy depositions below a certain threshold.

If the total quanta production continues to follow the Lindhard curve shown in Fig. 9.1 to lower energies, the expectation is $\sim$1 quanta produced at $\mathcal{O}(0.1\ \mathrm{keV_{nr}})$. We use this value as the low-energy benchmark value for this discussion.

9.5.1 Calibration strategy limitations

The LUX D-D calibration demonstrates the power of the *in situ* TPC neutron calibration using neutron scattering kinematics, and provides a baseline level of performance to which we can compare potential improvements to the technique required to overcome limitations due to the current calibration strategy. The low-energy Q_y measurement in Ch. 5 was primarily limited by the small scattering angle required to measure the current lowest-energy point at 0.7 keV$_{\rm nr}$. The lowest-energy Q_y bin in the LUX analysis contained 19 events with a scattering angle between 7°–11°. Using the 2.45 MeV neutrons from the D-D source, we would need to measure scattering angles $<7°$ to obtain a calibration at lower recoil energies. The systematic effects associated with energy reconstruction (described in Ch. 1, Ch. 5, and Ch. 6) using these small angles provides additional complication. The use of quasi-monoenergetic 272 keV neutrons—produced using the technique described in Sec. 1.3.2—overcomes these challenges by providing a larger scattering angle for a given recoil energy. The lowest-energy Q_y bin in the current LUX analysis would have a scattering angle range of 22°–33° using these lower energy neutrons. In addition, the number of very low-energy (0–4 keV$_{\rm nr}$) nuclear recoils is enhanced when using the lower energy neutron source, as discussed in Sec. 1.3.2.

The lowest-energy total quanta data point is at 1.1 keV$_{\rm nr}$—a value dictated by position of the lowest-energy L_y data point. The limitations of the low-energy reach of the L_y measurement in Ch. 7 are different than those just discussed for the Q_y measurement. This scintillation yield measurement technique requires that the ionization yield has been measured over the recoil energy region used to determine L_y. There are two primary limitations that affect the low-energy reach of the single-scatter-based analysis used in Ch. 7. The first limitation is due to the limited statistical leverage available at the lowest energies. The lowest-energy Q_y data point at 1.1 keV$_{\rm nr}$ has an expectation of 0.5 phd, while the S1 threshold requires $\geq$2 photons for the detection of an S1 pulse. The second limitation is that there is a non-negligible accidental coincidence background that can masquerade as valid low-energy L_y signal events (described and quantified in Ch. 7). The advanced calibration techniques described in Sec. 1.3 come to the rescue in both cases. The reduction in the neutron bunch width time structure described in Sec. 1.3.1 can be used to eliminate the majority of accidental coincidence events (∼99.5% for typical operating parameters) by requiring that events in the TPC are coincident with the neutron production time window. As described in that section, this type of operation also allows the use of valid neutron scatter events with 0 phd and 1 phd S1 signals—effectively eliminating the detector's S1 threshold and increasing the statistical leverage at very low energies. Additionally, the S1 separation technique described in Sec. 1.3.3 enables a direct light yield measurement using an angle based energy scale similar to the Q_y measurement. This final technique removes the dependence of the L_y measurement on the energy scale provided by the Q_y measurement, provides additional statistical leverage due to the direct energy measurement, and has a kinematically defined energy scale based directly on the data.

9.5.2 Detector performance limitations

The main detector-performance-based limitations on the low-energy reach of this nuclear recoil calibration technique are a result of the finite efficiency for the detection of signal carriers in the detector. The photon detection efficiency (g_1) value for S1 light is determined by the geometric light collection, PMT quantum efficiency, and PMT photoelectron collection efficiency. During the LUX D-D period $g_1 = 0.115 \pm 0.004$, which means that for every 10 photons produced due to scintillation in the liquid xenon 1 photon is detected in a PMT. The combination of the electron extraction efficiency and the electron lifetime in the liquid xenon determine the efficiency for the detection of ionization electrons produced by particle interactions in the liquid xenon. The electron extraction efficiency during the LUX D-D campaign was determined to be 0.48 ± 0.04 and the average electron lifetime in the liquid xenon was around 650 μs. This electron lifetime value, when combined with the average drift time of 107 μs for events in the D-D neutron beam, indicates that 85% of ionization electrons produced at the interaction site drift to the liquid surface without being absorbed by impurities. The combination of the electron extraction efficiency and the electron lifetime effects give a 41% probability that a given ionization electron will be extracted from the liquid xenon and contribute to an observed S2 signal.

It is difficult to build a large ($\gtrsim$300 kg) xenon TPC a with g_1 value larger than the 11.5% achieved by LUX without an improvement in the detection efficiency of available photo-detectors; PMTs suitable for liquid xenon TPCs currently have a detection efficiency of 30%.[2] Additionally, nearly all non-photocathode surfaces inside the LUX active region are covered in PTFE, which has a reflectivity for xenon scintillation light that is consistent with 100% [73].

One potential improvement to the light yield measurement would be to install a thin (<1 mm) light-tight wall between two regions of a large TPC—call them region A and region B [42]. The double-scatter nuclear recoil energy reconstruction technique could be used to great effect by selecting events where the first scatter occurs in region A and the second scatter occurs in region B inside the TPC. The (x, y, z) positions of the first and second neutron scatters would still be used to reconstruct the nuclear recoil energy at the first vertex, but the separator would isolate the scintillation light from the first vertex. The scintillation light from the first vertex could then be directly related to the deposited energy to provide an L_y measurement with an angle-based energy scale. The smaller volume of region A could potentially be optimized for higher light collection. The challenges of such an experiment include the precise characterization of the detector parameters and event reconstruction in the compartmentalized TPC.

There is more room for improvement in the electron detection efficiency of the LUX experiment. The LUX extraction field of 6 kV/cm in the gas provides a measured extraction efficiency of 0.48. The electric field used for electron extraction can be increased to obtain an extraction efficiency of close to 100%. As an example, the baseline electron extraction field for the next-generation LZ dark matter experiment discussed in Sec. 9.6 is 10.6 kV/cm in the gas phase, which corresponds to

[2] The PMT detection efficiency is defined as the product of the quantum efficiency and the photoelectron collection efficiency.

~100% efficiency for electron extraction in the liquid [142]. If, in addition, the electron lifetime can be be improved to ~6 ms, >99% of the ionization electrons will be extracted from the liquid for a D-D calibration conduit 10 cm below the liquid surface assuming a 2 mm/μs electron drift speed. At some periods during LUX operation, the electron lifetime exceeded 1 ms, which corresponds to the survival of 95% of ionization electrons for these calibration parameters.

It is reasonable to assume that future large xenon TPCs can obtain a g_1 value similar to the LUX value, and an improved electron detection efficiency of ~100%. The number of scintillation photons and ionization electrons produced at the interaction site for energies spanning 0.1–100 keV$_{\mathrm{nr}}$ are listed in Table 9.1 as determined from the Lindhard-based NEST model described in Sec. 9.2. The expectation for the detected number of photons and electrons is also provided. The corresponding low-energy extrapolation of the models described in Sec. 9.2 is shown in Fig. 9.5.

Table 9.1: The expected number of quanta as a function of nuclear recoil energy for LUX operating parameters. The mean number of photons and electrons escaping the interaction site are listed in columns two and four. These values are calculated using the average LUX drift field of 180 V/cm. The mean observed number of photons and extracted electrons are listed in columns three and five. These values were generated using the Lindhard-based NEST model described in Sec. 9.2. The LUX purity, extraction efficiency, and g_1 value of 0.115 ± 0.004 were used to calculate the average observed quantities.

Recoil Energy [keV$_{\mathrm{nr}}$]	n$_p$ [photons]	$S1$ [phd]	n$_e$ [electrons]	extracted electrons
0.1	0.29	0.03	0.56	0.23
0.4	1.4	0.16	2.7	1.1
0.7	2.6	0.30	5.0	2.0
1.0	4.0	0.46	7.3	3.0
1.1	4.5	0.52	8.1	3.3
10	78.1	9.0	62.5	25.5
100	1150	132	283	116

It will be challenging to obtain a lower energy L_y measurement that reported in Ch. 7 given the expectation of 0.5 phd for the current data point at 1.1 keV$_{\mathrm{nr}}$. In any case, the majority of the potential increase in sensitivity to low-mass WIMPs has already been realized by lowering the assumed xenon signal response cutoff from 3 keV$_{\mathrm{nr}}$ to 1.1 keV$_{\mathrm{nr}}$ as described in Sec. 9.3. There is greater potential to obtain a Q_y measurement at lower energies. At 0.7 keV$_{\mathrm{nr}}$, the value of the

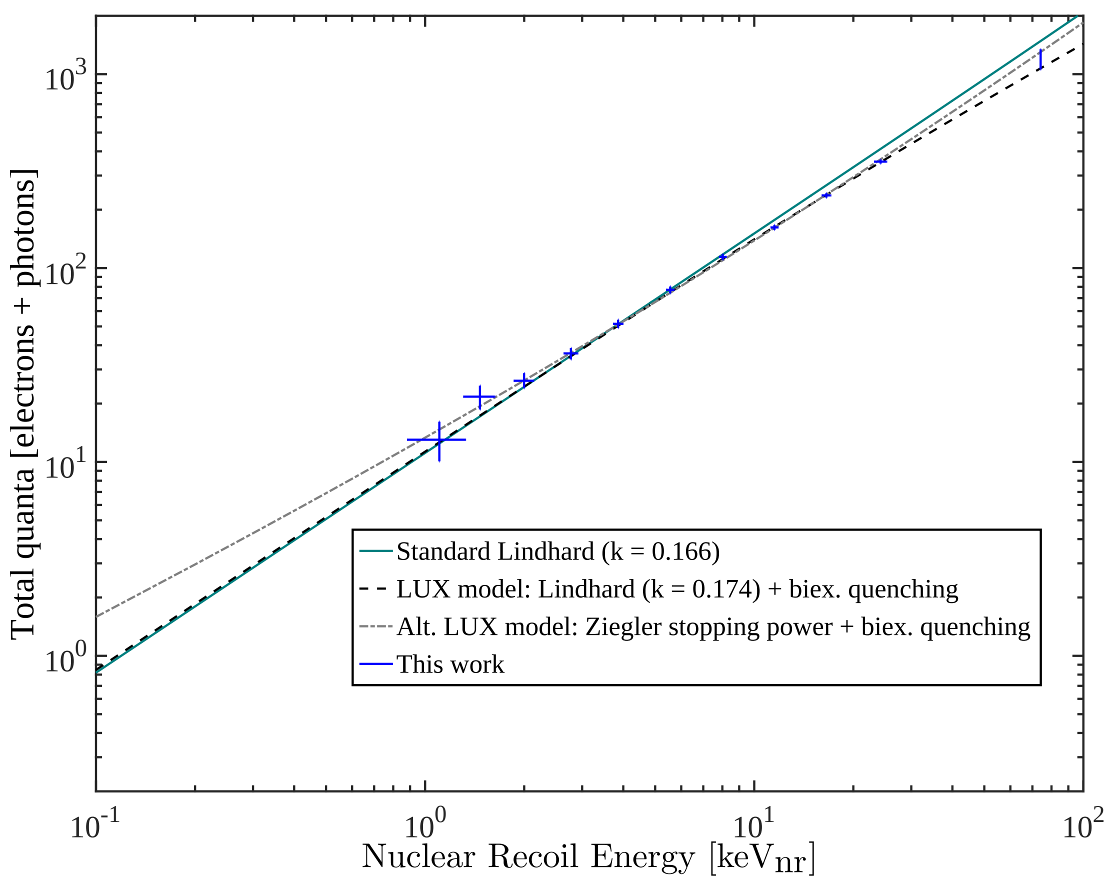

Figure 9.5: A zoomed out view of Fig. 9.1 to show the low-energy extrapolation of the nuclear recoil signal models. This figure was produced by Brian Lenardo UC Davis.

lowest-energy Q_y data point, the expectation is 5 ionization electrons produced at the interaction site and a corresponding detected S2 signal from 2 extracted electrons. At the low-energy benchmark of 100 eV$_{\mathrm{nr}}$, there is an expectation of 0.6 ionization electrons produced at the interaction site at 180 V/cm. In the case of 100% conversion from ionization electrons to detected electrons—which is realistic as described in the preceding paragraphs—all of the ionization electrons are converted into detected electrons. Assuming an underlying Poisson distribution of ionization electrons (currently consistent with the LUX Q_y data), we calculate that 45% of events have $\geq$1 detected electron extracted into the gas and 2% of events have 3 detected electrons. Even in LUX where the expectation is 0.23 extracted electrons it may be possible to obtain a 100 eV$_{\mathrm{nr}}$ measurement. In this case, we expect 18% of events will have 1 detected electron and 2% of events will have 2 detected electrons.

Given the reach of the calibration techniques described in Sec. 1.3 and experimentally achievable detector performance parameters, it should be possible to measure the ionization yield of $\mathcal{O}$(100 eV$_{\mathrm{nr}}$) nuclear recoils in liquid xenon (if signal exists—see Sec. 9.5.3). An ultra-low energy calibration of the ionization yield would further establish the effectiveness of liquid xenon for S2-only dark matter searches in liquid xenon TPCs [143]. Plans are currently underway to obtain a lower-energy calibration in LUX using some of the advanced calibration techniques described in Ch. 1 during the summer of 2016 after the conclusion of the Run04 WIMP search.

9.5.3 Fundamental physics limitations

The Lindhard model of nuclear recoil signal quenching has been a standard in the field since its introduction in 1963 [68]. The Lindhard model has been very successful in predicting the fraction of energy given to measurable electronic excitation for a wide range of target materials used for dark matter detector targets including germanium [144–151], silicon [152, 153] (at energies >5 keV$_{\mathrm{nr}}$), xenon [69], and argon [20].[3] Recent nuclear recoil measurements in silicon indicate that there is a

[3] Achieving good agreement of the Lindhard model with recent argon data requires a non-standard $k = 0.110$ [20, 154]. The variable k is defined in Sec. 9.2.

departure from standard Lindhard theory in that material at energies below $\sim$5 keV$_{\rm nr}$.

It has been that noted in the literature that there may be a suppression of measurable electronic excitation for dimensionless energy of less than about $\epsilon \approx 10^{-2}$ beyond that predicted by the Lindhard theory [154–156]. One favored mechanism for this predicted sharp drop in signal yield is due to the approximation in Lindhard theory that the atomic binding energy of electrons is negligible; alternative mechanisms have also been proposed [154]. For high-energy nuclear recoils this is a reasonable approximation, but as the energy transfer to the nucleus approaches the minimum energy required to excite or ionize an electron the effects could be significant. In the extreme case where the energy transfer to the nucleus is below the minimum energy required for a single electronic excitation, no signal carriers can be generated by the interaction. The onset of this roll-off in signal generation for common target materials used for WIMP direct detection experiments is commonly suggested to occur between 1–10 keV$_{\rm nr}$, which could potentially have a significant effect on the ability of these detector materials to observe low-mass WIMPs that typically produce nuclear recoils of only a few keV$_{\rm nr}$. The existing data for germanium, xenon, and argon does not favor the kinematic cutoff hypothesis at $\epsilon \approx 10^{-2}$ [154]. The standard Lindhard model is consistent with LUX D-D calibration data down to the lowest-energy data point at a dimensionless energy of $\epsilon \approx 10^{-3}$. The LUX D-D measurement has confirmed the validity of Lindhard theory $\times 4$ lower in energy than previous achieved. This result is in tension with the kinematic cutoff model proposed in Ref. [154] for recoil energies between 1–4 keV$_{\rm nr}$.

A plot of the measured nuclear recoil quenching fraction for germanium, silicon, xenon, and argon is shown in Fig. 9.6. In terms of dimensionless energy, the LUX nuclear recoil measurement extends to $\epsilon \approx 10^{-3}$—as low in energy as the lowest-energy quenching factor results in germanium. It is worth noting the agreement of the xenon data over more than two orders of magnitude in energy from roughly $\epsilon = 10^{-3}$ to 3×10^{-1}.

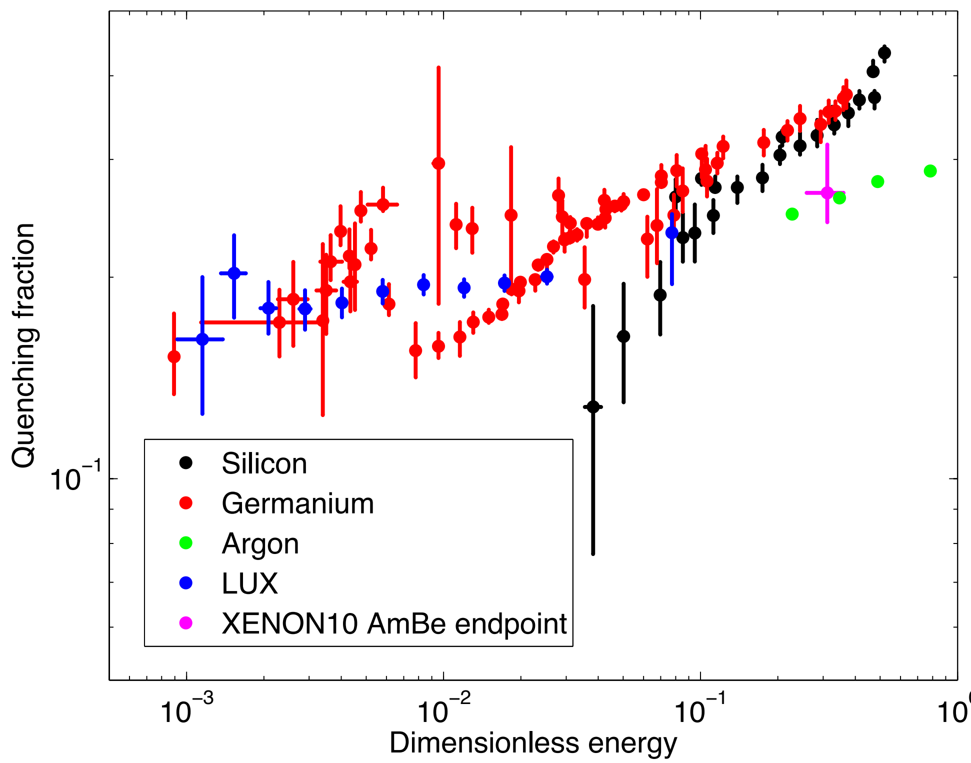

Figure 9.6: A compilation of measurements showing the nuclear recoil quenching fraction vs. dimensionless energy for germanium (red) [144–151], silicon (black) [152, 153], xenon (this work in blue and Ref. [69] in magenta), and argon (green) [20]. This figure was produced by Brian Lenardo from UC Davis.

9.6 The LZ dark matter experiment

The next-generation LUX-ZEPLIN (LZ) dark matter experiment is a dual-phase liquid xenon TPC with a 10 tonne (7 tonne active) target mass. The LZ detector will replace the LUX detector inside the existing water tank in the Davis Cavern. A cutout of the LZ solid model is shown in Fig. 9.7.

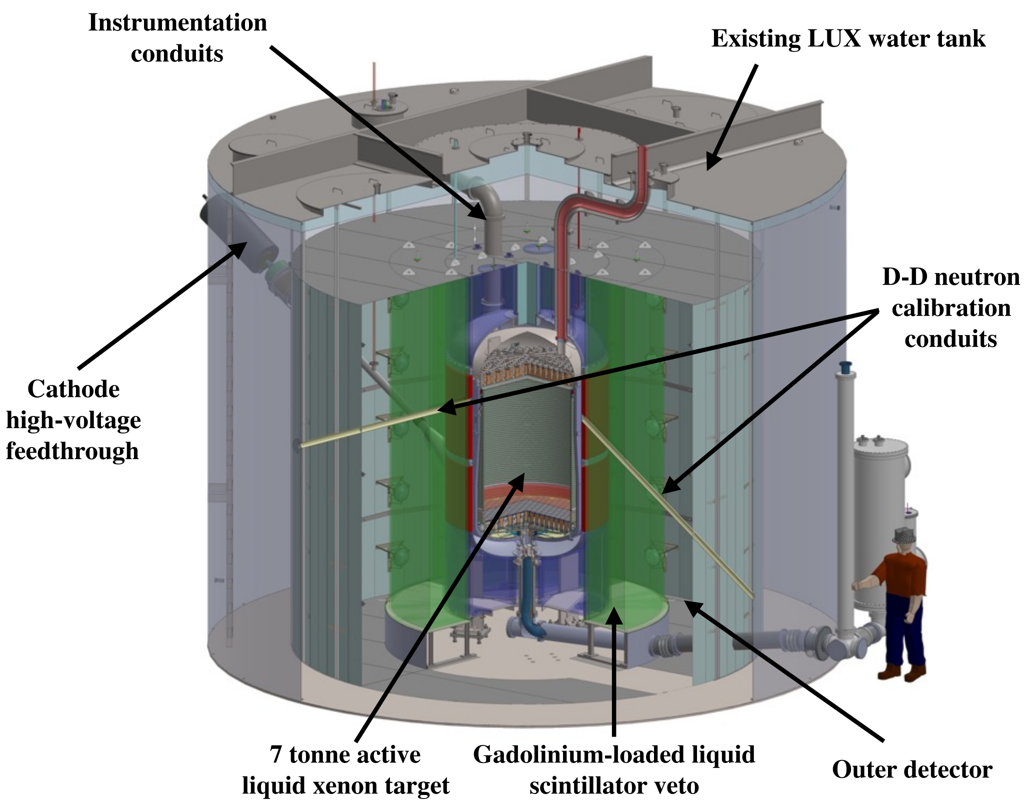

Figure 9.7: A cutout view of the LZ detector solid model. The water tank, outer detector active veto, liquid scintillator tanks (green), cryostat, and TPC active region are shown as nested volumes (order starting from the outside). The two D-D neutron calibration conduits are shown in yellow penetrating from the outer water tank wall to the cryostat. One conduit is installed horizontally, and the other is installed at an angle. This solid model snapshot was produced by Matt Hoff of the LZ Collaboration.

Due to the success of the LUX calibration using the D-D source, the D-D technique is a core component of the calibration program for LZ.[4] It is critical to demonstrate the nuclear recoil response at low-energies *in situ* in the dark matter detector itself to ensure credibility when reporting the

[4] I was the L3 manager of the D-D program within the LZ work breakdown structure during the early conceptual design stages. Dongqing Huang (Brown University) has since taken over this role.

exclusion or detection of low-mass WIMPs. As was discussed in Sec. 9.4, the nuclear recoil event rate from ^{8}B neutrinos is an expected irreducible background for low-mass WIMPs in liquid xenon detectors the size of LZ. It is necessary to have an *in situ* calibration of the low-energy nuclear recoil signal yields to provide a precise expectation for the ^{8}B neutrino signal in LZ. The LZ D-D calibration program builds upon the now established canon of LUX experience in order to achieve its low-energy nuclear recoil calibration needs.

The LZ design includes two neutron conduits, one installed horizontally and one installed at an angle. The horizontal tube will be located between 10–15 cm below the liquid level, duplicating the orientation of the LUX conduit. The angled tube is located at a 90° offset from the horizontal tube as shown in Fig. 9.7. In a departure from the LUX design, both conduits are permanently fixed in position. The neutron collimation conduits are backfilled with water during LZ WIMP search operation. The conduits will be drained and purged with N_2 during D-D calibration campaigns. The two conduits separated by 90° in the azimuthal direction provide redundancy if one of the conduits has a significant leak. This design also provides redundancy against multiple xenon PMTs failing above the neutron beam entry point from a single conduit. Both locations will feature two separate sealed neutron conduits, one of 5 cm diameter and one of 15 cm diameter, that can be independently filled with water and purged with N_2. The 5 cm diameter conduit provides a beam profile similar to the LUX experimental setup, while the 15 cm conduit provides a wider beam with a corresponding $\times 9$ increase in the neutron rate incident upon the LZ TPC.

Several of the advanced calibration techniques proposed in Sec. 1.3 have been incorporated as core components in the LZ D-D calibration program. As described in that section, these advanced calibration techniques will allow lower-energy nuclear recoil calibration with an alternative set of systematics. The Brown DD108 neutron generator hardware used for the LUX calibration will undergo hardware upgrades to meet the needs of these advanced calibration techniques in the LZ D-D calibration program. In particular, the nominal maximum neutron yield will be upgraded from 10^8 n/s to 10^9 n/s, and the minimum neutron bunch width will be reduced to ≤ 10 μs via hardware upgrades performed by the vendor. The deuterium-reflector-based 272 keV neutron source will be used to extend the demonstrated calibration technique using 2.45 MeV neutrons nearly an order of magnitude lower in energy. This lower-energy neutron source produces forward neutron scatters with a recoil energy of 0–4 keV$_{\mathrm{nr}}$ and the recoil energy spectrum endpoint is 8 keV$_{\mathrm{nr}}$—well suited for the nuclear recoil energies associated to low-mass WIMP and CENNS signals in LZ. In addition, the large (1.5 m $\times$ 1.5 m) xenon volume and reduced velocity of the 272 keV neutrons will allow a direct calibration of the S1 signal with an angle-based recoil energy scale.

The R&D effort for these advanced techniques planned for the LZ program is underway. After LUX WIMP search running is complete in the summer of 2016, current hardware prototypes of the $\leq$10 μs neutron bunch width setup and the deuterium-loaded reflector will be tested using the LUX detector in the well understood calibration setup. The results of these advanced studies at the end of LUX operation will help the LZ D-D calibration program approach the theoretical limits of the nuclear recoil calibration technique using neutron scattering kinematics.

9.7 Conclusions

A new type of calibration technique was used to measure the nuclear recoil signal yields in liquid xenon at 180 V/cm *in situ* in the LUX dark matter detector. The ionization and scintillation yields were absolutely measured to energies as low as 0.7 keV$_{\mathrm{nr}}$ and 1.1 keV$_{\mathrm{nr}}$, respectively. The Q_y (L_y) result is a factor of $\times$5 ($\times$3) lower in energy than previous measurements with a scattering-angle-based energy scale, and features a reduction in calibration uncertainties. This is the first time that the light yield has been reported directly in the absolute units of photons/keV$_{\mathrm{nr}}$. The predictions of Lindhard theory are consistent with the measured nuclear recoil signal yields over two orders of magnitude in recoil energy. These measurements constrain theories of a kinematic cutoff affecting liquid xenon signal production at low recoil energies.

The measured nuclear recoil signal yields significantly improve the demonstrated sensitivity of liquid xenon TPCs to low-mass WIMPs. The already world-leading sensitivity of the LUX dark matter experiment improved by a factor of $\times 7$ at 7 GeV/c^2 as a direct result of this calibration. The improved sensitivity to low-mass WIMPs increases the already strong disagreement of the LUX WIMP search results with the low-mass WIMP interpretations of anomalous signals in several other recent dark matter experiments. In addition, this calibration provides a foundation for the accurate calculation of the expected CENNS signal from ^{8}B neutrinos in large liquid xenon TPCs. Due to the success of this calibration in the LUX detector, this technique is now a core component of the next generation LZ dark matter experiment.

Appendix A

Datasets Used for Run03 D-D Analysis

Here is the complete list of D-D calibration datasets used for the Run03 nuclear recoil analyses. These datasets contain the full 107.2 live hours.

A.1 D-D datasets

lux10_20131031T0850_cp10022	lux10_20131112T0225_cp10035
lux10_20131031T1334_cp10023	lux10_20131112T2053_cp10036
lux10_20131031T1605_cp10024	lux10_20131113T0052_cp10037
lux10_20131110T1524_cp10025	lux10_20131113T1327_cp10038
lux10_20131110T2006_cp10027	lux10_20131113T1929_cp10039
lux10_20131110T2355_cp10028	lux10_20131113T2225_cp10040
lux10_20131111T1624_cp10031	lux10_20131114T0407_cp10041
lux10_20131111T2326_cp10034	lux10_20131114T0747_cp10042

lux10_20131114T2103_cp10043

lux10_20131114T2236_cp10044

lux10_20131115T0209_cp10058

lux10_20131115T0359_cp10059

lux10_20131115T0914_cp10060

lux10_20131115T1659_cp10062

lux10_20131115T2140_cp10070

lux10_20131116T0139_cp10071

lux10_20131116T0509_cp10072

lux10_20131116T0832_cp10073

lux10_20131116T1159_cp10074

lux10_20131116T1748_cp10075

lux10_20131117T0321_cp10076

lux10_20131117T0536_cp10077

lux10_20131117T1011_cp10078

lux10_20131117T1348_cp10079

lux10_20131117T1958_cp10080

lux10_20131117T2354_cp10081

lux10_20131118T0300_cp10082

lux10_20131118T0809_cp10083

lux10_20131118T1713_cp10084

lux10_20131118T2128_cp10085

lux10_20131118T2321_cp10086

lux10_20131119T0801_cp10087

lux10_20131119T1121_cp10088

lux10_20131119T1440_cp10093

lux10_20131119T1925_cp10094

lux10_20131119T2254_cp10095

lux10_20131120T0311_cp10099

lux10_20131120T0801_cp10101

lux10_20131120T0934_cp10102

lux10_20131120T1021_cp10106

lux10_20131120T1825_cp10108

lux10_20131120T2139_cp10109

lux10_20131121T0217_cp10111

Appendix B

LUX Engineering Surface Runs at SURF

B.1 Run02: liquid xenon circulation

This section contains several muon studies performed during LUX Run02. The LUX detector was operated on the surface at the surface lab at SURF during this engineering run. These analysis results are published in Ref. [73].

B.1.1 Cosmic ray muon flux

We expect $\mathcal{O}$(100 Hz) of cosmic ray muons to pass through the LUX active region during surface operation. The rate of muons passing through the LUX detector was determined by measuring the observed rate of S1-like pulses when the detector was evacuated. These prompt signals were produced by muons passing through the PTFE walls or the PMTs themselves. The muon rate through the TPC active region was measured to be 108.8 ± 0.3 Hz using this technique.

Muons passing through the windows of one of the 122 PMTs produce prompt light signals, which are predominantly collected in the individual tube that was penetrated by the incident muon. The window area of each PMT is 20.3 cm^2 [73]. The total muon flux was precisely measured using the observed rate of this type of event. The muon flux at the surface lab ($\sim$5000 ft in elevation) was measured to be 0.019 ± 0.003 cm^{-2} s^{-1}, which is roughly 14% higher than the value at sea level [73].

B.1.2 Muon lifetime

During the LUX Surface Run02 when the detector was full of liquid xenon, several datasets were acquired without applying any electric field across the liquid xenon bulk or liquid/gas interface. This mode of operation provides S1 signals for particle interactions only. The smaller signal size and reduced time structure of S1-only operation lends itself well to a measurement of the characteristic antimuon lifetime given $\mathcal{O}$(100 Hz) muon rate and 6 MeV/cm^2 [157] deposited for muon tracks in liquid xenon. The ionization electron drift, electron extraction, and S2 generation through electroluminescence in the gas was turned off.

Once a muon or antimuon stops in the liquid xenon bulk it can undergo a decay or capture reaction. The decay reactions for both muons and antimuons are shown in Eq. B.1 and Eq. B.2:

$$\mu^- \rightarrow e^- + \nu_\mu + \bar{\nu}_e \,, \tag{B.1}$$

$$\mu^+ \rightarrow e^+ + \bar{\nu}_\mu + \nu_e \,. \tag{B.2}$$

The negatively charged muon has an expected lifetime of $\sim$100 ns in xenon due to the competing capture reaction on protons in the xenon nuclei [158, 159]:

$$\mu^- + p \rightarrow n + \nu_\mu \,. \tag{B.3}$$

This analysis focuses on measuring the expected 2.2 μs lifetime of the antimuon, which is not affected by the competing capture reaction in Eq. B.3. It is likely that the shorter ∼100 ns characteristic lifetime is measurable in LUX data through the study of the S1 pulse shape envelope for candidate muon decay events. The characteristic decay time of S1 pulses at 0 V/cm electric field is 45 ns, which should give sufficient separation between the S1 associated with the muon entry into the liquid xenon bulk and the subsequent liquid xenon decay.

For this analysis of the antimuon lifetime, we use a single LUX surface dataset with the identifier lux10_20111229T1615_fp01032. This dataset corresponds to 1.69 hours and contains a total of 992627 events. The PMTs were operated at a lower gain of 10^5 to avoid saturation and all electrode grids were grounded. An example antimuon decay event from this dataset is shown in Fig. B.1.

Several simple cuts were used to identify the candidate muon decay events. First, only events with two and only two S1 pulses were accepted. This cut ensures we select events with an S1 due to the incident muon track and a second S1 from the subsequent ejected positron from the antimuon decay. The first pulse must have a pulse area $> 10^5$ phe to select potential muon tracks, while the second pulse must have an area in the range $5 \times 10^4 - 2 \times 10^5$ phe to select candidate positrons from antimuon decay. After all cuts, 2921 events remain in the region of interest. The histogram of the remaining events is fit in the range 3–50 μs using an exponential decay model with a floating flat background as shown in Fig. B.2. The best measured antimuon lifetime is 2.18 ± 0.02 μs. This is in agreement with the expectation of 2.1969811 ± 0.0000022 μs from the particle data group [160].

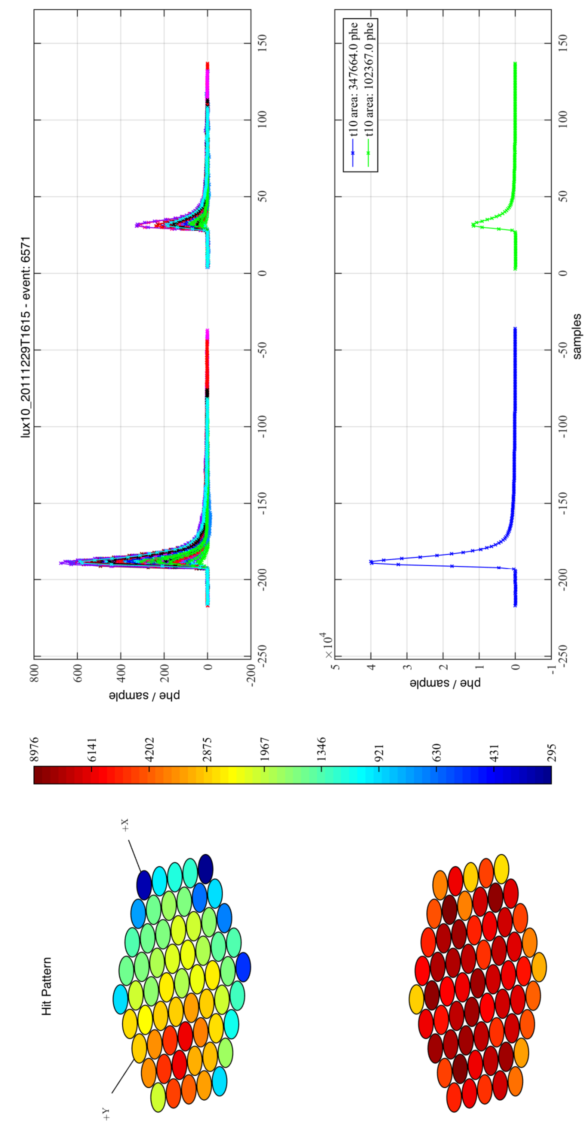

Figure B.1: Example event record for a muon decay event in LUX Run02 S1-only surface data. The PMT hit pattern is shown on the left for the sum of both S1 pulses in units of photoelectrons. The waveform data for all 122 PMTs is shown on the upper right plot, while the summed waveform across all PMTs is shown in the bottom right plot. The first summed S1 pulse shown in blue corresponds to the muon entry into the detector. The smaller second summed S1 in green corresponds to the muon decay. The lifetime of this particular muon is determined by measuring the time between the beginning of the two S1 pulses.

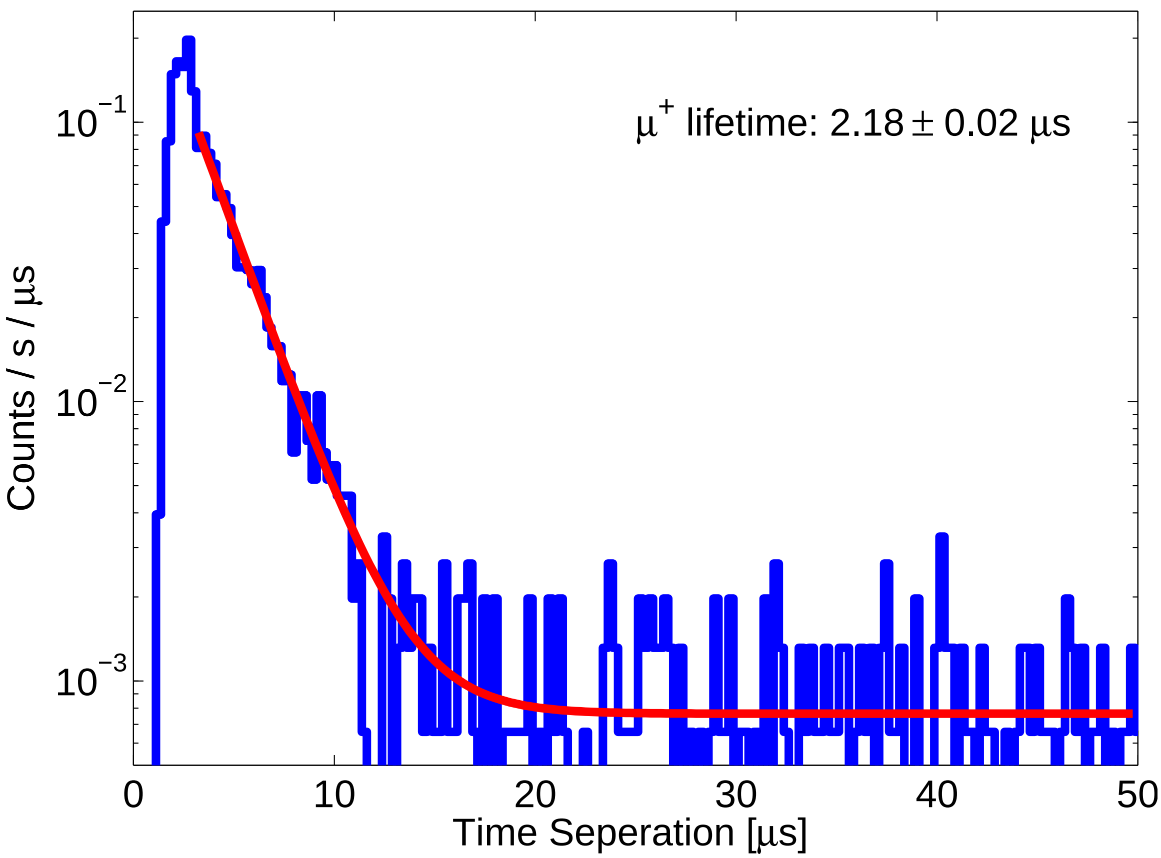

Figure B.2: Histogram of all candidate events passing muon decay cuts with a time separation between 0–50 μs is shown in blue. An exponential decay model with a floating flat background was fit to the histogram in the range 3–50 μs. The fit is depicted by the red line. The best measured antimuon lifetime is 2.18 ± 0.02 μs.

Bibliography

[1] J. R. Verbus, C. Rhyne, D. C. Malling, M. Genecov, S. Ghosh, A. Moskowitz, S. Chan, J. J. Chapman, L. de Viveiros, C. H. Faham, S. Fiorucci, D. Q. Huang, M. Pangilinan, W. C. Taylor, and R. J. Gaitskell, "Proposed low-energy absolute calibration of nuclear recoils in a dual-phase noble element TPC using D-D neutron scattering kinematics," (2016), in preperation.

[2] D. S. Akerib *et al.*, "Low-energy (0.7–74 keV) nuclear recoil calibration of the LUX dark matter experiment using D-D neutron scattering kinematics," (2016), in preperation.

[3] E. Aprile, R. Mukherjee, and M. Suzuki, Nucl. Instrum. Methods **A307**, 119 (1991).

[4] R. T. Scalettar, P. J. Doe, H. J. Mahler, and H. H. Chen, Phys. Rev. A **25**, 2419 (1982).

[5] D. S. Akerib *et al.* (LUX Collaboration), Phys. Rev. Lett. **116**, 161301 (2016).

[6] C. E. Aalseth *et al.* (CoGeNT Collaboration), Phys. Rev. D **88**, 012002 (2013).

[7] G. Angloher *et al.* (CRESST Collaboration), Eur. Phys. J. C **72**, 1971 (2012).

[8] R. Bernabei, P. Belli, F. Cappella, R. Cerulli, C. J. Dai, A. d'Angelo, H. L. He, A. Incicchitti, H. H. Kuang, J. M. Ma, F. Montecchia, F. Nozzoli, D. Prosperi, X. D. Sheng, and Z. P. Ye, Eur. Phys. J. C **56**, 333 (2008).

[9] E. Aprile *et al.* (XENON100 Collaboration), Phys. Rev. Lett. **109**, 181301 (2012).

[10] G. F. Knoll, *Radiation Detection and Measurement*, 3rd ed. (John Wiley & Sons, Inc., 2000).

[11] Z. Liu, J. Chen, P. Zhu, Y. Li, and G. Zhang, Appl. Radiat. Isotopes **65**, 1318 (2007).

[12] A. Hotzel, P. Thirolf, C. Ender, D. Schwalm, M. Mutterer, P. Singer, M. Klemens, J. P. Theobald, M. Hesse, F. Gnnenwein, and H. v. d. Ploeg, Z. Phys. A **356**, 299 (1996).

[13] I. Murata, I. Tsuda, R. Nakamura, S. Nakayama, M. Matsumoto, and H. Miyamaru, Prog. Nucl. Sci. Technol. **4**, 345 (2014).

[14] P. Sorensen *et al.* (XENON10 Collaboration), Nucl. Instrum. Methods **A601**, 339 (2009).

[15] M. Horn *et al.* (ZEPLIN-III Collaboration), Phys. Lett. B **705**, 471 (2011).

[16] E. Aprile *et al.* (XENON100 Collaboration), Phys. Rev. D **88**, 012006 (2013).

[17] E. Aprile, L. Baudis, B. Choi, K. L. Giboni, K. Lim, A. Manalaysay, M. E. Monzani, G. Plante, R. Santorelli, and M. Yamashita, Phys. Rev. C **79**, 045807 (2009).

[18] A. Manzur, A. Curioni, L. Kastens, D. N. McKinsey, K. Ni, and T. Wongjirad, Phys. Rev. C **81**, 025808 (2010).

[19] G. Plante, E. Aprile, R. Budnik, B. Choi, K.-L. Giboni, L. W. Goetzke, R. F. Lang, K. E. Lim, and A. J. Melgarejo Fernandez, Phys. Rev. C **84**, 045805 (2011).

[20] H. Cao *et al.* (SCENE Collaboration), Phys. Rev. D **91**, 092007 (2015).

[21] J. I. Collar, Phys. Rev. Lett. **110**, 211101 (2013).

[22] E. Aprile *et al.*, Astropart. Phys. **35**, 573 (2012).

[23] T. Alexander *et al.* (DarkSide Collaboration), J. Inst. **8**, C11021 (2013).

[24] D. S. Akerib *et al.* (LUX Collaboration), Phys. Rev. Lett. **112**, 091303 (2014).

[25] D. S. Akerib *et al.* (LZ Collaboration), (2015), arXiv:1509.02910 .

[26] J. Csikai, *CRC Handbook of Fast Neutron Generators*, Vol. 1 (CRC Press, Boca Raton, Florida, 1987).

[27] T. Joshi, S. Sangiorgio, V. Mozin, E. Norman, P. Sorensen, M. Foxe, G. Bench, and A. Bernstein, Nucl. Instrum. Methods **B333**, 6 (2014).

[28] T. H. Joshi, S. Sangiorgio, A. Bernstein, M. Foxe, C. Hagmann, I. Jovanovic, K. Kazkaz, V. Mozin, E. B. Norman, S. V. Pereverzev, F. Rebassoo, and P. Sorensen, Phys. Rev. Lett. **112**, 171303 (2014).

[29] P. Agnes *et al.* (DarkSide Collaboration), Phys. Lett. B **743**, 456 (2015).

[30] D. C. Malling, Ph.D. thesis, Brown University (2014).

[31] J. Angle *et al.* (XENON10 Collaboration), Phys. Rev. Lett. **100**, 021303 (2007).

[32] V. N. Lebedenko *et al.* (ZEPLIN-III Collaboration), Phys. Rev. D **80**, 052010 (2009).

[33] K. Shibata, O. Iwamoto, T. Nakagawa, N. Iwamoto, A. Ichihara, S. Kunieda, S. Chiba, K. Furutaka, N. Otuka, T. Ohasawa, T. Murata, H. Matsunobi, A. Zukeran, and S. K. J. Katakura, J. Nucl. Sci. Technol. **48**, 1 (2011).

[34] A. Hitachi, T. Takahashi, N. Funayama, K. Masuda, J. Kikuchi, and T. Doke, Phys. Rev. B **27**, 5279 (1983).

[35] J. Mock, N. Barry, K. Kazkaz, D. Stolp, M. Szydagis, M. Tripathi, S. Uvarov, M. Woods, and N. Walsh, J. Inst. **9**, T04002 (2014).

[36] J. Brodsky, Ph.D. thesis, Princeton University (2015).

[37] C. H. Faham, Ph.D. thesis, Brown University (2014).

[38] V. N. Solovov *et al.* (ZEPLIN-III Collaboration), IEEE Trans. Nucl. Sci. **59**, 3286 (2012).

[39] T. Doke and K. Masuda, Nucl. Instrum. Methods **A420**, 62 (1999).

[40] L. E. Strigari, New J. Phys. **11**, 105011 (2009).

[41] J. Billard, E. Figueroa-Feliciano, and L. Strigari, Phys. Rev. D **89**, 023524 (2014).

[42] R. J. Gaitskell, Private communication (2015).

[43] S. Agostinelli *et al.* (GEANT4 Collaboration), Nucl. Instrum. Methods **A506**, 250 (2003).

[44] C. Rhyne, Private communication (2016).

[45] M. B. Chadwick *et al.*, Nucl. Data Sheets **112**, 2887 (2011).

[46] F. Zwicky, Astrophys. J. **86**, 217 (1937).

[47] D. J. Eisenstein *et al.* (SDSS Collaboration), Astrophys. J. **633**, 560 (2005).

[48] D. Clowe, M. Bradač, A. H. Gonzalez, M. Markevitch, S. W. Randall, C. Jones, and D. Zaritsky, Astrophys. J. **648**, L109 (2006).

[49] F. Iocco, G. Mangano, G. Miele, O. Pisanti, and P. D. Serpico, Phys. Rep. **472**, 1 (2009).

[50] N. Suzuki *et al.* (The Supernova Cosmology Project), Astrophys. J. **746**, 85 (2012).

[51] A. Slosar *et al.*, J. Cosmol. Astropart. Phys. **2013**, 026 (2013).

[52] P. A. R. Ade *et al.* (Planck Collaboration), Astron. Astrophys. **571**, A16 (2014).

[53] R. J. Gaitskell, Annu. Rev. Nucl. Part. Sci. **54**, 315 (2004).

[54] J. L. Feng, Annu. Rev. Astron. Astro. **48**, 495 (2010).

[55] J. Lewin and P. Smith, Astropart. Phys. **6**, 87 (1996).

[56] R. H. Helm, Phys. Rev. **104**, 1466 (1956).

[57] D. S. Akerib *et al.*, Phys. Rev. Lett. **116**, 161302 (2016).

[58] D. S. Akerib *et al.* (LUX Collaboration), Nucl. Instrum. Methods **A704**, 111 (2013).

[59] D. S. Akerib *et al.* (LUX collaboration), "Calibration, event reconstruction, data analysis and limits calculation for the LUX dark matter experiment," (2016), in preperation.

[60] C. H. Faham, V. M. Gehman, A. Currie, A. Dobi, P. Sorensen, and R. Gaitskell, J. Inst. **10**, P09010 (2015).

[61] S. Kubota, M. Hishida, and J. Raun, J. Phys. C: Solid State Phys. **11**, 2645 (1978).

[62] E. Aprile and T. Doke, Rev. Mod. Phys. **82**, 2053 (2010).

[63] A. Hitachi, Astropart. Phys. **24**, 247 (2005).

[64] C. M. B. Monteiro, L. M. P. Fernandes, J. A. M. Lopes, L. C. C. Coelho, J. F. C. A. Veloso, J. M. F. dos Santos, K. Giboni, and E. Aprile, J. Inst. **2**, P05001 (2007).

[65] https://github.com/BrownParticleAstro/, Brown Particle Astrophysics Group GitHub.

[66] C. E. Dahl, Ph.D. thesis, Princeton University (2009).

[67] T. Shutt, C. E. Dahl, J. Kwong, A. Bolozdynya, and P. Brusov, Nucl. Phys. B (Proc. Suppl.) **173**, 160 (2007).

[68] J. Lindhard, V. Nielsen, M. Scharff, and P. V. Thomsen, Mat. Fys. Medd. Dan. Vid. Selsk. **33** (1963).

[69] P. Sorensen and C. E. Dahl, Phys. Rev. D **83**, 063501 (2011).

[70] P. Sorensen *et al.* (XENON10 Collaboration), in *PoS(IDM2010)017* (2010) arXiv:1011.6439 .

[71] M. J. Berger, J. H. Hubbell, S. M. Seltzer, J. Chang, J. S. Coursey, R. Sukumar, D. S. Zucker, and K. Olsen, "XCOM: Photon cross sections database," National Institute of Standards and Technology, Gaithersburg, MD. (2010), http://physics.nist.gov/xcom.

[72] D. S. Akerib *et al.* (LUX Collaboration), Phys. Rev. D **93**, 072009 (2016).

[73] D. S. Akerib *et al.* (LUX collaboration), Astropart. Phys. **45**, 34 (2013).

[74] P. Phelps, Ph.D. thesis, Case Western Reserve University (2015).

[75] A. W. Bradley, Ph.D. thesis, Case Western Reserve University (2014).

[76] D.-M. Mei and A. Hime, Phys. Rev. D **73**, 053004 (2006).

[77] C. Lee, Ph.D. thesis, Case Western Reserve University (2015).

[78] D. S. Akerib *et al.* (LUX Collaboration), (2016), arXiv:1605.03844 .

[79] P. Benetti *et al.*, Nucl. Instrum. Methods **A574**, 83 (2007).

[80] D. S. Akerib *et al.* (LUX collaboration), Nucl. Instrum. Methods **A668**, 1 (2012).

[81] J. Chapman, Ph.D. thesis, Brown University (2014).

[82] D. Akerib *et al.* (LUX Collaboration), Nucl. Instrum. Methods **A818**, 57 (2016).

[83] "Globus," https://www.globus.org/.

[84] L. W. Kastens, S. B. Cahn, A. Manzur, and D. N. McKinsey, Phys. Rev. C **80**, 045809 (2009).

[85] A. Manalaysay, T. M. Undagoitia, A. Askin, L. Baudis, A. Behrens, A. D. Ferella, A. Kish, O. Lebeda, R. Santorelli, D. Ve'nos, and A. Vollhardt, Rev. Sci. Instrum. **81**, 073303 (2010).

[86] M. Szydagis, A. Fyhrie, D. Thorngren, and M. Tripathi, J. Inst. **8**, C10003 (2013).

[87] F. Bezrukov, F. Kahlhoefer, and M. Lindner, Astropart. Phys. **35**, 119 (2011).

[88] J. H. Vainionpaa, J. L. Harris, M. A. Piestrup, C. K. Gary, D. L. Williams, M. D. Apodaca, J. T. Cremer, Q. Ji, B. A. Ludewigt, and G. Jones, in *AIP Conference Proceedings*, 1525 (2013) pp. 118–122.

[89] J. Vainionpaa, C. Gary, J. Harris, M. Piestrup, R. Pantell, and G. Jones, Physics Procedia **60**, 203 (2014).

[90] F. J. Wilkinson and F. E. Cecil, Phys. Rev. C **31**, 2036 (1985).

[91] A. Poon, Private communication (2013).

[92] *Neutron generators for analytical purposes*, IAEA Radiation Technology Reports, Vol. 1 (International Atomic Energy Agency, 2012).

[93] "Adelphi Technology," Private communication (2015).

[94] H. Chagani, P. Majewski, E. J. Daw, V. A. Kudryavtsev, and N. J. C. Spooner, J. Inst. **3**, P06003 (2008).

[95] J. I. Collar, Phys. Rev. C **88**, 035806 (2013).

[96] M. J. Oreglia, Ph.D. thesis, SLAC (1980).

[97] J. E. Gaiser, Ph.D. thesis, SLAC (1982).

[98] T. Skwarnicki, Ph.D. thesis, DESY (1986).

[99] D. M. Santos and F. Dupertuis, Nucl. Instrum. Methods **A764**, 150 (2014).

[100] J. R. Verbus, "Neutron generator operation," (2014), (LCP-018, DocRev 12).

[101] "Title 10, code of federal regulations," Nuclear Regulatory Commission (2016).

[102] "Backgrounder on tritium, radiation protection limits, and drinking water standards," Nuclear Regulatory Commission (2016), http://www.nrc.gov/reading-rm/doc-collections/fact-sheets/tritium-radiation-fs.html.

[103] D. Huang, Ph.D. thesis, Brown University (2018).

[104] T. L. Johnson *et al.*, in *Proceedings of the American Nuclear Society Topical Meeting on Theory and Practices in Radiation Protection and Shielding* (1987).

[105] D. E. Hankins, *A neutron monitoring instrument having a response approximately proportional to the dose rate from thermal to 7.0 MeV*, Tech. Rep. LA-2717 (Los Alamos Nat. Lab., Los Alamos, NM, 1962).

[106] J. W. Marsh, D. J. Thomas, and M. Burke, Nucl. Instrum. Methods **A366**, 340 (1995).

[107] R. Martin, J. Knauer, and P. Balo, Appl. Radiat. Isotopes **53**, 785 (2000).

[108] P. R. Coelho, A. A. D. Silva, and J. R. Maiorino, Nucl. Instrum. Methods **A280**, 270 (1989).

[109] M. Koçak, H. Ahmadov, and G. Dere, Ann. Nucl. Energy **70**, 82 (2014).

[110] H. Hsu, K. Alvar, and D. Vasilik, IEEE Trans. Nucl. Sci. **41**, 938 (1994).

[111] S. Garny, V. Mares, and W. Rhm, Nucl. Instrum. Methods **A604**, 612 (2009).

[112] C. Jing, J. Xiaofei, J. Chunyu, C. Hongrui, and Y. Zejie, Plasma Sci. Technol. **17**, 80 (2005).

[113] D. S. Akerib *et al.* (LUX collaboration), Nucl. Instrum. Methods **A675**, 63 (2012).

[114] A. S. Eddington, Mon. Not. R. Astron. Soc. **73**, 359 (1913).

[115] A. S. Eddington, Mon. Not. R. Astron. Soc. **100**, 354 (1940).

[116] P. Teerikorpi, Astron. Astrophys. **424**, 73 (2004).

[117] P. Sorensen, Nucl. Instrum. Methods **A635**, 41 (2011).

[118] B. Lenardo, K. Kazkaz, A. Manalaysay, J. Mock, M. Szydagis, and M. Tripathi, IEEE Trans. Nucl. Sci. **62**, 3387 (2015).

[119] R. Barlow, Nucl. Instrum. Methods **A297**, 496 (1990).

[120] G. D'Agostini, (2004), arXiv:physics/0403086 .

[121] E. Aprile, C. E. Dahl, L. de Viveiros, R. J. Gaitskell, K. L. Giboni, J. Kwong, P. Majewski, K. Ni, T. Shutt, and M. Yamashita, Phys. Rev. Lett. **97**, 081302 (2006).

[122] B. Lenardo and M. Szydagis, Private communication (2015), development of new NEST model based upon LUX D-D measured nuclear recoil yields.

[123] C. Carmona and C. Nehrkorn, Private communication (2015), ran LUXSim simulations using LUX measured D-D nuclear recoil yields.

[124] K. Kazkaz, Private communication (2016).

[125] W. H. Press, S. A. Teukolsky, W. T. Vetterling, and B. P. Flannery, *Numerical Recipes in C: The Art of Scientific Computing*, 2nd ed. (Cambridge University Press, 2002).

[126] C. Silva, Private communication.

[127] S. Chan, Ph.D. thesis, Brown University (2018).

[128] "Eddington versus malmquist," The AstroStat Slog (2008), http://hea-www.harvard.edu/AstroStat/slog/groundtruth.info/AstroStat/slog/2008/eddington-versus-malmquist/index.html.

[129] E. Pease, Private communication (2014).

[130] A. Robinson, Private communication (2014).

[131] A. Dobi, Ph.D. thesis, University of Maryland (2014).

[132] L. Baudis, H. Dujmovic, C. Geis, A. James, A. Kish, A. Manalaysay, T. M. Undagoitia, and M. Schumann, Phys. Rev. D **87**, 115015 (2013).

[133] S. Stephenson, J. Haefner, Q. Lin, K. Ni, K. Pushkin, R. Raymond, M. Schubnell, N. Shutty, G. Tarlé, C. Weaverdyck, and W. Lorenzon, J. Inst. **10**, P10040 (2015).

[134] J. F. Ziegler, J. P. Biersack, and U. Littmark, *The Stopping and Range of Ions in Solids* (Pergamon New York, 1985).

[135] A. Manalaysay, (2010), arXiv:1007.3746 .

[136] R. Agnese *et al.* (SuperCDMS Collaboration), Phys. Rev. Lett. **112**, 241302 (2014).

[137] R. Agnese *et al.* (SuperCDMS Collaboration), Phys. Rev. Lett. **116**, 071301 (2016).

[138] M. Xiao *et al.* (PandaX Collaboration), Sci. China Phys. Mech. Astron. **57**, 2024 (2014).

[139] D. Akimov *et al.* (COHERENT Collaboration), (2015), arXiv:1509.08702 .

[140] W. C. Haxton, R. G. H. Robertson, and A. M. Serenelli, Annu. Rev. Astron. Astro. **51**, 21 (2013).

[141] A. Dobi, Private communication (2016).

[142] E. Aprile, K. Giboni, P. Majewski, K. Ni, and M. Yamashita, IEEE Trans. Nucl. Sci. **51**, 1986 (2004).

[143] J. Angle *et al.*, Phys. Rev. Lett. **107**, 051301 (2011).

[144] C. Chasman, K. W. Jones, H. W. Kraner, and W. Brandt, Phys. Rev. Lett. **21**, 1430 (1968).

[145] K. W. Jones and H. W. Kraner, Phys. Rev. C **4**, 125 (1971).

[146] K. W. Jones and H. W. Kraner, Phys. Rev. A **11**, 1347 (1975).

[147] Y. Messous *et al.*, Astropart. Phys. **3**, 361 (1995).

[148] P. S. Barbeau, J. I. Collar, and O. Tench, J. Cosmol. Astropart. Phys. **2007**, 009 (2007).

[149] P. Barbeau, J. Collar, and P. Whaley, Nucl. Instrum. Methods **A574**, 385 (2007).

[150] S. M. Fallows, Ph.D. thesis, The University of Minnesota (2014).

[151] A. K. Soma *et al.* (TEXONO Collaboration), (2014), arXiv:1411.4802 .

[152] G. Gerbier *et al.*, Phys. Rev. D **42**, 3211 (1990).

[153] J. Tiffenberg, "Results from the antonella experiment," LOWECAL2015 (2015), https://kicp-workshops.uchicago.edu/2015-lowecal/depot/talk-tiffenberg-javier.pdf.

[154] P. Sorensen, Phys. Rev. D **91**, 083509 (2015).

[155] J. Lindhard, M. Scharff, and H. E. Schiott, Mat. Fys. Medd. Dan. Vid. Selsk. **33** (1963).

[156] J. I. Collar and D. N. McKinsey, (2010), arXiv:1005.0838 .

[157] D. E. Groom, N. V. Mokhov, and S. I. Striganov, At. Data Nucl. Data Tables **78**, 183 (2001).

[158] T. Suzuki, D. F. Measday, and J. P. Roalsvig, Phys. Rev. C **35**, 2212 (1987).

[159] T. N. Mamedov, V. G. Grebinnik, K. I. Gritsa, V. N. Duginov, V. A. Zhukov, V. G. Olshevski, and A. V. Stokov, JETP Letters **71**, 451 (2000).

[160] J. Beringer *et al.*, Phys. Rev. D **86**, 010001 (2012).